

## Partially Ionized Plasmas in Astrophysics

José Luis Ballester · Igor Alexeev ·  
Manuel Collados · Turlough Downes ·  
Robert F. Pfaff · Holly Gilbert · Maxim  
Khodachenko · Elena Khomenko · Ildar F.  
Shaikhislamov · Roberto Soler · Enrique  
Vázquez-Semadeni · Teimuraz Zaqarashvili

Received: date / Accepted: date

**Abstract** Partially ionized plasmas are found across the Universe in many different astrophysical environments. They constitute an essential ingredient of the solar atmosphere, molecular clouds, planetary ionospheres and protoplanetary disks,

---

J. L. Ballester  
Departament de Física & Institut d'Aplicacions Computacionals de Codi Comunitari (IAC<sup>3</sup>)  
Universitat de les Illes Balears  
E-07122 Palma de Mallorca (Spain)  
Tel.: +34 971 173228  
Fax: +34 971 173426  
E-mail: joseluis.ballester@uib.es

I. I. Alexeev  
Lomonosov Moscow State University Skobeltsyn Institute of Nuclear Physics (MSU SINP)  
leninskie Gory, 119992, Moscow, Russia  
Tel.: +7-495-9391036  
Fax: +7-495-9393553  
E-mail: iialexeev@mail.ru

M. Collados  
Instituto de Astrofísica de Canarias  
C/ Vía Láctea s/n  
La Laguna, 38205 Tenerife, (Spain)  
Tel.: +34 922 605317  
Fax: +34 922 605210  
E-mail: mcv@iac.es

T. Downes  
School of Mathematical Sciences, Dublin City University,  
Glasnevin, Dublin 9, Ireland  
Tel.: +353 1 700 5270  
Fax: +353 1 700 5786  
E-mail: turlough.downes@dcu.ie

R. F. Pfaff  
NASA/Goddard Space Flight Center  
Mail Code 674.0 Greenbelt, MD 20771 USA  
Tel.: +1 301 286 6328  
Fax. +1 301 286 1648  
E-mail: : Robert.F.Pfaff@nasa.gov

among other environments, and display a richness of physical effects which are not present in fully ionized plasmas. This review provides an overview of the physics of partially ionized plasmas, including recent advances in different astrophysical areas in which partial ionization plays a fundamental role. We outline outstanding observational and theoretical questions and discuss possible directions for future progress.

---

H. Gilbert

Solar Physics Laboratory Heliophysics Science Division  
Goddard Space Flight Center  
Mail Code 671 Greenbelt, MD 20771 (USA)  
Tel.: +1 301 286 3042  
Fax: +1 301 286 5348  
E-mail: holly.r.gilbert@nasa.gov

M. Khodachenko

Space Research Institute, Schmiedlstrasse 6, A-8042  
Austrian Academy of Sciences, Graz (Austria)  
Tel.: +43 +43-316-4120661  
Fax: +43 +43-316-4120690  
E-mail: maxim.khodachenko@oeaw.ac.at

E. Khomenko

Instituto de Astrofísica de Canarias  
C/ Vía Láctea s/n  
La Laguna, 38205 Tenerife, (Spain)  
Tel.: +34 922 605319  
Fax: +34 922 605210  
E-mail: khomenko@iac.es

I. F. Shaikhislamov

Institute of Laser Physics SB RAS  
Novosibirsk (Russia)  
E-mail: ildars@ngs.ru

R. Soler

Departament de Física & Institut d'Aplicacions Computacionals de Codi Comunitari (IAC<sup>3</sup>)  
Universitat de les Illes Balears  
E-07122 Palma de Mallorca (Spain)  
Tel.: +34 971 172391  
Fax: +34 971 173426  
E-mail: roberto.soler@uib.es

E. Vázquez-Semadeni

Instituto de Radioastronomía y Astrofísica (IRyA), UNAM. Campus Morelia. Apdp Postal  
3-72 (Xangari) Morelia Mich. 58089. México  
Tel.: +55 56232753  
Fax: + 55 56232726  
E-mail: e.vazquez@crya.unam.mx

T. V. Zaqarashvili

IGAM, Institute of Physics, University of Graz,  
Universitätsplatz 5, 8010 Graz (Austria)  
Tel.: +43 316 4120 672  
Fax: + 43 316 4120 690  
Abastumani Astrophysical Observatory at Ilia State University, 3/5 Cholokashvili avenue, 0162  
Tbilisi (Georgia)  
Space Research Institute, Austrian Academy of Sciences, Schmiedlstrasse 6, A-8042 Graz (Austria)  
E-mail: teimuraz.zaqarashvili@oeaw.ac.at

---

**Keywords** Plasmas · Magnetohydrodynamics · Sun · Molecular clouds · Ionospheres · Exoplanets

---

## 1 Introduction

Plasma pervades the Universe at all scales, and the term plasma universe was coined by Hannes Alfvén to point out the important role played by plasmas across the universe (Alfvén 1986). In general, the study of plasmas beyond Earth's atmosphere is called Plasma Astrophysics, and includes many different astrophysical environments such as the Sun, the heliosphere, magnetospheres of the Earth and the planets, the interstellar medium, molecular clouds, accretion disks, exoplanet atmospheres, stars and astrospheres, cometary tails, exoplanetary ionospheres, etc. In these environments, the ionization level varies from almost no ionization in cold regions to fully ionized in hot regions which, consequently, leads to a wide range of parameters being relevant to astrophysical plasmas. Furthermore, in some cases the plasma is influenced by, or coupled to, embedded dust, giving rise to dusty plasmas. While the use of non-ideal Magnetohydrodynamics (MHD for short) is relatively infrequent in solar physics, in recent years the study of partially ionized plasmas has become a hot topic because solar structures such as spicules, prominences, as well as layers of the solar atmosphere (photosphere and chromosphere), are made of partially ionized plasmas (PIP for short). On the other hand, considerable developments have taken place in the study of partially ionized plasmas applied to the physics of the interstellar medium, molecular clouds, the formation of protostellar discs, planetary magnetospheres/ionospheres, exoplanets atmospheres, etc. For instance, molecular clouds are mainly made up of neutral material which does not interact with magnetic fields. However, neutrals are not the only constituent of molecular clouds since there are also several types of charged species which do interact with magnetic fields. Furthermore, the charged fraction also interacts with the neutral material through collisions. These multiple interactions produce many different physical effects which may have a strong influence on star formation and molecular cloud turbulence. A further example can be found in the formation of dense cores in molecular clouds induced by MHD waves. Because of the low ionization fraction, neutrals and charged particles are weakly coupled and ambipolar diffusion plays an important role in the formation process. Even in the primeval universe, during the recombination era, when the plasma, from which all the matter of the universe was formed, evolved from fully ionized to neutral, it went through a phase of partial ionization. Partially ionized plasmas introduce physical effects which are not considered in fully ionized plasmas, for instance, Cowling's resistivity, isotropic thermal conduction by neutrals, heating due to ion/neutral friction, heat transfer due to collisions, charge exchange, ionization energy, etc., which are crucial to fully understand the behaviour of astrophysical plasmas in different environments. Therefore, in this comprehensive review we focus on the description of PIP in different astrophysical areas in which this type of plasmas play a key role. The scheme of the review is as follows: In the second, third and fourth sections, general equations for a multifluid magnetized plasma are introduced as well as MHD waves and numerical techniques suitable for numerical simulations including PIP; next, the remaining sections are devoted to describe the physics of PIP in astrophysical environments such as the solar atmosphere, planetary ionospheres, molecular clouds and exoplanets atmospheres and magnetospheres.

## 2 Formulation of the multifluid plasma description

### 2.1 Conservation equations for individual micro-states

It is assumed that a PIP is composed of multiple kind of particles such as electrons, ions that can have different ionization states  $l \geq 1$  and excited to states  $E \geq 0$ , neutral particles with  $l = 0$  and  $E \geq 0$ , as well as dust grains, positively or negatively charged with  $E = 0$ . The concept of a fluid can be applied separately to each of these components in all the environments of interest. Therefore the behavior of such a plasma can be described by a set of equations of mass, momentum and energy conservation for each of the components. Separate sets of equations can be written for particles in a given micro-state  $\{a|E\}$  corresponding to a given chemical element or dust grain  $a$  (the notation of a micro-state  $\{a|E\}$  reduces to just  $e$  for electrons). The conservation equations are derived as usual from the moments of Boltzmann equation and have the following form:

$$\frac{\partial \rho_{a|E}}{\partial t} + \nabla \cdot (\rho_{a|E} \mathbf{u}_{a|E}) = S_{a|E} \quad (1)$$

$$\frac{\partial (\rho_{a|E} \mathbf{u}_{a|E})}{\partial t} + \nabla \cdot (\rho_{a|E} \mathbf{u}_{a|E} \otimes \mathbf{u}_{a|E} + \hat{\mathbf{p}}_{a|E}) = \rho_{a|E} r_{a|E} (\mathbf{E} + \mathbf{u}_{a|E} \times \mathbf{B}) + \rho_{a|E} \mathbf{g} + \mathbf{R}_{a|E} \quad (2)$$

$$\begin{aligned} & \frac{\partial}{\partial t} \left( e_{a|E} + \frac{1}{2} \rho_{a|E} u_{a|E}^2 \right) + \nabla \cdot \left( \mathbf{u}_{a|E} (e_{a|E} + \frac{1}{2} \rho_{a|E} u_{a|E}^2) + \hat{\mathbf{p}}_{a|E} \mathbf{u}_{a|E} + \mathbf{q}_{a|E} \right) = \\ & = M_{a|E} + \frac{E_{a|E}}{m_a} S_{a|E} + \rho_{a|E} \mathbf{u}_{a|E} \mathbf{g} + \rho_{a|E} r_{a|E} \mathbf{u}_{a|E} \mathbf{E} \end{aligned} \quad (3)$$

In these equations,  $\hat{\mathbf{p}}_{a|E} = \rho_{a|E} \langle \tilde{\mathbf{c}}_{a|E} \otimes \tilde{\mathbf{c}}_{a|E} \rangle$  is the pressure tensor defined through random velocities,  $\tilde{\mathbf{c}}_{a|E}$ , taken with respect to the mean velocity of each individual component (note that this makes the system of reference for velocities different for all components). It is also assumed that velocities corresponding to different excitation states are the same for a given ionization state, but energies and number densities are different. The heat flow vector is given by  $\mathbf{q}_{a|E} = \frac{1}{2} \rho_{a|E} \langle \tilde{c}_{a|E}^2 \tilde{\mathbf{c}}_{a|E} \rangle$ . The variable  $e_{a|E}$  is the internal energy that makes up of thermal energy by random motion and potential energy of ionization/excitation states

$$e_{a|E} = \rho_{a|E} \langle \tilde{c}_{a|E}^2 \rangle / 2 + n_{a|E} E_{a|E} = \frac{3}{2} p_{a|E} + n_{a|E} E_{a|E}. \quad (4)$$

where  $p_{a|E}$  is the scalar pressure,  $p_{a|E} = \frac{1}{3} \rho_{a|E} \langle c_{a|E}^2 \rangle$ , and

$$r_{a|E} = q_{a|E} / m_{a|E} \quad (5)$$

is charge over mass ratio. The rest of the notation is standard.

The above equations are written in conservation form. The momentum conservation equation can be also rewritten as

$$\rho_{a|E} \frac{D\mathbf{u}_{a|E}}{Dt} = \rho_{a|E} r_{a|E} (\mathbf{E} + \mathbf{u}_{a|E} \times \mathbf{B}) + \rho_{a|E} \mathbf{g} - \nabla \cdot \hat{\mathbf{p}}_{a|E} + \mathbf{R}_{a|E} - \mathbf{u}_{a|E} S_{a|E}, \quad (6)$$

leading to appearance of the  $-\mathbf{u}_{a|E}S_{a|E}$  term on the right hand side. Similarly, the energy conservation equation can be written for the internal energy alone leading to

$$\frac{\partial e_{a|E}}{\partial t} + \nabla(\mathbf{u}_{a|E}e_{a|E} + \mathbf{q}_{a|E}) + \hat{\mathbf{p}}_{a|E} \nabla \mathbf{u}_{a|E} = Q_{a|E} \quad (7)$$

Generally speaking, conservation equations as above can be written as well for photons as another type of fluid particles. However, since photons move at the speed of light and are mass-less, the conservation equations for them acquire the particular form of the radiative transfer equations (see, e.g., Mihalas 1986).

The source terms on the right-hand side of these equations result from collisions of particles in micro-state  $\{a|E\}$  with particles in other micro-states (generally including photons, or the radiation field), and are the mass collision term,  $S_{a|E}$ , the momentum collision term,  $\mathbf{R}_{a|E}$ , and the internal energy collision term,  $Q_{a|E}$ . The source terms either lead to appearance/disappearance of new particles (in the case of the mass conservation) and bring/remove momentum and energy to/from micro-state  $\{a|E\}$ . Expressions for these terms are obtained through collisional integrals of the distribution function  $f_{a|E}$  of particles in a given micro-state and depend on the particular physical conditions of the medium:

$$S_{a|E} = m_{a|} \int_V \left( \frac{\partial f_{a|E}}{\partial t} \right)_{\text{coll}} d^3v = \left( \frac{\partial \rho_{a|E}}{\partial t} \right)_{\text{coll}}, \quad (8)$$

$$\mathbf{R}_{a|E} = m_{a|} \int_V \mathbf{v} \left( \frac{\partial f_{a|E}}{\partial t} \right)_{\text{coll}} d^3v = \left( \frac{\partial [\rho_{a|E} \mathbf{u}_{a|E}]}{\partial t} \right)_{\text{coll}}, \quad (9)$$

$$\mathbf{R}_{a|E} - \mathbf{u}_{a|E} S_{a|E} = \left( \frac{\partial [\rho_{a|E} \mathbf{u}_{a|E}]}{\partial t} \right)_{\text{coll}} - \mathbf{u}_{a|E} \left( \frac{\partial \rho_{a|E}}{\partial t} \right)_{\text{coll}} = \rho_{a|E} \left( \frac{\partial \mathbf{u}_{a|E}}{\partial t} \right)_{\text{coll}}, \quad (10)$$

$$M_{a|E} = \frac{1}{2} m_{a|} \int_V v^2 \left( \frac{\partial f_{a|E}}{\partial t} \right)_{\text{coll}} d^3v = \left( \frac{\partial [\frac{1}{2} \rho_{a|E} u_{a|E}^2]}{\partial t} \right)_{\text{coll}} + \left( \frac{\partial [\frac{3}{2} p_{a|E}]}{\partial t} \right)_{\text{coll}}, \quad (11)$$

and

$$\begin{aligned} Q_{a|E} &= M_{a|E} - \mathbf{u}_{a|E} \mathbf{R}_{a|E} + \left( \frac{1}{2} u_{a|E}^2 + \frac{E_{a|E}}{m_{a|}} \right) S_{a|E} = \left( \frac{\partial [\frac{1}{2} \rho_{a|E} u_{a|E}^2]}{\partial t} \right)_{\text{coll}} + \\ &+ \left( \frac{\partial [\frac{3}{2} p_{a|E}]}{\partial t} \right)_{\text{coll}} - \mathbf{u}_{a|E} \left( \frac{\partial [\rho_{a|E} \mathbf{u}_{a|E}]}{\partial t} \right)_{\text{coll}} + \left( \frac{1}{2} u_{a|E}^2 + \frac{E_{a|E}}{m_{a|}} \right) \left( \frac{\partial \rho_{a|E}}{\partial t} \right)_{\text{coll}} = \\ &= \frac{1}{2} u_{a|E}^2 \left( \frac{\partial \rho_{a|E}}{\partial t} \right)_{\text{coll}} + \rho_{a|E} \mathbf{u}_{a|E} \left( \frac{\partial \mathbf{u}_{a|E}}{\partial t} \right)_{\text{coll}} + \left( \frac{\partial [\frac{3}{2} p_{a|E}]}{\partial t} \right)_{\text{coll}} - \\ &- u_{a|E}^2 \left( \frac{\partial \rho_{a|E}}{\partial t} \right)_{\text{coll}} - \rho_{a|E} \mathbf{u}_{a|E} \left( \frac{\partial \mathbf{u}_{a|E}}{\partial t} \right)_{\text{coll}} + \frac{1}{2} u_{a|E}^2 \left( \frac{\partial \rho_{a|E}}{\partial t} \right)_{\text{coll}} + \\ &+ \frac{E_{a|E}}{m_{a|}} \left( \frac{\partial \rho_{a|E}}{\partial t} \right)_{\text{coll}} = \left( \frac{\partial [\frac{3}{2} p_{a|E}]}{\partial t} \right)_{\text{coll}} + E_{a|E} \left( \frac{\partial n_{a|E}}{\partial t} \right)_{\text{coll}} = \\ &= \left( \frac{\partial e_{a|E}}{\partial t} \right)_{\text{coll}}. \end{aligned} \quad (12)$$

It is interesting to note the difference between the terms  $\mathbf{R}_{a|E} - \mathbf{u}_{a|E} S_{a|E}$  and  $\mathbf{R}_{a|E}$ , as well as between  $M_{a|E}$  and  $Q_{a|E}$ .  $\mathbf{R}_{a|E} - \mathbf{u}_{a|E} S_{a|E}$  represents the momentum change exclusively due to velocity variation by collisions, while  $\mathbf{R}_{a|E}$  gives the total momentum exchange. Concerning the energy terms,  $M_{a|E}$  provides losses/gains of

thermal ( $\frac{3}{2}p_{aE}$ ) and kinetic ( $\frac{1}{2}\rho_{aE}u_{a1}^2$ ) energies due to collisions and  $Q_{aE}$  is the rate of internal (i.e., thermal plus excitation) energy variation.

The above equations are written for particles at different excitation states. Such level of detail is necessary when considering interactions with the radiation field (see Khomenko et al. 2014a), but is possibly too detailed for most of the practical astrophysical applications. Therefore, the general way to proceed is to add up equations for all excitation states of a particle  $a$  in a given ionization state  $l$ . This provides the following system of equations:

$$\frac{\partial \rho_{a1}}{\partial t} + \nabla(\rho_{a1}\mathbf{u}_{a1}) = S_{a1}, \quad (13)$$

$$\frac{\partial(\rho_{a1}\mathbf{u}_{a1})}{\partial t} + \nabla(\rho_{a1}\mathbf{u}_{a1} \otimes \mathbf{u}_{a1} + \hat{\mathbf{p}}_{a1}) = \rho_{a1}r_{a1}(\mathbf{E} + \mathbf{u}_{a1} \times \mathbf{B}) + \rho_{a1}\mathbf{g} + \mathbf{R}_{a1}, \quad (14)$$

$$\begin{aligned} \frac{\partial}{\partial t} \left( e_{a1} + \frac{1}{2}\rho_{a1}u_{a1}^2 \right) + \nabla \left( \mathbf{u}_{a1}(e_{a1} + \frac{1}{2}\rho_{a1}u_{a1}^2) + \hat{\mathbf{p}}_{a1}\mathbf{u}_{a1} + \mathbf{q}_{a1} \right) = \\ = M_{a1} + \frac{E_{a1}}{m_a}S_{a1} + \rho_{a1}\mathbf{u}_{a1}\mathbf{g} + \rho_{a1}r_{a1}\mathbf{u}_{a1}\mathbf{E} \end{aligned} \quad (15)$$

with  $\hat{\mathbf{p}}_{a1} = \rho_{a1}\langle \tilde{\mathbf{c}}_{a1} \otimes \tilde{\mathbf{c}}_{a1} \rangle$ , and  $\mathbf{q}_{a1} = \frac{1}{2}\rho_{a1}\langle \tilde{\mathbf{c}}_{a1}^2 \tilde{\mathbf{c}}_{a1} \rangle$ .

This notation is usually simplified when dealing with particular cases of plasmas, e.g., those composed by hydrogen or hydrogen-helium or those containing grains.

## 2.2 Components of pressure tensor and viscosity

In the above equations the pressure tensor,  $\hat{\mathbf{p}}_{a1}$ , has been defined. Its diagonal components provide the scalar pressure, which in a general situation can be anisotropic and depend on the direction parallel and perpendicular to the magnetic field. The non-diagonal components of  $\hat{\mathbf{p}}_{a1}$  provide viscosity. The expressions for the components of the complete tensor for electrons and ions of a fully ionized plasma can be found in Braginskii (1965), see his equations (2.19–2.28), where he considered approximate expressions for the limiting cases of weak and strong magnetic field. For a PIP, Khodachenko et al. (2004, 2006) propose to modify the expressions given in Braginskii (1965) to include ion-neutral and ion-electron collisions.

The heat flow vector  $\mathbf{q}_{a1}$ , is given by:

$$\mathbf{q}_{a1} = -\hat{\kappa}_{a1}\nabla T_{a1}, \quad (16)$$

where  $\hat{\kappa}_{a1}$  is thermal conductivity tensor, and  $T_{a1}$  is the temperature of the plasma species  $a$ . Similarly, Braginskii (1965) provides expressions for the components of the electron and ion conductivity tensors of the fully ionized plasma (see his equations 2.10–2.16).

### 2.3 Collisional terms

Two different sub-sets of collisions are elastic and inelastic. If particle identity at the micro-state  $\{a|E\}$  is maintained during the collision, such collision is called “elastic”. For elastic collisions, the term  $S_{a|}$  is zero and the term  $\mathbf{R}_{a|}$  simplifies to a large extent.

Collisions that lead to creation/destruction of particles are called “inelastic”. Inelastic processes most relevant for the solar atmosphere are ionization, recombination, excitation and de-excitation. Charge-transfer processes, in which two colliding species modify their ionization state by exchanging an electron as a result of the interaction, also belong to this type of interaction. Chemical reactions, if they occur, are also inelastic collisions. In a general case, the collisional  $S$  term summed over all excitation states can be written in the following form

$$S_{a|} = \sum_E \sum_{|' \neq |, E'} (\rho_{a|'E'} P_{a|'E'|E} - \rho_{a|E} P_{a|E'|E'}), \quad (17)$$

where the  $P$ -terms are the probabilities of a transition between energy levels of the atom  $a$  that include radiative and collisional contributions. Their expressions depend on the particular atom and transition and can be found in standard tutorials on radiative transfer, see Carlsson (1986); Rutten (2003).

The sum of all  $S_{a|}$  terms over all possible micro-states and all possible species is zero if no nuclear reaction is taking place. Each particular  $S_{a|}$  term can also become zero if the plasma is in local thermodynamical equilibrium (LTE), i.e., when a detailed balance holds between the forward and backward transitions. The  $S_{a|}$  terms are usually neglected in applications to ionospheric and interstellar medium plasmas. In the solar atmosphere, LTE conditions are usually assumed in the photosphere. However, in the chromosphere the individual  $S_{a|}$  terms can not be neglected and contribute as source terms in their corresponding mass conservation equation (Carlsson and Stein 2002; Leenaarts et al. 2007).

The term  $\mathbf{R}_{a|E}$  provides the momentum exchange due to collisions of particles in the micro-state  $\{a|E\}$  with other particles and is the result of the variation induced by elastic and inelastic collisions:

$$\mathbf{R}_{a|E} = \mathbf{R}_{a|E}^{\text{el}} + \mathbf{R}_{a|E}^{\text{inel}}. \quad (18)$$

The expressions for elastic collisions between two particles of two different micro-states  $\{a|E\}$  and  $\{b|'E'\}$  (excluding photons) can be defined as:

$$\mathbf{R}_{a|E; b|'E'}^{\text{el}} = -\rho_{a|E} \rho_{b|'E'} K_{a|; b|'}(\mathbf{u}_{a|} - \mathbf{u}_{b|'}), \quad (19)$$

so that the total momentum transfer due to elastic collisions between particles of kind  $\{a|E\}$  with all other particles is given by

$$\mathbf{R}_{a|E}^{\text{el}} = -\rho_{a|E} \sum_{b|'E'} \rho_{b|'E'} K_{a|; b|'}(\mathbf{u}_{a|} - \mathbf{u}_{b|'}), \quad (20)$$

where

$$K_{a|; b|'} = \langle \sigma v \rangle_{a|; b|'} / (m_{a|} + m_{b|'}) , \quad (21)$$

and  $\sigma$  is the cross-section of the interaction and  $\langle \sigma v \rangle_{a|; b|'}$  the collisional rate between particles in microstate  $\{a|E\}$  and particles in microstate  $\{b|'E'\}$ , which can be reasonably assumed to be independent of the excitation state.



The total momentum transfer term due to elastic collisions, summing over all excitation states, is trivially obtained (with  $\nu_{aI;bI'} = \sum_{E'} \nu_{aIE;bI'E'} = \rho_{bI'} K_{aI;bI'}$ ):

$$\mathbf{R}_{aI}^{\text{el}} = - \sum_E \rho_{aIE} \sum_{bI'E'} \nu_{aIE;bI'E'} (\mathbf{u}_{aI} - \mathbf{u}_{bI'}) = -\rho_{aI} \sum_{bI'} \nu_{aI;bI'} (\mathbf{u}_{aI} - \mathbf{u}_{bI'}). \quad (22)$$

The momentum transfer due to inelastic radiative collisions follows from Eq. 17, taking into account the velocity of the particle that has appeared or disappeared due to the absorption or emission of a photon:

$$\mathbf{R}_{aI}^{\text{inel,rad}} = \sum_E \sum_{I' \neq I, E'} (\rho_{aI'E'} P_{aI'E'I} \mathbf{u}_{aI'} - \rho_{aIE} P_{aIE'I} \mathbf{u}_{aI}), \quad (23)$$

Inelastic collisional processes follow similar expressions for the momentum transfer as Eq. (22) for chemical reactions or general charge transfer interactions (Draine 1986). A special case of the latter collisions is that involving charge transfer between a neutral and a singly-ionized atom of the same chemical element (or, in general, charge transfer between two ionized states differing in one electron). In this case, there is no net mass variation (the corresponding S-term is zero for the species involved in the interaction) despite the change of nature of both particles (the ion becomes a neutral atom and vice versa) and the collision can be regarded as an elastic collision that also follows Eq. (22) with  $b = a$  and  $I' = I \pm 1$ . The cross-section of the charge-transfer interaction should be used in Eq. (21), which in general is larger than the elastic collisional cross-section.

A collisional frequency of interaction between two types of particles is usually defined as

$$\nu_{aIE;bI'E'} = \rho_{bI'E'} K_{aI;bI'}. \quad (24)$$

The notation containing explicit terms with the densities of the two interacting species leads to the symmetry condition  $K_{aI;bI'} = K_{bI';aI}$ , while for collisional frequencies one has that, in general,  $\nu_{aIE;bI'E'} \neq \nu_{bI'E';aIE}$ .

Collisional frequencies for momentum transfer between different species have been known for a long time. The expression differs depending on the nature of the colliding particles. The collisional frequency,  $\nu_{aI;b0}$ , between a neutral or a charged particle, in an ionization stage  $l$ , with neutral particles (i.e.,  $I' = 0$ ) has the following expression for Maxwellian velocity distributions with, in general, different temperatures for both species,  $T_{aI}$  and  $T_{b0}$ , (Braginskii 1965; Draine 1986):

$$\nu_{aI;b0} = n_{b0} \frac{m_{b0}}{m_{aI} + m_{b0}} \frac{4}{3} \sqrt{\frac{8k_B T_{aI}}{\pi m_{aI}} + \frac{8k_B T_{b0}}{\pi m_{b0}}} \sigma_{aI;b0}, \quad (25)$$

where  $\sigma_{aI;b0}$  is the cross-section of the interaction. The same equation can be applied for electrons as the charged particles. Temperature-dependent values of  $\sigma_{aI;b0}$ , including charge-transfer effects, have been calculated by Vranjes and Krstic (2013). For temperatures below 1 eV ( $\sim 10^4 K$ ), values range in the intervals  $\sigma_{H^+;H} = [0.5 - 2] \times 10^{-18} \text{ m}^2$ ,  $\sigma_{e^-;H} = \text{few} \times 10^{-19} \text{ m}^2$  for the  $H^+ - H$  and the  $e^- - H$  collisions, respectively (Khodachenko et al. 2004; Leake and Arber 2006; Soler et al. 2009a; Khomenko and Collados 2012). For large particles, such as interstellar medium dust grains, with sizes of the order of  $10^2 - 10^3 \text{ \AA}$  (Wardle and Ng 1999), a hard sphere model is taken with a cross-section equal to  $\pi a^2$ , where  $a$  is the size of the grains.

The expression corresponding to collisions between charged particles of species  $\{a\}$  and  $\{b'\}$  reads as (Braginskii 1965; Lifschitz 1989; Rozhansky and Tsedin 2001):

$$\nu_{a_i;b'} = \frac{n_{b'} I^2 I'^2 e^4 \ln \Lambda}{3\epsilon_0^2 m_{a_i;b'}^2} \left( \frac{2\pi k_B T_{a_i}}{m_{a_i}} + \frac{2\pi k_B T_{b'}}{m_{b'}} \right)^{-3/2}, \quad (26)$$

where  $m_{a_i;b'}$  is the reduced mass and  $\ln \Lambda$  is the Coulomb logarithm, where  $\Lambda$  is given by the expression (Bittencourt 1986)

$$\Lambda = \frac{12\pi(\epsilon_0 k_B T_e)^{3/2}}{n_e^{1/2} e^3}, \quad (27)$$

which leads to the usual expression

$$\ln \Lambda = 23.4 - 1.15 \log_{10} [n_e (\text{cm}^{-3})] + 3.45 \log_{10} [T_e (\text{eV})]. \quad (28)$$

Small deviations from this expression depending on the colliding species can be found in Huba (1998).

The term  $M_{a|E}$  includes (bulk and thermal) kinetic energy losses/gains of the particles of micro-state  $\{a|E\}$  due to collisions with other particles, and in general does not vanish. Draine (1986) gives expressions for the term  $Q_{a|E}$  (total thermal energy exchange by collisions) for different cases. In general,  $Q_{a|E}$  is a function of the difference in temperature between the colliding species and of the squared difference of their velocities.

## 2.4 Ohm's law

In the literature, the Ohm's law is frequently derived following Braginskii (1965) by using the electron momentum equation

$$\frac{\partial(\rho_e \mathbf{u}_e)}{\partial t} + \nabla(\rho_e \mathbf{u}_e \otimes \mathbf{u}_e + \hat{\mathbf{p}}_e) = \rho_e r_e (\mathbf{E} + \mathbf{u}_e \times \mathbf{B}) + \rho_e \mathbf{g} + \mathbf{R}_e, \quad (29)$$

In this approach, from the very beginning one neglects the electron inertia terms,  $\partial(\rho_e \mathbf{u}_e)/\partial t$ ,  $\nabla(\rho_e \mathbf{u}_e \otimes \mathbf{u}_e)$ , and the gravity acting on electrons,  $\rho_e \mathbf{g}$ . Such an approach is recently used in, e.g. Zaqarashvili et al. (2011a).

Here we provide a derivation of the Ohm's law in a more general situation for a plasma composed of an arbitrary number of positively and negatively charged and neutral species. Therefore, the strategy from Bittencourt (1986) and Krall and Trivelpiece (1973) is followed. In this approach the momentum equations of each species (Eq. 14) are multiplied by the charge over mass ratio (Eq. 5) and are summed up. So far, no force acting on particles is neglected, and electro-magnetic force, gravitational force, inertia terms and momentum exchange by collisions are all included. Since neutral species have zero charge, their contribution in such summation is null, and the final summation goes over  $N + 1$  charged components (where  $N$  is the number of ions and charged grains plus one electron component).

$$\begin{aligned} & \sum_{a,i \neq 0}^{N+1} \left( r_{a_i} \frac{\partial(\rho_{a_i} \mathbf{u}_{a_i})}{\partial t} + r_{a_i} \nabla(\rho_{a_i} \mathbf{u}_{a_i} \otimes \mathbf{u}_{a_i}) \right) = \\ & = \sum_{a,i \neq 0}^{N+1} \left( \rho_{a_i} r_{a_i}^2 (\mathbf{E} + \mathbf{u}_{a_i} \times \mathbf{B}) + \rho_{a_i} r_{a_i} \mathbf{g} - r_{a_i} \nabla \hat{\mathbf{p}}_{a_i} + r_{a_i} \mathbf{R}_{a_i} \right) \end{aligned} \quad (30)$$

The left hand side of this equation can be manipulated using the continuity equations. For that, the total current density is defined

$$\mathbf{J} = \sum_{a,l \neq 0}^{N+1} \rho_{al} r_{al} \mathbf{u}_{al} \quad (31)$$

Another useful parameter is drift velocities of species, defined as a difference between the individual velocity of a species with respect to the center of mass velocity of all charged species

$$\mathbf{w}_{al} = \mathbf{u}_{al} - \mathbf{u}_c \quad (32)$$

This way the general form of the Ohm's law is obtained:

$$\begin{aligned} \sum_{a,l \neq 0}^{N+1} \rho_{al} r_{al}^2 (\mathbf{E} + \mathbf{u}_{al} \times \mathbf{B}) &= \frac{\partial \mathbf{J}}{\partial t} + \nabla (\mathbf{J} \otimes \mathbf{u}_c + \mathbf{u}_c \otimes \mathbf{J}) + \\ + \nabla \sum_{a,l \neq 0}^{N+1} (\rho_{al} r_{al} \mathbf{w}_{al} \otimes \mathbf{w}_{al}) &+ \sum_{a,l \neq 0}^{N+1} r_{al} \nabla \hat{\mathbf{p}}_{al} - \sum_{a,l \neq 0}^{N+1} r_{al} \mathbf{R}_{al} \end{aligned} \quad (33)$$

The gravity term cancels out because of the charge neutrality. Up to now it is the most general form of the Ohm's law and no assumptions have been made except for the charge neutrality. Starting from this point particular version of the Ohm's law are to be considered.

#### 2.4.1 Solar atmosphere

In the case of the solar atmosphere, Eq. (33) can be simplified in several ways to make it of practical use. It is assumed that only singly ionized ions are present, since the abundance of the multiply ionized ones is small in the regions where the partial ionization of plasma is important. Separating the contribution of electrons with  $r_e = -e/m_e$ , the following equation is obtained:

$$\begin{aligned} \rho_e r_e^2 \left( \sum_{a,l=1}^N \frac{\rho_{al} r_{al}^2}{\rho_e r_e^2} + 1 \right) [\mathbf{E} + \mathbf{u}_c \times \mathbf{B}] &+ \rho_e r_e^2 \left( \sum_{a,l=1}^N \frac{n_{al} \mathbf{w}_{al}}{n_e} \left( 1 - \frac{r_{al}}{r_e} \right) \right) \times \mathbf{B} + \\ + r_e [\mathbf{J} \times \mathbf{B}] &= \frac{\partial \mathbf{J}}{\partial t} + \nabla (\mathbf{J} \otimes \mathbf{u}_c + \mathbf{u}_c \otimes \mathbf{J}) + \nabla \sum_{a,l \neq 0}^{N+1} (\rho_{al} r_{al} \mathbf{w}_{al} \otimes \mathbf{w}_{al}) + \\ + r_e \nabla \left( \sum_{a,l=1}^N \hat{\mathbf{p}}_{al} \frac{r_{al}}{r_e} + \hat{\mathbf{p}}_e \right) &- \sum_{a,l \neq 0}^N r_{al} \mathbf{R}_{al} \end{aligned} \quad (34)$$

The collisional term (see sect. 2.3) needs further simplification as the particular velocities of species have to be removed and expressed in terms of the average reference velocity of neutral and charge species. This brings us to the following expression:

$$\begin{aligned} \sum_{a,l \neq 0} r_{al} \mathbf{R}_{al} &\approx -\mathbf{J} \left( \sum_{a,l=1} \nu_{e;a1} + \sum_b \nu_{e;b0} \right) + \\ + e n_e (\mathbf{u}_c - \mathbf{u}_n) &\left( \sum_b \nu_{e;b0} - \sum_{a,l=1} \sum_b \nu_{al;b0} \right) \end{aligned} \quad (35)$$

where  $\mathbf{u}_n$  is used to denote the average center of mass velocity of the neutral species and  $\nu_{e;a1}$ ,  $\nu_{e;b0}$ ,  $\nu_{a1;b0}$  for collisional frequencies between electrons, neutral and ions as defined in the section above. In the expression above the terms containing  $\sum_a n_{a1}/n_e \mathbf{w}_{a1}$  were neglected, and it was assumed that the variation of the coefficient containing atomic mass of the colliding particles,  $\sqrt{(A_a + A_b)/A_a A_b}$  is weak and can also be neglected. This can be done in the particular case of the solar atmosphere since the abundance of the heavy atoms and their probability of collisions is not large (see Khomenko et al. (2014a)).

Finally, Eq. (34) is additionally simplified by assuming small electron to ion mass ratio  $r_{a1}/r_e = m_e/m_{a1} \approx 0$  and the following Ohm's law is obtained:

$$\begin{aligned} [\mathbf{E} + \mathbf{u}_c \times \mathbf{B}] &= \eta_H \frac{[\mathbf{J} \times \mathbf{B}]}{|\mathbf{B}|} - \eta_H \frac{\nabla \hat{\mathbf{p}}_e}{|\mathbf{B}|} + \eta \mathbf{J} - \chi(\mathbf{u}_c - \mathbf{u}_n) + \\ &+ \frac{\rho_e}{(en_e)^2} \left( \frac{\partial \mathbf{J}}{\partial t} + \nabla(\mathbf{J} \otimes \mathbf{u}_c + \mathbf{u}_c \otimes \mathbf{J}) \right) \end{aligned} \quad (36)$$

where magnetic resistivities are defined in units of  $ml^3/tq^2$  as

$$\eta = \frac{\rho_e}{(en_e)^2} \left( \sum_{a,l=1} \nu_{e;a1} + \sum_b \nu_{e;b0} \right); \quad \eta_H = \frac{|\mathbf{B}|}{en_e} \quad (37)$$

and the coefficient  $\chi$  has the same units as magnetic field,  $m/tq$ ,

$$\chi = \frac{\rho_e}{en_e} \left( \sum_b \nu_{e;b0} - \sum_{a,l=1} \sum_b \nu_{a1;b0} \right). \quad (38)$$

The charge velocity  $\mathbf{u}_c$  in the Ohm's law (see sect. 2.4) can be substituted for the ion velocity  $\mathbf{u}_i$ , by neglecting the contribution of electrons to the center of mass velocity of charged species.

Eq. (36) can be further modified for the cases of hydrogen and hydrogen-helium plasma. In the case of pure hydrogen plasma, the summation of the collision coefficients is not necessary since only one type of particle is present. The Ohm's law in Pandey and Wardle (2008); Zaqarashvili et al. (2011b) and Leake et al. (2014a) is obtained as above, with simplified expressions for some of the coefficients

$$\eta = \frac{\rho_e(\nu_{ei} + \nu_{en})}{(en_e)^2}; \quad \chi = \frac{\rho_e \nu_{en}}{en_e} \quad (39)$$

In the case of hydrogen-helium plasma one gets the Ohm's law similar to Zaqarashvili et al. (2011a) (except that terms  $D\mathbf{J}/Dt$  and the one proportional to  $(\mathbf{u}_i - \mathbf{u}_n)$  are not present because they were specifically neglected by the authors in that particular application) with  $\eta$  given by:

$$\eta = \frac{\rho_e(\nu_{eH^+} + \nu_{eHe^+})}{(en_e)^2} \quad (40)$$

The Ohm's law (Eq. 36) explicitly contains velocities of the charged and neutral components,  $\mathbf{u}_c$  (or  $\mathbf{u}_i$ ) and  $\mathbf{u}_n$ . Therefore it can be only applied in combination with the motion equations providing the velocities of these components. In the case of strongly collisionally coupled plasma, as in the case of the solar photosphere and

possibly low chromosphere, a more approximate and less general form of the Ohm's law is often used, where the individual velocities are eliminated in the favor of the center of mass velocity of the whole plasma, by applying an approximate expression using the motion equations. The relation between both reference systems is

$$[\mathbf{E} + \mathbf{u} \times \mathbf{B}] = [\mathbf{E} + \mathbf{u}_c \times \mathbf{B} - \xi_n \mathbf{w} \times \mathbf{B}] \quad (41)$$

where  $\xi_n = \rho_n/\rho$  is neutral fraction.

By neglecting the term  $\rho\xi_n(1-\xi_n)\partial\mathbf{w}/\partial t$  for processes slow compared to the typical collisional times, the following expression for the relative charge-neutral velocity is obtained,

$$\mathbf{w} = \mathbf{u}_c - \mathbf{u}_n \approx \frac{\xi_n}{\alpha_n} [\mathbf{J} \times \mathbf{B}] - \frac{\mathbf{G}}{\alpha_n} + \sum_b \frac{\rho_e \nu_{e;b0}}{en_e} \frac{\mathbf{J}}{\alpha_n} \quad (42)$$

where

$$\mathbf{G} = \xi_n \nabla \hat{\mathbf{p}}_c - \xi_i \nabla \hat{\mathbf{p}}_n \quad (43)$$

and

$$\alpha_n = \sum_b \rho_e \nu_{e;b0} + \sum_{a,i=1} \sum_b \rho_{ai} \nu_{ai;b0} \quad (44)$$

being  $\hat{\mathbf{p}}_c$  and  $\hat{\mathbf{p}}_n$  charged and neutral pressure tensors. Then, neglecting the terms proportional to the ratio of the electron to ion mass and the term  $D\mathbf{J}/Dt$ , the following Ohm's law is obtained:

$$\begin{aligned} [\mathbf{E} + \mathbf{u} \times \mathbf{B}] &= \eta_H \frac{[\mathbf{J} \times \mathbf{B}]}{|\mathbf{B}|} - \eta_H \frac{\nabla \hat{\mathbf{p}}_e}{|\mathbf{B}|} + \eta \mathbf{J} - \eta_A \frac{[(\mathbf{J} \times \mathbf{B}) \times \mathbf{B}]}{|\mathbf{B}|^2} \\ &+ \eta_p \frac{[\mathbf{G} \times \mathbf{B}]}{|\mathbf{B}|^2} \end{aligned} \quad (45)$$

where additional resistivity coefficients are defined as

$$\eta_A = \frac{\xi_n^2 |\mathbf{B}|^2}{\alpha_n}; \quad \eta_p = \frac{\xi_n |\mathbf{B}|^2}{\alpha_n} \quad (46)$$

In the Ohm's laws given by Eq. (36) and (45), the first three terms in common are Hall, battery and Ohmic terms. The fourth term in Eq. (45) proportional to  $[(\mathbf{J} \times \mathbf{B}) \times \mathbf{B}]$  is the ambipolar diffusion term that appears due to substitution of the charge velocity,  $\mathbf{u}_c$ , in the expression for electric field by the centre of mass velocity of the whole plasma,  $\mathbf{u}$  (see Eq. 41).

Various terms of the Ohm's law containing  $\mathbf{J}$  can be elegantly combined in a form of the conductivity tensor.

### 2.4.2 Ionosphere

The magnetosphere, ionosphere and thermosphere of the Earth are also characterized by similar transitions as solar atmosphere, ranging from highly ionized collisionless plasma in the magnetosphere (above approximately 400 km), to progressively more collisional (below 400 km) and neutral (below 150 km) plasma in the ionosphere (Song et al. 2001; Leake et al. 2014a). The ionosphere is therefore usually described as a three-fluid system. The chemical composition of the ionosphere, (usually divided into by F, E, and D layers), changes with height. In the lowest, D, layer the dominant neutral is molecular nitrogen ( $N_2$ ), while its dominant ion is nitric oxide ( $NO^+$ ); in the E layer in addition to nitrogen there appears molecular oxygen ions  $O_2^+$ ; in the highest F layer, atomic oxygen is dominant both in neutral and ionized states (Leake et al. 2014a). Therefore, only singly ionized contributors can be retained in Eq. (33), and approximations of  $m_e/m_{ai}$  and  $m_{ai} \approx m_{b0}$  can be made, leading to an equation similar to Eq. (36).

However, as discussed in many works, system of reference of the ions (i.e. using  $\mathbf{u}_i$  in Eq. 36) generally is not the best choice for a frame of reference in a weakly ionized ionospheric mixture with weak collisions (Song et al. 2001; Vasyliūnas 2012; Leake et al. 2014a). Therefore, for ionospheric applications, the plasma velocity in the Ohm's law (see sect.2.4) is replaced by the velocity of neutral particles. The relation between both reference systems is

$$[\mathbf{E} + \mathbf{u}_n \times \mathbf{B}] = [\mathbf{E} + \mathbf{u}_i \times \mathbf{B} - \mathbf{w} \times \mathbf{B}] \quad (47)$$

The following Ohm's law is obtained

$$\begin{aligned} [\mathbf{E} + \mathbf{u}_n \times \mathbf{B}] &= \eta_H \frac{[\mathbf{J} \times \mathbf{B}]}{|\mathbf{B}|} - \eta_H \frac{\nabla \hat{\mathbf{p}}_e}{|\mathbf{B}|} + \eta \mathbf{J} - \eta_A \frac{[(\mathbf{J} \times \mathbf{B}) \times \mathbf{B}]}{|\mathbf{B}|^2} \\ &+ \eta_p \frac{[\mathbf{G} \times \mathbf{B}]}{|\mathbf{B}|^2} \end{aligned} \quad (48)$$

with

$$\eta_A = \frac{\xi_n |\mathbf{B}|^2}{\alpha_n}; \quad \eta_p = \frac{|\mathbf{B}|^2}{\alpha_n} \quad (49)$$

and the rest of the resistive coefficients given by Eq. (37). This equation is similar to the Ohm's law in a neutral reference frame given in Leake et al. (2014a) (see their Eq. 33), when reduced to our notation and removing time derivatives of currents and drift velocity, with the resistivities given by:

$$\eta = \frac{\rho_e}{(en_e)^2} (\nu_{ei} + \nu_{en}); \quad \eta_A = \frac{2\xi_n |\mathbf{B}|^2}{\rho_i \nu_{in}}; \quad \eta_p = \frac{2|\mathbf{B}|^2}{\rho_i \nu_{in}} \quad (50)$$

taking into account that  $\alpha_n \approx \rho_i \nu_{in}$  (i.e. ignoring collisions with electrons), so the only difference are the two coefficients before the ambipolar and  $[\mathbf{G} \times \mathbf{B}]$  terms. Similar equation is also provided in Vasyliūnas (2012).

Note, that the choice of the system of reference affects the expression for ambipolar diffusion and the  $[\mathbf{G} \times \mathbf{B}]$  terms that can be seen by comparing the corresponding coefficients between Eqs. (46) and (50). The choice of the system of reference also affects the Joule heating, as discussed in Vasyliūnas and Song (2005); Leake et al. (2014a).

### 2.4.3 Interstellar medium (ISM)

In the case of the interstellar medium, the ionization degree may be very low and the center of mass velocity of the plasma is assumed to be that of neutrals. It is also assumed that the majority of collisions experienced by each charged particle will be with the neutral fluid, and so all other collisions can be neglected. In addition, inertia and pressure forces acting on charged particles is also neglected. In this case, the momentum equation for the charged species (Eq. 14) reduces to:

$$\rho_{a_i} r_{a_i} (\mathbf{E} + \mathbf{u}_{a_i} \times \mathbf{B}) + \mathbf{R}_{a_i} - \mathbf{u}_{a_i} S_{a_i} = 0 \quad (51)$$

In applications of weakly ionized plasmas of molecular clouds, the  $S_{a_i}$  terms are usually neglected assuming there is no mass charges between the species, which results in neglecting the charge exchange process.

According to Eq. (22) the total collisional term is equal to

$$\mathbf{R}_{a_i} = -\rho_{a_i} \rho_n K_{a_i;n} (\mathbf{u}_{a_i} - \mathbf{u}_n) \quad (52)$$

where only the collisions with the neutral species with its average speed  $\mathbf{u}_n$  are taken into account.

Similarly to the previous section, the electric field in ISM applications is expressed in the frame of reference of the neutral component, by defining

$$\mathbf{w}'_{a_i} = \mathbf{u}_{a_i} - \mathbf{u}_n \quad (53)$$

leading to the following momentum equation:

$$\rho_{a_i} r_{a_i} (\mathbf{E} + \mathbf{u}_n \times \mathbf{B} + \mathbf{w}'_{a_i} \times \mathbf{B}) - \rho_{a_i} \rho_n K_{a_i;n} \mathbf{w}'_{a_i} = 0 \quad (54)$$

Defining the coefficients

$$\beta_{a_i} = \frac{r_{a_i} |B|}{\rho_n K_{a_i;n}} \quad (55)$$

it becomes

$$(\mathbf{E} + \mathbf{u}_n \times \mathbf{B} + \mathbf{w}'_{a_i} \times \mathbf{B}) - \frac{|B|}{\beta_{a_i}} \mathbf{w}'_{a_i} = 0 \quad (56)$$

and the coefficients  $\beta_{a_i}$  are known as the Hall parameters. Manipulating this equation, summing it up over all the charged species, using the definition of current  $\mathbf{J} = \sum_a \rho_{a_i} r_{a_i} \mathbf{w}'_{a_i}$ , and taking into account charge neutrality, leads to the following Ohm's law (Falle 2003; Ciolek and Roberge 2002):

$$[\mathbf{E} + \mathbf{u}_n \times \mathbf{B}] = r_0 \frac{(\mathbf{J} \cdot \mathbf{B}) \mathbf{B}}{|B|^2} - r_1 \frac{\mathbf{J} \times \mathbf{B}}{|B|} + r_2 \frac{\mathbf{B} \times (\mathbf{J} \times \mathbf{B})}{|B|^2} \quad (57)$$

where the following resistive coefficients have been defined

$$r_0 \equiv \frac{1}{\sigma_{\parallel}}, \quad r_1 \equiv \frac{\sigma_H}{\sigma_{\perp}^2 + \sigma_H^2}, \quad r_2 \equiv \frac{\sigma_{\perp}}{\sigma_{\perp}^2 + \sigma_H^2} \quad (58)$$

$$\sigma_H \equiv \frac{1}{|B|} \sum_{a,l \neq 0} \frac{r_{al} \rho_{al} \beta_{al}^2}{(1 + \beta_{al}^2)} = -\frac{1}{|B|} \sum_{a,l \neq 0} \frac{r_{al} \rho_{al}}{(1 + \beta_{al}^2)} \quad (59)$$

$$\sigma_{\perp} \equiv \frac{1}{|B|} \sum_{a,l \neq 0} \frac{r_{al} \rho_{al} \beta_{al}}{(1 + \beta_{al}^2)} \quad (60)$$

$$\sigma_{\parallel} \equiv \frac{1}{|B|} \sum_{a,l \neq 0} r_{al} \rho_{al} \beta_{al} \quad (61)$$

The equality of both definitions of  $\sigma_H$  can be verified using the condition of charge neutrality,  $\sum r_{al} \rho_{al} = 0$ . These coefficients can be rewritten in the form similar to those defined above (see Eq. 37 and first equation in 46) in the case only one type of positively charged particles is present.

## 2.5 Induction equation

To get the induction equation, Ohm's law, together with the Faraday's law and Ampere's law are used, neglecting Maxwell's displacement current:

$$\frac{\partial \mathbf{B}}{\partial t} = -\nabla \times \mathbf{E}; \quad \mathbf{J} = \frac{1}{\mu} \nabla \times \mathbf{B} \quad (62)$$

A particular form of the induction equation depends on the frame of reference for the electric field. In the case the center of mass fluid velocity,  $\mathbf{u}$ , is taken as a reference, by using Eq. (45) one gets:

$$\frac{\partial \mathbf{B}}{\partial t} = \nabla \times \left[ (\mathbf{u} \times \mathbf{B}) - \eta_H \frac{[\mathbf{J} \times \mathbf{B}]}{|B|} + \eta_H \frac{\nabla \hat{\mathbf{p}}_e}{|B|} - \eta \mathbf{J} + \eta_A \frac{[(\mathbf{J} \times \mathbf{B}) \times \mathbf{B}]}{|B|^2} - \eta_p \frac{[\mathbf{G} \times \mathbf{B}]}{|B|^2} \right] \quad (63)$$

where the coefficients are defined by equations Eq. (37) and (46). For ionospheric applications, applying Eq. (62) to Eq. (48), replacing  $\mathbf{u}$  by  $\mathbf{u}_n$ , the average neutral velocity, and using the resistive coefficients given by Eq. (37) and Eq. (49), a similar induction equation can be obtained.

In the case of extremely weakly ionized plasmas such as the ISM, Ohm's law in the form of Eq. (57) is used leading to,

$$\frac{\partial \mathbf{B}}{\partial t} = \nabla \times \left[ (\mathbf{u}_n \times \mathbf{B}) - r_0 \frac{(\mathbf{J} \cdot \mathbf{B}) \mathbf{B}}{|B|^2} + r_1 \frac{\mathbf{J} \times \mathbf{B}}{|B|} - r_2 \frac{\mathbf{B} \times (\mathbf{J} \times \mathbf{B})}{|B|^2} \right] \quad (64)$$

where the coefficients are defined by Eq. (58) above.

Finally, using the average charged velocity,  $\mathbf{u}_c$ , as a reference, the use of Eq. 36 (neglecting  $D\mathbf{J}/Dt$  term) leads to

$$\frac{\partial \mathbf{B}}{\partial t} = \nabla \times \left[ (\mathbf{u}_c \times \mathbf{B}) - \eta_H \frac{[\mathbf{J} \times \mathbf{B}]}{|B|} + \eta_H \frac{\nabla \hat{\mathbf{p}}_e}{|B|} - \eta \mathbf{J} - \chi (\mathbf{u}_c - \mathbf{u}_n) \right] \quad (65)$$



## 2.6 Two-fluid and single-fluid description

Sect. 2.1 defined equations for particular charged and neutral components composing the plasma, see Eqs. (13), (14), and (15). In many applications it is convenient to sum these equations separately for charges and neutrals, leading to a two-fluid system of equations,

$$\frac{\partial \rho_n}{\partial t} + \nabla \cdot (\rho_n \mathbf{u}_n) = S_n \quad (66)$$

$$\frac{\partial \rho_c}{\partial t} + \nabla \cdot (\rho_c \mathbf{u}_c) = -S_n \quad (67)$$

$$\frac{\partial (\rho_n \mathbf{u}_n)}{\partial t} + \nabla \cdot (\rho_n \mathbf{u}_n \otimes \mathbf{u}_n + \hat{\mathbf{p}}_n) = \rho_n \mathbf{g} + \mathbf{R}_n \quad (68)$$

$$\frac{\partial (\rho_c \mathbf{u}_c)}{\partial t} + \nabla \cdot (\rho_c \mathbf{u}_c \otimes \mathbf{u}_c + \hat{\mathbf{p}}_c) = [\mathbf{J} \times \mathbf{B}] + \rho_c \mathbf{g} - \mathbf{R}_n \quad (69)$$

$$\begin{aligned} \frac{\partial}{\partial t} \left( e_n + \frac{1}{2} \rho_n u_n^2 \right) + \nabla \cdot \left( \mathbf{u}_n \left( e_n + \frac{1}{2} \rho_n u_n^2 \right) + \hat{\mathbf{p}}_n \mathbf{u}_n + \mathbf{q}'_n + \mathbf{F}_R^n \right) = \\ = \rho_n \mathbf{u}_n \mathbf{g} + M_n \end{aligned} \quad (70)$$

$$\begin{aligned} \frac{\partial}{\partial t} \left( e_c + \frac{1}{2} \rho_c u_c^2 \right) + \nabla \cdot \left( \mathbf{u}_c \left( e_c + \frac{1}{2} \rho_c u_c^2 \right) + \hat{\mathbf{p}}_c \mathbf{u}_c + \mathbf{q}'_c + \mathbf{F}_R^c \right) = \\ = \rho_c \mathbf{u}_c \mathbf{g} + \mathbf{J} \mathbf{E} - M_n \end{aligned} \quad (71)$$

where  $\mathbf{F}_R^n$  and  $\mathbf{F}_R^c$  are radiative energy fluxes for neutrals and charges, and  $\mathbf{q}'_n$  and  $\mathbf{q}'_c$  are heat flow vectors, corrected for ionization-recombination effects, see Khomenko et al. (2014a). The  $R$  terms for elastic collisions are given by:

$$\mathbf{R}_n \approx -\rho_e (\mathbf{u}_n - \mathbf{u}_e) \sum_b^N \nu_{e;b0} - \rho_i (\mathbf{u}_n - \mathbf{u}_i) \sum_{a,i=1}^N \sum_b^N \nu_{ai;b0} \quad (72)$$

and the rest of the collisional terms depend on the particular application.

This approach is valid when the the difference in behavior between neutrals and charges is larger than between the neutrals/charges of different kind themselves. The latter is a reasonable assumption given that only charges feel the presence of the magnetic field. However, different kinds of neutral (or charged) components themselves can also behave differently from one another because of the different inertia, which happens for the cases of weak collisional coupling (Zaqarashvili et al. 2011b). In that case, multi-fluid equations as in previous sections can be used.

The above equations are useful for solar and ionospheric applications. In the case of the ISM, the assumption of extremely weak ionization fraction allows us to simplify the system above. The ion inertia, energy and pressure are neglected. The radiation field-related effects and thermal conduction are also usually neglected, leading to the drop of the  $S$  terms,  $\mathbf{F}_R$  terms and  $\mathbf{q}$  terms. Gravity is usually not taken into account. Nevertheless, separate equations for different ions and grains are maintained, so strictly speaking the system of equations is multi-fluid, and not just two-fluid (Falle 2003; Ciolek and Roberge 2002; O'Sullivan and Downes 2006),

$$\frac{\partial \rho_n}{\partial t} + \nabla(\rho_n \mathbf{u}_n) = 0, \quad (73)$$

$$\frac{\partial \rho_{a_i}}{\partial t} + \nabla(\rho_{a_i} \mathbf{u}_{a_i}) = 0, \quad (74)$$

$$\frac{\partial \rho_n \mathbf{u}_n}{\partial t} + \nabla(\rho_n \mathbf{u}_n \otimes \mathbf{u}_n + \hat{\mathbf{p}}_n) = \mathbf{J} \times \mathbf{B}, \quad (75)$$

$$r_{a_i}(\mathbf{E} + \mathbf{u}_{a_i} \times \mathbf{B}) + \rho_n K_{a_i;n}(\mathbf{u}_{a_i} - \mathbf{u}_n) = 0 \quad (76)$$

$$\frac{\partial}{\partial t} \left( e_n + \frac{1}{2} \rho_n u_n^2 \right) + \nabla \left( \mathbf{u}_n \left( e_n + \frac{1}{2} \rho_n u_n^2 \right) + \hat{\mathbf{p}}_n \mathbf{u} \right) = \mathbf{J} \mathbf{E} + M_n \quad (77)$$

$$M_{a_i} + \rho_{a_i} r_{a_i} \mathbf{u}_{a_i} \mathbf{E} = 0, \quad (78)$$

Finally, in the case that collisional coupling is strong enough, a single fluid approach can be used, with an appropriate induction equation and Ohm's law:

$$\frac{\partial \rho}{\partial t} + \nabla(\rho \mathbf{u}) = 0 \quad (79)$$

$$\frac{\partial(\rho \mathbf{u})}{\partial t} + \nabla(\rho \mathbf{u} \otimes \mathbf{u} + \hat{\mathbf{p}}) = \mathbf{J} \times \mathbf{B} + \rho \mathbf{g} \quad (80)$$

$$\frac{\partial}{\partial t} \left( e + \frac{1}{2} \rho u^2 \right) + \nabla \left( \mathbf{u} \left( e + \frac{1}{2} \rho u^2 \right) + \hat{\mathbf{p}} \mathbf{u} + \mathbf{q}' + \mathbf{F}_R \right) = \mathbf{J} \mathbf{E} + \rho \mathbf{u} \mathbf{g} \quad (81)$$

### 3 Numerical approaches for partially ionized systems

There are significant challenges when moving from numerically solving the equations of ideal MHD to those of non-ideal, or multi-fluid, MHD (see sect. 2). The most well-known is that of the introduction of diffusive (parabolic) terms in the induction equation. However, depending on the philosophy of the approach being used one may also have to deal with very large signal speeds in the ions (for example in the case of weakly ionised, two-fluid approaches), and the Hall effect. The latter is a dispersive term which leads to a class of waves, known as Whistler waves, which have higher speeds for shorter wavelengths and for which  $\lim_{k \rightarrow \infty} \frac{\omega}{k} = \infty$ . All of these issues lead to short stable time-steps, at least for explicit schemes. Further, in many systems of astrophysical interest, studying the impact of these non-ideal effects leads to a requirement for high spatial resolution. The computational cost of high resolution simulations may mean the necessity of using massively parallel compute environments, and implicit numerical schemes are notoriously difficult to implement efficiently in such environments.

Typically, then, the goal will be to have an explicit scheme to deal with non-ideal, or multi-fluid, effects. The rest of this section will focus primarily on such schemes, although we will also point out possibilities for using implicit or semi-implicit schemes.

We begin our discussion of numerical methods for non-ideal and/or multi-fluid MHD systems by exploring the possibility of directly solving the full multi-fluid MHD equations, pointing out that in many systems of interest this would be an extremely computationally challenging task to perform accurately. We then point out the convenience of operator splitting approaches for extending any of the well-tested schemes for ideal MHD to non-ideal and multi-fluid MHD. If a sufficiently simple generalised Ohm's law can be written for the system of interest (see Sect. 2.4) we do not need to solve the Poisson equation for the electric field and so the non-ideal terms arise as either diffusive (parabolic) or dispersive (hyperbolic) terms in our equations. We thus discuss numerical approaches to diffusive terms. These are applicable to systems in which Ohmic and/or ambipolar diffusion are of interest. We go on to discuss methods of dealing with the Hall term. Finally we discuss the heavy ion approximation which is a rather different approach and can be used in situations where ambipolar diffusion is the only non-ideal process of interest.

#### 3.1 The full system of multi-fluid MHD equations

One can use existing standard discretisations to solve the full system of multi-fluid MHD equations, after making suitable approximations to enable evaluation of the induction equation (see sect. 2.5) combined with a generalised Ohm's law (see sect. 2.4). One might reasonably ask why this approach should not be used generally. Two of the most significant disadvantages of such an approach are the possibility of extremely high magnetic field mediated wave speeds in the charged species in the case where the ionisation fraction is low, and the stiffness of the system when the interaction terms in the momentum equations are large due to high collision frequencies or cross-sections. Both of these considerations lead to short time-steps being necessary for both accuracy and stability reasons, meaning

that both implicit and explicit schemes will lead to challenging computational requirements. As a general approach this is not promising.

In the case of protoplanetary disks, where the ionisation fraction can be of order  $10^{-8}$  or lower, the Alfvén speed in the charged species can be of order  $10^6$  m/s. Coupling between the charged species and the neutrals through collisions reduces the effective Alfvén speed by 4 orders of magnitude. Thus, for these systems, one has a very high signal speed and one relies on the stiff source terms in the system in order to reduce the propagation speed of waves to the correct speed. Numerically, this is fraught with danger arising from finite digit arithmetic in addition to any truncation errors associated with the scheme. The situation is not quite so difficult in the solar photosphere where the effective Alfvén speed and the Alfvén speed in the charged species differ by only 2 orders of magnitude, but it is nonetheless advisable to pursue other approaches which have a higher possibility of yielding computationally tractable equations. We also refer the reader to Sect. 3.3 for a description of a different approach in which the ion density is arbitrarily raised in order to reduce the Alfvén speed in the ions, making numerical solution of the two-fluid equations tractable in this case.

### 3.2 Operator Splitting

A most convenient way to extend an ideal MHD code to deal with non-ideal effects is through operator splitting. In this case we have a state vector at time level  $n$  and grid zone  $(i, j, k)$ ,  $U_{ijk}^n$  say, which we wish to update to time level  $n + 1$ . If we split our update into the effect of  $N$  different operators then we can write our update as

$$U_{ijk}^{n+1} = L_N L_{N-1} \cdots L_1 U_{ijk}^n \quad (82)$$

If we update  $U$  repeatedly in this fashion we have a truncation error of order  $\Delta t$  - i.e. a scheme which is first order in time. One can improve on this by permuting the operators appropriately (Strang 1968; Ryu et al. 1995). In this way one can achieve a scheme which is second order in time. In the situation under discussion here we can apply a standard ideal MHD scheme to our system as one operator, and then add in the non-ideal effects as one or more other operators.

### 3.3 Dealing with diffusive terms

It is well-known that the stable time-step for explicit schemes for diffusion (parabolic) equations is proportional to  $\Delta x^2$ . This makes the use of these schemes to investigate many systems of astrophysical interest impractical. As mentioned, it is natural to consider implicit schemes for such calculations, but these are computationally expensive and unsuited to massively parallel compute environments. Instead we pursue explicit schemes which are accelerated in some way so as to make their use practical.

*Super-Time-Stepping* Alexiades et al. (1996) drew attention to a widely overlooked method of accelerating explicit schemes for diffusion equations. First applied in an astrophysical context by O’Sullivan and Downes (2006, 2007), the method results

in a speed-up of the underlying scheme by using unstable (large) time-steps and stabilising the result by taking a sequence of short time-steps afterwards. The lengths of the time-steps are chosen using Chebyshev polynomials, making this scheme an example of a Chebyshev-Runge-Kutta scheme. If we write our numerical scheme as

$$\mathbf{U}^{n+1} = \mathbf{U}^n - \Delta t \mathbf{A} \mathbf{U}^n \quad (83)$$

then we have the usual time-step restriction of

$$\rho(\mathbf{I} - \Delta t \mathbf{A}) < 1 \quad (84)$$

where  $\rho$  is the spectral radius of its argument. Now let us consider a slightly different approach. Writing  $\Delta t = \sum_{i=1}^N \tau_i$  and only requiring stability over the time-step  $\Delta t$  and *not* over the individual time-steps  $\tau_i$ , we can write

$$\mathbf{U}^{n+1} = \left[ \prod_{i=1}^N (I - \tau_i A) \right] \mathbf{U}^n. \quad (85)$$

Our stability condition becomes

$$\rho \left( \prod_{i=1}^N (I - \tau_i A) \right) < 1, \quad (86)$$

and we can satisfy this inequality if

$$\left| \prod_{i=1}^N (I - \tau_i \lambda) \right| < 1, \quad (87)$$

for every eigenvalue,  $\lambda$ , of  $\mathbf{A}$ . We wish to have this condition satisfied while at the same time maximising the value of  $\Delta t$ . Making the choice

$$\tau_i = \Delta t_{\text{exp}} \left\{ (\nu - 1) \cos \left[ \frac{2i - 1}{N} \frac{\pi}{2} \right] + \nu + 1 \right\}^{-1} \quad i = 1 \dots N \quad (88)$$

where  $\nu$  and  $N$  are then free parameters which can be tuned to optimise the performance as desired and  $\Delta t_{\text{exp}}$  is the maximum stable time-step of the underlying scheme (for our purposes this would be the ideal MHD time-step). Letting  $\nu$  become small we find  $\lim_{\nu \rightarrow 0} \Delta t = N^2 \Delta t_{\text{exp}}$  and hence, recalling that we must take  $N$  time-steps to integrate from  $t$  to  $t + \Delta t$ , we get an overall speed-up of a factor  $N$ , the number of steps in our super-time-step. For good acceleration of the underlying scheme it is important to choose  $\nu$  small, but if it is too small then the scheme destabilises and produces meaningless results. Some sample values of  $\nu$  are given in Sect. 3.5 for specific systems. It should be realised that the values of  $\mathbf{U}^n$  at the intermediate time-steps do not have any approximation properties (i.e. they do not approximate the solution of the original differential equation in an obvious way). It is only the result after the composite ‘‘super-time-step’’,  $N^2 \Delta t_{\text{exp}}$ , which has the usual properties such as convergence. For appropriate choices of  $N$  and  $\nu$  (and double precision arithmetic) the inherently unstable nature of the intermediate values of  $\mathbf{U}$  has not proven to be an issue in a wide range of simulations (O’Sullivan and Downes 2006, 2007; Jones and Downes 2011; Downes and O’Sullivan 2011; Downes 2012; Gressel et al. 2013).

This scheme can be applied easily to the induction equation with either ambipolar or Ohmic resistivity, but has the drawback of being first order accurate in time. This can be dealt with using Richardson extrapolation (e.g. Press et al. 1992). This approach has since been used in many works (e.g. Mignone et al. 2007; Downes and O’Sullivan 2011; Jones and Downes 2011; Lee et al. 2011; Jones and Downes 2012; Downes 2012; Tsukamoto et al. 2013; Gressel et al. 2013).

An attempt to extend STS technique to the higher order was presented in Meyer et al. (2012) and used in, for example, Gressel et al. (2015). In the latter work a super-time-stepping scheme second order accurate in time was achieved. In this case, the technique relies on Legendre polynomials rather than Chebyshev polynomials and so is a Runge-Kutta-Legendre method. In common with the super-time-stepping algorithm above, this method is easy to implement on top of any existing scheme. A drawback is that it requires the simultaneous storage of 4 copies of the state vector throughout the grid. For large-scale simulations this requirement may be prohibitive. It also requires two evaluations of the diffusion operator for each sub-step (the first order method requires one, but this should be balanced with the need for Richardson extrapolation for the first order scheme), making it less efficient than the first order scheme as noted by Tsukamoto et al. (2013). An advantage is that it is possible to automate the choice of the number of sub-steps to be taken, rather than setting it as a parameter and hoping it is appropriate for the system under scrutiny.

*The Heavy Ion approximation* In systems such as molecular clouds (see sect.7) where ambipolar diffusion is believed to be the dominant non-ideal MHD mechanism one can represent the system as a two-fluid one: a neutral fluid and a charged fluid (see the discussion in sect. 2.6). In the case of molecular cloud simulations it is typical to write the induction equation as

$$\frac{\partial \mathbf{B}}{\partial t} = \nabla \times (\mathbf{u}_c \times \mathbf{B}). \quad (89)$$

with the resulting implication that the magnetic field and charged fluid are perfectly coupled. The lack of distinction between various charged fluids in this approach prevents detailed modeling of the Hall effect. In weakly ionised systems it can also result in very high Alfvén speeds since the density of the charged species is low and the Alfvén speed is given by  $v_A = \sqrt{\frac{B^2}{\mu\rho_c}}$  in appropriate MKS units. One then relies on the coupling terms,  $\mathbf{R}_n$ , to reduce the effective Alfvén speed through the bulk fluid. Numerically modeling such a system is extremely challenging: the high Alfvén speed leads to a very short time-step, while the strong coupling terms lead to a stiff set of equations.

In order to work around this one can adopt the following approach (introduced by Li et al. 2006). Since ambipolar diffusion occurs as a result of imperfect collisional coupling between the neutral and charged species, one might imagine that if the momentum transfer terms  $\mathbf{R}_n$  are calculated correctly then we should capture the evolution of the system properly. To reduce the Alfvén speed in the ions we would like them to have a higher mass density so we arbitrarily increase the mass of the ions, and reduce the cross section for collisions between neutrals and ions by the same factor. Then the size of  $\mathbf{R}_n$  is unaffected, while the Alfvén speed is reduced. Thus we adopt the “Heavy ion approximation”. This approach has been used in, for example, McKee et al. (2010), McKee et al. (2010) and Li et al. (2012).

There are some limitations of this approach. In a weakly ionised medium one can generally assume that the ion inertia is small. It must be ensured that when the mass of the ions is increased, it is done in such a way that the inertia of these “heavy” ions is still negligible. This yields the requirement that  $M_{A_c}^2 \ll R_{AD}(l_{u_c})$ , where  $M_{A_c}$  is the Mach number based on the Alfvén speed in the charged fluid and  $R_{AD}(l_{u_c})$  is the ambipolar Reynolds number at a length-scale  $l_{u_c}$ . As noted by Li et al. (2006), for flows with large gradients as in the case of turbulence this can be difficult to ensure (see, for example, Li et al. 2008, where it is only marginally satisfied in some of the simulations). The values of  $M_{A_i}^2/R_{AD}(l_{u_c})$  in this latter work are root-mean-square values and therefore it is difficult to tell whether this condition is satisfied throughout the grid at all times, as would be necessary for the approximation to be valid.

*Other methods* In situations where implicit schemes are acceptable, such as in cases where the use of massively parallel compute systems is not anticipated, one can adopt the approach of updating the ideal MHD system of equations using an explicit scheme and then performing an implicit update for the non-ideal terms (see, e.g., Falle 2003). Thus, denoting the ideal MHD operator as  $L_{\text{mhd}}$  and the operator for the non-ideal, or multi-fluid, effects as being  $L_{\text{mf}}$ , and using Strang splitting for two operators, the algorithm is

$$\mathbf{U}^{n+1/2} = L_{\text{mhd}}(\mathbf{U}^n), \quad (90)$$

$$\mathbf{U}^{n+3/2} = L_{\text{mf}}(\mathbf{U}^{n+1/2}, \mathbf{U}^{n+3/2}), \quad (91)$$

$$\mathbf{U}^{n+2} = L_{\text{mhd}}(\mathbf{U}^{n+3/2}). \quad (92)$$

where we note the implicit update in equation 91. This avoids all the time-step restrictions alluded to above although one is still required to restrict the time-step for accuracy, rather than stability, reasons. It is worth noting that O’Sullivan and Downes (2006) showed that for dynamically evolving systems, where accuracy constraints are non-negligible, the first order super-time-stepping method using Richardson extrapolation to achieve second order temporal accuracy, is faster than the mixed implicit, explicit scheme above.

### 3.4 The Hall term

The Hall term in the induction equation is one worthy of considerable attention when attempting to produce numerical solutions for systems in which it dominates over the other terms. As discussed in sections 2.4.1 and 2.5, this is a dispersive term which does not remove energy from the system and leads to waves with near infinite propagation speed for near zero wavelengths. Falle (2003) showed that a standard, centred difference approach to this term leads to a stable time-step,  $\Delta t_{\text{exp}}$ , of zero if the Hall term dominates other terms in the induction equation. Such dominance of the Hall term is thought to happen in, for example, certain regions of protoplanetary disks, near the surfaces of neutron stars (Hollerbach and Rüdiger 2002, 2004) and potentially in the solar photosphere (Sect. 5.1). Works prior to this in the field of star formation, such as Hollerbach and Rüdiger (2002), Sano and Stone (2002b), Sano and Stone (2002a), Ciolek and Roberge (2002), all used schemes which were subject to the severe stable time-step restriction noted

by Falle (2003). It is likely that many of these schemes successfully simulated the required systems only as a result of the presence of terms, such as Ohmic diffusion, in the governing equations which stabilised the numerical schemes employed.

Note that the stability limit above is much *worse* than what would be expected if one were to calculate the stable time-step on the basis of the propagation speed of the fastest wave in the system, as one is tempted to do based on the famous Courant-Friedrich-Lewy condition. Following this philosophy, since the Hall term gives rise to Whistler waves which have speed approximately inversely proportional to their wavelength and since the minimum wavelength representable on a grid with resolution  $\Delta x$  is  $2\Delta x$  one ends up with a stable time-step,  $\Delta t_{\text{exp}} \propto (\Delta x)^2$  and not identically zero. Thus the Hall term, when differenced naively results in an unexpectedly pathological difference equation. Nonetheless, two approaches have been devised which allow for explicit differencing of the Hall term while still retaining the usual (parabolic) time-step restriction.

*Hyper-diffusivity* In the field of space science particularly, the Hall term has been dealt with using standard explicit discretisations which are then stabilised using 4<sup>th</sup> or 6<sup>th</sup> order hyper-diffusivity, an analogue of the 2<sup>nd</sup> order artificial viscosity employed in shock-capturing advection schemes for inviscid systems (Yin et al. 2001; Ma and Bhattacharjee 2001). In this case, the term  $(\eta_{\text{hyp}} \nabla^2 \mathbf{J})$  is added onto  $\mathbf{E} + \mathbf{u}_e \times \mathbf{B}$ . While this can be argued to have physical origins, as indeed can the artificial viscosity used in shock-capturing schemes, it is nonetheless used to stabilise the underlying MHD scheme and not to reflect underlying physics.

In Tóth et al. (2008) a similar approach is put forward, and applied to block-adaptive mesh simulations, in which this hyper-diffusivity is effectively incorporated into the usual limiters used in TVD schemes so that it does not appear explicitly in the equations being solved. In solar physics, hyper-diffusivity is frequently used in magneto-convection simulations, as in Stein and Nordlund (1998), Caunt and Korpi (2001) and Vögler et al. (2005). There have been attempts to use it to deal with simulations including Hall term in the photosphere by Cameron et al. (2012) and Martínez-Sykora et al. (2012).

*The Hall Diffusion Scheme* Another approach which can be adopted is known as the Hall Diffusion Scheme, first introduced by O’Sullivan and Downes (2006) and extended to the 3D case in O’Sullivan and Downes (2007). While this was applied specifically to the Hall effect, the general philosophy is applicable to any equation of the form

$$\frac{\partial \mathbf{U}}{\partial t} = \frac{\partial}{\partial x} \left\{ \mathbf{R} \frac{\partial \mathbf{U}}{\partial x} \right\}, \quad (93)$$

where  $\mathbf{R}$  has zeroes on the diagonal. In the case of the Hall effect,  $\mathbf{R}$  is skew-symmetric and this is a special case of such operators.

Noting that  $\mathbf{R}$  has zeroes on its diagonal, we see that the instantaneous rate of change of any one component of  $\mathbf{B}$  depends only on the spatial gradients of the other two components. In order to illustrate the idea, let us take

$$\mathbf{R} = (-\mathbf{I})^{1/2} = \begin{pmatrix} 0 & 1 \\ -1 & 0 \end{pmatrix}, \quad (94)$$



for simplicity and assume our system is a 1D flow (with variation in the  $x$  direction only). Hence we can write

$$\frac{\partial B_y}{\partial t} = \frac{\partial^2 B_z}{\partial x^2} \quad (95)$$

$$\frac{\partial B_z}{\partial t} = -\frac{\partial^2 B_y}{\partial x^2} \quad (96)$$

and we can difference this as

$$\frac{(B_y)_i^{n+1} - (B_y)_i^n}{\Delta t} = \frac{(B_z)_{i+1}^n - 2(B_z)_i^n + (B_z)_{i-1}^n}{(\Delta x)^2} \quad (97)$$

$$\frac{(B_z)_i^{n+1} - (B_z)_i^n}{\Delta t} = -\frac{(B_y)_{i+1}^{n+1} - 2(B_y)_i^{n+1} + (B_y)_{i-1}^{n+1}}{(\Delta x)^2}, \quad (98)$$

yielding

$$(B_y)_i^{n+1} = (B_y)_i^n + \frac{\Delta t}{(\Delta x)^2} [(B_z)_{i+1}^n - 2(B_z)_i^n + (B_z)_{i-1}^n], \quad (99)$$

$$(B_z)_i^{n+1} = (B_z)_i^n - \frac{\Delta t}{(\Delta x)^2} [(B_y)_{i+1}^{n+1} - 2(B_y)_i^{n+1} + (B_y)_{i-1}^{n+1}]. \quad (100)$$

This appears to be a scheme which is implicit in some sense for  $B_z$ , but explicit for  $B_y$ . If the values of  $B_y$  are updated throughout the computational grid prior to updating  $B_z$  then the difference equations are explicit in the sense that no matrix inversions, or approximations of matrix inversions, are required. Thus this scheme, in common with the hyper-diffusivity approach, fulfills the requirement that it be easily and efficiently parallelisable to enable large-scale simulations on massively parallel systems. A potential advantage of the Hall Diffusion Scheme, though, is that no arbitrary parameters are required unlike the hyper-diffusivity schemes where  $\eta_{\text{hyp}}$  must be chosen.

Tóth et al. (2008) suggested that the Hall Diffusion Scheme is simply a two-step version of the usual one-step hyper-diffusivity approach of, for example, Ma and Bhattacharjee (2001). This, however, is a misinterpretation since in the hyper-diffusive approach one introduces the free parameter  $\eta_{\text{hyp}}$ , which must be chosen in a somewhat subjective manner, in order to over-power the instability arising from the nature of the truncation error in the underlying scheme. The Hall Diffusion Scheme is successful because its truncation error does not lead to instability in the first place.

### 3.5 A Numerical Test Suite

In this section we suggest a suite of numerical tests which might be useful in determining whether a code is producing sufficiently accurate results for a multi-fluid, or non-ideal, MHD system. We first suggest a suite of shock tube tests, the conditions for which are given in Table 1.

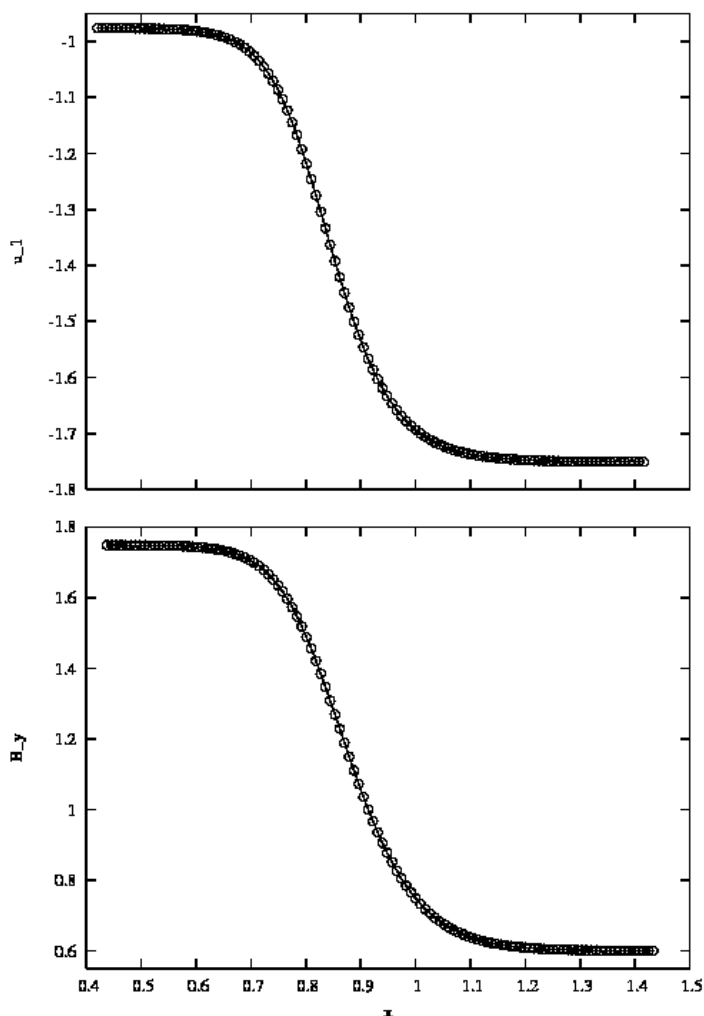


**Fig. 1** Numerical shock tube test, case A. Plots of the  $x$  component of the velocity and the  $y$  component of the magnetic field as functions of  $x$ . The solid line is a semi-analytic solution for the problem, while the circles are solution values from the HYDRA code.

*Shock tube tests* The first test presented suggested here is Case A from Falle (2003), also published in O’Sullivan and Downes (2006) and O’Sullivan and Downes (2007). It is an MHD shock tube test in a system in which ambipolar diffusion is significant. Under the particular conditions for this test we expect the shock to be fully smoothed out to a C-shock and there to be no discontinuities present. Since the solution is a single C-shock, the initial conditions are set to the left- and right- states, separated by a region in which a tanh function is used to interpolate smoothly between the two states. Recall that in multifluid MHD it is not possible to have discontinuities in the magnetic field and hence this interpolation

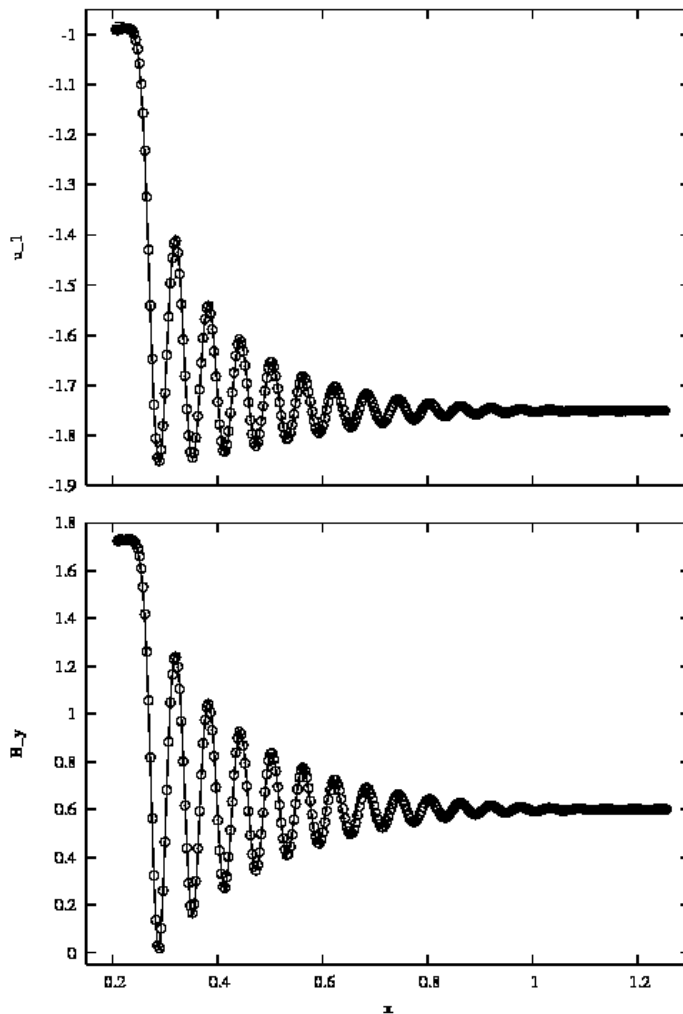


**Fig. 2** Numerical shock tube test, case B. The format of the figure is the same as Fig 1. The influence of the Hall effect, through the presence of a Whistler wave, is clearly visible in the solution.

is a rational thing to do. The system is then allowed to evolve until it reaches a steady state. Results are plotted for the HYDRA code, as presented in O’Sullivan and Downes (2007), compared with a semi-analytic solution of the same set of equations in figure 1.

The second test, Case B, is a Hall dominated system with the same left and right neutral states. In this case we expect the usual MHD shock to be broken down into a set of Whistler waves. The steady state solution will then only contain the whistler wave which has the same velocity as the MHD shock (see Fig. 2). The test presented here was also presented in O’Sullivan and Downes (2007) and is more highly Hall dominated than the Hall dominated test presented in Falle (2003).

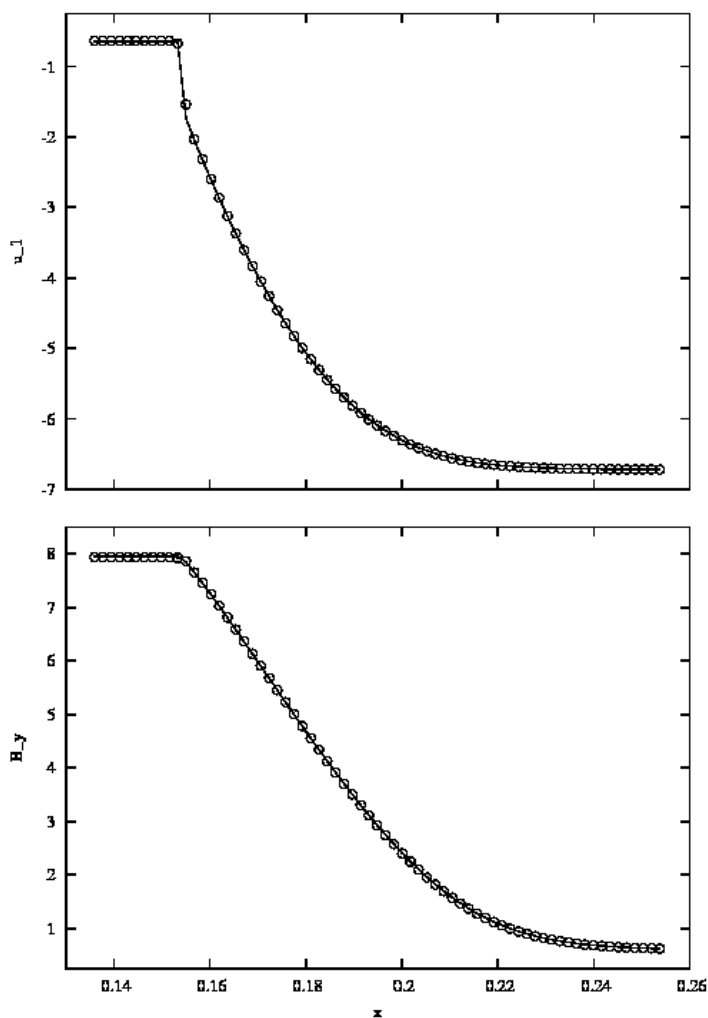


**Fig. 3** Numerical shock tube test, case C. The format of the figure is the same as Fig 1. A sub-shock (discontinuity) is visible in the velocity, but not in the magnetic field.

The third case, Case C, involves a flow which has a shock precursor and a sub-shock, in contrast to Case A in which the ambipolar diffusion is strong enough to completely smear out all the fluid variables. Since this test contains a discontinuity (see Fig. 3) it acts as a test of the shock-capturing abilities of the numerical scheme being employed.

*Test for Battery effect.* The Biermann battery effect is different from the other effects in the generalized Ohm's law. The presence of this term (usually small in most of the systems) does not present significant numerical problems, since it is only acting as a small source term. Nevertheless, it represents an interesting

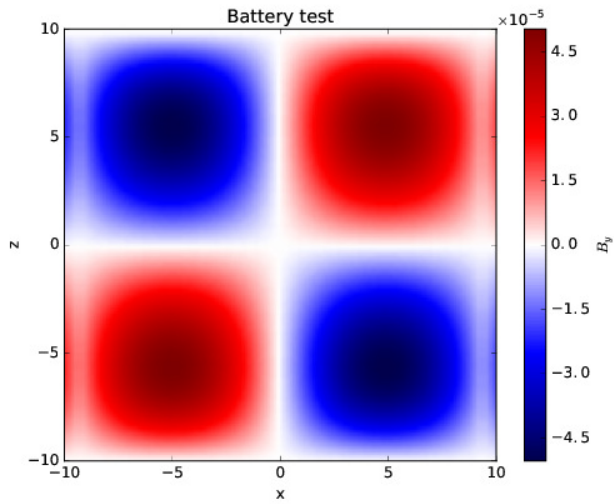


**Fig. 4** Numerical test for Biermann battery effect. Plot of the  $y$  component of the magnetic field after one time-step of the MANCHA code. The influence of the battery term is clearly reflected by the presence of a magnetic field.

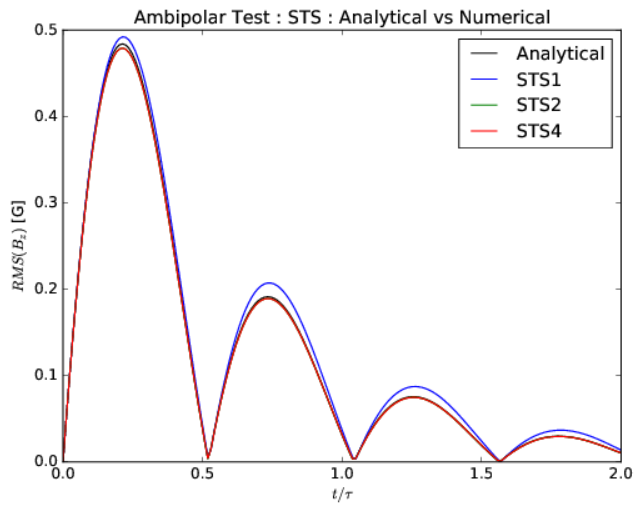


**Fig. 5** Numerical test for Alfvén wave decay in the presence of ambipolar diffusion. Plots of the RMS value of the  $z$  component of the magnetic field as a function of time. Plots are shown for both the analytic solution, as well as super-time-stepping combined with Runge-Kutta schemes of order 1, 2 and 4.

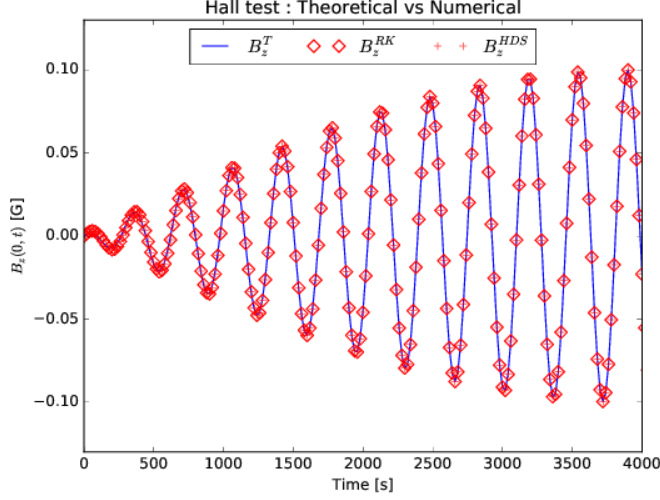


**Fig. 6** Numerical test for plane-polarized Alfvén wave in the presence of the Hall effect. The plot shows the  $z$  component of the magnetic field as a function of time. It can be seen that HDS and RK2 agree remarkably well both with each other and the analytic solution.

**Table 1** Conditions for the shock tube tests encompassing a flow containing a C-shocks a shock disrupted by the Hall effect and a flow containing a sub-shock. In each case the flow is assumed to have 3 fluids (one neutral, one positively charged and one negatively charged). Here we are assuming weak ionisation and so we ignore collisions between charged fluids, and only take account of collisions between charged and neutral fluids. We also explicitly ignore the ionisation state for the collision coefficients,  $K_{i;j}$ , and so we do not include them in the notation here for clarity. We assume that each charged species has a single ionisation state leading to a single charge-to-mass ratio,  $r_a$ , and so do not label this in the notation below. The units are chosen for numerical simplicity to be Gaussian scaled so that the speed of light and factors of  $4\pi$  do not appear.

Case A					
Right State	$\rho_1 = 1$	$\mathbf{u}_1 = (-1.751, 0, 0)$	$\mathbf{B} = (1, 0.6, 0)$	$\rho_2 = 5 \times 10^{-8}$	$\rho_3 = 1 \times 10^{-3}$
Left State	$\rho_1 = 1.7942$	$\mathbf{u}_1 = (-0.9759, -0.6561, 0)$	$\mathbf{B} = (1, 1.74885, 0)$	$\rho_2 = 8.9712 \times 10^{-8}$	$\rho_3 = 1.7942 \times 10^{-3}$
	$r_2 = -2 \times 10^{12}$	$r_3 = 1 \times 10^8$	$K_{2;1} = 4 \times 10^5$	$K_{3;1} = 2 \times 10^4$	$a = 0.1$
	$\nu = 0.05$	$N_{STS} = 5$	$N_{HDS} = 0$		
Case B					
Right State	As case A				
Left State	As case A				
	$r_2 = -2 \times 10^9$	$r_3 = 1 \times 10^5$	$K_{2;1} = 4 \times 10^2$	$K_{3;1} = 2.5 \times 10^6$	$a = 0.1$
	$\nu = 0$	$N_{STS} = 1$	$N_{HDS} = 8$		
Case C					
Right State	$\rho_1 = 1$	$\mathbf{u}_1 = (-6.7202, 0, 0)$	$\mathbf{B} = (1, 0.6, 0)$	$\rho_2 = 5 \times 10^{-8}$	$\rho_3 = 1 \times 10^{-3}$
Left State	$\rho_1 = 10.421$	$\mathbf{u}_1 = (-0.6449, -1.0934, 0)$	$\mathbf{B} = (1, 7.9481, 0)$	$\rho_2 = 5.2104 \times 10^{-7}$	$\rho_3 = 1.0421 \times 10^{-2}$
	$r_2 = -2 \times 10^{12}$	$r_3 = 1 \times 10^8$	$K_{2;1} = 4 \times 10^5$	$K_{3;1} = 2 \times 10^4$	$a = 1$
	$\nu = 0.05$	$N_{STS} = 15$	$N_{HDS} = 0$		

physical effect and allows the creation of magnetic field from misaligned gradients in density and pressure. It was used recently in the context of solar physics to seed the solar local dynamo by Felipe and Kholmenko (2017). To test how well the influence of the Biermann battery is captured we suggest a test from Tóth (2012). In this test a fluid is at rest without any magnetic field present. A perturbation in the electronic number density and pressure is imposed following

$$n_e = n_0 + n_1 \cos(k_x x), \quad (101)$$

$$p_e = p_0 + p_1 \cos(k_z z). \quad (102)$$

The misalignment between the pressure and density gradients will give rise to a current which will produce a magnetic field in the system. In the results presented in Fig 4 we choose  $n_0 = p_0 = 1$ ,  $n_1 = p_1 = 0.1$  and  $k_x = k_z = \pi/L$  with  $L = 10$ .

*Test for Alfvén waves decay*. It is well known that Alfvén waves decay in the presence of ambipolar diffusion. Fortunately this decay is relatively easy to determine analytically and so this serves as a good test of the treatment of ambipolar diffusion. Following Balsara (1996), the dispersion relation for Alfvén waves in this system is

$$\omega^2 + ik^2 \eta_A \omega - k^2 c_A^2 = 0, \quad (103)$$

where  $c_A$  is the usual Alfvén speed and  $k^2 = k_x^2 + k_y^2$ . This can easily be solved in the case where  $k_x = k_y$  to find that the decay rate,  $\omega_I = -k_x^2 \eta_A^2 / 2$ . Figure 5 contains the RMS of the  $z$  component of the magnetic field as a function of time.

*Test for Alfvén waves in the presence of Hall effect*. Finally, in addition to the shock tube proposed, we suggest a further test of the Hall effect as follows. The magnetic field associated with a plane-polarised Alfvén wave propagating along the  $x$ -axis in a fluid with Hall coefficient  $\eta_H$  obeys

$$B_x(x, t) = B_0, \quad (104)$$

$$B_y(x, t) = b \cos(\sigma t) \cos(kx) \cos(\omega t), \quad (105)$$

$$B_z(x, t) = b \sin(\sigma t) \cos(kx) \cos(\omega t), \quad (106)$$

where  $B_0$  is the magnitude of a guide field in the  $x$  direction,  $b$  is the (small) amplitude of the Alfvén wave, and  $\sigma = \eta_H k^2 / 2$ . We set  $\eta_H = 2.03 \times 10^7 \text{ m}^2 \text{ s}^{-1}$ ,  $B_0 = 100 \text{ G}$ ,  $T = 4000 \text{ K}$ ,  $b = 0.1 \text{ G}$ ,  $p_{\text{gas}} = 10 \text{ N m}^{-2}$ ,  $\rho = 10^{-6} \text{ kg m}^{-3}$  and finally  $L = 10^5 \text{ m}$ . Figure 6 contains a plot of  $B_z$  for two different schemes, a Runge-Kutta 2 scheme and the Hall Diffusion Scheme.

## 4 Magnetohydrodynamic waves in partially ionized plasmas

Since the pioneering works by, e.g., Piddington (1956), Osterbrock (1961), and Kulsrud and Pearce (1969) it is known that the presence of neutral particles in the plasma affects the dynamics of magnetohydrodynamic waves. In this section, we review some basic properties of Alfvén and magneto-acoustic waves in partially ionized plasmas. To do so, we consider the simplest model possible: a homogeneous partially ionized plasma permeated by a straight and constant magnetic field.

We consider a partially ionized plasma, which consists of electrons, protons and neutral hydrogen atoms. The unperturbed state is described by a uniform magnetic field  $\mathbf{B}$ , electron ( $P_e$ ), proton ( $P_i$ ) and hydrogen ( $P_n$ ) thermal pressures, and electron ( $\rho_e$ ), proton ( $\rho_i$ ) and hydrogen ( $\rho_n$ ) mass densities. We suppose that each sort of species has a Maxwell velocity distribution and, therefore, they can be described as separate fluids. For time scales longer than proton-electron collision time, the electron and ion gases can be considered as a single fluid. This significantly simplifies the equations taking into account the smallness of electron mass with regards to the masses of ion and neutral atoms. Then the three-fluid description can be replaced by two-fluid description (Eqs. 66-71), where one component of the plasma is the on-electron fluid and the second component is a fluid made of neutral atoms. The linearized two-fluid MHD equations in a homogeneous plasma can be easily derived from Eqs. (66)-(71) as

$$\rho_i \frac{\partial \mathbf{u}_i}{\partial t} = -\nabla p_i - \frac{\nabla(\mathbf{B} \cdot \mathbf{b})}{\mu} + \frac{(\mathbf{B} \cdot \nabla)\mathbf{b}}{\mu} - \alpha_{in}(\mathbf{u}_i - \mathbf{u}_n) \quad (107)$$

$$\rho_n \frac{\partial \mathbf{u}_n}{\partial t} = -\nabla p_n + \alpha_{in}(\mathbf{u}_i - \mathbf{u}_n) \quad (108)$$

$$\frac{\partial \mathbf{b}}{\partial t} = (\mathbf{B} \cdot \nabla)\mathbf{u}_i - \mathbf{B}\nabla \cdot \mathbf{u}_i - \frac{1}{\mu n_e} \nabla \times [(\nabla \times \mathbf{b}) \times \mathbf{B}] \quad (109)$$

$$\frac{\partial p_i}{\partial t} + \gamma P_i \nabla \cdot \mathbf{u}_i = 0 \quad (110)$$

$$\frac{\partial p_n}{\partial t} + \gamma P_n \nabla \cdot \mathbf{u}_n = 0, \quad (111)$$

where  $\mathbf{b}$ ,  $\mathbf{u}_i$  ( $\mathbf{u}_n$ ) and  $p_i$  ( $p_n$ ) are the perturbations of magnetic field, proton (neutral hydrogen) velocity and proton (neutral hydrogen) pressure respectively. For simplicity, in these equations we have neglected electron inertia, viscosity, magnetic diffusion, and electron-neutral collisions. These equations describe MHD waves in a homogeneous medium, which are modified by collisions of ions with neutral hydrogen atoms (see sect. 2.3). We shall consider Alfvén and magneto-acoustic waves separately. Alfvén waves are incompressible and produce vorticity perturbations. On the contrary, magneto-acoustic waves are compressible and have no fluid vorticity associated with them.

### 4.1 Alfvén waves

We consider the unperturbed magnetic field,  $B_z$ , directed along the  $z$  axis and the wave propagation along the magnetic field. The perpendicular components



of magnetic field ( $\mathbf{b}_\perp$ ) and velocity ( $\mathbf{u}_{i\perp}$ ,  $\mathbf{u}_{n\perp}$ ) perturbations describe the Alfvén waves. Then, Eqs. (107)-(111) give

$$\frac{\partial \mathbf{u}_{i\perp}}{\partial t} = \frac{B_z}{\mu \rho_i} \frac{\partial \mathbf{b}_\perp}{\partial z} - \frac{\alpha_{in}}{\rho_i} (\mathbf{u}_{i\perp} - \mathbf{u}_{n\perp}), \quad (112)$$

$$\frac{\partial \mathbf{u}_{n\perp}}{\partial t} = \frac{\alpha_{in}}{\rho_n} (\mathbf{u}_{i\perp} - \mathbf{u}_{n\perp}), \quad (113)$$

$$\frac{\partial b_\perp}{\partial t} = B_z \frac{\partial \mathbf{u}_{i\perp}}{\partial z} - \frac{1}{\mu n_e} \nabla_\perp \times [(\nabla \times \mathbf{b}_\perp) \times \mathbf{B}]. \quad (114)$$

First we neglect the Hall term in the induction equation and perform a Fourier analysis assuming disturbances to be proportional to  $\exp[i(k_z z - \omega t)]$ . This gives the dispersion relation (see, e.g., Zaqarashvili et al. 2011a, Soler et al. 2013a)

$$\omega^3 + i \frac{\alpha_{in}}{\rho \xi_i \xi_n} \omega^2 - v_A^2 k_z^2 \omega - i \frac{\alpha_{in}}{\rho \xi_n} v_A^2 k_z^2 = 0, \quad (115)$$

where

$$\rho = \rho_i + \rho_n, \quad \xi_i = \frac{\rho_i}{\rho}, \quad \xi_n = \frac{\rho_n}{\rho}, \quad v_A = \frac{B_z}{\sqrt{\mu \rho_i}}.$$

Note that only the ion density appears in the present definition of the Alfvén velocity,  $v_A$ .

We assume a real wavenumber,  $k_z$ , and solve the dispersion relation (Equation (115)) to obtain the complex frequency,  $\omega = \omega_R + i\omega_I$ , with  $\omega_R$  and  $\omega_I$  the real and imaginary parts of  $\omega$ , respectively. Since  $\omega$  is complex the amplitude of perturbations is multiplied by the factor  $\exp(\omega_I t)$ , with  $\omega_I < 0$ . Therefore the perturbations are damped in time. Physically, the damping is caused by the dissipation associated with ion-neutral collisions.

Equation (115) is a cubic equation in  $\omega$  so it has three solutions. The exact analytic solution to Equation (115) is too complicated to shed any light on the physics. However we can investigate the nature of the solutions using the concept of the polynomial discriminant, as done by Soler et al. (2013a). We perform the change of variable  $\omega = is$ , so that Equation (115) becomes

$$s^3 + (1 + \chi) \nu_{ni} s^2 + k_z^2 v_A^2 s + \nu_{ni} k_z^2 v_A^2 = 0. \quad (116)$$

with

$$\chi = \frac{\rho_n}{\rho_i}, \quad \nu_{ni} = \frac{\alpha_{in}}{\rho \xi_n}.$$

Equation (116) is a cubic equation and all its coefficients are real. From Equation (116) we compute the polynomial discriminant,  $\Lambda$ , namely

$$\Lambda = -k_z^2 v_A^2 \left[ 4(1 + \chi)^3 \nu_{ni}^4 - (\chi^2 + 20\chi - 8) \nu_{ni}^2 k_z^2 v_A^2 + 4k_z^4 v_A^4 \right], \quad (117)$$

The discriminant,  $\Lambda$ , is defined so that (i) Equation (116) has one real zero and two complex conjugate zeros when  $\Lambda < 0$ , (ii) Equation (116) has a multiple zero and all the zeros are real when  $\Lambda = 0$ , and (iii) Equation (116) has three distinct real zeros when  $\Lambda > 0$ . This classification is very relevant because the complex zeros of Equation (116) result in damped oscillatory solutions of Equation (115) whereas the real zeros of Equation (116) correspond to evanescent solutions of Equation (115).

It is instructive to consider again the situation in which there are no collisions between the two fluids, so we set  $\nu_{\text{ni}} = 0$ . The discriminant becomes  $\Lambda = -4k_z^6 v_A^6 < 0$ , which means that Equation (116) has one real zero and two complex conjugate zeros. Indeed, when  $\nu_{\text{ni}} = 0$  the zeros of Equation (116) are

$$s = \pm i k_z v_A, \quad s = 0, \quad (118)$$

which correspond to the following values of  $\omega$ ,

$$\omega = \pm k_z v_A, \quad \omega = 0. \quad (119)$$

The two non-zero solutions correspond to the classic, ideal Alfvén waves, as expected, while the third solution vanishes.

We go back to the general case  $\nu_{\text{ni}} \neq 0$ . To determine the location where the nature of the solutions changes we set  $\Lambda = 0$  and find the corresponding relation between the various parameters. For given  $\nu_{\text{ni}}$  and  $\chi$  we find two different values of  $k_z$ , denoted by  $k_z^+$  and  $k_z^-$ , which satisfy  $\Lambda = 0$ , namely

$$k_z^\pm = \frac{\nu_{\text{ni}}}{v_A} \left[ \frac{\chi^2 + 20\chi - 8}{8(1+\chi)^3} \pm \frac{\chi^{1/2}(\chi-8)^{3/2}}{8(1+\chi)^3} \right]^{-1/2}. \quad (120)$$

Since we assume that  $k_z$  is real, Equation (120) imposes a condition on the minimum value of  $\chi$  which allows  $\Lambda = 0$ . This minimum value is  $\chi = 8$  and the corresponding critical  $k_z$  is  $k_z^+ = k_z^- = 3\sqrt{3}\nu_{\text{ni}}/v_A$ . When  $\chi > 8$ , Equation (120) gives  $k_z^+ < k_z^-$ . For  $k_z$  outside the interval  $(k_z^+, k_z^-)$  we have  $\Lambda < 0$  so that there are two damped Alfvén waves, while the remaining solution is evanescent. For  $k_z \in (k_z^+, k_z^-)$  we have  $\Lambda > 0$  and so all three zeros of Equation (116) are real, i.e., they correspond to purely imaginary solutions of Equation (115). There are no propagating waves for  $k_z \in (k_z^+, k_z^-)$ . We call this interval the cut-off region. Kulsrud and Pearce (1969) were the first to report on the existence of a cut-off region of wavenumbers for Alfvén waves in a partially ionized plasma, when studying the propagation of cosmic rays.

The physical reason for the existence of a range of cut-off wavenumbers in partially ionized plasmas can be understood as follows. When  $k_z > k_z^-$  magnetic tension drives ions to oscillate almost freely, since the friction force is not strong enough to transfer significant inertia to neutrals. In this case, disturbances in the magnetic field affect only the ionized fluid as happens for classic Alfvén waves in fully ionized plasmas. Conversely, when  $k_z < k_z^+$  the ion-neutral friction is efficient enough for neutrals to be nearly frozen into the magnetic field. After a perturbation, neutrals are dragged by ions almost instantly and both species oscillate together as a single fluid. The intermediate situation occurs when  $k_z \in (k_z^+, k_z^-)$ . In this case, a disturbance in the magnetic field decays due to friction before the ion-neutral coupling has had time to transfer the restoring properties of magnetic tension to the neutral fluid. In other words, neutral-ion collisions are efficient enough to dissipate perturbations in the magnetic field but, on the contrary, they are not efficient enough to transfer significant inertia to neutrals before the magnetic field perturbations have decayed. Hence, oscillations of the magnetic field are suppressed when  $k_z \in (k_z^+, k_z^-)$ .

For wavenumbers outside the cut-off region, two of the solutions of the dispersion relation are complex with real and imaginary parts, which represent usual

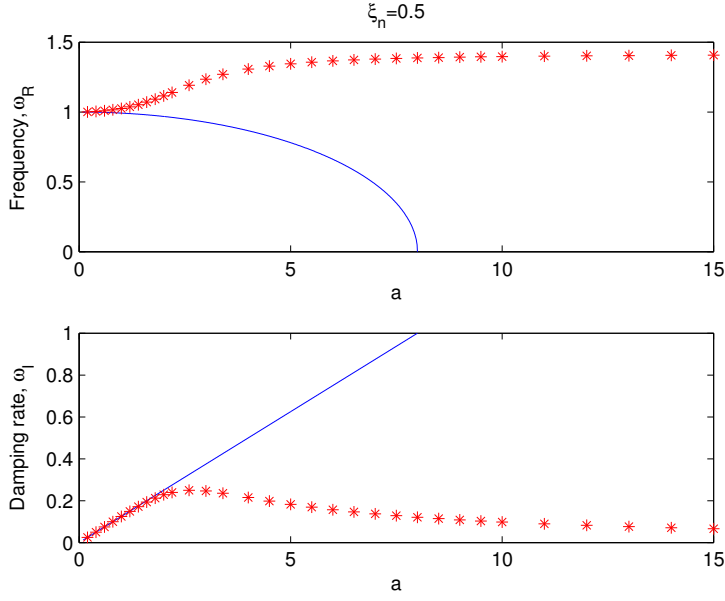


**Fig. 7** Real ( $\omega_R$ ) and imaginary ( $\omega_I$ ) parts of Alfvén wave frequency normalized by  $v_A k_z \sqrt{\xi_i}$  vs  $a = k_z v_A \rho \sqrt{\xi_i} / \alpha_{in}$ . The blue line corresponds to the solution of single-fluid dispersion relation, i.e. Eq. (130) and red asterisks are the solutions of two-fluid dispersion relation, Eq. (115). The values are calculated for 50% of neutral hydrogen,  $\xi_n=0.5$ . Adapted from Zaqqarashvili et al. (2011a).

Alfvén waves damped by ion-neutral collisions. The third solution is purely imaginary and is connected to the so-called vortex mode (with  $Re(\omega) = 0$ ) of neutral hydrogen fluid that damps through ion-neutral collisions. The vortex modes are solutions of fluid equations and they correspond to the fluid vorticity. The vortex modes have zero frequency in the ideal fluid, but may gain a purely imaginary frequency if dissipative processes are evolved. The reason that the vortex mode is a purely imaginary solution is that, for incompressible perturbations, there is no restoring force in the neutral fluid. Consequently, vortex modes are unable to propagate in the form of waves.

Now we may go a step further and derive the single-fluid MHD equations (see sect. 2.6). Comparing the two-fluid and single-fluid results can shed light on the accuracy of the single-fluid model. We define the total velocity (i.e. velocity of center of mass)

$$\mathbf{u}_\perp = \frac{\rho_i \mathbf{u}_{i\perp} + \rho_n \mathbf{u}_{n\perp}}{\rho}, \quad (121)$$

and relative velocity

$$\mathbf{w}_\perp = \mathbf{u}_{i\perp} - \mathbf{u}_{n\perp}. \quad (122)$$

Then, Eqs. (112-114) are rewritten as:

$$\rho \frac{\partial \mathbf{u}_\perp}{\partial t} = \frac{B_z}{\mu} \frac{\partial \mathbf{b}_\perp}{\partial z}, \quad (123)$$

$$\frac{\partial \mathbf{w}_\perp}{\partial t} = \frac{B_z}{\mu \rho_i} \frac{\partial \mathbf{b}_\perp}{\partial z} - \alpha_{in} \left( \frac{1}{\rho_i} + \frac{1}{\rho_n} \right) \mathbf{w}_\perp, \quad (124)$$

$$\frac{\partial \mathbf{b}_\perp}{\partial t} = B_z \frac{\partial \mathbf{u}_\perp}{\partial z} + \xi_n B_z \frac{\partial \mathbf{w}_\perp}{\partial z} - \frac{1}{\mu e n_e} \nabla_\perp \times [(\nabla \times \mathbf{b}_\perp) \times \mathbf{B}]. \quad (125)$$

The single-fluid linearized Hall MHD equations are obtained from Eqs. (123-125) as follows. The inertial term (the left hand-side term in Eq. 124) is neglected, which is a good approximation for time scales longer than ion-neutral collision time, but fails for the shorter time scales (Zaqarashvili et al. 2011a). Then  $\mathbf{w}_\perp$  defined from Eq. (124) is substituted into Eq. (125) and one can obtain the linearized Hall MHD equations

$$\rho \frac{\partial \mathbf{u}_\perp}{\partial t} = \frac{B_z}{\mu} \frac{\partial \mathbf{b}_\perp}{\partial z}, \quad (126)$$

$$\frac{\partial \mathbf{b}_\perp}{\partial t} = B_z \frac{\partial \mathbf{u}_\perp}{\partial z} + \frac{\xi_n^2 B_z^2}{\mu \alpha_{in}} \frac{\partial^2 \mathbf{b}_\perp}{\partial z^2} - \frac{1}{\mu e n_e} \nabla_\perp \times [(\nabla \times \mathbf{b}_\perp) \times \mathbf{B}]. \quad (127)$$

The usual single-fluid MHD equations, which are widely used for description of Alfvén waves in partially ionized plasmas, are obtained from Eqs. (126-127) after neglecting the Hall term in Eq. (127)

$$\rho \frac{\partial \mathbf{u}_\perp}{\partial t} = \frac{B_z}{\mu} \frac{\partial \mathbf{b}_\perp}{\partial z}, \quad (128)$$

$$\frac{\partial \mathbf{b}_\perp}{\partial t} = B_z \frac{\partial \mathbf{u}_\perp}{\partial z} + \frac{\xi_n^2 B_z^2}{\mu \alpha_{in}} \frac{\partial^2 \mathbf{b}_\perp}{\partial z^2}. \quad (129)$$

As before, Fourier analysis with  $\exp[i(k_z z - \omega t)]$  gives the dispersion relation

$$\omega^2 + i \frac{v_A^2 k_z^2 \rho \xi_i \xi_n^2}{\alpha_{in}} \omega - v_A^2 k_z^2 \xi_i = 0. \quad (130)$$

This is the usual dispersion relation of Alfvén waves, which is obtained in single fluid partially ionized plasmas (Haerendel 1992; De Pontieu et al. 2001). For  $v_A k_z \rho \sqrt{\xi_i \xi_n^2} / \alpha_{in} < 2$ , it gives the damping rate

$$2\omega_i = \frac{\xi_n^2 B_z^2}{\mu \alpha_{in}} k_z^2 \quad (131)$$

in full agreement with previous works (e.g. Braginskii 1965, etc.). In order to understand the wave damping due to ion-neutral collision, we rewrite Eq. (131) as follows

$$\frac{\omega_i}{k_z v_A} = \frac{k_z v_A}{\nu_{in}} \frac{\xi_n^2}{2}. \quad (132)$$

This expression clearly indicates that the normalized damping rate depends on the ratio of Alfvén and ion-neutral collision frequencies and plasma ionization rate. The earlier statement that the damping rate depends on the magnetic field strength can be translated as follows: the increase in the magnetic field leads to an increase in the Alfvén speed, therefore the waves with the same wavenumber have a higher frequency, which is closer to ion-neutral collision frequency, so the normalized damping rate increases. In fact, it is the ratio of neutral and total (proton+hydrogen) fluid densities ( $\xi_n$ ) that determines the damping rate of a particular wave harmonic. High-frequency waves are damped quickly. However,

this statement is valid for a low-frequency wave spectrum below the ion-neutral collision frequency since the single-fluid model has been adopted.

On the other hand, the condition  $v_A k_z \rho \sqrt{\xi_i \xi_n^2} / \alpha_{in} < 2$  in Eq. (131) retains only the imaginary part, which gives the cut-off wave number

$$k_c = \frac{2\alpha_{in}}{\rho \xi_n^2 v_A \sqrt{\xi_i}}, \quad (133)$$

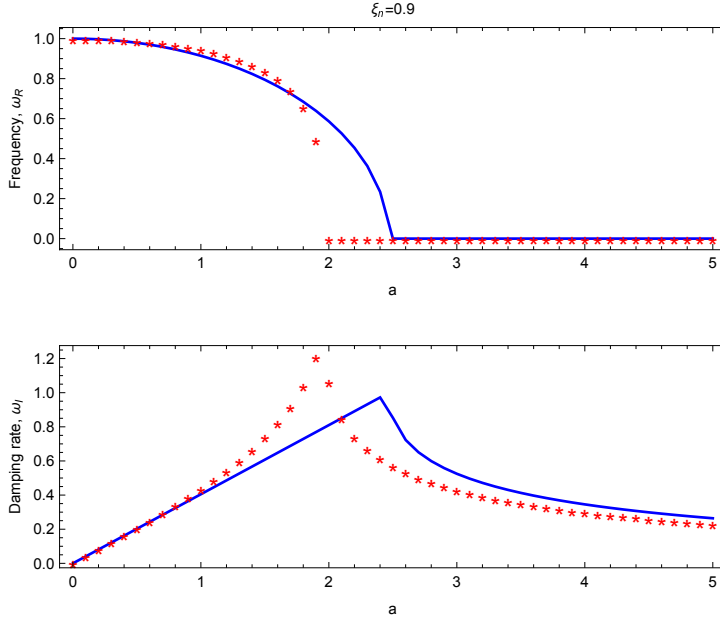
which means that the waves with higher wave number than  $k_c$  are evanescent. We note that, of the two cutoff wavenumbers that appear in the two-fluid description, only the lowest one, i.e.,  $k_z^+$ , remains in the single-fluid approximation. Also, the threshold value  $\chi = 8$  is absent in the single-fluid approximation. The second propagating window that is present in the two-fluid model when  $k_z > k_z^-$  is absent from the single-fluid model. This result points out that the single-fluid model breaks down at very small scales.

Figure 7 displays the solutions of the single-fluid (Eq. 130, blue lines) and two-fluid (Eq. 115, red asterisks) dispersion relations for  $\xi_n = 0.5$ . We see that the frequencies and damping rates of Alfvén waves are same in single-fluid and two-fluid approaches for the low-frequency branch of the spectrum (small  $a = k_z v_A \rho \sqrt{\xi_i} / \alpha_{in}$ ). But, as expected, the behaviour is dramatically changed when the wave frequency becomes comparable to or higher than the ion-neutral collision frequency,  $\nu_{in}$ , i.e. for  $a > 1$ . The damping time linearly increases with  $a$  and the wave frequency becomes zero at some point in single-fluid case (blue lines). The point where the wave frequency becomes zero corresponds to the single-fluid cut-off wave number  $k_c$ . However, for the parameters used in Figure 7 there is no cut-off wave number (Zaqarashvili et al. 2012) in solutions of the two-fluid dispersion relation: Eq. (115) always has a solution with a real part. But the situation is changed when lower values of the ionization degree are considered, i.e., for  $\chi > 8$ , for which the two-fluid cutoff wavenumbers appear (see Soler et al. (2013, 2015) and the subsection 4.3.1). Figure 8 shows equivalent results to those displayed in Figure 1 but with  $\xi_n = 0.9$ . In this case, the cutoff appears in both single-fluid and two-fluid cases, and the single-fluid results are now much more accurate than for  $\xi_n = 0.5$ .

Damping rates derived in the two-fluid approach reach a peak near the ion-neutral collision frequency and then decrease for higher frequencies unlike the single-fluid approach, where the damping increases linearly with increasing frequency (Fig. 7). This result can be checked analytically. To do so, we look for approximate analytic solutions to the two-fluid dispersion relation (Equation (115)) assuming that  $k_z$  is outside the cut-off interval  $(k_z^+, k_z^-)$ , so that there are two complex solutions and one purely imaginary solution. First we look for an approximate expression for the two oscillatory solutions. To do so we write  $\omega = \omega_R + i\omega_I$  and insert this expression in Equation (115). We assume  $|\omega_I| \ll |\omega_R|$  and neglect terms with  $\omega_I^2$  and higher powers. After some algebraic manipulations we derive approximate expressions for  $\omega_R$  and  $\omega_I$ , namely

$$\omega_R \approx \pm k_z v_A \sqrt{\frac{k_z^2 v_A^2 + (1 + \chi) \nu_{ni}^2}{k_z^2 v_A^2 + (1 + \chi)^2 \nu_{ni}^2}}, \quad (134)$$

$$\omega_I \approx -\frac{\chi \nu_{ni}}{2 [k_z^2 v_A^2 + (1 + \chi)^2 \nu_{ni}^2]} k_z^2 v_A^2. \quad (135)$$



**Fig. 8** Same as in Figure 7 but with  $\xi_n=0.9$ . Adapted from Zaqarashvili et al. (2011a).

On the other hand, the remaining purely imaginary, i.e., evanescent, solution is  $\omega = i\epsilon$ , with the approximation to  $\epsilon$  given by

$$\epsilon \approx -\nu_{ni} \frac{k_z^2 v_A^2 + (1 + \chi)^2 \nu_{in}^2}{k_z^2 v_A^2 + (1 + \chi) \nu_{in}^2}. \quad (136)$$

When  $\nu_{in} = 0$ , we find  $\omega_R = \pm k_z v_A$ ,  $\omega_I = 0$  and  $\epsilon = 0$ , hence we recover the solutions in the ideal case. It is useful to investigate the behavior of the solutions in the various limits of  $\nu_{in}$ . First we consider the limit  $\nu_{in} \ll k_z v_A$ , i.e., the case of low collision frequency, which means that the coupling between fluids is weak. Equations (134) and (136) simplify to

$$\omega_R \approx \pm k_z v_A, \quad (137)$$

$$\omega_I \approx -\frac{\chi \nu_{in}}{2}, \quad (138)$$

$$\epsilon \approx -\nu_{in}. \quad (139)$$

In this limit  $\omega_R$  coincides with its value in the ideal case and  $\omega_I$  is independent of  $k_z$ . Hence, the damping of Alfvén waves does not depend on the wavenumber. On the other hand, when  $\nu_{in} \gg k_z v_A$ , i.e., the case of strong coupling between fluids, we find

$$\omega_R \approx \pm \frac{k_z v_A}{\sqrt{1 + \chi}}, \quad (140)$$

$$\omega_I \approx -\frac{\chi}{2(1 + \chi)^2} \frac{k_z^2 v_A^2}{\nu_{in}}, \quad (141)$$

$$\epsilon \approx -(1 + \chi) \nu_{ni}. \quad (142)$$

Now the expression of  $\omega_R$  involves the factor  $\sqrt{1+\chi}$  in the denominator, so that the larger the amount of neutrals, the lower  $\omega_R$  compared to the value in the fully ionized case. Now  $\omega_I$  is proportional to  $k_z^2$ , meaning that the shorter the wavelength, the more efficient damping. In this last limit, the two-fluid results agree with those obtained in the single-fluid model.

Finally, Eqs. (126-127) give the dispersion relation of Alfvén waves in Hall MHD, which has an expression (Pandey & Wardle 2008, Zaqarashvili et al. 2012)

$$\omega^2 + \left[ i \frac{\xi_n^2 B_z^2 k_z^2}{\mu \alpha_{in}} \pm \frac{v_A^2 k_z^2}{\Omega_{cp}} \right] \omega - v_A^2 k_z^2 \xi_i = 0, \quad (143)$$

where  $\Omega_{cp} = eB/m_p$  is the proton cyclotron frequency. Contrary to the case in which Hall's term is not included, the solutions of Equation (143) always have a real part. Therefore the single-fluid Hall MHD approach does not include a cut-off wavenumber for Alfvén waves. Multi-fluid results obtained by Soler et al. (2015) also show that the strict two-fluid cut-offs disappear when Hall's term is included. However, as discussed in Soler et al. (2015), the absence of strict cut-offs makes no practical difference concerning the behavior of the waves. The presence of Hall's current and electron inertia cause the strict frequency cut-offs to be replaced by zones where Alfvén waves are overdamped, i.e., the waves are unable to propagate. In the absence of Hall's current and electron inertia, electrons can be considered as tightly coupled to ions, in the sense that electrons just follow the behavior of ions. Both ions and electrons are frozen into the magnetic field. In this case, ion-neutral collisions can completely suppress the magnetic field perturbations and so cause the strict cut-offs. However, when either Hall's current or electron inertia are included, electrons can have a different dynamics than that of ions. Ions may not be able to follow the magnetic field fluctuations due to the effect of ion-neutral collisions, but it is easier for electrons to remain coupled to magnetic field, i.e., magnetized. Therefore, ion-neutral collisions cannot completely suppress the fluid oscillations because of the distinct behavior of electrons when Hall's current and/or electron inertia are included (see also the discussion in Pandey & Wardle 2008).

#### 4.2 Magneto-acoustic waves

Now we move to the case of compressible magneto-acoustic waves. As before, we consider the unperturbed magnetic field,  $B_z$ , directed along the  $z$ -axis and perform a Fourier analysis as  $\exp[-i\omega t + ik_x x + ik_y y + ik_z z]$ . We define  $\Delta_i$  and  $\Delta_n$  as the compressibility perturbations of the electron-ion and the neutral fluids, respectively,

$$\Delta_i = \nabla \cdot \mathbf{u}_i = ik_x u_{ix} + ik_y u_{iy} + ik_z u_{iz}, \quad (144)$$

$$\Delta_n = \nabla \cdot \mathbf{u}_n = ik_x u_{nx} + ik_y u_{ny} + ik_z u_{nz}. \quad (145)$$

We combine Eqs. (107)-(111) and after some algebraic manipulations we obtain the two following coupled equations involving  $\Delta_i$  and  $\Delta_n$  only, namely (Soler et al. 2013b)

$$(\omega^4 - k^2(v_A^2 + c_i^2)\omega^2 + k^2 k_z^2 v_A^2 c_i^2) \Delta_i = -i\nu_{in} \omega^3 (\Delta_i - \Delta_n) +$$

$$+ \frac{i\nu_{in}}{\omega + i(\nu_{in} + \nu_{ni})} k^2 k_z^2 v_A^2 (c_i^2 \Delta_i - c_n^2 \Delta_n), \quad (146)$$

$$(\omega^2 - k^2 c_n^2) \Delta_n = -i\nu_{ni} \omega (\Delta_n - \Delta_i), \quad (147)$$

where  $k^2 = k_x^2 + k_y^2 + k_z^2$  and  $c_i$  ( $c_n$ ) is ion-electron (neutral hydrogen) fluid acoustic speed defined as follows

$$c_i^2 = \frac{\gamma P_i}{\rho_i}, \quad c_n^2 = \frac{\gamma P_n}{\rho_n}. \quad (148)$$

Eqs. (146)-(147) give the dispersion relation of magneto-acoustic waves

$$\begin{aligned} & [(\omega^4 + i\nu_{in}\omega^3 - k^2(v_A^2 + c_i^2)\omega^2)(\omega + i(\nu_{in} + \nu_{ni})) + \\ & k^2 k_z^2 v_A^2 c_i^2 (\omega + i\nu_{ni})] (\omega^2 - k^2 c_n^2 + i\nu_{ni}\omega) + \\ & + \nu_{in} \nu_{ni} \omega [\omega^3 (\omega + i(\nu_{in} + \nu_{ni})) - k^2 k_z^2 v_A^2 c_n^2] = 0. \end{aligned} \quad (149)$$

The dispersion relation Eq. (149) is a seventh order equation with  $\omega$ , therefore it has seven different solutions. If we neglect the collision between neutrals and protons, then the dispersion relation is transformed into the expression

$$\omega(\omega^4 - k^2(v_A^2 + c_i^2)\omega^2 + k^2 k_z^2 v_A^2 c_i^2)(\omega^2 - k^2 c_n^2) = 0. \quad (150)$$

Here we see that the seven different modes are four magneto-acoustic modes of ion-electron fluid, two magneto-acoustic modes of neutral hydrogen and one  $\omega = 0$  solution, which is associated with the so-called entropy mode (Soler et al. 2013b). As expected, in the absence of ion-neutral collisions we consistently recover the classic (forward and backward) magnetoacoustic waves in the ion-electron fluid and the classic (forward and backward) acoustic waves in the neutral fluid. Therefore, three distinct waves are present in the uncoupled, collisionless case, in addition to the non-propagating entropy mode. These modes do not interact and are undamped in the absence of collisions.

Conversely to the uncoupled case, the strongly coupled limit represents the situation in which ion-electrons and neutrals behave as one fluid. To study this case, we take the limits  $\nu_{in} \rightarrow \infty$  and  $\nu_{ni} \rightarrow \infty$  in Equations (146) and (147). We realize that, if  $\omega \neq 0$ , it is necessary that  $\Delta_i = \Delta_n$  for the equations to remain finite. This is equivalent to assume that the two fluids move as a whole. Then, when  $\nu_{in} \rightarrow \infty$  and  $\nu_{ni} \rightarrow \infty$ , we find a single equation for the compressibility perturbations, namely

$$\omega^3 \left( \omega^4 - \omega^2 k^2 \frac{v_A^2 + c_i^2 + \chi c_n^2}{1 + \chi} + k^4 \frac{v_A^2 (c_i^2 + \chi c_n^2)}{(1 + \chi)^2} \cos^2 \theta \right) \Delta_{i,n} = 0, \quad (151)$$

where we use  $\Delta_{i,n}$  to represent either  $\Delta_i$  or  $\Delta_n$  and  $\theta$  is the angle that forms the wavevector,  $\mathbf{k}$ , with the equilibrium magnetic field,  $\mathbf{B}$ . For nonzero  $\Delta_{i,n}$ , the solutions to Equation (151) must satisfy

$$\omega^3 \left( \omega^4 - \omega^2 k^2 \frac{v_A^2 + c_i^2 + \chi c_n^2}{1 + \chi} + k^4 \frac{v_A^2 (c_i^2 + \chi c_n^2)}{(1 + \chi)^2} \cos^2 \theta \right) = 0. \quad (152)$$



This is the wave dispersion relation in the strongly coupled case. Its solutions are, on the one hand,

$$\omega^2 = k^2 \frac{v_A^2 + c_i^2 + \chi c_n^2}{2(1 + \chi)} \pm k^2 \frac{v_A^2 + c_i^2 + \chi c_n^2}{2(1 + \chi)} \left[ 1 - \frac{4v_A^2(c_i^2 + \chi c_n^2) \cos^2 \theta}{(v_A^2 + c_i^2 + \chi c_n^2)^2} \right]^{1/2}, \quad (153)$$

where the + sign is for the modified (forward and backward) fast wave and the – sign is for the modified (forward and backward) slow wave. We use the adjective ‘modified’ to stress that these waves are the counterparts of the classic fast and slow modes but modified by the presence of the neutral fluid. On the other hand,  $\omega^3 = 0$  is also a solution.

The first important difference between the uncoupled and strongly coupled cases is in the number of independent solutions. In the uncoupled case there are three distinct waves, namely the classic slow and fast magnetoacoustic waves and the neutral acoustic wave, plus a non-propagating mode. However, in the strongly coupled limit we only find two propagating waves, i.e., the modified version of the slow and fast magnetoacoustic modes, plus three non-propagating modes. The modified counterpart of the classic neutral acoustic wave is apparently absent, although the truth is that the neutral acoustic wave has become a non-propagating solution. The classic neutral acoustic mode and the classic ion-electron magnetoacoustic modes interact heavily when ion-neutral collisions are at work. The two resulting modes in the strongly coupled regime (modified fast mode and modified slow mode) have mixed properties in general and are affected by the physical conditions in the two fluids. The degree to which the properties of the classic waves are present in the resulting waves depends on the relative values of the Alfvén and sound velocities and on the ionization fraction of the plasma. In addition, the wave frequencies in the strongly coupled limit are real as in the uncoupled case. This means that the waves are undamped in the limit of high collision frequencies as well. The damping of magnetoacoustic waves due to ion-neutral collisions takes place for intermediate collision frequencies.

Parameter studies of the solution to the general dispersion relation (Eq. (149)) were performed in Soler et al. (2013b). The ion-neutral coupling strongly affects the behavior and properties of the waves. There is a large number of possible scenarios for wave propagation depending on the plasma physical properties. The various waves supported by a partially ionized plasma display complex interactions and couplings that are not present in the fully ionized case (see also Mouschovias et al. (2011)). Among these complex interactions, the presence of cut-offs and forbidden intervals has a strong impact since the allowed wavelengths of the propagating modes become heavily constrained. An example of this complex coupling is seen in Figure 9, which shows the dispersion diagram of obliquely propagating waves in a strongly magnetized plasma as a function of the normalised ion-neutral collision frequency,  $\bar{\nu} = 2\alpha_{in}/(\rho_i + \rho_n)$ , and different values of the ionization ratio,  $\chi$ .

### 4.3 General remarks

Investigation of the modes present in two-fluid and single-fluid models reveals the complexity that ion-neutral collisions impose on the behavior of the waves. Several general conclusions can be drawn. First, the efficiency of the damping, and so that

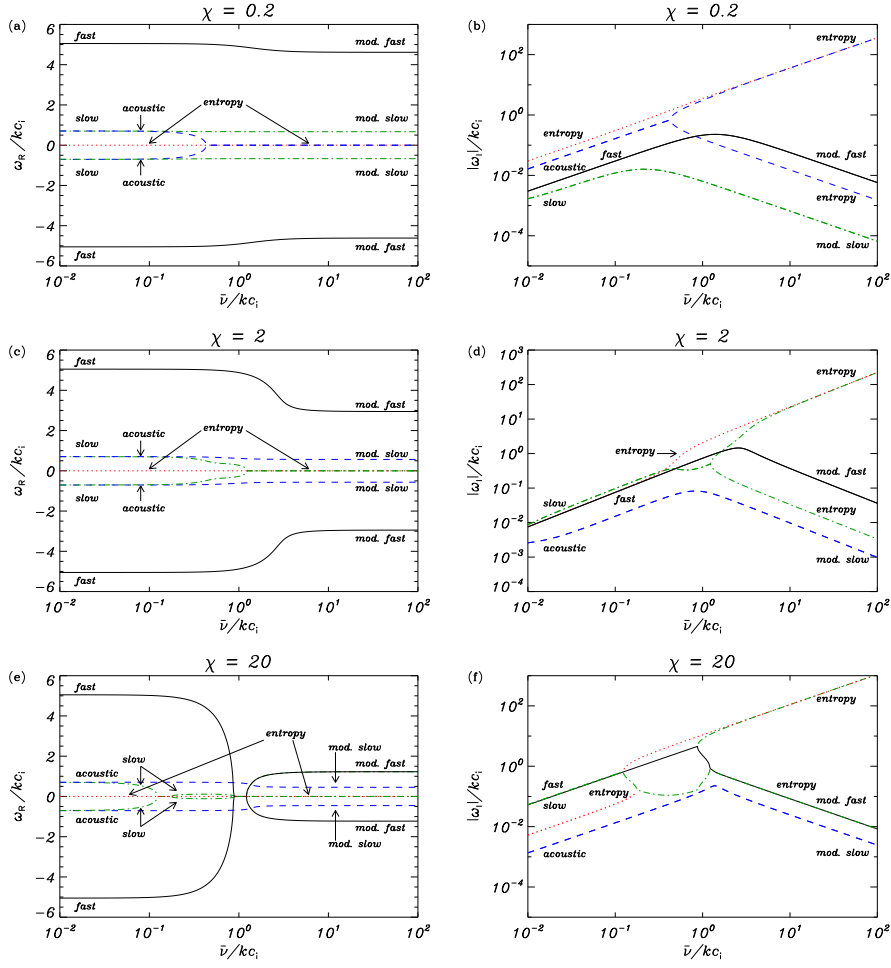


**Fig. 9** Real (left) and imaginary (right) parts of the frequency of the various waves versus the averaged collision frequency (in logarithmic scale) for oblique propagation to the magnetic field, i.e.,  $\theta = \pi/4$ , in a strongly magnetized plasma with  $c_1^2 = 0.04c_A^2$ . Panels (a)–(b) are for  $\chi = 0.2$ , panels (c)–(d) for  $\chi = 2$ , and panels (e)–(f) for  $\chi = 20$ . All frequencies are expressed in units of  $kc_i$ . Note that the absolute value of  $\omega_I$  is plotted. Adapted from Soler et al. (2013b).

of the wave energy dissipation, is determined by the relative values of the wave frequency and the collision frequency. The damping is most efficient when these two frequencies are of the same order of magnitude. Second, dissipation can be so strong for some parameter combinations that wave propagation is suppressed. This leads to the presence of cut-offs and forbidden windows in the dispersion diagrams. Third, the number of possible waves that exist in the partially ionized plasma is determined by the strength of the coupling between species. Hence, the neutral fluid may be able to sustain its own acoustic waves when the coupling is weak, but the neutral waves and the ion-electron waves become unavoidably entangled when the coupling between fluids is strong.

Apart from being of academic interest, the theoretical properties of waves in partially ionized plasmas reveal interesting features that may be important for applications in real astrophysical environments. For instance, the deposition of wave energy associated to ion-neutral damping may be necessary to explain plasma heating in the solar chromosphere (see sect. 5.1.5).

## 5 Applications to Astrophysical Environments

### 5.1 Solar atmosphere

#### 5.1.1 Introduction

Coupling between ions and neutrals in magnetized plasmas is of great importance in many aspects of heliophysics. The plasma is weakly ionized in the photosphere/lower chromosphere, but temperature increase with height leads to the ionization of neutral atoms, which become fully ionized in the solar corona. Therefore, the transition between partially and fully ionized plasma states occurs near the transition region with sharp temperature gradient. Usually, the ideal MHD approximation is used to study the dynamical processes taking place in magnetized solar plasmas from the photosphere to the corona. However, in some layers and structures of the solar atmosphere, the effects of partial ionization are of particular importance. For instance, in the lower solar atmosphere where the temperature is relatively cool, the degree of ionization is very small. This fact, together with the decrease in the collision frequency with height, produces conditions under which the assumptions supporting the ideal MHD approximation are not valid. Therefore, in these layers other additional effects such as the Hall effect and ambipolar diffusion must be taken into account, and could produce interesting effects related, for instance, to chromospheric heating (Khomenko and Collados 2012). Furthermore, it has been also shown that the single-fluid MHD approximation fails in some circumstances, therefore multi-fluid theory must be adopted. Another region in the solar atmosphere where ion-neutral coupling needs to be considered is in the physics of solar prominences, which are dense cold plasma clouds supported by coronal magnetic field against gravity, where cross-field diffusion of neutrals may play a critical role in determining the cross-field structure and mass variation of prominences (terradas15). Recently, high-resolution observations made by the HINODE satellite have revealed a lot of dynamical processes taking place in limb prominences (Berger et al. 2008). Most of these dynamical features have been interpreted and modeled in terms of different instabilities (Rayleigh-Taylor, Kelvin-Helmholtz, etc.) which develop in the prominence plasma considered as fully ionized. However, because of low temperature, prominence plasmas are PIP, with physical properties similar to those of chromosphere, and the study of thermal, Rayleigh-Taylor and Kelvin-Helmholtz instabilities in PIP has been already started (Soler et al. 2012; Díaz et al. 2012; Khomenko et al. 2014b) with the aim of determining the modifications in the instability thresholds and growth rates produced by partial ionization effects. For all these reasons, the solar atmosphere is an excellent laboratory to study the effects of partial ionization on plasma dynamics.

#### 5.1.2 Ionization, collisions and magnetization in the lower solar atmosphere

Figure 10 shows the dependence of plasma parameters on height according to the FAL93-F model (Fontenla et al. 1993). This model includes the dependence of ionization degree on heights for both hydrogen and helium atoms. The upper panel shows the plasma temperature vs. height. The temperature minimum is located near 500 km above the base of the photosphere, while the transition region is just above 2000 km height. The neutral hydrogen number density is much higher

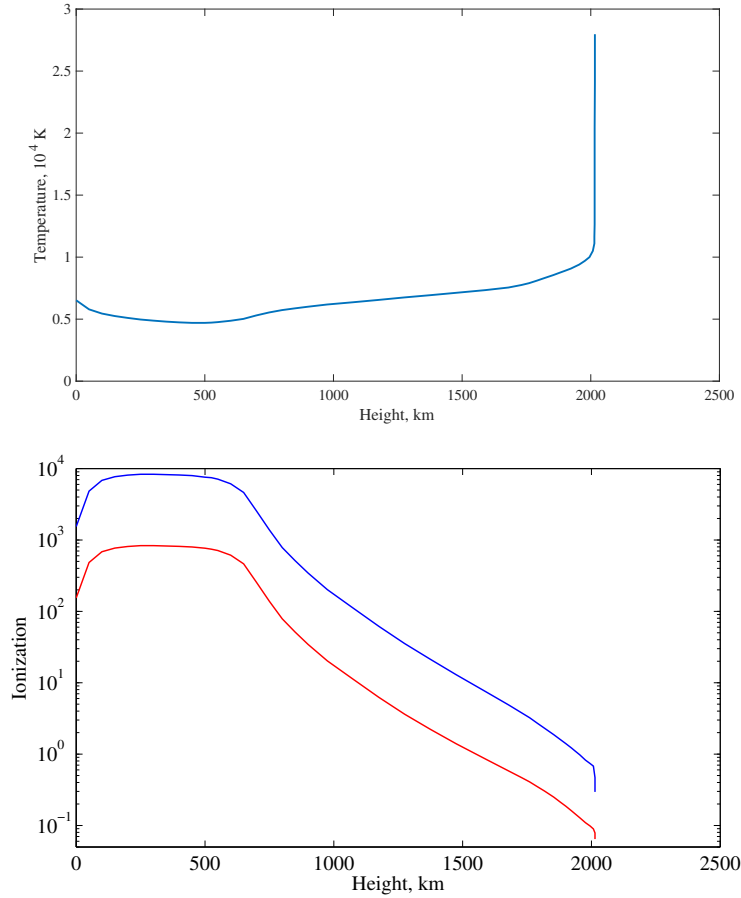


**Fig. 10** Height dependence of atmospheric parameters according to FAL93-F model (Fontenla et al. 1993). Upper panel: the plasma temperature. Lower panel: blue (red) solid line - the ratio of neutral hydrogen (neutral helium) and electron number densities.

than the electron number density at the lower heights, but becomes comparable near  $\approx 1900$  km, which corresponds to the temperature of 9400 K (lower panel). Hydrogen atoms quickly become ionized above this height. The neutral helium number density is also higher than the electron number density at the lower heights (lower panel). They become comparable near  $\approx 1600$  km, which corresponds to the temperature of  $\approx 7300$  K. The ratio becomes smaller and smaller just above this height. The ratio of neutral helium and neutral hydrogen number densities stays nearly constant ( $\approx 0.1$ ) up to 1500 km height, then it quickly increases up to 0.2 at height of 2000 km (Zaqarashvili et al. 2011a).

The change of plasma parameters with height leads to variation of cyclotron and collision frequencies as well as transport coefficients. These values are important in understanding the fundamental processes in the solar atmospheric plasma. The fluid theory implicitly assumes that collisions between species are frequent enough to keep the Maxwell-Boltzmann velocity distribution. This imposes time

scales where the fluid theory is either applicable or breaks down. Magnetization of ions and electrons is also important for various instabilities and wave dynamics.

The collision frequencies between charged species are essentially determined by the densities and the temperature, while the collision frequencies involving neutrals also depend on the neutral collision cross section. The classical approach to compute the collision cross section is the so-called model of hard spheres, from here on HS. In the HS model the particles are considered as solid spheres that interact by means of direct impacts only (e.g., Chapman and Cowling 1970). The HS cross section is usually computed as  $\sigma_{\beta\beta'} = \pi (r_{\beta} + r_{\beta'})^2$ , where  $r_{\beta}$  and  $r_{\beta'}$  are the radii of particles  $\beta$  and  $\beta'$ , respectively. In the case of ion-neutral and electron-neutral collisions, the radii of both ions and electrons are much smaller than the radius of neutral atoms, so that their HS cross sections are approximately the same, namely  $\sigma_{in} \approx \sigma_{en} \approx 10^{-20} \text{ m}^2$ . Likewise, the HS cross section for neutral-neutral collisions is  $\sigma_{nn} \approx 4 \times 10^{-20} \text{ m}^2$ .

Recently, Vranjes and Krstic (2013), from here on VK, presented quantum-mechanical computations of collision cross sections that include several important ingredients missing from the classic HS model. For instance, VK considered variations of the cross section with temperature, quantum indistinguishability corrections, and charge transfer. The VK cross sections coincide with the classical ones at high temperatures, but are different at low temperatures akin to those in the chromosphere. In their paper, VK plot the computed cross section as a function of the energy of the colliding species, which is related to the temperature. For chromospheric temperatures of interest here, we have to consider the results at low energies. The ion-neutral collision cross section from Figure 1 of VK is  $\sigma_{in} \approx 10^{-18} \text{ m}^2$ , while the electron-neutral collision cross section from their Figure 4 is  $\sigma_{en} \approx 3 \times 10^{-19} \text{ m}^2$ . Concerning neutral-neutral collisions, VK provide in their Figure 3 different cross sections for momentum transfer and viscosity. The cross section for momentum transfer is  $\sigma_{nn} \approx 10^{-18} \text{ m}^2$ , while the cross section for viscosity is  $\sigma_{nn} \approx 3 \times 10^{-19} \text{ m}^2$ . In summary, the VK cross sections are between one and two orders of magnitude larger than the classic HS cross sections.

The value of the cross section is not only important from the academic point of view but also from the practical one. The reason is that the value of the cross section directly affects the collision frequency and, therefore, it is important to determine both the applicability of the fluid theory and the optimal frequency for wave damping in the multi-fluid description. Uncertainties in the collision frequency also cause uncertainties in the various transport coefficients that govern basic collisional phenomena in the plasma (e.g., Martínez-Sykora et al. 2012). The value of the collision cross section may play an important role in theoretical computations.

Figure 11 shows the dependence on height of the relevant collision frequencies for protons, electrons, neutral hydrogen, neutral helium and singly ionized helium taking into account collision cross sections from Vranjes and Krstic (2013). Concerning protons (Figure 11(a)), we find that  $\nu_{pH} \gg \nu_{pp}$  in the low chromosphere. Collisions with neutrals are too frequent for protons to reach a Maxwell-Boltzmann distribution independently. In other words, protons collide too frequently with neutral hydrogen so that proton-proton collisions do not have enough time to make the proton distribution Maxwellian on their own without the influence of neutrals. Protons are too coupled with neutrals. This means that the condition for protons to be treated as an individual fluid is not satisfied. The multi-fluid theory

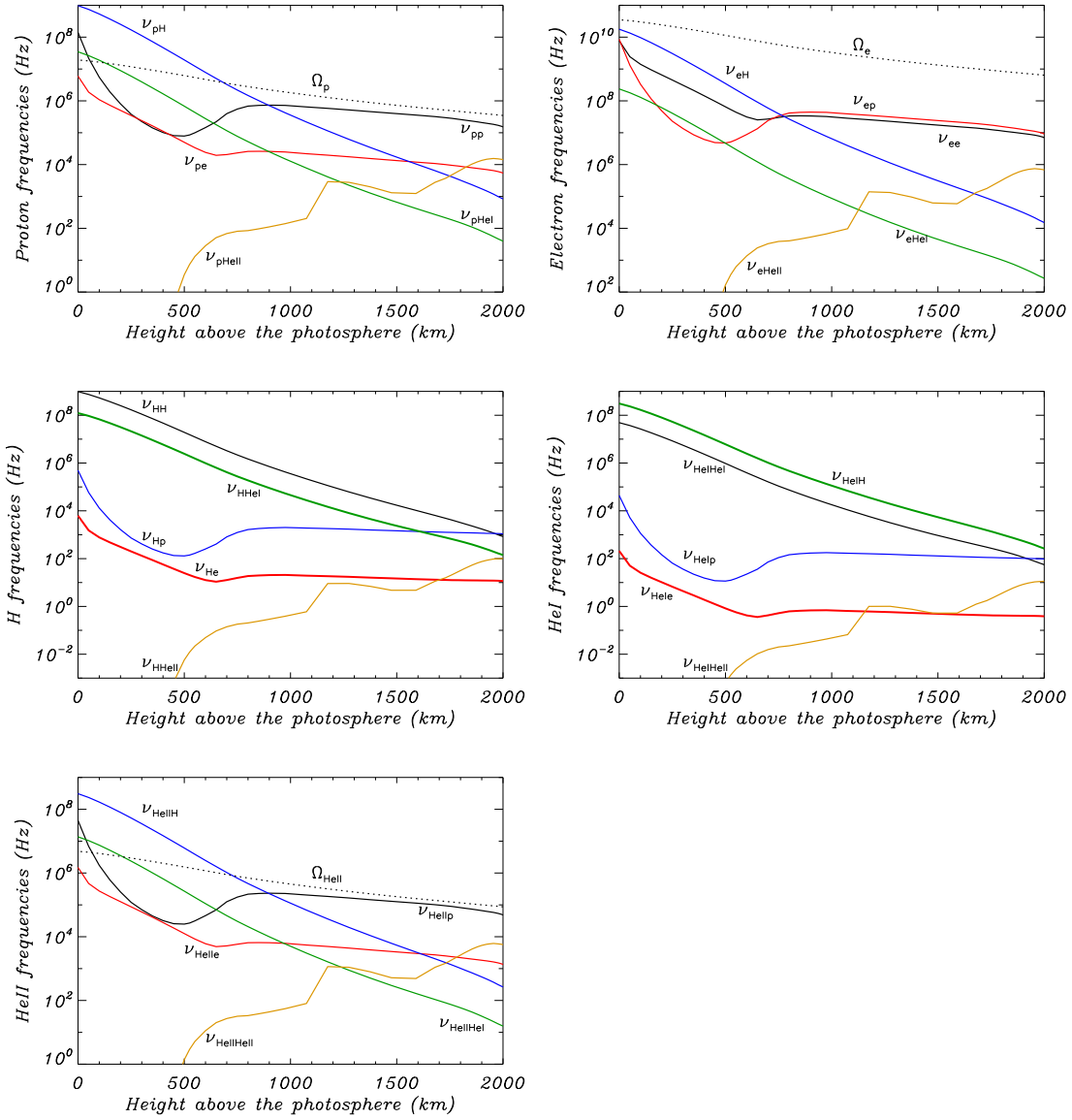


**Fig. 11** Collision frequencies for (a) protons, (b) electrons, (c) neutral hydrogen, (d) neutral helium and (e) singly ionized helium vs height above the photosphere. Here we use the collision cross sections from Vranjes and Krstic (2013). In panels (a), (b) and (e)  $\Omega_{cp}$ ,  $\Omega_{ce}$ , and  $\Omega_{cHeII}$  denote the proton, electron and singly ionized helium cyclotron frequencies, respectively, and are represented by dotted lines.

breaks down for  $h \sim 900$  km. We also see that protons would not be magnetized for  $h \sim 700$  km in the VK case since  $\nu_{pH} > \Omega_{cp}$  at those low heights, where  $\Omega_{cp} = eB/m_p$  is the proton cyclotron frequency (see a discussion on this issue in Vranjes et al. 2008).

In the case of electrons (Figure 11(b)), we also see that electrons should not be treated as a separate fluid at low heights due to the very frequent collisions with neutral hydrogen, i.e.,  $\nu_{eH} \gg \nu_{ee}$ . At large heights, however, it is found that  $\nu_{ee} \gg \nu_{eH}$  and  $\nu_{ee} \sim \nu_{ep}$ , so that electrons are strongly coupled to protons (they effectively behave as an ion-electron single fluid) but are weakly affected by neutrals. In all cases, the electron cyclotron frequency,  $\Omega_{ce} = eB/m_e$ , remains larger than the electron-electron collision frequency.

It is seen from Figures 11(a) and 11(e) that protons and singly ionized heliums are magnetized below the height of  $\sim 700$  km, but become unmagnetized above this height. On the other hand, electrons are magnetized through whole solar chromosphere.

Finally, the collision frequencies for neutral hydrogen and neutral helium (Figure 11(c) and (d)) show that  $\nu_{nn}$  is always the largest frequency at all heights, so that treating neutrals as a separate fluid is a valid assumption. This last result remains the same for both HS and VK cross sections.

The discussion in previous paragraphs implies that for the waves near the proton-neutral collision frequency, protons should not be considered as an individual fluid separate from neutrals at low heights in the chromosphere. This was previously noted by Vranjes and Krstic (2013). The same restriction applies to electrons. The multi-fluid theory is applicable for the height of  $\sim 600$  km using the HS cross sections and for  $h \sim 900$  km using the VK cross sections. Hence, the use of the more accurate VK cross sections results in a more restrictive criterion for the applicability of the multi-fluid theory than that obtained with the classical HS cross sections. The correct study of high-frequency waves in the low chromosphere should be done using hybrid fluid-kinetic models, or even fully kinetic models, since standard fluid theory is not applicable for those high-frequencies. Of course, for wave frequencies lower than all the collision frequencies the plasma dynamics can be studied using the single-fluid approximation (e.g., De Pontieu et al. 2001; Khodachenko et al. 2004), which assumes that ions, electrons, and neutrals are strongly coupled.

It is also important to realize that the solar atmosphere is not only strongly stratified but is also strongly horizontally inhomogeneous. Therefore, even at the same heights, the typical values of the ionisation fraction, magnetisation and transport coefficients strongly vary. Khomenko et al. (2014a) evaluated the magnitude of the different terms in the Ohm's law (as Ohmic, Hall, Ambipolar and battery terms, see Sect. 2) for several representative models of the solar atmosphere, covering quiet and active regions. This evaluation has shown that in the quiet solar regions (those covering at least 90% of solar surface at any time), Hall and Ambipolar terms dominate the electric current, being largest at the borders of intergranular lanes with strongest gradients of all parameters. In the sunspot model, the Ambipolar term dominates by 3 orders of magnitude over the next in magnitude Hall term. These order of magnitude estimates can be taken as a guidance.



### 5.1.3 Magnetic reconnection in partially ionized photospheric plasma

Magnetic reconnection is a fundamental process in magnetized plasmas, when the magnetic energy of oppositely directed magnetic field is transformed into radiation and heat (Priest and Forbes 2000). Martin et al. (1985) observed that the photospheric magnetic fragments with opposite polarity, which were characterized by fluxes exceeding  $10^{17}$  Mx and sizes of about 1 arc sec or larger, approached each other and disappeared. Litvinenko (1999) showed that the photospheric magnetic reconnection is a mechanism for the cancellation. The reconnection process should be most efficient around the temperature minimum region about 600 km above the lower photospheric boundary. The observation of Martin et al. (1985) is believed to be the first observational evidence of magnetic reconnection at the photosphere.

More recently, Katsukawa et al. (2007) reported the discovery of small jetlike features in sunspot penumbra, using Ca II H observations from the Hinode satellite. The observed penumbral microjets are highly transient events with lifetimes of less than 2 minutes, lengths of 1000-4000 km, and widths of  $\approx 400$  km. Sakai and Smith (2008) performed 2.5D numerical simulation of two horizontal penumbral filaments using a two-fluid model of partially ionized plasmas, where one fluid is neutral hydrogen atoms and second one is charged particles (protons+electrons). They showed that inclined bidirectional jet-like flows, driven by the magnetic reconnection, propagate along the vertical magnetic flux tube, which exists between the filaments. Strong proton heating, up to 25 times their original temperature, was observed in these generated jets. Conversely, the neutral-hydrogen particles are only very weakly heated. Sakai and Smith (2008) proposed that these plasma jets may explain the phenomenon of penumbral microjets observed by Katsukawa et al. (2007).

Sakai and Smith (2009) found that the magnetic reconnection rate of the coalescing penumbral filaments is strongly enhanced by an initial velocity of filaments. An initial collision velocity corresponding to 10 % of the sound speed increases the magnetic reconnection rate by a factor of 50 when compared to spontaneous coalescence. They concluded that the magnetic reconnection rate of coalescing penumbra filaments can be strongly enhanced by weak photospheric neutral-hydrogen flows.

### 5.1.4 Energy flux of transverse waves in the photosphere

Mechanical energy of photospheric motions has been considered to be a source for chromospheric and coronal heating. Granular cells may excite transverse waves (MHD kink or torsional Alfvén waves) in intense magnetic flux tubes, which carry energy up and heat the surrounding plasma. These waves can be observed in the chromosphere by a transverse displacement or Doppler shift in magnetic structures (see recent review by Zaqarashvili and Erdélyi 2009). Vranjes et al. (2008) suggested that the energy flux of Alfvén waves in the weakly ionized photospheric plasma is orders of magnitude smaller than in the ideal case, which makes ineffective the generation of the waves near the solar surface. Consequently, they raised a question of applicability of photospheric Alfvén waves as a possible energy source for chromospheric and coronal heating. On the other hand, Tsap et al. (2011) concluded that the energy flux of Alfvén waves in the weakly ionized photospheric plasma is the same as in the ideal case. This discrepancy was clarified by Soler et al. (2013), who showed that the energy flux depends on initial velocities of both,

ion and neutral fluids. Vranjes et al. (2008) considered zero initial velocity of neutral fluid putting initial energy only into the ion fluid, therefore they obtained much smaller energy flux due to the small density of ions with regards to neutrals at the photosphere. But Tsap et al. (2011) assumed that both ions and neutrals are initially perturbed with the same velocity due to the strong coupling, although this condition is not explicitly stated in the paper. Therefore, they obtained the energy flux of Alfvén waves similar to the ideal plasma.

Transverse (kink or Alfvén) waves are excited in magnetic flux tubes by buffeting of granular cells which means that initial energy is mostly stored in the neutral fluid. Therefore, the initial conditions assumed by Vranjes et al. (2008) are not adequate to the photosphere. Consequently, the energy flux of generated Alfvén waves can be considered as a source for chromospheric and coronal heating.

### 5.1.5 Damping of Alfvén waves and associated heating in the solar chromosphere

There is extensive observational evidence of Alfvénic waves propagating in the solar chromosphere (e.g., Kukhianidze et al. 2006; Zaqarashvili et al. 2007; De Pontieu et al. 2007, 2012; Okamoto and De Pontieu 2011; Kuridze et al. 2012; Morton et al. 2013). The plasma heating of the solar atmosphere is one of the long-standing problems in solar physics, and it is believed that energy transport by Alfvén waves and its dissipation may play a relevant role (see, e.g., Erdélyi and Fedun 2007; Cargill and de Moortel 2011; McIntosh et al. 2011; Hahn and Savin 2014; Arregui 2015; Jess et al. 2015). The relatively cool temperature in the chromosphere causes the plasma to be partially ionized, with a predominance of neutrals at low heights in the chromosphere. It has been shown that partial ionization effects have a strong impact on chromospheric dynamics (see, e.g., Martínez-Sykora et al. 2012; Leake et al. 2014a). Ion-neutral collisions may play a crucial role in the release of magnetic energy in the form of heat (Khomenko and Collados 2012; Shelyag et al. 2016). In this context, ion-neutral collisions have been invoked as a viable energy dissipation mechanism for Alfvén waves by, e.g., De Pontieu et al. (2001); Khodachenko et al. (2004); Leake et al. (2005); Russell and Fletcher (2013), among others. Strongly damped waves are good candidates to produce significant heating of the chromospheric plasma via conversion of wave energy into thermal energy. Estimations of the heating rate due to Alfvén waves damped by ion-neutral collisions computed by Song and Vasyliūnas (2011) and Goodman (2011) indicate that this mechanism may generate sufficient heat to compensate the radiative losses at low altitudes in the solar atmosphere. Ion-neutral interaction can lead to dissipation of perpendicular currents produced by waves, converting the magnetic energy of waves into thermal energy and producing an important heating of the magnetized chromosphere above magnetic elements (Khomenko and Collados 2012; Shelyag et al. 2016).

Zaqarashvili et al. (2011a) used a two-fluid MHD model of partially ionized plasma, where ion-electron plasma and neutral hydrogen atoms are considered as separate fluids, to obtain the dispersion relations of linear MHD waves in the simplest case of a homogeneous medium for different parameters of background plasma. The dispersion relation of Alfvén waves in the two-fluid approach is

$$\omega^3 + i \frac{\alpha_H}{\rho_H} \left( 1 + \frac{\rho_H}{\rho_{H^+}} \right) \omega^2 - k_z^2 v_A^2 \omega - i \frac{\alpha_H}{\rho_H} k_z^2 v_A^2 = 0, \quad (154)$$

where  $\omega$  and  $k_z$  are the frequency and wave number of Alfvén waves,  $\rho_H$  and  $\rho_{H^+}$  are the density of neutral hydrogen atoms and protons, respectively,  $v_A = B_0/\sqrt{\mu\rho_{H^+}}$  is the Alfvén speed of electron-proton fluid and  $\alpha_H$  is the coefficient of friction between protons and neutral hydrogen atoms. This equation has three different solutions, where two correspond to Alfvén waves and the third corresponds to the vortex solution of neutral hydrogen fluid. Fig. 12 (blue asterisks) shows the damping rate of Alfvén waves using the two-fluid model. The maximal damping of Alfvén waves occurs near the ion-neutral collision frequency. The damping rates are reduced for the higher frequency waves contrary to the single-fluid approach (blue solid line), where the higher frequency waves show stronger damping.

Recently, Soler et al. (2015a) investigated Alfvén wave damping as a function of height in a simplified chromospheric model based on the semi-empirical model F of Fontenla et al. (1993). They found that there is a critical interval of wavelengths for which impulsively excited Alfvén waves are overdamped as a result of the strong ion-neutral dissipation. All the energy stored in the impulsively generated perturbations with wavelengths belonging to the critical interval is necessarily dissipated in the vicinity of the location of the impulsive driver instead of being transported away by propagating waves. Strong plasma heating might therefore be produced by these overdamped waves. Equivalently, for periodically driven Alfvén waves there is an optimal frequency for which the damping is most effective. Soler et al. (2015a) concluded that ion-neutral collisions heating is much more important than Ohmic heating in the upper chromosphere for wave frequencies near the optimal frequency. Soler et al. (2015a) compared their results for two sets of collision cross sections, namely those of the classic hard-sphere model and those based on recent quantum-mechanical computations (Vranjes and Krstic 2013), and found important differences between the results for the two sets of cross sections. For instance, the optimal frequency for the damping varies from 1 Hz to  $10^2$  Hz for the hard-sphere cross sections, and from  $10^2$  Hz to  $10^4$  Hz for the quantum-mechanical cross sections, which points out the importance of using accurate transport coefficients that govern basic collisional phenomena in the plasma.

Subsequently, Soler et al. (2015b) used a more complete description of the chromospheric physics to further investigate the dissipation mechanisms responsible for the overdamping of chromospheric waves and the corresponding spatial scales of the perturbations. Soler et al. (2015b) found that the critical dissipation lengthscale for waves depends strongly on the magnetic field strength. For realistic field strength in the chromosphere, the Alfvén wave critical dissipation lengthscale ranges from 10 m to 1 km (see Fig. 13). The mechanism responsible for the critical damping of Alfvén waves is Ohmic diffusion at low heights in the chromosphere and ambipolar diffusion at medium/large heights in the chromosphere. It is found that viscosity plays no important role in the damping of chromospheric Alfvén waves. The results by Soler et al. (2015b) suggest that the spatial scales at which strong Alfvén wave heating may work in the chromosphere are unresolved by current observational instruments.

A step beyond the simplified analytical description in studies of dissipation and heating by Alfvén waves was reported recently by Shelyag et al. (2016). The authors studied numerically the non-linear propagation of waves in three-dimensional strongly stratified solar flux tubes, including the effects of the mode transformation and dissipation by neutrals in a single-fluid approximation. It was shown that up to 80% of the Poynting flux associated to these waves can be dissipated and

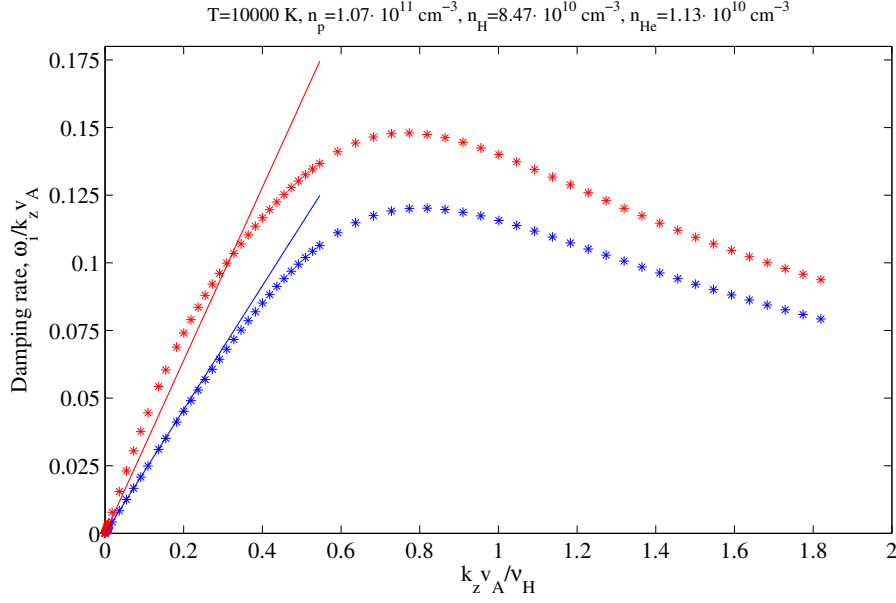


**Fig. 12** Damping rate (imaginary part of frequency) of Alfvén waves (normalized by Alfvén frequency  $k_z v_A$ ), vs Alfvén frequency normalized by hydrogen collision frequency  $\nu_H$  for the temperature of 10000 K. Blue asterisks correspond to the damping rates due to ion collision with neutral hydrogen atoms only, while red asterisks correspond to the damping rates due to ion collision with both, neutral hydrogen and neutral helium atoms. Red (blue) solid line corresponds to the damping rate derived in the single-fluid approach with (without) neutral helium. The collision frequency is defined as  $\alpha_H/\rho_H + \alpha_{H^+}/\rho_{H^+}$  for the case of neutral hydrogen and  $\alpha_{H+H}/\rho_H + \alpha_{H+H}/\rho_{H^+} + \alpha_{He+H}/\rho_H + \alpha_{He+H}/\rho_{He^+}$ . The values of temperature and number densities are taken from the FAL93-3 model (Fontenla et al. 1993).

converted into heat due to the effect of ambipolar diffusion providing an order of magnitude larger amount of energy to the chromosphere compared to the dissipation of stationary currents (Khomenko and Collados 2012). Nevertheless, Arber et al. (2016) argued that heating produced by acoustic shocks is more important than that by Alfvén wave dissipation through ion-neutral collisions. Therefore, the question of chromospheric heating due to the ion-neutral interaction will require further studies in the future.

Most of the atoms in the chromosphere are neutral hydrogen, but a significant amount of neutral helium may also be present in the plasma with a particular temperature. The neutral helium atoms may enhance the damping of MHD waves due to the collisions with ions. Zaqarashvili et al. (2011b) considered three-fluid MHD approximation, where one component is electron-proton-singly ionized helium and other two components are the neutral hydrogen and neutral helium atoms. They derived the dispersion relation of linear Alfvén waves in isothermal and homogeneous plasma, which has a following form:

$$\omega^4 + i \left( \frac{\alpha_H}{\rho_H} + \frac{\alpha_{He}}{\rho_{He}} + \frac{\alpha_H + \alpha_{He}}{\rho_i} \right) \omega^3 + \left( k_z^2 v_A^2 + \frac{\alpha_H \alpha_{He} \rho_0}{\rho_H \rho_{He} \rho_i} \right) \omega^2 - i k_z^2 v_A^2 \left( \frac{\alpha_H}{\rho_H} + \frac{\alpha_{He}}{\rho_{He}} \right) \omega + \frac{\alpha_H \alpha_{He}}{\rho_H \rho_{He}} k_z^2 v_A^2 = 0, \quad (155)$$

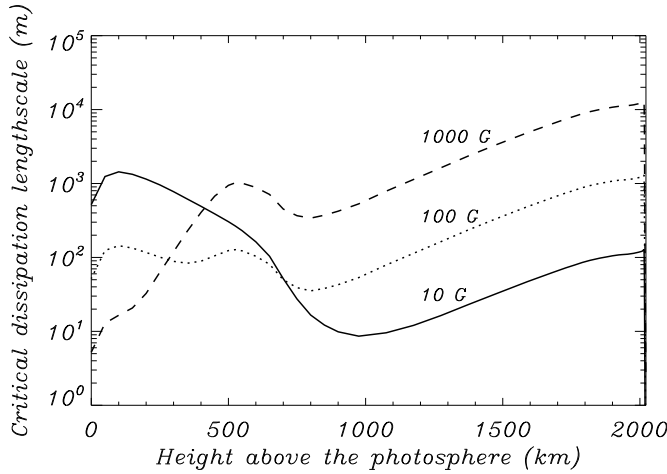


**Fig. 13** Critical dissipation lengthscale for Alfvén waves as a function of height above the solar photosphere according to the chromospheric model F of Fontenla et al. (1993). The various linestyles correspond to a magnetic field strength of 10 G (solid), 100 G (dotted), and 1000G (dashed). Adapted from Soler et al. (2015b).

where  $\rho_{\text{He}}$  is the density of neutral helium atoms,  $\rho_i$  is the density of ions (protons+singly ionized helium),  $\rho_0 = \rho_{\text{H}} + \rho_{\text{He}} + \rho_i$  is the total density of all fluids,  $v_A = B_0/\sqrt{\mu\rho_i}$  is the Alfvén speed of electron-proton-singly ionized helium fluid,  $\alpha_{\text{H}}$  is the coefficient of friction between neutral hydrogen atoms and ions (protons and singly ionized helium) and  $\alpha_{\text{He}}$  is the coefficient of friction between neutral helium atoms and ions (protons and singly ionized helium). The dispersion relation has four different roots: two complex solutions, which correspond to Alfvén waves damped by ion-neutral collision, and two purely imaginary solutions, which correspond to damped vortex solutions of neutral hydrogen and neutral helium fluids. Fig. 12 (red asterisks) shows the damping rate of Alfvén waves obtained by three-fluid MHD model when neutral helium atoms are also included. Zaqarashvili et al. (2011a) concluded that the presence of neutral helium may significantly enhance the damping of Alfvén waves compared to the damping due to neutral hydrogen at certain values of plasma temperature (10 000-40 000 K) and ionization. Therefore, the height dependence of the ionization degrees of hydrogen and helium may influence the damping rate of Alfvén waves.

Recently, Zaqarashvili et al. (2013) studied the effect of neutral helium on the damping of torsional Alfvén waves in stratified, partially ionized plasma of the solar chromosphere. They considered a magnetic flux tube, which is expanded up to 1000 km height and then becomes vertical owing to merging with neighboring tubes. Consecutive derivation of single-fluid MHD equations resulted in a new Cowling diffusion coefficient in the presence of neutral helium, which has a following form

$$\eta_c = \frac{B_0^2}{\mu} \frac{\alpha_{\text{He}}\xi_{\text{H}}^2 + \alpha_{\text{H}}\xi_{\text{He}}^2 + \alpha_{\text{HeH}}(\xi_{\text{H}} + \xi_{\text{He}})^2}{\alpha_{\text{H}}\alpha_{\text{He}} + \alpha_{\text{H}}\alpha_{\text{HeH}} + \alpha_{\text{He}}\alpha_{\text{HeH}}}, \quad (156)$$

where  $\xi_{\text{H}} = \rho_{\text{H}}/\rho$ ,  $\xi_{\text{He}} = \rho_{\text{He}}/\rho$ , while  $\alpha_{\text{H}} = \alpha_{\text{H+H}} + \alpha_{\text{He+H}}$  and  $\alpha_{\text{He}} = \alpha_{\text{H+He}} + \alpha_{\text{He+He}}$  are friction coefficients between collisions of neutral hydrogen and neutral

helium atoms with ions. Based on the analytical study, Zaqarashvili et al. (2013) concluded that shorter-period ( $< 5$  s) torsional Alfvén waves, which are generated at the photosphere, may damp quickly in the chromospheric network due to ion-neutral collisions, but the longer-period ( $> 5$  s) waves may not reach the transition region as they become evanescent at lower heights due to stratification. But the authors also noted that the torsional Alfvén waves with all periods may penetrate the corona if they are excited in the higher part of the chromosphere probably due to magnetic reconnection. This point needs further clarification.

### 5.1.6 Formation of spicules by ion-neutral collisions

Spicules were discovered almost 130 years ago, but they still remain one of the most mysterious phenomena in the solar atmosphere. Spicules are usually detected in chromospheric  $H\alpha$ ,  $D_3$  and  $Ca II H$  lines as thin and elongated structures in the solar limb (Sterling 2000). Spicule formation mechanisms can be formally divided into three different groups: pulses (Suematsu et al. 1982; Murawski and Zaqarashvili 2010), Alfvén waves (Hollweg et al. 1982; Kudoh and Shibata 1999) and p-mode leakage (De Pontieu et al. 2004).

Haerendel (1992) suggested that damping of upwardly propagating Alfvén waves due to collisions between ions and neutrals provide average net force, which may act against gravity and lift up transition region. The net force can be calculated from MHD equations using WKB approach (De Pontieu and Haerendel 1998)

$$F_z = \rho_n v_{1y}^2 \frac{\omega^2}{2\nu_{ni}v_A}, \quad (157)$$

where  $\rho_n$  is the density of neutrals,  $v_{1y}$  is the perturbation of Alfvén waves,  $\omega$  is the wave frequency,  $\nu_{ni}$  is the neutral-ion collision frequency and  $v_A$  is the Alfvén speed. De Pontieu and Haerendel (1998) showed that Alfvén waves with frequencies of 0.2-0.6 Hz may produce spicules.

However, James and Erdélyi (2002) numerically solved a set of fully nonlinear, dissipative 1.5D MHD equations with continuous sinusoidal driver. They found that spicule formation is primarily caused by the impact of a series of slow shocks generated by the continuous interaction between the upward propagating driven wave train and the downward propagating train of waves created by reflection off the transition region. At lower frequencies, the heating due to ion-neutral damping was found to provide only a small benefit due to the increased thermal pressure gradient. At higher frequencies, whilst the heating effect becomes stronger, the much reduced wave amplitude reaching the transition region hinders spicule formation. James et al. (2003) and Erdélyi and James (2004) came to essentially the same conclusions. The results of these works suggest that ion-neutral damping may not support spicules as described by Haerendel (1992). However, the authors concluded that the effect is highly sensitive to the level of ionisation and therefore to the energy balance. Including the effects of thermal conduction and radiation may well lead to different results and hence the Alfvén wave damping due to ion-neutral collisions may still play a role in the formation of spicules. This point is opened for further discussion.

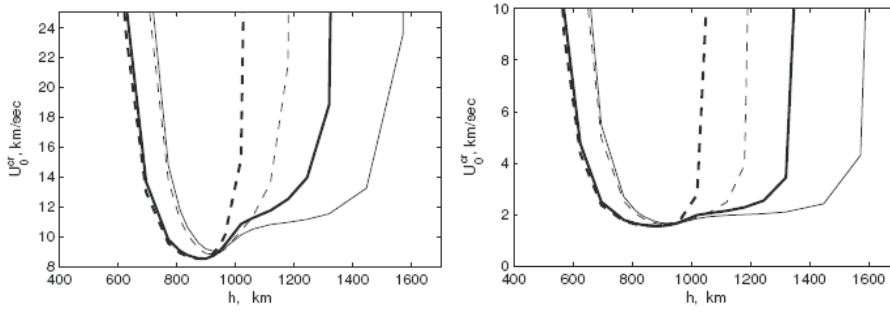


**Fig. 14** Dependence of the threshold value of the velocity  $U_0^{cr}$  on height with (solid lines) and without (dashed lines) Coulomb collisions, for  $B = 30$  G (thin lines) and for  $B = 60$  G (thick lines). The left panel corresponds to the protons and the right panel to ions with  $m_i = 30m_p$ . Adapted from Gogoberidze et al. (2009).

### 5.1.7 Farley-Buneman instability in chromospheric plasma

Motion of neutral atoms across the magnetic field in partially ionized plasmas may lead to Farley-Buneman instability (FBI) which is well studied in the Earth's ionosphere (Farley 1963; Buneman 1963). When electrons are strongly magnetized then the collisional drag of ions due to the neutral flow may generate electric currents which lead to the instability in some circumstances. Fontenla (2005) suggested that upward propagating fast magnetoacoustic waves could be unstable to FBI in partially ionized plasmas of the solar chromosphere, which may heat the ambient medium. The instability threshold can be expressed by the condition:

$$U_{thr} = C_s(1 + \psi_{\perp}), \quad (158)$$

where  $U_{thr}$  is the threshold plasma flow,  $C_s$  is the ion-acoustic speed and

$$\psi_{\perp} = \frac{\nu_{ea}\nu_{pa}}{\Omega_e\Omega_p} \quad (159)$$

is the parameter, which controls the particle magnetization. Fontenla (2005) showed that the FBI would be triggered in the mid- and upper-chromosphere by wave velocity amplitudes larger or equal to the ion-acoustic speed, which is below but close to the adiabatic sound speed. Fontenla et al. (2008) set up similar considerations, but instead of fast MHD waves they suggested that convective overshoot motions are drivers of the FBI, which provide enough energy to account for the upper chromospheric radiative losses in the quiet-Sun internetwork and network lanes. Recently, Madsen et al. (2014) used a multi-component approach to FBI and showed that the instability may be triggered by velocities as low as  $4 \text{ km s}^{-1}$ , which is well below the neutral acoustic speed.

Gogoberidze et al. (2009, 2014) studied the FBI taking into account Coulomb collisions and particle thermal effects, respectively. Figure 14 shows the dependence of critical velocity on height with and without Coulomb collisions. It is seen that Coulomb collisions reduce the threshold value of the critical velocity. However, Gogoberidze et al. (2009) concluded that the FBI is a less efficient heating mechanism than the collisional dissipation of cross-field currents that drive the instability.

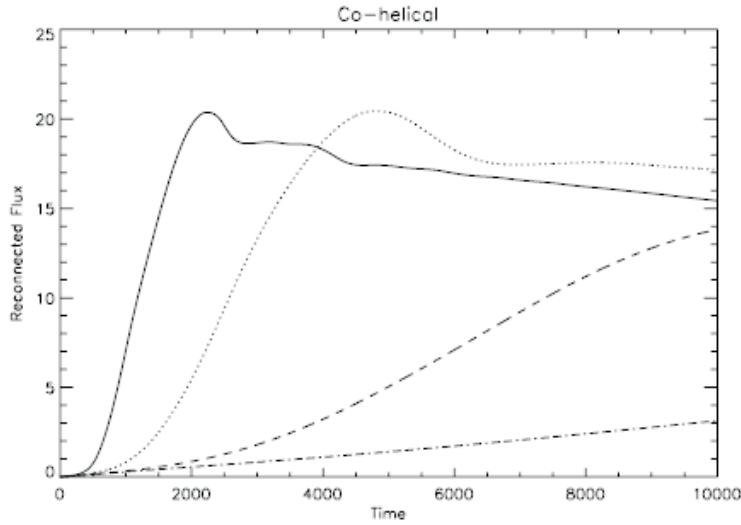


**Fig. 15** Effect of neutral-hydrogen to proton density ratio on the reconnected magnetic flux for two co-helical current loops. (solid)  $\rho_n/\rho_p = 1$ , (dotted)  $\rho_n/\rho_p = 10$ , (dashed)  $\rho_n/\rho_p = 100$ , and (dot-dashed)  $\rho_n/\rho_p = 1000$ . Adapted from Smith and Sakai (2008).

This conclusion concerns both the lower chromosphere, where the threshold velocity is decreased by heavy ions, and the middle/upper chromosphere, where the threshold velocity is decreased by the Coulomb collisions. However, local development of FBI in the presence of strong cross-field currents and/or strong small-scale magnetic fields can not be excluded. In such cases, FBI should produce locally small-scale, 10-100 cm, density irregularities in the solar chromosphere. These irregularities can cause scintillations of radio waves with similar wave lengths and provide a tool for remote chromospheric sensing.

#### 5.1.8 Magnetic reconnection in partially ionized chromospheric plasma

Shibata et al. (2007) discovered chromospheric anemone jets with the Solar Optical Telescope (SOT) onboard the Hinode spacecraft, which are typically 2–5 Mm long with mean speed 10–20 km s<sup>-1</sup>. The anemone jets are probably connected to small scale magnetic reconnection in the solar chromosphere. Therefore, their discovery revived interests in chromospheric reconnection. Reconnection is also supposed to be one of the possible mechanisms of spicule formation. As the chromospheric plasma is partially ionized, it is desired to consider magnetic reconnection in the presence of neutral atoms.

Smith and Sakai (2008) performed 2.5D numerical simulations of coalescing current loops using a two-fluid model of partially ionized plasmas, where one fluid is neutral hydrogen atoms and second one is charged particles (protons+electrons). Figure 15 shows total reconnected magnetic flux as a function of time for various neutral-hydrogen to proton density ratios. The slope of each line is a direct measure of the magnetic reconnection rate. It is seen from this figure that the rates of magnetic reconnection strongly depend on the neutral-hydrogen to proton density ratio,  $\rho_n/\rho_p$ : the rate of magnetic reconnection for the ratio of  $\rho_n/\rho_p = 1$



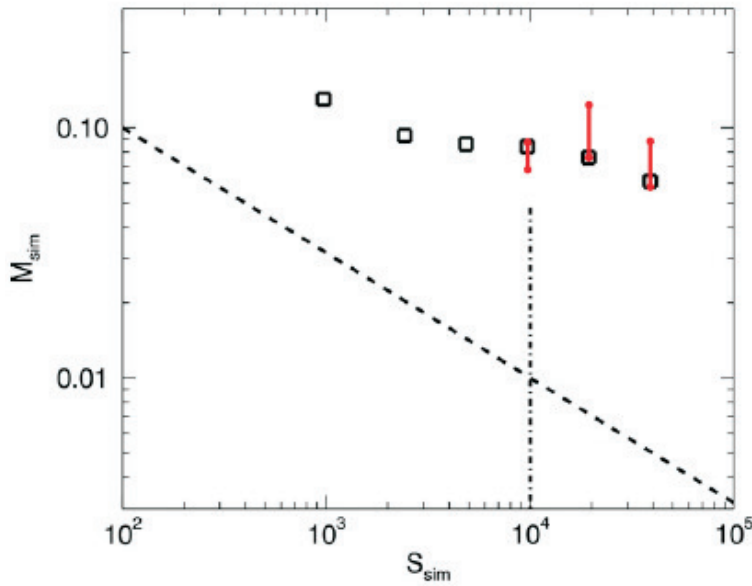


**Fig. 16** Normalized magnetic reconnection rate  $M_{sim}$  for six simulations with different Lundquist number ( $S_{sim}$ ). The squares show the reconnection rate taken at a time in each simulation when the length of the current sheet has reached  $L_{sim} = 2.75 L_0$ , and in all simulations is before the onset of the plasmoid instability. The red lines show the range in reconnection rate taken again at later times in the three plasmoid-unstable simulations, after the plasmoids are formed. The dashed line is the Sweet-Parker scaling law  $M \sim 1/S$ . The dot-dashed line shows the separation between plasmoid-stable and plasmoid-unstable regimes for these multi-fluid simulations. Adapted from Leake et al. (2012).

(upper chromosphere) is twenty times faster than for  $\rho_n/\rho_p = 1000$  (lower chromosphere). This important result implies that observed anemone jets associated with fast magnetic reconnection tend to occur in the upper chromosphere. Comparisons of two-fluid and single-fluid simulations show significant differences in the measured rates of magnetic reconnection, particularly for the density ratios representative of the lower chromosphere. On the other hand, Smith and Sakai (2008) showed that the rate of magnetic reconnection does not significantly depend on recombination/ionization effects and the value of ion-neutral collision frequency.

Leake et al. (2012) presented the self-consistent multi-fluid simulations of magnetic reconnection in a chromospheric weakly ionized plasma. They simulated two-dimensional magnetic reconnection in a Harris current sheet with a numerical model which includes ion-neutral scattering collisions, ionization, recombination, optically thin radiative loss, collisional heating, and thermal conduction. They found that in the resulting tearing mode reconnection the neutral and ion fluids become decoupled upstream from the reconnection site, creating an excess of ions in the reconnection region and therefore an ionization imbalance. Ion recombination in the reconnection region, combined with Alfvénic outflows, quickly removes ions from the reconnection site, leading to a fast reconnection rate independent of Lundquist number,  $S = \mu v_A L / \eta$ . Figure 16 shows the dependence of the normalized magnetic reconnection rate on Lundquist number. It is seen that the

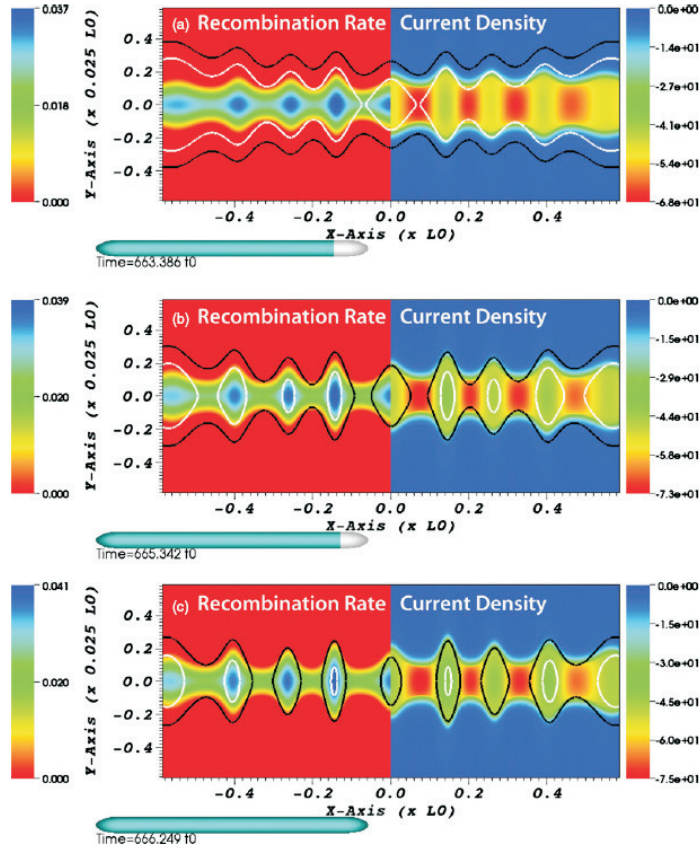


**Fig. 17** Plasmoid formation and evolution: recombination rate  $\Gamma_i^{rec} L_0^3 t_0$  (left) and current density  $j\mu L_0/B_0$  (right), and two contour levels of  $A_z$  of  $-0.0681 B_0 L_0$  (white) and  $-0.0687 B_0 L_0$  (black), at three different times in the simulation where  $\eta = 0.5 \times 10^{-5} \eta_0$ . Adapted from Leake et al. (2012).

consideration of neutrals significantly enhances the reconnection rate for all values of Lundquist number as compared to the single fluid Sweet-Parker reconnection rate.

In addition, Leake et al. (2012) found that the non-equilibrium partial ionization effects lead to the onset of the nonlinear secondary tearing instability (known as the plasmoid instability) at lower values of the Lundquist number than has been found in fully ionized plasmas (Figure 17). The increase in the ion and electron densities in the plasmoids led to an increase in the recombination rate that allowed further contraction of the magnetic islands on timescales comparable to the advection time of islands out of the current sheet.

Recently, Murphy and Lukin (2015) performed 2.5D simulations of asymmetric reconnection in weakly ionized, reacting plasmas where the magnetic field strengths, ion and neutral densities, and temperatures were different in each upstream region. The plasma and neutral components were evolved separately to allow non-equilibrium ionization. The asymmetric reconnection in the chromo-

sphere may occur when newly emerged flux interacts with pre-existing, overlying flux. During simulations of asymmetric reconnection, the ion and neutral flows remained decoupled, but the decoupling was asymmetric. In the case of magnetic asymmetry, there was net neutral flow through the current sheet from the weak magnetic field upstream region into the strong field region, which resulted from a large scale neutral pressure gradient and imperfect coupling between ions and neutrals along the inflow direction. Similarly, the greater Lorentz force acting on the ions from the strong field upstream region led to the ions pulling the X-point into the weak field upstream region. These effects were not present during symmetric simulations. An observational consequence of these neutral flows through the current sheet is that most of the neutrals swept along with the outflow are more likely to have originated from the weak magnetic field upstream region. This may be especially important if there are different elemental abundances in each upstream region. Murphy and Lukin (2015) also studied the Hall effect, which led to the development of a characteristic quadrupole magnetic field modified by asymmetry, but they did not find the X-point geometry expected during Hall reconnection. All simulations showed the development of plasmoids after an initial laminar phase.

The results presented in this subsection demonstrate that neutral atoms should be considered to describe magnetic reconnection in the solar chromosphere.

#### *5.1.9 Kelvin-Helmholtz instability in solar chromospheric jets*

The chromosphere is a highly inhomogeneous layer of the solar atmosphere, populated by a wide range of dynamical, jet-like features such as type I and II spicules at the solar limb and fibrils, mottles, Rapid Redshifted and Blueshifted Excursions (REs) on the disk (see the review by Tsiropoula et al. 2012). These small-scale plasma structures are observed near the network boundaries in strong chromospheric spectral lines such as  $H\alpha$ , Ca II H & K, and the Ca II infrared (IR) triplet. Some of these structures, in particular, REs (on-disk counterparts of type II spicules) which are absorption features detected in the blue and red wings of chromospheric lines (Langangen et al. 2008; Rouppe van der Voort et al. 2009; Kuridze et al. 2015), are characterised by very fast upflow velocities ( $\sim 50 - 150 \text{ km s}^{-1}$ ) and short lifetimes ( $\sim 20-60 \text{ s}$ ).

It is suggested that the short lifetime of the spicular jets in the chromospheric lines may be the result of their fast heating to transition region (TR) or even coronal temperatures. De Pontieu et al. (2011) have provided evidence that TR and coronal brightenings in AIA passbands are occurring co-spatially and co-temporally with chromospheric REs. Furthermore, Vanninathan et al. (2012) showed that the coronal hole large spicules observed with HINODE in the Ca II H line are appearing in the TR O v 629.76 Å line observed with the SUMER instrument on-board SOHO. Recently, Pereira et al. (2014) studied the thermal evolution of type II spicules using combined observations with the HINODE and Interface Region Imaging Spectrograph (IRIS) satellites and showed that the fading of spicules from the chromospheric Ca II H line is caused by rapid heating of the upward moving spicular plasma to higher temperatures. More recently, Henriques et al. (2016) found a statistically significant match between automatically detected heating signatures in the corona, as observed in the AIA pass-bands, and

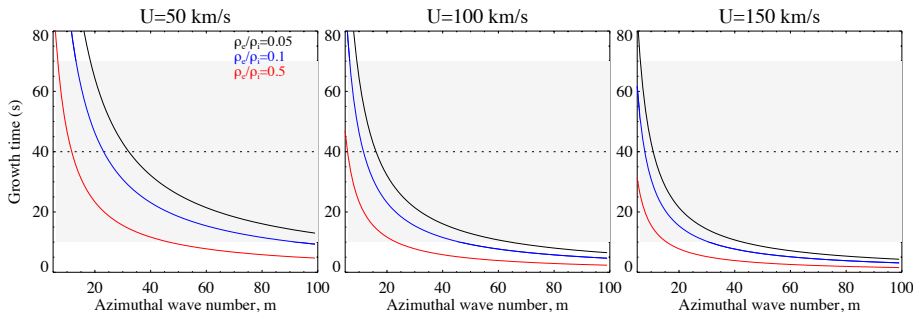


**Fig. 18** KHI growth times as a function of  $m$  for the twisted jets with different density ratios outside and inside the jet,  $\rho_e/\rho_i$ , and flow speed  $U$  from Kuridze et al. (2016). The grey-shaded areas indicate the typical range of lifetime ( $\sim 10 - 70$  s) with the horizontal dotted lines indicate the average lifetime of REs and type II spicules.

quiet-Sun REs, with a minimum of 6% of the detections at  $\sim 10^6$  K (AIA Fe IX 171 Å) being attributable to REs.

Despite a wealth of observations, the heating mechanism associated with chromospheric jets remains a mystery as far as heating timescales estimated with various dissipation mechanisms such as diffusivity, thermal conduction, radiative losses are much longer than the dynamic timescales of observed chromospheric jets. Recent theoretical studies suggest that the Kelvin-Helmholtz Instability (KHI) could have a significant effect on the dynamics of chromospheric jets (Zaqarashvili 2011; Kuridze et al. 2015; Zaqarashvili et al. 2014, 2015). Mass flows in the chromospheric fine structures can create velocity discontinuities between the surface of the jets and surrounding media, which may trigger the KHI in some circumstances depending on the directions of flows and magnetic fields.

Kuridze et al. (2016) have investigated the dynamics and stability of quiet-Sun chromospheric jets observed at disk center using data obtained by the high resolution CRisp Imaging SpectroPolarimeter instrument on the Swedish 1-m Solar Telescope (Scharmer et al. 2003). The data revealed REs appearing as high speed jets in the wings of the H $\alpha$  line, are characterized by short lifetimes and rapid fading without any descending behavior. To study the theoretical aspects of the stability of observed REs appearing as high speed upflows, they modelled chromospheric jets as twisted magnetic flux tubes moving along their axis, and used the ideal magnetohydrodynamic approximation to derive the governing dispersion equation. Analytical solutions of the dispersion equation indicate that this type of jet is unstable to Kelvin-Helmholtz instability (KHI), with a very short (few seconds) instability growth time (Figure 18).

Kuridze et al. (2016) have also detected a larger H $\alpha$  jet, which appears as a circular shaped absorption feature in the blue wing of H $\alpha$  (Figure 19). Its radius ( $\sim 400$  km) and LOS velocity ( $\sim 34$  km s $^{-1}$ ) suggest that this jet could be the on-disk counterpart of a macrospicule or H $\alpha$  surge frequently observed at the solar limb. The morphology of the jet suggests that the plasma flow was oriented along the LOS. Figure 19 shows that the structure develops azimuthal nodes over timescales of tens of seconds around its boundary. From a visual inspection they estimated  $m \sim 8$  projected vortex-like flows at around  $t = 37.52$  s (Figure 19)

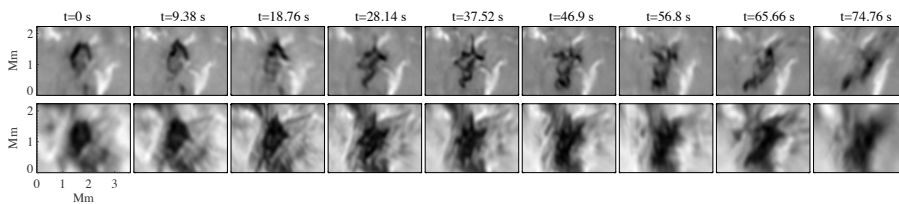


**Fig. 19** Sequence of frames showing the temporal evolution of the jet ejected along the LOS in  $H\alpha - 0.906 \text{ \AA}$  (top) and  $H\alpha - 0.543 \text{ \AA}$  of  $H\alpha$  (bottom) images from Kuridze et al. (2016). Initially the jet has circular top, however, it rapidly develops azimuthal nodes around its boundary.

and obtained growth time  $\sim 52 - 145$  s, which appears to be consistent with the timescale ( $\sim 37$  s) for the structure to develop the nodes in the image sequence presented in Figure 19.

To investigate non-linear, non-adiabatic effects Kuridze et al. (2016) have provided estimates of characteristic heating times for various dissipation processes through the analysis of the energy equation in the partially ionized plasma. The analysis shows that the ion-neutral collisions could be the most important process for the heating of the KH vortices and consequently the structure itself. For REs we estimate timescales of the heating due to the ion-neutral collisions, for KHI vortices with a high order of azimuthal wavenumbers, to be  $\sim 20 - 130$  s, comparable to the lifetimes of these chromospheric jets.

### 5.1.10 Prominence equilibrium in partially ionized plasmas

Quiescent solar prominences are clouds of cool and dense plasma suspended against gravity by forces thought to be of magnetic origin. They form over a wide range of latitudes on the Sun (Mackay 2015), but always along inversion polarity lines. Since the temperature of prominences is typically of the order of  $10^4$  K, the prominence plasma is only partially ionized. The exact ionization degree of prominences is unknown and the reported ratio of electron density to neutral hydrogen density (Patsourakos and Vial 2002; Heinzel et al. 2015) covers about two orders of magnitude (0.1-10). Partial ionization brings the presence of neutrals in addition to ions and electrons, thus collisions between the different species are possible and the effects on the prominence equilibrium should be considered.

On the other hand, small amplitude oscillations in prominences and filaments are a commonly observed phenomenon (Oliver and Ballester 2002). These oscillations appear to be of local nature, and observational evidence reveals that, once excited, are damped in short spatial and temporal scales. Commonly, these oscillations have been interpreted in terms of linear magnetohydrodynamic (MHD) waves and to explain the damping different mechanisms (thermal, resonant damping in non-uniform media, partial ionization, etc.) have been invoked. The relevance of each mechanism can be assessed by comparing the spatial and time scales produced by each of them with those obtained from observations. An extensive review on small amplitude oscillations in prominences can be found in Arregui et al. (2012).

One of the key problems in prominence physics is how these cool and dense structures are supported in the hotter and lighter solar corona. Usually, promi-

nences have been considered as composed of fully ionized plasma and it has been assumed that its support is provided by the magnetic field (Mackay et al. 2010; Vial and Engvold 2015). However, the consideration of prominences as composed by partially ionized plasmas and their support has received slight attention. In order to take into account the downward plasma motions observed in prominences, Mercier and Heyvaerts (1977) analysed the relative motion between charged and neutral species taking into account collisions between these species and found that the downward diffusion velocity of neutrals with respect to charged particles was about 6 m/s which is much less than the global downward velocity (about 1 km/s) in prominences. Therefore, they concluded that this effect was negligible and it can not explain the mass loss in these structures. Then, from the observational point of view the motions of both species could be considered identical. Building up on a model by Sakai (1984), Bakhareva et al. (1992) studied the dynamic regimes of a prominence using a Kippenhahn-Schlüter (Kippenhahn and Schlüter 1957) configuration and considering the prominence plasma as partially ionized. First of all, they consider a generalized Ohm's law taking into account the presence of neutrals and, then, they derived an induction equation which contains further terms coming from the non-stationarity of the problem and the presence of neutrals. Next, they assumed time dependent velocity and magnetic fields, and described the prominence dynamics in terms of a dimensionless function  $a(t)$  which characterizes the degree of current-sheet compression. After perturbing the Kippenhahn-Schlüter equilibrium, the resulting equations indicated that the equilibrium is unstable and that three different regimes can be studied. In the first dynamical regime, the non equilibrium is correlated with the process of material density oscillations growing up in the prominence, and if the relative density of neutrals decreases, the period of oscillations decreases too, and the growth time tends to infinity; in the second case, the density decreases aperiodically although the basic features of the previous regime remain; finally, in the third case, a process of slow condensation towards equilibrium density values is possible. In summary, the model shows that partially ionized plasma causes instability of the considered Kippenhahn-Schlüter configuration, and that the excited oscillations of density, magnetic field and material velocity are able to destroy the prominence. The cause of this instability seems to be the inability of the magnetic field to support the plasma neutral component which starts to fall down, then, through ion-neutral collisions all the plasma starts to move which means that an additional current appears in the filament which, at the same time, affects the Lorentz force.

One of the typical features of solar prominences is its filamentary structure (Dunn 1960; Engvold 2015). The nature of these thin, long and inclined filament threads is still a matter of debate, and if one assumes that these threads delineate the magnetic field, then, the supporting mechanism against gravity remains to be understood. Pécseli and Engvold (2000) proposed a model to explain the support of prominence threads based on the levitation of prominence plasma produced by weakly damped MHD waves in almost vertical flux tubes. The wave damping produced by ion-neutral collisions provides a wave pressure and levitation enough to support prominence plasma in the low corona. In the model, they consider that only the Lorentz force is at work and assuming that it fluctuates in time, they calculated the time average. The magnetic field is assumed to be composed of a background field,  $B_0$ , and a fluctuating part,  $\tilde{B}_1$ , and the time average of the

Lorentz force is given by:

$$\bar{F} = \frac{1}{2\mu} k_I |B_1|^2 e^{-2k_I z} \hat{z} \quad (160)$$

where  $k_I$  is the imaginary part of the wavenumber. From a physical point of view, the wave produces a force on the medium due to the loss of wave momentum and, as a consequence, the wave is damped. Using the two fluid approach, assuming incompressibility and taking into account resistivity, the dispersion relation for this case is given by,

$$\omega^2 = k^2 v_a^2 + k^2 \frac{\nu_{in}}{\mu\sigma} \left( 1 - i \frac{\omega}{\nu_{in}} - \frac{\nu_{ni}}{\nu_{ni} - i\omega} \right) - i\omega\nu_{in} + i\omega \frac{\nu_{in}\nu_{ni}}{\nu_{ni} - i\omega} \quad (161)$$

where  $v_a$  is the Alfvén velocity. Two limiting cases can be considered: (1)  $\sigma \rightarrow \infty$  but  $\nu_{in} \neq 0$ , and (2)  $\sigma$  finite and  $\nu_{in} = 0$

For infinite conductivity, the dispersion relation becomes,

$$\omega^2 = \frac{k^2 v_a^2}{1 + \frac{\rho_n}{\rho_0} \frac{1+i\tau_1}{1+\tau_1^2}} \quad (162)$$

where  $\tau_1 = \frac{\omega}{\nu_{ni}}$ , and ion-neutral collisions will damp Alfvén waves. Considering spatial damping, and in the limit of weak damping,  $k_I = \frac{\omega^2 \rho_n}{2\nu_{ni} v_a (\rho_0 + \rho_n)}$ , when a real frequency is considered. For finite conductivity and the collisionless case, the dispersion relation is given by,

$$\omega^2 = v_a^2 k^2 - i \frac{\omega}{\sigma\mu} k^2 \quad (163)$$

and, in the case of spatial damping,  $k_I = \frac{\omega^2}{2\sigma\mu v_a^2}$ . Then, using typical parameters for prominence conditions, a comparison between the gravitational force and the time averaged Lorentz force was done. Numerical estimates suggest that the force exerted by Alfvén waves at frequencies  $\omega \geq 2$  rad/s could possibly dominate over gravity. Therefore, spatial damping of Alfvén waves, produced by ion-neutral collisions, could give a non-negligible contribution to a force density coming from weakly damped Alfvén waves which could help to sustain the prominence mass.

As stated before, Bakhareva et al. (1992) concluded that the draining of neutrals was responsible for the destabilization of the dynamical prominence model considered, since they are not attached to the magnetic field. This problem of how neutrals are supported in prominences is a matter of great interest. Terradas et al. (2015) have used the most simple version of two-fluid equations, including ion-neutral collisions and charge exchange collisions, to study the temporal behaviour of a prominence plasma located inside the solar corona. In the model, the prominence is represented by a large density enhancement, with respect to the background, composed by 75% of neutrals and 25% of ions, and the magnetic configuration is a quadrupolar configuration with dips (Terradas et al. 2013). The system of time dependent nonlinear equations together with boundary conditions have been solved in two dimensions and Figure 20 shows the two dimensional distribution of both plasmas after  $t = 4.8$  min. for two different collisional frequencies between neutrals and ions,  $\nu_{ni}$ , and in the absence of charge exchange collisions. In the top panel, we can observe that both fluids, ion-electron and neutrals, are

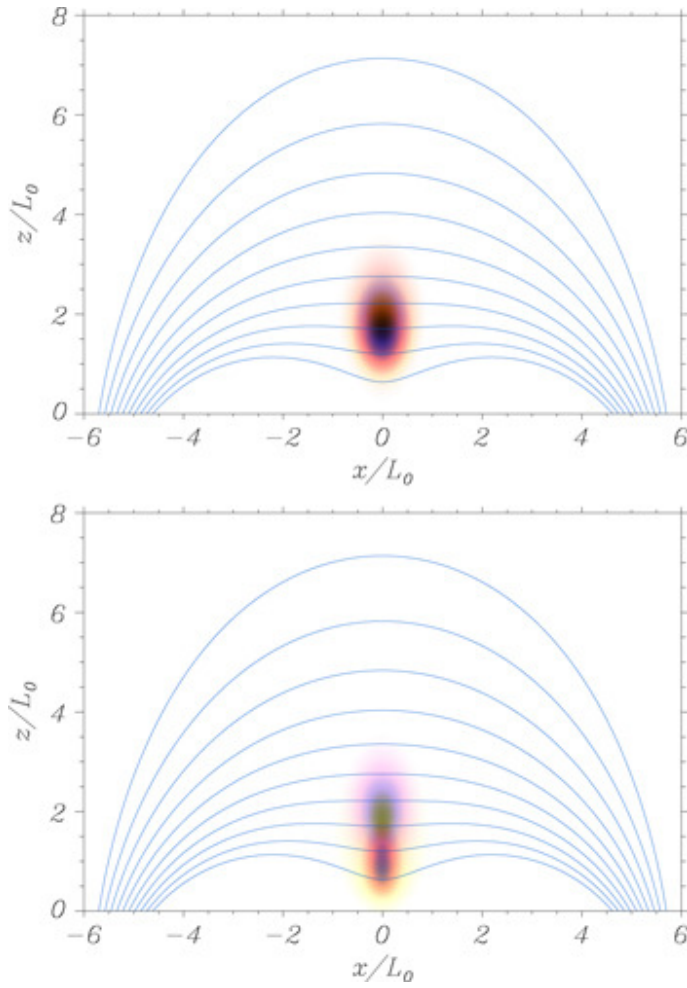


**Fig. 20** Magnetic field lines (blue lines) and densities of ion-electron fluid (blue-green colours) and neutrals (yellow-pink colours) at  $t=4.8$  min. Top panel: simulation corresponding to a collisional frequency  $\nu_{ni} = 8.5$  Hz. Bottom panel: simulation corresponding to a collisional frequency  $\nu_{ni} = 0.8$  Hz (See movie). Adapted from Terradas et al. (2015).

essentially superimposed and that the spatial shape of the densities is very similar to that of the beginning of the simulation which means that mass redistribution is very small. On the contrary, in the bottom panel we observe that for a smaller collisional frequency neutrals fall, quickly diffusing through the magnetic field, therefore, neutrals can not be supported. Next, considering the top panel situation, and allowing the system to evolve longer, up to 10 hr, the changes at the prominence core are very small since neutrals move downwards with an almost negligible velocity. This means that a partially ionized prominence plasma can be efficiently supported when the coupling between ions and neutrals is very strong, and we have a single fluid behaviour at the prominence body. In spite of the fact that the drift velocity is very small, the friction coefficient is large which means that the



frictional force, oriented upwards because the drift velocity is positive, is enough to counterbalance the effect of gravity on neutrals. Considering the momentum equation for neutrals, the drift velocity in the  $z$ -direction can be approximated by  $v_{Dz} \approx g/\nu_{ni}$ , in agreement with Gilbert et al. (2002, 2011), which means that for strong coupling the vertical component of the drift velocity is small, which is also in agreement with Mercier and Heyvaerts (1977). On the other hand, from the momentum equation for the ion-electron fluid it can be seen that the ionized fluid is supported by the magnetic field, but the inclusion of a neutral component produces the need to increase the deformation of the magnetic field in order to increase the restoring force. This result is only valid for strong coupling between the two fluids. Finally, including the effect of charge exchange collisions means that friction is increased (of the order of three times with respect to momentum-transfer collisions) and, as a consequence, neutrals downwards velocity suffers a further reduction which helps to sustain the prominence. In conclusion, the draining of neutrals is not an important issue for prominence evolution when a strong coupling between fluids is present.

### *5.1.11 Damping of oscillations in partially ionized prominence plasmas*

Observational studies have allowed reliable values for the damping time of small amplitude prominence/filament oscillations to be obtained (Molowny-Horas et al. 1999; Terradas et al. 2002; Lin 2004). The values obtained are usually between 1 and 4 times the corresponding period, and large regions of prominences/filaments display similar damping times. Several studies have considered the damping of MHD waves in partially ionized structures of the solar atmosphere (De Pontieu et al. 2001; James et al. 2003; Khodachenko et al. 2004; Leake et al. 2005; Soler et al. 2013) and, since prominences can be considered as partially ionized plasmas, a possible mechanism to damp prominence oscillations could be ion-neutral collisions. In this sense, Khodachenko et al. (2004, 2006) made a qualitative study of the damping of MHD waves in a partially ionized plasma considering as damping mechanisms viscosity, collisional friction and thermal conduction. From this study, they concluded that collisional friction is the dominant damping mechanism for MHD waves in prominences. On the other hand, flows in prominences are routinely observed in  $H_\alpha$ , UV and EUV lines (Labrosse et al. 2010). In  $H_\alpha$  quiescent filaments, the observed velocities range from 5 to 20 km s<sup>-1</sup> (Zirker et al. 1998; Lin et al. 2003) and, because of physical conditions in filament plasma, they seem to be field-aligned. Furthermore, observations made with Hinode/SOT by Okamoto et al. (2007) reported the presence of synchronous vertical oscillatory motions in the threads of an active region prominence, together with the presence of flows along the same threads. However, in limb prominences different kinds of flows are observed and, for instance, observations made by Berger et al. (2008) with Hinode/SOT have revealed a complex dynamics with vertical downflows and upflows.

In the following, assuming as general background model an unbounded, flowing, magnetized and partially ionized prominence plasma, we describe several quantitative studies which point out the role that could be played by ion-neutral collisions in the damping of MHD waves in prominence plasmas.

### 5.1.12 Basic Equilibrium and Governing Equations

Forteza et al. (2007) derived the full set of MHD equations for a partially ionized, single-fluid hydrogen plasma (see sect. 2.6) which were applied to the study of the time damping of linear, adiabatic fast and slow magnetoacoustic waves in an unbounded prominence medium. This study was later extended to the non-adiabatic case, including thermal conduction by neutrals and electrons and radiative losses (Forteza et al. 2008). Next, Barceló et al. (2011) considered a homogeneous, unbounded and flowing partially ionised hydrogen plasma characterized by a plasma density,  $\rho_0$ , temperature,  $T_0$ , and number densities of neutrals,  $n_n$ , ions,  $n_i$ , and electrons  $n_e$ , with  $n_e = n_i$ . Thus, the gas pressure is  $p_0 = (2n_i + n_n)k_B T_0$ , where  $k_B$  is Boltzmann's constant. The relative densities of neutrals,  $\xi_n$ , and ions,  $\xi_i$ , are given by

$$\xi_n = \frac{n_n}{n_i + n_n}, \quad \xi_i = \frac{n_i}{n_i + n_n}, \quad (164)$$

where we have neglected the contribution of electrons. We can now define a quantity,  $\tilde{\mu}$ , given by,

$$\tilde{\mu} = \frac{1}{1 + \xi_i}, \quad (165)$$

which gives us information about the plasma degree of ionisation. Following Eq. (165), for a fully ionised plasma  $\tilde{\mu} = 0.5$ , while for a neutral plasma  $\tilde{\mu} = 1$ . This medium is threaded by a uniform magnetic field along the  $x$ -direction, with a field-aligned background flow. The equilibrium magnitudes of the medium are given by

$$p_0 = \text{const.}, \quad \rho_0 = \text{const.}, \quad T_0 = \text{const.},$$

$$\mathbf{B}_0 = B_0 \hat{x}, \quad \mathbf{v}_0 = v_0 \hat{x},$$

where  $B_0$  and  $v_0$  are constants, and the effect of gravity has been ignored. Since a medium with physical properties akin to those of a quiescent solar prominence was considered, the density is  $\rho_0 = 5 \times 10^{-11} \text{ kg/m}^3$ , the temperature  $T_0 = 8000 \text{ K}$ , the magnetic field  $|\mathbf{B}_0| = 10 \text{ G}$ , and a field-aligned flow with  $v_0 = 15 \text{ km/s}$ , subalfvénic but slightly supersonic, simulating the typical flows observed in the spines of quiescent filaments was included.

Using this background model, the dispersion relation for linear MHD waves was obtained by considering small perturbations from equilibrium, linearising the single fluid basic equations (Forteza et al. 2007; Barceló et al. 2011), and performing a Fourier analysis in terms of plane waves, assuming that perturbations behave as  $f_1(\mathbf{r}, t) = f e^{i(\omega t - \mathbf{k} \cdot \mathbf{r})}$ . With no loss of generality, the wavevector  $\mathbf{k}$  lies in the  $xz$ -plane ( $\mathbf{k} = k_x \hat{x} + k_z \hat{z}$ ), and the wave frequency,  $\omega$ , could be obtained from

$$\omega = \Omega + k_x v_0 \quad (166)$$

$\Omega$  being the wave frequency in absence of flow.

Following this procedure, the dispersion relation for Alfvén waves is given by,

$$\Omega^2 - i\Omega k^2 (\eta_C \cos^2 \theta + \eta \sin^2 \theta) - v_a^2 k^2 \cos^2 \theta = 0, \quad (167)$$

where  $\theta$  is the angle between the wavenumber vector and the magnetic field,  $v_a$  is the Alfvén speed, while  $\eta$  and  $\eta_C$  are Spitzer's and Cowling's resistivities, respectively. Eq. (167) points out that the time damping of Alfvén waves must be dominated by resistive effects.

The corresponding dispersion relation for thermal and magnetoacoustic waves is

$$(\Omega^2 - k^2 \Lambda^2)(ik^2 \eta_C \Omega - \Omega^2) + k^2 v_a^2 (\Omega^2 - k_x^2 \Lambda^2) + ik^2 k_z^2 v_a^2 \Lambda^2 \Xi \rho_0 \Omega = 0, \quad (168)$$

where  $\Lambda^2$  is the non-adiabatic sound speed squared (Forteza et al. 2008; Soler et al. 2008, 2010) defined as

$$\Lambda^2 = \frac{c_s^2}{\gamma} \left[ \frac{(\gamma - 1)(\kappa_{e\parallel} k_x^2 + \kappa_n k^2 + \omega_T - \omega_\rho) + i\gamma \Omega}{(\gamma - 1)(\kappa_{e\parallel} k_x^2 + \kappa_n k^2 + \omega_T) + i\Omega} \right], \quad (169)$$

with

$$\begin{aligned} \kappa_{e\parallel} &= \frac{T_0}{p_0} \kappa_{e\parallel}, & \kappa_n &= \frac{T_0}{p_0} \kappa_n \\ \omega_\rho &= \frac{\rho_0}{p_0} \rho_0 L_\rho, & \omega_T &= \frac{\rho_0}{p_0} T_0 L_T \end{aligned}$$

and where the effects of optically thin radiative losses, thermal conduction by electrons and neutrals, and a constant heating per unit volume are included, and  $\Xi$  is,

$$\Xi = \frac{\xi_n^2 \xi_i}{(1 + \xi_i) \alpha_n}, \quad (170)$$

with  $\alpha_n$  a friction coefficient (Braginskii 1965; Khodachenko et al. 2004; Leake et al. 2005). Depending on the value given to  $\tilde{\mu}$  and to both Spitzer's and Cowling's resistivities, one may have different types of plasmas, and that of interest in this case is a partially ionized plasma characterized by  $0.5 < \tilde{\mu} < 1$ ,  $\eta \neq \eta_C$  and  $\Xi \neq 0$ . Other important parameters are the numerical value and behaviour of the sound ( $c_s$ ) and Alfvén ( $v_a$ ) speeds. In the case of density and magnetic field assumed, the Alfvén speed has a constant numerical value of 126.15 km/s. However, since the sound speed depends on gas pressure, which is a function of the number densities of ions and neutrals, its numerical value is not constant but depends on the ionisation fraction considered. For a fully ionised plasma, the sound speed is 14.84 km/s, while for a partially ionised plasma with  $\tilde{\mu} = 0.95$  its value decreases to 10.76 km/s. This variation in the sound speed can be important since depending on the flow speed and ionisation fraction chosen, the flow speed could be greater than, smaller than, or equal to the sound speed, which affects the direction of propagation of slow and thermal waves (Carbonell et al. 2009).

### 5.1.13 Temporal damping of Alfvén waves

The solutions to the dispersion relation (167) written in terms of  $\omega$ , frequency measured by an observer external to the flow, are,

$$\begin{aligned} \omega_{\text{hfb}} &= k_x v_0 + \\ &+ \frac{\sqrt{4v_a^2 k^2 \cos^2 \theta - (\eta_C \cos^2 \theta + \eta \sin^2 \theta)^2 k^4}}{2} + \\ &+ \frac{ik^2 (\eta_C \cos^2 \theta + \eta \sin^2 \theta)}{2}, \end{aligned} \quad (171)$$

and

$$\begin{aligned} \omega_{\text{lfb}} = & k_x v_0 - \\ & - \frac{\sqrt{4v_a^2 k^2 \cos^2 \theta - (\eta_C \cos^2 \theta + \eta \sin^2 \theta)^2 k^4}}{2} + \\ & + \frac{ik^2(\eta_C \cos^2 \theta + \eta \sin^2 \theta)}{2}, \end{aligned} \quad (172)$$

where hfb and lfb mean high frequency and low frequency branch, respectively.

The real part of the frequency for the low frequency branch becomes zero for,

$$k_{\text{lfb}} = \frac{2\sqrt{v_a^2 - v_0^2} \cos \theta}{\eta_C \cos^2 \theta + \eta \sin^2 \theta}. \quad (173)$$

Since in this case  $c_s < v_0 < v_a$ , when  $k < k_{\text{lfb}}$  the real part of the frequency is negative and the low frequency Alfvén wave propagates towards the negative part of the x-axis; when  $k = k_{\text{lfb}}$ , the low frequency Alfvén wave becomes non propagating, and when  $k > k_{\text{lfb}}$ , the real part of the frequency is positive and the low frequency Alfvén wave propagates towards the positive part of x-axis, with the reversal of the behaviour occurring at  $k = k_{\text{lfb}}$ . Furthermore, the square root in Eqs. (171) and (172) becomes zero when  $k = k_c$ ,

$$k_c = \frac{2v_a \cos \theta}{\eta_C \cos^2 \theta + \eta \sin^2 \theta}. \quad (174)$$

with  $k_c > k_{\text{lfb}}$ . For  $k = k_c$ , both real parts of the high and low frequency branches become  $k_x v_0$ , however, for  $k > k_c$ , while the real part of both Alfvén waves is still given by  $k_x v_0$ , the imaginary parts of the frequency for both branches become,

$$\begin{aligned} \omega_{i,\text{hfb}} = & \frac{k^2(\eta_C \cos^2 \theta + \eta \sin^2 \theta)}{2} + \\ & + \frac{\sqrt{(\eta_C \cos^2 \theta + \eta \sin^2 \theta)^2 k^4 - 4v_a^2 k^2 \cos^2 \theta}}{2}. \end{aligned} \quad (175)$$

and

$$\begin{aligned} \omega_{i,\text{lfb}} = & \frac{k^2(\eta_C \cos^2 \theta + \eta \sin^2 \theta)}{2} - \\ & - \frac{\sqrt{(\eta_C \cos^2 \theta + \eta \sin^2 \theta)^2 k^4 - 4v_a^2 k^2 \cos^2 \theta}}{2}, \end{aligned} \quad (176)$$

Therefore, for  $k > k_c$ , we end up with two Alfvén waves propagating in the same direction, with the same real frequency ( $k_x v_0$ ) but with different imaginary parts of the frequency i. e. having different damping times.

Figure 21 displays the period ( $P = \frac{2\pi}{\omega_r}$ ), damping time ( $\tau_D = \frac{1}{\omega_i}$ ) and the ratio of damping time to period ( $\tau_D/P$ ) versus the wavenumber and confirms the above analytical results. It shows the unfolding in period due to the flow and the behaviour of the period, for both waves, around the critical wavenumbers. For wavenumbers larger than  $k_c$ , both waves display the same period. Also, in the case of the damping time it can be seen that once the critical wavenumber  $k_c$

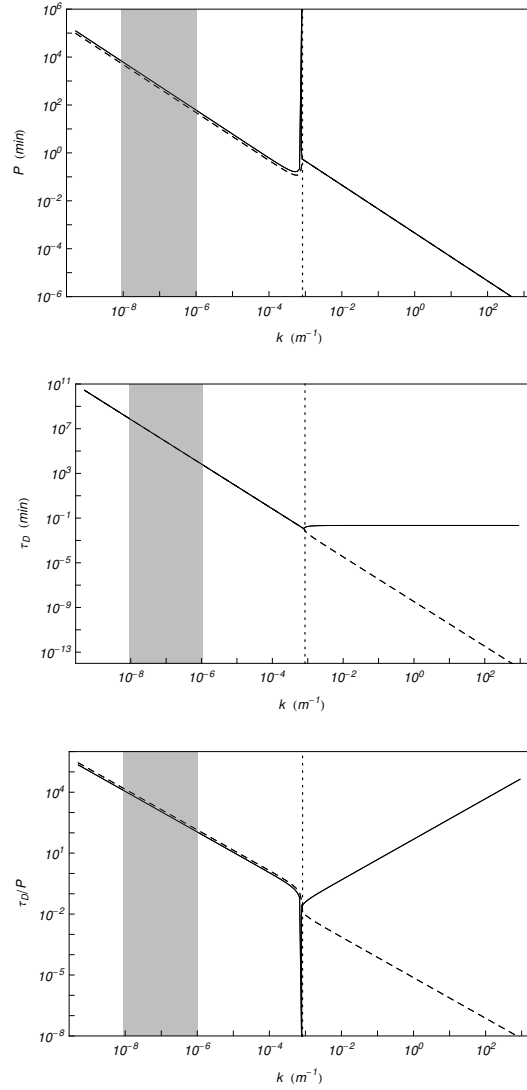


**Fig. 21** Period, damping time, and ratio of the damping time to period versus the wavenumber for the long (solid) and short (dashed) period Alfvén waves in a PIP with  $\tilde{\mu} = 0.8$ . The background flow speed is 15 km/s. In all the panels, the shaded region corresponds to the interval of observed wavelengths in prominence oscillations. Adapted from Barceló et al. (2011).

is attained we are left with two different damping times for wavenumbers larger than  $k_c$ . One damping time is almost constant while the other decreases in a continuous way. Of course, the ratio  $\tau_D/P$  has also two branches which behave quite differently for wavenumbers larger than  $k_c$ . Furthermore, we can also observe that the critical wavenumbers,  $k_{lfb}$  and  $k_c$ , are outside the region of observed wavelengths in prominence oscillations. Regarding the damping time of Alfvén waves, Figure 21 clearly shows that, within the range of observed wavelengths, it

is very large and quite incompatible with the up to now reported damping times from observations. The same happens with the ratio between the damping time and the period. This clearly points out that, at least within the range of observed wavelengths in prominence oscillations, the ion-neutral collisions mechanism can not provide with an explanation for the temporal damping of Alfvén waves in partially ionised prominence plasmas.

#### 5.1.14 Temporal damping of magnetoacoustic waves

In this case, the obtained dispersion relation (Eq. 168) couples fast, slow and thermal waves. This dispersion relation is a fifth degree polynomial in the frequency providing two fast, two slow and one thermal wave. For non-parallel propagation, the dispersion relation can be solved numerically and Figure 22 displays the period, damping time and the ratio of damping time to period versus the wavenumber for magnetoacoustic and thermal waves. The results suggest that the behaviour of fast waves is similar to that of Alfvén waves (see 5.1.13), although in a partially ionized plasma the presence of Cowling's resistivity results in the critical wavenumbers for fast waves being displaced towards small wavenumbers with respect to the case of a fully ionized and resistive plasma. On the other hand, the effect of the coupling is reflected in the behaviour of the damping times for fast and slow waves. At small wavenumbers, the damping time of fast waves is affected by thermal effects and additional distortions, with respect to the uncoupled case, appear for slow waves at large wavenumbers. On the contrary, the thermal wave is not affected by the coupling. Regarding the damping ratio,  $\tau_D/P$ , Figure 22 shows that, within the region of interest, it is very large for fast waves and very small for the thermal wave, while for slow waves, for wavenumbers between  $10^{-7}$  and  $10^{-6} \text{ m}^{-1}$ , it is close to damping ratios found in observations. However, this ratio correspond to very long period oscillations having a more or less similar damping time.

Another important parameter is the ionisation fraction  $\tilde{\mu}$ . Varying this parameter, going from an almost fully ionised to an almost neutral prominence, the main effects appear in fast and Alfvén waves since they are influenced by Cowling's resistivity which depends on the ionisation fraction. The modification of Cowling's resistivity modifies the location of critical wavenumbers appearing in fast and Alfvén waves. Furthermore, our results suggest that in flowing partially ionised prominence plasmas, and within the range of observed wavelengths in prominence oscillations, resistive effects, dominated by Cowling's resistivity, are not enough efficient to damp MHD waves responsible for these oscillations. However, the efficiency of ion-neutral collisions could be improved if the commonly assumed values for the characteristic prominence parameters (density, magnetic field, ionisation fraction) were different and as a result the numerical value of Cowling's resistivity was increased. This points out the need for an accurate and proper determination of these characteristic magnitudes.

Finally, for a particular flow speed we may have that at two additional wavenumbers the period of the high-period branch of slow waves becomes infinite, which is due to the coincidence between the numerical values of flow speed and the real part of the non-adiabatic sound speed. Since the non-adiabatic sound speed is determined by plasma physical conditions, these conditions become of paramount importance.

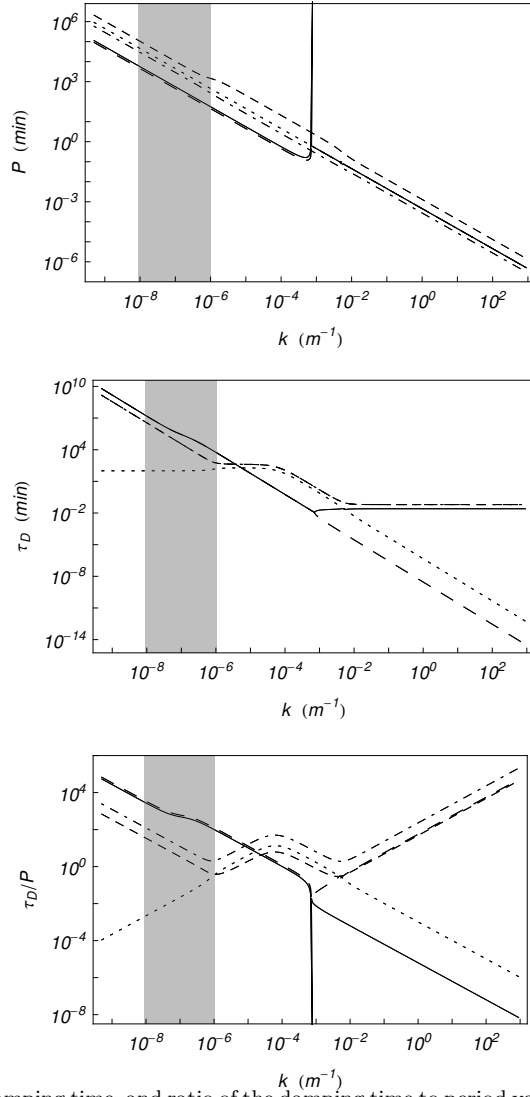


**Fig. 22** Period, damping time, and ratio of the damping time to period versus the wavenumber for magnetoacoustic waves in a PIP with  $\tilde{\mu} = 0.8$ . Slow waves (short-dashed and dot-dashed lines), fast waves (continuous and long-dashed lines), thermal wave (dotted line). The location of the critical wavenumbers is defined by the presence of peaks and bifurcations in the plots. The background flow speed is 15 km/s and the shaded region corresponds to the interval of observed wavelengths in prominence oscillations. Adapted from Barceló et al. (2011).

### 5.1.15 Effect of Helium

Along above studies, a hydrogen plasma has been considered, however, 90% of the prominence chemical composition is hydrogen while the remaining 10% is helium. Therefore, it is of great interest to know the effect of the presence of helium on the behaviour of magnetohydrodynamic waves in a partially ionized plasma with prominence physical properties. This study has been done by Soler

et al. (2010) in an unflowing prominence plasma like that considered in previous paragraphs, but composed of hydrogen and helium. The species present in the medium are electrons, protons, neutral hydrogen, neutral helium (HeI), and singly ionized helium (HeII), while the presence of He III is negligible (Gouttebroze and Labrosse 2009). Under such conditions the basic MHD equations for a non-adiabatic, partially ionized, unflowing single-fluid plasma have been generalized.

The hydrogen ionization degree is characterized by  $\tilde{\mu}_H$  which varies between 0.5, for fully ionized hydrogen, and 1 for fully neutral hydrogen. The helium ionization degree is characterized by  $\delta_{He} = \frac{\xi_{HeII}}{\xi_{HeI}}$ , where  $\xi_{HeII}$  and  $\xi_{HeI}$  denote the relative densities of single ionized and neutral helium, respectively. Figure 23 displays  $\tau_D/P$  as a function of the wavenumber  $k$  for the Alfvén, fast, and slow waves, and the results corresponding to several helium abundances are compared for hydrogen and helium ionization degrees of  $\tilde{\mu}_H = 0.8$  and  $\delta_{He} = 0.1$ , respectively. It is observed that the presence of helium has a minor effect on the results. In the case of Alfvén and fast waves (Fig. 23a,b), a critical wavenumber,  $k_c$  occurs (See Eq. (174)) and, since Cowling's diffusivity  $\eta_C$  is larger in the presence of helium because of additional collisions of neutral and singly ionized helium species,  $k_c$  is shifted toward slightly lower values than when only hydrogen is considered, so the larger  $\xi_{HeI}$ , the smaller  $k_c$ . In the case of the slow wave (Fig. 23c), the maximum and the right hand side minimum of  $\tau_D/P$  are also slightly shifted toward lower values of  $k$ . Previous results from Carbonell et al. (2004) and Forteza et al. (2008) suggest that thermal conduction is responsible for these maximum and minimum of  $\tau_D/P$ . The additional contribution of neutral helium atoms to thermal conduction produces this displacement of the curve of  $\tau_D/P$ . In the case of Alfvén and fast waves, this effect is not very important. Finally, the thermal mode has been considered. Since it is a purely damped, non-propagating disturbance, only the plot of the damping time,  $\tau_D$ , as a function of  $k$  for  $\tilde{\mu}_H = 0.8$  and  $\delta_{He} = 0.1$  is shown (Fig. 23d). We observe that the effect of helium is different in two ranges of  $k$ . For  $k > 10^{-4} \text{ m}^{-1}$ , thermal conduction is the dominant damping mechanism, so the larger the amount of helium, the smaller  $\tau_D$  because of the enhanced thermal conduction by neutral helium atoms. On the other hand, radiative losses are more relevant for  $k < 10^{-4} \text{ m}^{-1}$ . In this region, the thermal mode damping time grows as the helium abundance increases. Since these variations in the damping time are very small, we again conclude that the damping time obtained in the absence of helium does not significantly change when helium is taken into account. In summary, this study points out that the consideration of neutral or single ionized helium in partially ionized prominence plasmas does not modify the behaviour of MHD waves found by Forteza et al. (2007, 2008). However, Zaqarashvili et al. (2011a) used a multifluid approach to study the damping of Alfvén waves in an isothermal and homogeneous partially ionized plasma when helium is included. They considered a three-fluid MHD approximation, where one component was electron-proton-singly ionized helium, and the other two components were neutral hydrogen and helium atoms. The results indicate that the presence of neutral helium enhances in a significant way the damping of Alfvén waves for a certain range of plasma temperature (10 000 - 40 000 K). Then, in the case of prominences, the damping of Alfvén waves in the prominence-corona transition region could be significantly enhanced while it is not affected in the prominence core, which agrees with the results by Soler et al. (2010) using the single-fluid approximation.



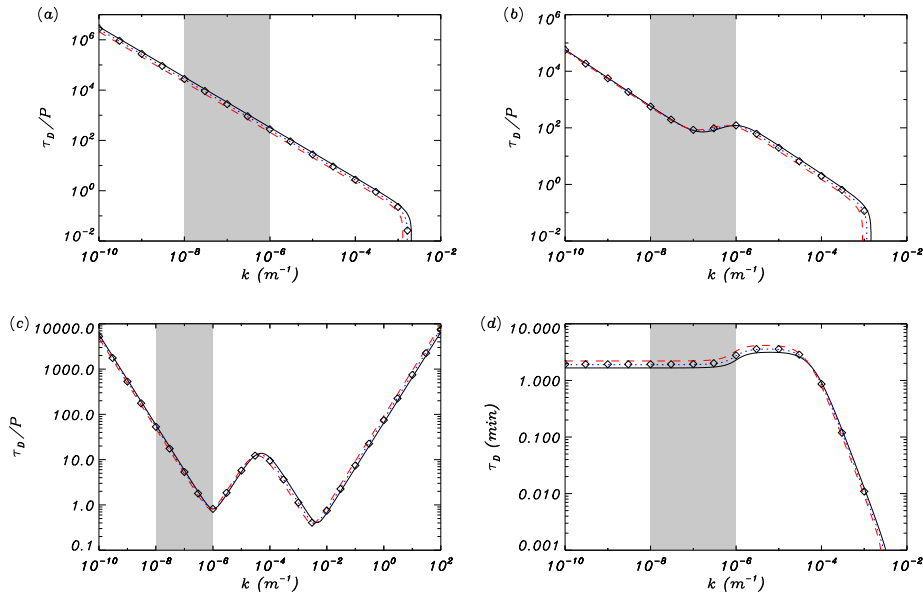


**Fig. 23** (a)–(c): Ratio of the damping time to the period,  $\tau_D/P$ , versus the wavenumber,  $k$ , corresponding to the Alfvén wave, fast wave, and slow wave, respectively. (d) Damping time,  $\tau_D$ , of the thermal wave versus the wavenumber,  $k$ . The different linestyles represent:  $\xi_{\text{HeI}} = 0\%$  (solid line),  $\xi_{\text{HeI}} = 10\%$  (dotted line), and  $\xi_{\text{HeI}} = 20\%$  (dashed line). In all computations,  $\bar{\mu}_H = 0.8$  and  $\delta_{\text{He}} = 0.1$ . The results for  $\xi_{\text{HeI}} = 10\%$  and  $\delta_{\text{He}} = 0.5$  are plotted by means of symbols for comparison. The shaded regions correspond to the range of typically observed wavelengths of prominence oscillations. In all the figures shown, the angle,  $\theta$ , between the wavevector and the x-axis is  $\pi/4$ . Adapted from Soler et al. (2010).

### 5.1.16 Spatial damping of Magnetohydrodynamic waves

Terradas et al. (2002) analyzed small amplitude oscillations in a polar crown prominence and reported the presence of a plane propagating wave as well as an standing wave. In the case of the propagating wave, which was interpreted as a slow MHD wave, the amplitude of the oscillations spatially decreased in a substantial way after a distance of  $2 - 5 \times 10^4$  km from the location where wave motion was being generated. This distance could be considered as a typical spatial damping length,  $L_d$ , of the oscillations.

Using the dispersion relations for Alfvén and magnetoacoustic-thermal waves given by Eqs. (167) and (168), respectively, Carbonell et al. (2010) studied the spatial damping of MHD waves in a flowing partially ionized prominence plasma. The wavelength of the waves is given by  $\lambda = \frac{2\pi}{k_r}$ , the damping length by  $L_d = \frac{1}{k_i}$  and the damping length per wavelength is  $L_d/\lambda$ , with  $k = k_r + ik_i$ .

In the case of Alfvén waves, three propagating Alfvén waves are obtained, and Figure 24 shows the numerical solution of dispersion relation (167). For all the interval of periods considered, a strongly damped additional Alfvén wave appears, while on the contrary, the other two Alfvén waves are very efficiently damped for periods below 1 s. However, within the interval of periods typically observed in

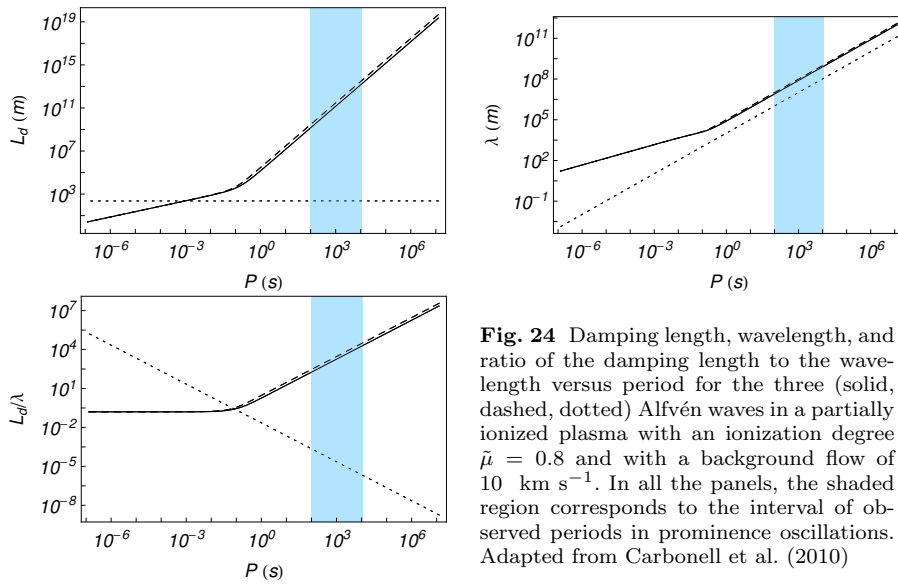


**Fig. 24** Damping length, wavelength, and ratio of the damping length to the wavelength versus period for the three (solid, dashed, dotted) Alfvén waves in a partially ionized plasma with an ionization degree  $\bar{\mu} = 0.8$  and with a background flow of  $10 \text{ km s}^{-1}$ . In all the panels, the shaded region corresponds to the interval of observed periods in prominence oscillations. Adapted from Carbonell et al. (2010)

prominence oscillations these waves are only efficiently attenuated when almost neutral plasmas are considered.

When Equation (168) is expanded, it becomes a seventh degree polynomial in the wavenumber  $k$ , whose solutions are three propagating fast waves, two slow waves and two thermal waves. Figure 25 displays the behaviour of the damping length, wavelength and ratio of damping length versus wavelength for fast and slow waves. The damping length of a fast wave in a partially ionized plasma is strongly diminished by neutral's thermal conduction for periods between 0.01 and 100 s, and, at the same time, the radiative plateau present in fully ionized ideal plasmas (Carbonell et al. 2006) almost disappears. The behaviour of slow waves is not so strongly modified as for fast waves, although thermal conduction by neutrals also diminishes the damping length for periods below 10 s, and a short radiative plateau still remains for periods between 10 and 1000 s (Carbonell et al. 2006). Finally, thermal waves are only slightly modified although the effect of partial ionization is to increase the damping length of these waves, just the opposite to what happens with the other waves. Also, in the presence of flow, wavelengths and damping lengths are modified, and since for slow waves sound speed and observed flow speeds are comparable this means that the change in wavelength and damping length are important, leading to an improvement in the efficiency of the damping. Moreover, the maximum of efficiency is displaced towards long periods when the ionization decreases, and for ionization fractions from 0.8 to 0.95 it is clearly located within the range of periods typically observed in prominence oscillations with a value of  $L_d/\lambda$  smaller than 1. This means that for a typical period of  $10^3 \text{ s}$ , the damping length would be between  $10^2$  and  $10^3 \text{ km}$ , the wavelength around  $10^3 \text{ km}$  and, as a consequence, in a distance smaller than a wavelength the slow wave would be strongly attenuated. In conclusion, the joint effect of non-adiabaticity, flows and partial ionization allows spatially damping of slow waves in an efficient way within the interval of periods typically observed in prominences.

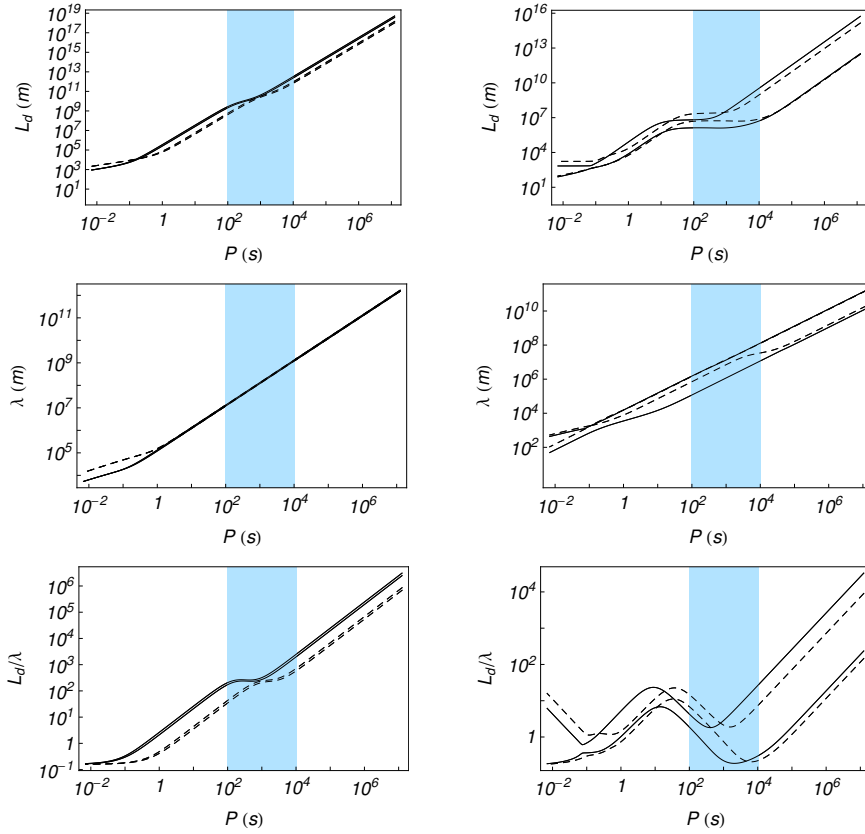


**Fig. 25** Damping length, wavelength, and ratio of the damping length to the wavelength versus period for the non-adiabatic fast (left panels), slow (right panels) waves in a partially ionized plasma with an ionization degree  $\tilde{\mu} = 0.8$  (solid) and  $\tilde{\mu} = 0.95$  (dashed). The flow speed is  $10 \text{ km s}^{-1}$ . Adapted from Carbonell et al. (2010)

### 5.1.17 Wave heating and energy balance in partially ionised prominences

The energy balance in solar prominences, and the understanding of the processes involved with heating and cooling of the plasma, are difficult problems that are intimately linked to the prominence formation and structure (see Gilbert 2015). Incident radiation is generally accepted as the dominant prominence heating mechanism. However, when the balance between incident radiation and cooling is taken into account, the obtained radiative-equilibrium temperatures are lower than what is typically inferred from observations. An additional, non-negligible source of heating seems to be necessary to raise the prominence temperature up to the expected values (Labrosse et al. 2010; Heinzel et al. 2010; Heinzel and Anzer 2012). Dissipation of magnetohydrodynamic (MHD) wave energy in the partially ionised prominence plasma is proposed as another possible source of prominence heating. Recently, Soler et al. (2016) explored the role of Alfvén waves in prominence heating. They used a slab model with a transverse magnetic field to represent a solar prominence embedded in the corona and modeled the prominence medium as a

three-fluid plasma composed of a charged ion-electron single fluid and two neutral fluids comprised of neutral hydrogen and neutral helium. These three fluids exchange momentum because of particle collisions, which cause the damping of the waves and dissipation of wave energy. Soler et al. (2016) consistently computed the plasma heating rate and compared it with the prominence radiative losses. They concluded that wave heating is efficient for waves with periods shorter than 100 s and may be efficient enough to compensate for a fraction of the radiated energy. Soler et al. (2016) estimated the volumetric heating integrated over the range of periods between 0.1 s and 100 s to be as large as 10% of the bulk radiative energy of the cool prominence plasma and it can possibly account for the additional heating necessary to explain the observed prominence core temperatures (Heinzl et al. 2010). Thus, partial ionisation effects are also shown to be an important actor concerning the energy balance in prominences.

#### *5.1.18 Kelvin-Helmholtz, Rayleigh-Taylor and dissipative instabilities*

Observations of quiescent prominences have revealed the presence of flows that show a turbulent behavior (see Berger et al. 2010; Ryutova et al. 2010). The Kelvin-Helmholtz instability (KHI) has been proposed as a feasible mechanism that can contribute to the development of turbulence in prominences (Ryutova et al. 2010). In solar coronal plasmas, this instability has also been observed in coronal mass ejections (Foullon et al. 2011; Ofman and Thompson 2011; Möstl et al. 2013) and coronal streamers (Feng et al. 2013).

The KHI is well studied in hydrodynamics and it arises at the interface of two fluid layers that move with different speeds. Flows are generally uniform in both layers, but strong velocity shear arises near the interface, which consequently becomes unstable to spiral-like perturbations. Inclusion of magnetic field obviously modifies the thresholds and growth rates of KHI. It has been shown that the flow-aligned magnetic field suppresses the KHI for sub-Alfvénic flows of fully ionized plasmas due to magnetic tension force (see, e.g., Chandrasekhar 1961). The flow velocities that are measured in quiescent prominences are typically lower than  $30 \text{ km s}^{-1}$  (e.g., Zirker et al. 1998; Berger et al. 2010), while the expected Alfvén velocity in prominence threads is of the order of  $100 \text{ km s}^{-1}$ . Therefore, the onset of the KHI in quiescent prominences seems unlikely according to the classical criterion as the mass flows are presumably field-aligned in prominence threads.

However, the prominence plasma is not fully ionized but partially ionized. The existence of a neutral component in the plasma may invalidate the classical criterion for the onset of the KHI and may allow its development for sub-Alfvénic field-aligned flows. The linear stage of the KHI in partially ionized plasmas was studied by Watson et al. (2004); Soler et al. (2012); Martínez-Gómez et al. (2015). These studies showed that partially ionized plasmas can develop the KHI even when the velocity of the shear flow is sub-Alfvénic. The physical reason for this result is that neutrals largely ignore the stabilizing effect of the magnetic field and only feel its influence indirectly through collisions with ions. Although the ion-neutral coupling exerts a significant influence, so that increasing the ion-neutral collision frequency reduces the growth rate of the instability, it is not possible to completely suppress the onset of the KHI originated in the neutral component (see Fig. 26). Because of the imperfect coupling between ions and neutrals that naturally occur in real prominence plasmas, the onset and development of the KHI

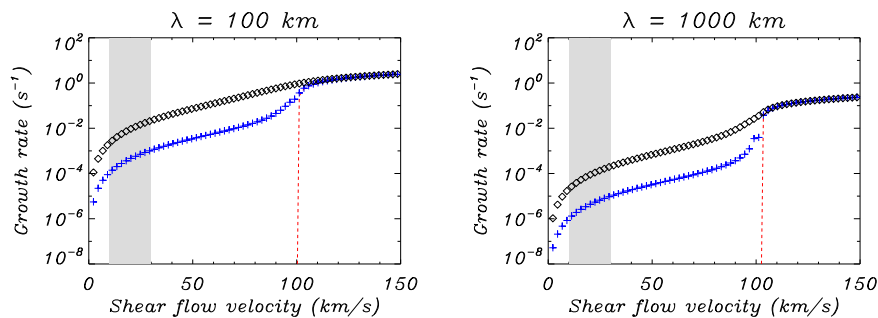


**Fig. 26** Growth rate of the KHI linear stage as a function of the shear flow velocity in a prominence thread model for two different values of the perturbation wavelength: 100 km (left) and 1000 km (right). The red dashed lines, blue crosses, and black diamonds correspond to fully ionized plasma, partially ionized plasma, and weakly ionized plasma, respectively. The shaded area denotes the region of typically observed flow velocities in quiescent prominences. Adapted from Martínez-Gómez et al. (2015).

appears to be unavoidable in such structures even for slow flow velocities. These theoretical results support the explanation of the origin of the observed turbulent flows in prominences in terms of the sub-Alfvénic KHI in partially ionized plasmas. The KHI can be also developed for sub-Alfvénic motion of fully ionized plasma if the magnetic field has small component perpendicular to the flow direction (see, e.g., Chandrasekhar 1961). This situation may arise if the prominence threads are modeled as twisted flux tubes moving along their axis. In this case, the threshold of KHI is reduced significantly, which allows to sub-Alfvénic flows to be unstable (Zaqarashvili et al. 2010, 2014). Obviously, consideration of neutral particles may enhance the growth rate of KHI in twisted tubes. However, it is not known which mechanism is dominant for occurrence of KHI in sub-Alfvénic flows. This point clearly needs further discussion.

Another instability of interest, which has been mostly studied in the context of fully ionized plasmas, is the Rayleigh-Taylor instability (RTI). Díaz et al. (2012) considered an equilibrium configuration made of two compressible and magnetized plasmas composed of ions, electrons and neutrals separated by a contact surface, and in the presence of gravity. Then, using the two-fluid description, Díaz et al. (2012) studied how the classical criterion for the onset and growing rate of the RTI is modified in a partially ionized plasma. It was found that compressibility and ion-neutral collisions reduce the linear growth rate, but do not affect the critical threshold of the onset of the RTI. In particular, due to ion-neutral collisions, the growth rate can be decreased by an order of magnitude as compared with the corresponding value for the collisionless case. Prominences are cool and dense structures embedded in the solar corona, supported against gravity by its magnetic field, which are likely to develop RTI. On the other hand, prominences are made of partially ionized plasma, therefore, Díaz et al. (2012) applied the above study to a plasma with physical properties akin to those of prominences. Using typical parameters for prominence threads as well as coronal values, the resultant time for the RTI instability was of the order of 30 min, which is of the same order as the observed lifetime of the prominence threads. This results greatly differs from

the classical result, of the order of 1 min, unable to explain the reported lifetime of threads.

Simulations of the non-linear phase of the RTI at the PCTR considering partial ionization of the prominence plasma in the single-fluid formulation were reported by Khomenko et al. (2014a). These simulations included the ambipolar term in the generalized Ohm's law, as the dominant effect. The ambipolar term is larger in the regions with low density, i.e. regions with, generally, low momentum  $\rho\mathbf{u}$ . Therefore, the impact of such regions into the overall flow dynamics was found to be not large. A similar conclusions were reached in the simulations of multi-fluid turbulence in molecular clouds (Downes and O'Sullivan 2011; Downes 2012). However, statistically, simulations with/without ambipolar term develop flows that are statistically different at small scales. In agreement with the linear theory, non-linear simulations demonstrate that the introduction of the ambipolar diffusion removes the cut-off wavelength for the growth rate of the instability and allows the small scales to develop. As the non-linear development of the instability is such that small scales merge and give rise to larger scales (Jun et al. 1995; Stone and Gardiner 2007; Hillier et al. 2012), the larger growth rate of small scales leads to larger extreme velocities in the ambipolar case Khomenko et al. (2014a). In addition, some 30% larger temperatures at the PCTR were found in the simulations with ambipolar term, as a result of the Joule dissipation. A significant drift momentum, defined as  $\mathbf{p}_D = \sqrt{(\rho_i\rho_n)}(\mathbf{u}_i - \mathbf{u}_n)$  is present at the PCTR Khomenko et al. (2014a).

Finally, another example of instability is the dissipative instability which arises at the interface between two media and is related with the phenomenon of negative energy waves. This instability appears for flows whose speeds are below the KH threshold value. Usually, the interface between two media allows the propagation of two modes travelling in opposite directions, however, for flow speeds larger than a critical value, the propagation direction of the two waves is the same. Then, the wave having the smaller phase speed is a negative energy wave which means that dissipation produces an amplification of the wave amplitude, which leads to an instability, while at the same time wave energy decreases. In this case, the dissipative mechanisms working in the two regions amplify this negative energy mode leading to dissipative instability. Ballai et al. (2015) have studied the dissipative instability at the interface between two magnetized media, representing the corona and the partially ionised prominence plasma, in the incompressible limit. The dissipative mechanisms at work in the coronal and prominence media are viscosity and Cowling's resistivity, respectively. Using the limit of weak damping, a dispersion relation for Alfvénic waves propagating along the interface was derived. The imaginary part of it describes the evolution of the instability, and the results show that while the forward propagating wave is always stable, for the backward propagating wave there is a threshold of the flow, below the KH threshold, for which the wave becomes unstable. This analysis also shows that partial ionisation has a stabilising effect on the interface, for any degree of ionisation, and that the unstable behaviour is due to the viscosity of the coronal plasma.

### *5.1.19 Resonant Absorption in partially ionized plasmas*

The process of resonant absorption, caused by plasma inhomogeneity across the magnetic field, has important implications in the behavior and energy transport

of transverse MHD waves in magnetic flux tubes of the solar atmosphere (see the review by Goossens et al. 2011). Heating of coronal loops involving the process of resonant absorption was first suggested by Ionson (1978) and has been extensively investigated in the literature afterward. Resonant absorption produces a radial flux of transverse wave energy toward the nonuniform boundary of the flux tube, where the energy is absorbed into the continuous Alfvén spectrum (see, e.g., Tataronis 1975; Poedts et al. 1989; Goossens et al. 2013). Phase mixing of the continuum Alfvén modes causes the energy to cascade from large spatial scales to small spatial scales (see, e.g., Heyvaerts and Priest 1983; Cally 1991; Soler and Terradas 2015). Dissipation of MHD wave energy by, e.g., magnetic resistivity and/or viscosity becomes efficient when the generated spatial scales are sufficiently small. Resonant absorption of wave energy and phase mixing occur simultaneously and are intimately linked as both processes are caused by inhomogeneities across the magnetic field. Such inhomogeneities naturally occur in magnetic flux tubes of the solar atmosphere, including solar prominence threads. Recent observations by Okamoto et al. (2015) and Antolin et al. (2015) claim to provide direct evidence of the process of resonant absorption of transverse waves taking place in solar prominence threads.

The theory of resonant waves in the solar atmosphere has mainly been studied assuming fully ionized plasma (see Goossens et al. 2011). Early attempts to study resonant waves in partially ionized plasmas were performed by Soler et al. (2009b, 2011). These authors used the single-fluid approximation to investigate resonant Alfvénic waves in a model of a partially ionized thread of a solar prominence. Soler et al. (2009b, 2011) found that the process of resonant absorption of wave energy is not altered by partial ionization in the single-fluid approximation. The results in partially ionized flux tubes concerning the damping of transverse waves and the energy flux toward the resonance location are the same as in fully ionized flux tubes when total density is equal in both cases. The single-fluid approximation breaks down when small length scales approaching the ion-neutral collision length are involved. Resonant wave perturbations can develop very small length scales in the vicinity of the resonance position owing to phase mixing (see, e.g., Tirry and Goossens 1996; Ruderman and Wright 1999; Vasquez 2005; Terradas et al. 2006). This led Soler et al. (2012) to analytically study resonant waves in partially ionized plasmas using the multi-fluid treatment. They found that ion-neutral collisions generate a dissipative layer around the location of the resonance in a similar way as magnetic resistivity and viscosity do in fully ionized plasmas (see, e.g., Hollweg and Yang 1988; Poedts et al. 1990; Sakurai et al. 1991). The conserved quantity at the resonance and the jump of the perturbations across the dissipative layer in the multi-fluid treatment are the same as in fully ionized plasmas (see Goossens and Ruderman 1995). In the case of Alfvénic waves in partially ionized flux tubes, Soler et al. (2012) found the resonant absorption rate is inversely proportional to the wave frequency, while the ion-neutral collisions damping rate is inversely proportional to the square of the frequency. For the observed wave frequencies in the solar atmosphere, the resonant absorption rate should be faster than the ion-neutral collisions damping rate. Hence, the resonant absorption process should not be altered in agreement with the single-fluid results. However, for wave frequencies of the order of the ion-neutral collision frequency the damping rate due to ion-neutral collisions could be faster, thus effectively suppressing the resonant energy transfer toward to nonuniform boundary of the tube. Numerical

simulations beyond analytic studies should be used in the future to determine the actual impact of partial ionization on the time dependent process of resonant absorption and on the deposition of resonant wave energy into the plasma.

#### *5.1.20 Coronal rain*

Coronal rain are dense condensations with chromospheric to transition region temperatures falling down in the much hotter corona. In most theoretical studies, these condensations have been considered to be made of fully ionized plasma (Oliver et al. 2014), however, these cold blobs are made of ionized and neutral material which must be strongly coupled, since they fall together, and they can be used as a tool to explore the interaction between neutral and ionized plasma. To describe the temporal evolution of a partially ionized hydrogen blob which falls under the action of gravity, pressure and friction forces, Oliver et al. (2016) considered a two-fluid description for charged and neutral fractions. After assuming a static atmosphere, at  $t=0$  a dense blob, composed of neutral and charged material, was injected and, using a one dimensional numerical simulation, its temporal evolution, along a vertical path, was investigated. The temporal evolution is described by a system of partial differential equations together with a set of imposed boundary conditions (Oliver et al. 2016), and the blob was left to evolve under the joint action of gravity, pressure and friction forces between ions and neutrals. The results indicate that the falling material displays two different phases: In the first, the blob accelerates while, in the following phase, it maintains a practically constant speed, the duration of the first phase being longer for denser blobs. Furthermore, the results also indicate that blob's dynamics is determined by its mass while the ionization degree is irrelevant, and that a correlation exists between the blob maximum speed and its initial density ratio with respect to the corona. On the other hand, the interplay of forces acting on the neutral and charged fractions of the blob is such that both fractions are subject to the same acceleration regardless of their respective densities. Finally, it must be taken into account that coronal rain condensations fall following a curved path, then, it becomes important to determine if the coupling, between the charged and neutral fraction, is strong enough to impose neutrals to follow the magnetic field lines or not. Therefore, for a full understanding of the temporal behaviour of partially ionized coronal rain blobs, multidimensional numerical simulations are needed.

#### *5.1.21 Multi-fluid modelling of high-frequency waves in the partially ionised solar plasma*

The single-fluid MHD approximation with a generalised Ohm's Law provides an accurate description of low-frequency waves in the solar plasma even when the plasma is only partially ionised. However, when the frequency of the waves is of the same order of or higher than the frequencies of the individual collisions between different species, the single-fluid model is not applicable and more complicated approaches are needed. Recently, Martínez-Gómez et al. (2016, 2017) theoretically studied high-frequency waves in a plasma composed of hydrogen and helium and went beyond the usual single-fluid description by considering a multi-fluid approach in which the various components of the plasma are treated as separate



---

fluids. In their model, electron inertia was neglected, which allowed them to obtain an expression for the electric field that includes the effects of Hall's current and magnetic resistivity. In addition, they took into account the friction due to collisions between different species.

First of all, Martínez-Gómez et al. (2016) considered the case of full ionisation, so that the background hydrogen-helium plasma was composed of three distinct ionic species, namely protons, HeII, and HeIII. Through the analysis of the wave dispersion relations and temporal numerical simulations, it was found that at high frequencies ions of different species are not as strongly coupled as in the low-frequency limit. Hence, different ions cannot be treated as a single fluid. In addition, elastic collisions between the distinct ionised species are not negligible for high-frequency waves and an appreciable damping and energy dissipation is obtained. Furthermore, Coulomb collisions between ions are able to remove the cyclotron resonances and the strict cutoff regions, which are present when those collisions are not taken into account.

Subsequently, Martínez-Gómez et al. (2017) extended their previous model by allowing the presence of neutrals. Hence, Martínez-Gómez et al. (2017) used a five-fluid model with three ionised (protons, HeII, and HeIII) and two neutral (H and HeI) components. They discussed the effect of momentum transfer collisions on the ion-cyclotron resonances and compared the importance of magnetic resistivity, ion-neutral and ion-ion collisions on the wave damping at various frequency ranges. Three specific environments were explored: the higher chromosphere (largely ionised), a solar prominence (partially ionised), and the lower chromosphere (weakly ionised). The investigation and comparison of environments with such different degrees of ionisation led to a comprehensive understanding of the influence of neutral species on the propagation of high-frequency waves in the small-amplitude regime. This improved our knowledge of the physics involved in the damping and energy dissipation and paved the way for future studies that should focus on the full nonlinear evolution of the waves and the associated plasma heating.

## 6 Planetary Ionospheres

Planetary ionospheres are created when an extended neutral atmosphere is subjected to sources of ionization. Accordingly, the planet's upper atmosphere consists of a neutral gas co-existing with an embedded ionized component which typically represents only a small fraction of the total gas density. In this manner, planetary upper atmospheres/ionospheres are quintessential examples of partially ionized plasmas.

Planetary ionospheres vary considerably among the planets in our solar system. Furthermore, they can be expected to differ considerably among the ionospheres of as yet undiscovered extra-solar planetary systems. The main characteristics of planetary ionospheres depend on a given planet's atmospheric constituents, characteristics of the ionizing radiation, intrinsic magnetic fields (if any), gravitation field, proximity to the stellar ionization source and stellar wind, the planet's rotation rate and the orientation of its rotation axis, etc. In this section, rather than review all planetary ionospheres, we consider only the ionospheres of the terrestrial planet, Earth, and those of the extended gaseous atmospheres of the outer planets, Jupiter and Saturn.

Among the many reviews of planetary ionospheres, we direct the reader in particular to Bauer (1973), Cravens (1997), Schunk and Nagy (2004), Mendillo et al. (2002), and Nagy et al. (2008). Leake et al. (2014b) compares the partially ionized gases of the Sun's chromosphere with the Earth's upper atmosphere/ionosphere.

### 6.1 Earth's Ionosphere: Introduction

The Earth's outer atmosphere is partially ionized due to three main ionizing sources: (1) photo-ionization due to impinging EUV and soft X-ray energy from the Sun, (2) impact ionization at high latitudes of energetic, precipitating particles such as those associated with the visible aurora, and (3) impact ionization due to meteor ablation which creates a small but important population of metallic ions. Charge exchange between neutrals and ions is another process that influences the distribution of ion species in the Earth's ionosphere.

As the ionosphere and upper atmosphere together form a partially ionized plasma, their characteristics are influenced by ion-neutral coupling, displaying an important dynamic interplay between upper atmospheric motions, or winds, and plasma drifts. Because the earth's strong, dipole geomagnetic field influences the charged particle dynamics, the ionospheric plasma supports an intrinsic system of electrical currents which depend on the local conductivities and collision frequencies, varying with altitude and latitude. Furthermore, as the magnetic field threads the partially ionized plasma to form the magnetosphere at much higher altitudes, it "connects" or couples the ionosphere/upper atmosphere to the magnetospheric plasma and solar wind and their sources of energy and momentum, including large electric fields, field-aligned currents, and highly variable particle precipitation.

The term "ionosphere" refers to the ionized component of the Earth's upper atmosphere (approximately 90 to 1000 km) and the term "thermosphere" refers to upper atmosphere neutral gases in the altitude region of approximately 90-600 km in which the neutral temperature is significantly increased. The "mesosphere" is that part of the upper atmosphere between the stratosphere and lower ionosphere,

essentially between 40-90 km. Collectively, these regions are often referred to as the ionosphere-thermosphere-mesosphere or “ITM” system.

An outline of this section is as follows: After a description of the basic properties of the earth’s ionosphere, we discuss how electrons and ions are magnetized at different altitudes because their collision frequencies with the neutral gas are substantially different. We then describe how the resulting Pedersen and Hall conductivities enable a global system of electrical currents to flow in the lower ionosphere followed by a discussion of the dynamics of the coupled neutral and ionized gases, magnetospheric coupling, and the creation of enhanced conductivity regions associated with the aurora. The discussion here follows the review article of Pfaff (2012). Other references that provide general descriptions of the earth’s ionosphere and upper atmosphere include the following monographs: Hargreaves (1992), Kelley (2009), Prölss (2004), Rishbeth and Garriott (1969), and Schunk and Nagy (2004), among others.

### *6.1.1 Basic properties of the Ionosphere*

The ionospheric environment is complex due to the many processes (chemical, dynamical, and electrodynamical) acting within the region and due to its interaction with external processes such as those related to coupling with the magnetosphere above and tropospheric forcing below. Distinct regions form within the ionosphere primarily as a function of altitude because the composition of the atmosphere varies with height as do the depths of the penetrating EUV and soft X-ray radiation. The ionosphere also varies considerably with latitude, since the high latitude gases are connected to the magnetosphere via highly inclined magnetic field lines of force whereas the mid and low latitude ionosphere exists on closed magnetic field lines. Accordingly, these regions are dominated by physical processes which also vary with altitude and latitude, including ion-neutral coupling, the creation of ionospheric currents, and the motions of plasma due to drifts associated with external and internal electric fields as well as due to forcing by neutral winds. Furthermore, we note that the physical processes operating on and within the ionosphere often have very different spatial and temporal scales.

The three main layers of the Earth’s ionosphere are characterized by its different plasma density regions, namely the D region (60-90 km altitude), E region (90-150 km altitude), and F region (above 150 km altitude), as shown in Figure 27. This figure illustrates how the ionospheric density varies between day and night and also how it varies between sunspot minimum and maximum, since the solar cycle governs the strength of the EUV ionizing source. During both the daytime and nighttime, the electron density is generally largest at the higher altitudes, 250-450 km or the F region, which is divided into two different regions (F1 and F2 layers) during the day. The E region densities are also largest during the daytime, yet diminish considerably during the night as the ion recombination rates in this region are rapid. The lowest altitude region, the D region, has a complex chemistry of positive and negative ions including water cluster ions. It has a much reduced plasma density which is even smaller at night.

To illustrate how the earth’s atmospheric constituents vary with altitude and provide a basis for the creation of ionosphere constituents via EUV and soft X-ray radiation, Figure 28 provides NRLMSISE-2000 model (Picone et al. 2002) distributions of the neutral atomic and molecular species as a function of altitude for

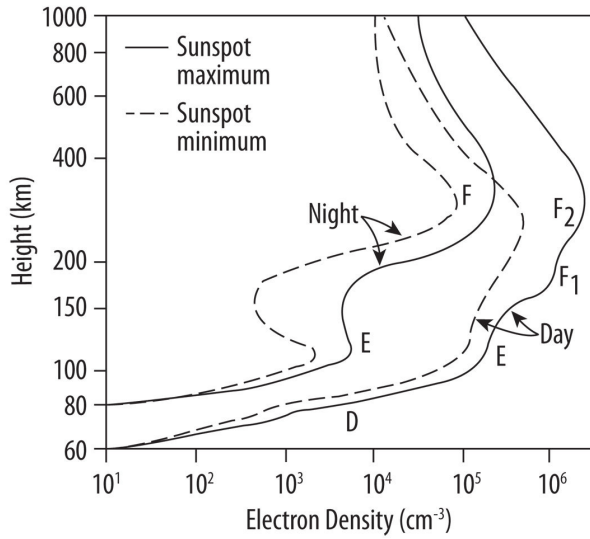


**Fig. 27** Representative plasma density profiles for day and night at solar minimum and maximum conditions at a mid-latitude location [Hargreaves, 1992].

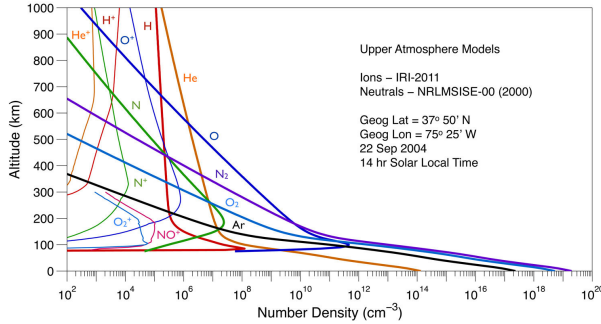
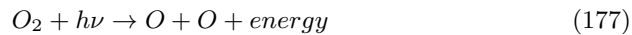


**Fig. 28** Model distributions of neutral and ion constituents as a function of altitude for a mid-latitude location (Wallops Island, Va., USA) at 14 hr Solar Local Time (Pfaff 2012). Ion distributions below 80 km are not provided by the model.

a mid-latitude location at 14hr LT (Pfaff 2012). The plot shows how the familiar nitrogen, oxygen, and argon atmospheric constituents at the earth's surface decrease exponentially with altitude until about 100 km, at which time the neutral atmosphere changes markedly in character. Above this altitude, the atmosphere changes from well mixed to free molecular flow, the temperature increases, the exponential decay of the total number density becomes less steep, and a variety of other atmospheric gas constituents emerge, as shown in the figure.

The upper atmosphere is subject to EUV radiation which serves two very important functions: First, it dissociates the diatomic oxygen molecules and releases heat, thereby expanding the upper atmosphere. Second, it ionizes a very small fraction of the upper atmosphere via photo-ionization. The main processes are diatomic oxygen dissociating to two oxygen atoms plus energy or:



and the photo-ionization of the oxygen atoms:



$N_2$  then charge exchanges with  $O^+$  to form  $NO^+ + N$  while  $O_2$  charge exchanges with  $O^+$  to form  $O_2^+ + O$ , both within the lower portions of the ionosphere. These molecular ions are the main ionospheric ions below about 180 km and are extremely important as they recombine very quickly, which means that the lower ionosphere essentially vanishes at night whereas the upper ionosphere (F region) generally remains throughout the evening. The bottomside ledge of the ionosphere is, hence, much higher in altitude at night. This characteristic of the earth's nighttime ionosphere has a variety of important consequences ranging from effects on radio wave propagation to instabilities which form on the bottomside ledge of the low latitude ionosphere just after sunset.

To complete the picture of the ionized component of the Earth's upper atmosphere, we comment briefly on metallic ions which result from the influx of meteoroids which laden the earth with 108 kg/yr of dust, grains, and atoms released via ablation (Cepolecha 1992). The main source of metallic ions in the ionosphere is impact ionization caused by meteors striking the atmosphere with sufficient kinetic energy to remove electrons from the neutral particles. Typical metallic ions in the upper atmosphere include  $Fe^+$ ,  $Mg^+$ , and  $Na^+$ . Metallic ions may also be created as meteoritic atoms undergo charge exchange and also via photo-ionization. Metallic ions recombine very slowly and, in general, form layers near the lower edge of the ionosphere (near 100 km) due to wind shear processes. They may also be transported over long distances due to upper atmospheric winds and electric fields.

The temperature of the various constituents of the upper atmosphere changes significantly with altitude and local time, as shown in Figure 29 (Pfaff 2012). This figure shows typical plasma ( $T_e$  and  $T_i$ ) and neutral temperatures ( $T_n$ ) based on the IRI model for 6LT, 12LT, 18LT, and 24LT at the equator. The greatest variation in temperature is with the electrons, whose average temperature is roughly 200 K at 100 km yet increases to 4000 K at 1500 km at 6LT. When neutral constituents such as oxygen are photo-ionized, the newly freed electrons that are emitted typically have energies of several eV, much higher than that of the newly created ions. This is due to the significantly lower mass of the electron compared to the ion and the conservation of momentum. The higher electron energy eventually dissipates via collisions with the neutral gas as well as with ions via electron-ion collisions.

As shown in the leftmost panel in Figure 29 corresponding to 6AM local time, the electron temperature,  $T_e$ , is highest in the early morning, as the neutral atmosphere has yet to warm and is still contracted from the nightside. Hence, the newly formed electrons have less neutral atmosphere with which to collide, particularly at the higher altitudes. During the day, the neutral atmosphere expands and the electron temperature is decreased, equilibrating with the ion temperature,  $T_i$ , at the higher altitudes. While photo-ionization continues during the day within the lower portion of the ionosphere, the electron temperature maintains a daytime enhancement near 250 km simply due to the fact that the neutral atmosphere density falls off with increasing altitude. At night, there are no newly formed electrons and ions and hence the temperatures of the neutrals, ions, and electrons converge to

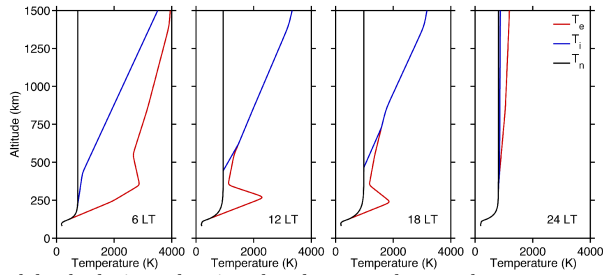


**Fig. 29** IRI model calculations showing the plasma and neutral temperatures at the magnetic equator at four different local times (Pfaff 2012).

similar values via collisions. At the higher latitudes, as discussed further on below, the plasma and neutral temperatures can increase locally due to Joule heating, precipitating particles, and plasma instabilities.

### 6.1.2 Ion-Neutral Coupling and Magnetization of Charged Particles

As the ions and neutrals are immersed in a common volume in the ionosphere, the two gases are coupled via collisions, with the coupling efficiency dependent on the gas densities and temperatures. A critical parameter within any partially ionized plasma in the presence of a magnetic field is under what conditions are the charged particles “magnetized” – in other words, at what altitudes are they able to execute their gyrations about the ambient magnetic field without their motions being substantially altered by collisions with neutral particles.

Charged particles in the ionosphere are compelled by the Lorentz force to gyrate about magnetic field lines at their cyclotron frequencies,  $\Omega_j$ , given by

$$\Omega_j = \frac{e|B|}{m_j} \quad (179)$$

where  $e$  is the electric charge,  $|B|$  is the magnetic field strength, and  $m_j$  is the mass of the species which is designated by  $j$ . For  $O^+$  ions and a magnetic field strength of 0.5 Gauss, the gyrofrequency is 48 Hz, whereas this frequency is 1.4 MHz for electrons for the same magnetic field.

As shown in Figure 30, the gyrofrequencies for the ions and electron species are plotted versus altitude for a mid-latitude location (Wallops Island, USA) where the ambient magnetic field on the ground is approximately 0.5 Gauss. Here, we use the mean mass of the ions which accounts for the slight variation of the ion gyro frequency near 180 km altitude as the dominant ion switches from molecular ( $O_2^+$  and  $NO^+$ ) to atomic oxygen ( $O^+$ ) above this altitude.

Since the ionospheric gases are dense and only weakly ionized, collisions with neutrals significantly influence the individual and bulk motions of the plasma. Because of these collisional effects, the statistical collective behavior of the particles is defined using the equations of hydrodynamics. The ion-neutral collision frequencies ( $\nu_{in}$ ) and the electron-neutral collision frequencies ( $\nu_{en}$ ) are also plotted versus altitude in Figure 30 using standard collision operators, in this case, those provided by Banks and Kockarts (1973).

Notice immediately in Figure 30 that the electron gyrofrequency,  $\Omega_e$ , is larger than the electron-neutral collision frequency throughout the ionosphere. Hence, we

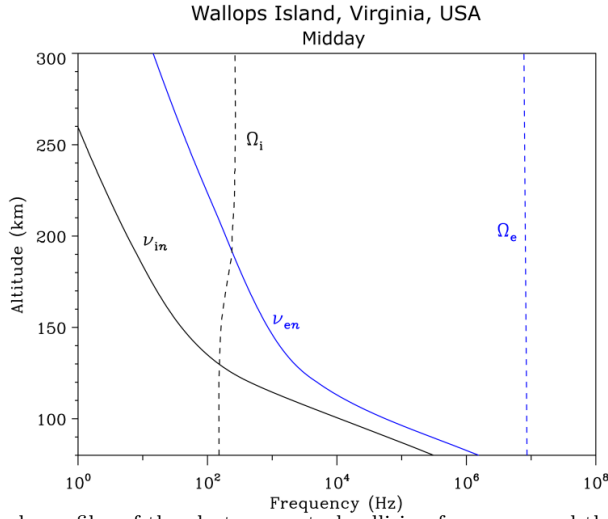


**Fig. 30** Altitude profiles of the electron-neutral collision frequency and the ion-neutral collision frequency. Profiles of the mean ion gyrofrequency and electron gyrofrequency are also shown (Pfaff 2012).

say that the electrons are “magnetized” throughout the region, since the electrons are able to execute their gyromotions about the magnetic field lines of force and consequently undergo unimpeded  $\mathbf{E} \times \mathbf{B}$  drifts across magnetic field lines. It is only at the very lowest altitudes, below 70 km, where the electron-neutral collision frequency succeeds in significantly altering the normal electron gyrations.

The ions, on the other hand, are collision dominated below about 130 km where  $\nu_{in} \sim \Omega_i$ . At lower altitudes, the ion motions are severely restrained by the neutral atmosphere to the extent that their motions become essentially those of the neutral gas or winds. Importantly, since the electrons are magnetized, the lower ionosphere region between 100-120 km, where  $\nu_{in}/\Omega_i > 1$  and  $\nu_{en}/\Omega_e < 1$ , constitutes the conducting or “dynamo” region where strong electrical currents flow, as discussed in the next section.

Above 130 km, the ion gyro frequency is greater than the ion-neutral collision frequency although the effect of ion-neutral collisions is still significant. At higher altitudes ( $> 200$  km) both the electrons and ions are considered magnetized and both execute  $\mathbf{E} \times \mathbf{B}$  drifts. However, even at these and higher altitudes, the ions and neutrals still “collide” to an extent where their motions influence each other, as we shall see further on below.

### 6.1.3 Mobility and Conductivity Tensors and Dynamo Currents

Because the plasma distribution function in the presence of a magnetic field is highly anisotropic, we define a mobility tensor,  $\underline{\underline{\mu}}$ , which relates the velocity ( $\mathbf{V}$ ) and force ( $\mathbf{F}$ ) vectors:

$$\mathbf{V} = \underline{\underline{\mu}} \cdot \mathbf{F} \quad (180)$$

where

$$\underline{\underline{\mu}} = \begin{pmatrix} \mu_1 & \mu_2 & 0 \\ -\mu_2 & \mu_1 & 0 \\ 0 & 0 & \mu_0 \end{pmatrix}$$

This tensor has been defined in a geometry such that the magnetic field,  $\mathbf{B}$ , is parallel to the z-axis. For single particle motion subject to an applied force, we have the following mobilities:

$$\mu_{0j} = 1/m\nu_{jn}$$

for parallel mobility,

$$\mu_{1j} = (1/m\nu_{jn})(\nu_{jn})^2/(\Omega_j^2 + \nu_{jn}^2)$$

for Pedersen mobility, and

$$\mu_{2j} = (1/m\nu_{jn})(\nu_{jn}\Omega_j)/(\Omega_j^2 + \nu_{jn}^2)$$

for Hall mobility. The mobilities are higher at lower latitudes due to the weaker magnetic field strength, since they are roughly proportional to  $1/\Omega_i^2$ .

We now define a conductivity tensor,  $\underline{\underline{\sigma}}$ , that relates the electric field,  $\mathbf{E}$ , and current density,  $\mathbf{J}$ :

$$\mathbf{J} = \underline{\underline{\sigma}} \cdot \mathbf{E} \quad (181)$$

which can also be expressed in terms of the difference of the ion and electron motions:

$$\mathbf{J} = N_e(\mathbf{V}_i - \mathbf{V}_e) \quad (182)$$

The conductivity may be expressed in terms of the mobilities such that  $\underline{\underline{\sigma}} = N_e^2(\mu_i + \mu_e)$ . The components of the conductivity are thus:

$$\sigma_0 = N_e^2(\mu_{0e} + \mu_{0i})$$

for parallel conductivity,

$$\sigma_1 = N_e^2(\mu_{1e} + \mu_{1i})$$

for Pedersen conductivity, and

$$\sigma_2 = N_e^2(\mu_{2e} - \mu_{2i})$$

for Hall conductivity

Clearly, the ionospheric conductivity depends linearly on the ambient plasma density and couples the neutral and ionized gases via the anisotropic mobilities as organized by the magnetic field. In Figure 31, typical parallel ( $\sigma_0$ ), Pedersen ( $\sigma_1$ ), and Hall ( $\sigma_2$ ) conductivities are plotted versus altitude for daytime, mid-latitude conditions (Akasofu and Chapman 1972). Notice how the Hall conductivity peaks at a lower altitude than the Pedersen conductivity where it is responsible for the global dynamo current system. The parallel conductivity is orders of magnitude larger than that of the Hall and Pedersen conductivity (see scale at top of figure).

Equation (181) may now be expressed more fully:



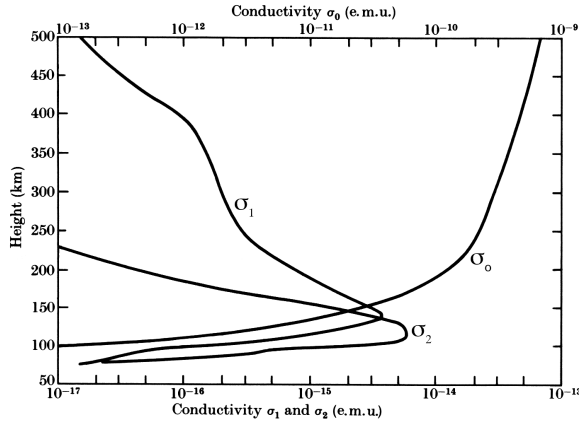


**Fig. 31** Ionospheric conductivities for daytime, mid-latitude conditions (Akasofu and Chapman 1972). (See text for explanation of symbols).

$$\mathbf{J} = \sigma_1 \mathbf{E}'_{\perp} + \sigma_2 \hat{\mathbf{b}}' \times \mathbf{E}'_{\perp} + \sigma_0 \mathbf{E}_{\parallel} \quad (183)$$

where  $\hat{\mathbf{b}}'$  is the unit vector along the magnetic field direction and  $\mathbf{E}_{\perp}$  is the perpendicular electric field in the earth-fixed frame, such that  $\mathbf{E}'_{\perp} = \mathbf{E}_{\perp} + \mathbf{U} \times \mathbf{B}$ . This expression shows that for an electric field,  $\mathbf{E}$ , perpendicular to the magnetic field,  $\mathbf{B}$ , the current will have two components: one along  $\mathbf{E}$  but perpendicular to  $\mathbf{B}$  (Pedersen) and one perpendicular to both  $\mathbf{E}$  and  $\mathbf{B}$  (Hall). Their magnitudes differ by  $\nu_{in}/\Omega_i$  and the angle,  $\alpha$ , between them is given by  $\alpha = \arctan(\Omega_i/\nu_{in})$ .

As the solar EUV heats the neutral upper atmosphere, the neutral gases generally expand away from the sub-solar point, creating a system of upper atmosphere tidal motions or winds. The neutral motions drag ions across magnetic field lines via ion-neutral collisions, creating a very small charge displacement with the electrons that subsequently sets up relatively weak, ionospheric electric fields. As discussed above, at the lower altitudes ( $< 130$  km), the ion-neutral collision frequencies become so large that the ions are collision dominated whereas the electrons, due to their much smaller mass, are not restricted and hence, remain magnetized. Due to the differential drifts of the ions and electrons at these low altitudes, a system of global scale, horizontal current patterns develops, in which internal, polarization electric fields are generated to restrict the current flow to be non-divergent. This worldwide system of currents is called the “solar quiet” (or sq) dynamo which form current loops at mid-latitudes which close at the magnetic equator, as shown in Figure 32 (Matsushita 1965).

The strongest current driven by the atmospheric dynamo is the equatorial electrojet. This current system exists as a result of both the dynamo action at all latitudes and the enhanced conductivity set up by the horizontal magnetic field geometry at the magnetic dip equator. At this location, in the altitude range of roughly 95 - 115 km, significant zonal (east-west) electron drifts are set up in the following way. Vertical  $\mathbf{E} \times \mathbf{B}$  drifts due to the ambient eastward electric fields (driven by the solar forcing discussed above) combined with the north-south magnetic field are inhibited for ions because the ion-neutral collisions are sufficiently

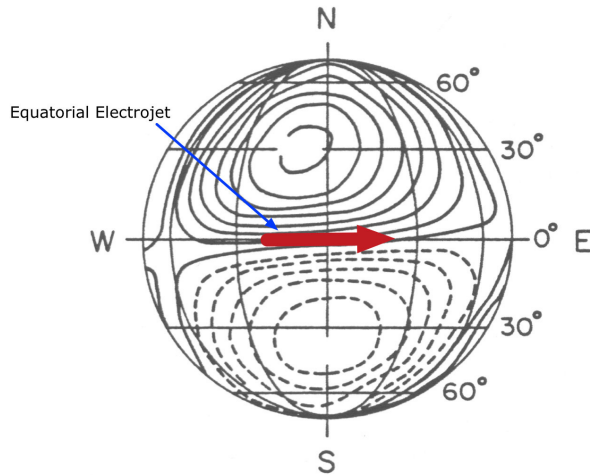


**Fig. 32** Current patterns set up by the atmospheric dynamo for the daytime hemisphere (Matsushita 1965).

large such that  $\mathbf{V}_i = 0$ . Hence, only the electrons are magnetized and the resulting vertical charge separation between the electrons and ions establishes a vertical polarization field,  $\mathbf{E}_p$ . This polarization electric field, in turn, creates a horizontal  $\mathbf{E}_p \times \mathbf{B}$  drift which reinforces the small, existing dynamo current and thus creates the strong electrojet current. The equatorial electrojet is strongest within a degree of the magnetic equator, where the magnetic field vector is precisely horizontal, thus enabling the vertical, polarization electric field described above to be set up. This current can also be explained in terms of the Cowling conductivity, which is an enhancement, by a factor of  $1 + \sigma_2^2/\sigma_1^2$ , of the Pedersen conductivity at the magnetic equator (Kelley 2009).

At night, the zonal electric field reverses direction and thus the polarization electric field is downward. The resulting  $\mathbf{E} \times \mathbf{B}$  drift again enhances the electrojet current since the zonal current is also of opposite direction at night. The magnitude of the nighttime current densities is much lower than during the daytime due to the greatly reduced ambient electron density.

In contrast to the low latitudes where the magnetic field is nearly horizontal, at high latitudes the magnetic field lines are highly inclined and connect the ionosphere to the large amplitude magnetospheric electric fields. These DC electric fields that map down from the magnetosphere set the high-latitude plasma in motion via  $\mathbf{E} \times \mathbf{B}$  drifts. At lower altitudes (below 200 km), however, the ion motion is appreciably affected by ion-neutral collisions such that the ion plasma drift is noticeably slowed and undergoes a change in direction. The electrons, on the other hand, remain fully magnetized and continue to execute  $\mathbf{E} \times \mathbf{B}$  drifts at altitudes as low as 70 - 80 km. Below these altitudes, the electron-neutral collision frequency becomes significant when compared to the electron gyrofrequency, as discussed earlier.

The ion and electron plasma drifts, calculated versus altitude for a 50 mV/m poleward (meridional) DC electric field at Poker Flat, Alaska ( $|\mathbf{B}| = 0.54$  G), are plotted in Figure 33 (Pfaff 2012). Ions and electrons both undergo an  $\mathbf{E} \times \mathbf{B}$  drift of approximately 950 m/s at 220 km. However, at lower altitudes, where the ion-

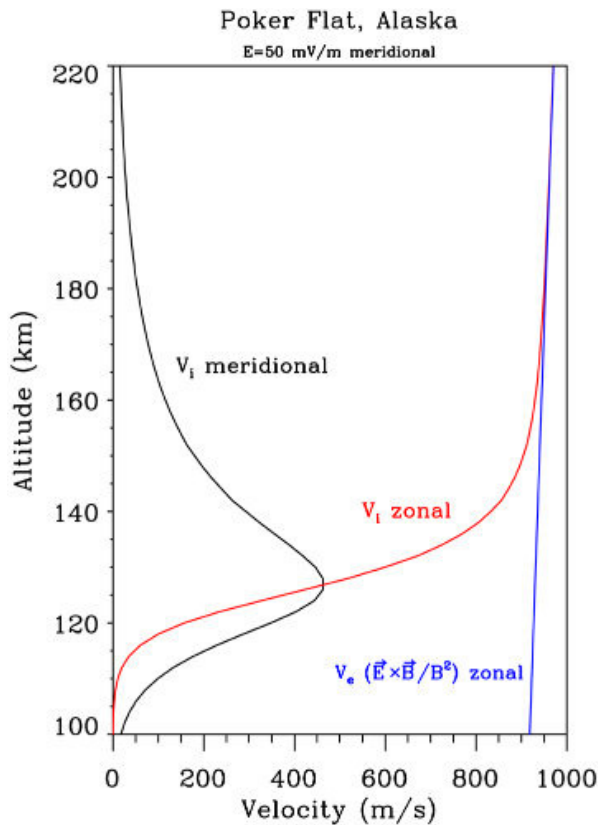


**Fig. 33** Ion drift velocity perpendicular to the magnetic field in the zonal (red) and meridional (black) directions, and the  $\mathbf{E} \times \mathbf{B}$  drift in the zonal direction (blue), as a function of altitude for a constant DC electric field of 50 mV/m applied in the meridional direction. The variations of the ion drift component with altitude are due to ion-neutral collisions, as explained in the text. The slight decrease of the  $\mathbf{E} \times \mathbf{B}$  magnitude at lower altitudes is due to the corresponding small increase of the magnetic field strength closer to the earth (Pfaff 2012).

neutral collisions become increasingly larger, the ion drift begins to both slow and change its orientation towards the direction of the DC electric field. At about 125 km altitude, where the Pedersen mobility peaks, the ion drift components are half the values of those of the  $\mathbf{E} \times \mathbf{B}$  components and are equally divided between flow along and perpendicular to the electric field direction. As the ion-neutral collisions slow the ion drifts, momentum is transferred to the neutral gas, as discussed in the next section.

#### 6.1.4 Coupled Neutral and Plasma Dynamics at Low, Middle, and High Latitudes

The coupled neutral and ionized gases within the Earth's ionosphere undergo a variety of circulation patterns and motions. The main dynamics at low and mid latitudes are driven by neutral motions or winds which collide with ions, setting them in motion. In addition, relatively small amplitude (0.5-5 mV/m) intrinsic DC electric fields are set up within the mid and low latitude ionosphere which

subsequently drive plasma motions via  $\mathbf{E} \times \mathbf{B}$  drifts. At high altitudes, on the other hand, magnetospheric electric fields with relatively large amplitudes (10-100 mV/m or greater) map down along the conducting field lines and set the plasma in motion. In this case, the plasma, in general, drives the neutral winds. The interplay between the motions of the two gas populations is quite complex, given the very different time constants to set the gases in motion which depend on the ion-neutral collision frequencies which vary significantly with altitude.

At low and mid-latitudes, the Earth's upper atmosphere has a global circulation of neutral winds created by pressure gradients from both solar and auroral heating. There is also forcing by tidal energy from the troposphere and mesosphere below. The global thermospheric winds tend to blow horizontally from the sub-solar heated region around the Earth to the coldest region on the nightside. As the wind develops, Coriolis forces act to deflect the flow. The horizontal wind speeds vary depending on the geomagnetic conditions. For quiet geomagnetic conditions the speeds typically range from 100 to 300 m/s at altitudes of several hundred km. Furthermore, because of the inclined angle of the magnetic field, the horizontal neutral winds are effective in transporting plasma to higher or lower altitudes.

Neutral winds move the conducting plasma of the ionosphere across geomagnetic field lines at low and middle latitudes on the Earth's day side, driving an atmospheric dynamo and equatorial electrojet discussed earlier. As part of this process, the winds also set up a global system of small (typically 0.5-2 mV/m) DC electric fields to ensure that the divergence of the currents is zero. These fields drive plasma motions, such as shown in Figure 34(a) in which a small zonal eastward electric field at the magnetic equator drives the plasma upwards which then slides back down along the magnetic fields on either side of the equator, creating enhanced plasma density at off-equator latitudes during the daytime. This process is called the "fountain effect" (Hargreaves 1992) and is an excellent example of how intrinsic electric fields, driven by neutral winds, alter the ambient plasma density distribution on a global scale, as shown in the plasma density model data in Figure 34(b). Indeed, this figure demonstrates how the plasma density on the dayside does not peak at the sub-solar point, which might otherwise be expected based solely on the maximum intensity of incoming solar EUV radiation.

In the polar regions, on the other hand, it is the strongly drifting ions, moving in response to the imposed higher amplitude magnetospheric electric fields, that "drag" the neutrals and thus generate neutral winds with speeds exceeding 1 km/s in the high-latitude F-region thermosphere. Such  $\mathbf{E} \times \mathbf{B}$  drifts drive the high latitude ionosphere with two-celled "convection" patterns that characterize the polar cap ionosphere. In this manner, the associated upper atmosphere wind system would exhibit corresponding patterns, at least initially. An example of the ion drifts and winds measured by the Dynamics Explorer-2 satellite traversing the high latitude region is shown in Figure 35(a) (Killeen et al. 1984).

In cases where the relative motions of the neutral and plasma gas populations are not the same, frictional or "Joule" heating occurs. The Joule heating rate per unit volume,  $Q_j$ , may be represented as:

$$Q_j = \mathbf{J} \cdot \mathbf{E}' = \sigma_p \mathbf{E}'^2 \quad (184)$$

where  $\mathbf{E}' = (\mathbf{E} + \mathbf{U} \times \mathbf{B})$  and  $\sigma_p$  is the Pedersen conductivity (Thayer 2000). An example of Joule heating measurements by satellite probes is shown in Fig-

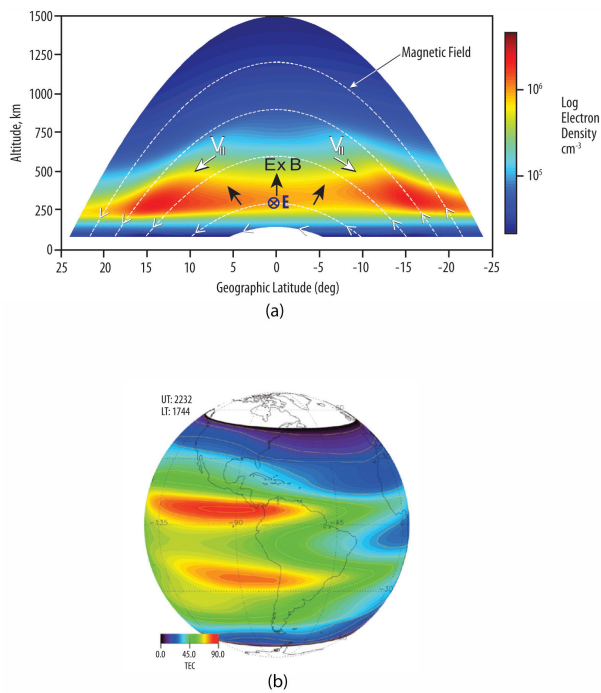


**Fig. 34** (a) SAMI2 model calculations versus latitude and altitude of the plasma density for 1500 SLT at 2050 East. The upward  $\mathbf{E} \times \mathbf{B}$  drift at the magnetic equator is driven by the eastward electric field, and there is subsequent flow downward along the magnetic field lines off the equator. (b) SAMI2 model calculations of the total electron content (TEC) at 22:32 UT, showing the equatorial anomaly enhancement in the late afternoon [Figure courtesy J. Huba].

ure 35(b) (Killeen et al. 1984) for the same data shown in Figure 35(a). This is a fundamental physical process inherent to differential velocities of ion and neutral gas populations within partially ionized plasmas.

Note that whereas the ionized gas motions are governed by the ambient magnetic field, the neutral gases are not. Thus, when the magnetospheric electric fields are shut off or change direction, the winds that were initially driven by the  $\mathbf{E} \times \mathbf{B}$  plasma drifts continue moving, and may proceed equatorward from the polar cap. The coupling of the neutral wind and plasma drifts underscores how the upper atmosphere/ionosphere of the earth must be understood as a dynamic system, in which the coupling efficiencies and time constants strongly depend on the ion-neutral collision frequencies and hence, altitude.

### 6.1.5 Response to energetic particles at high latitudes

In addition to responding to strong, imposed electric fields, the high latitude ionosphere also responds to vast swaths of precipitating energetic particles accelerated in the magnetosphere, with typical incoming energy spectra ranging from tens of eV to several keV (e.g., energetic electrons associated with the visual aurora). These energetic particles are responsible for subsequent increases in localized conductivity (discussed below), heating, and field-aligned currents. The field-aligned

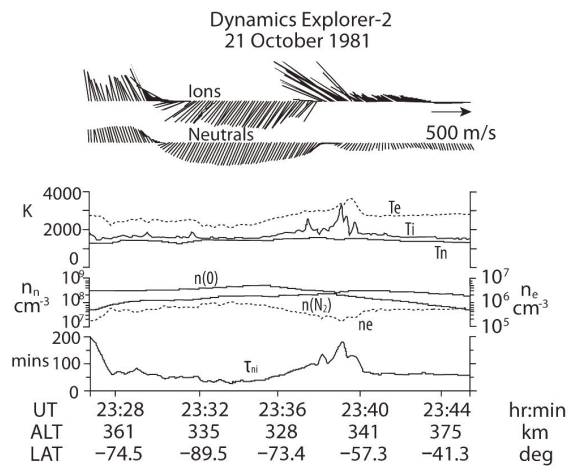
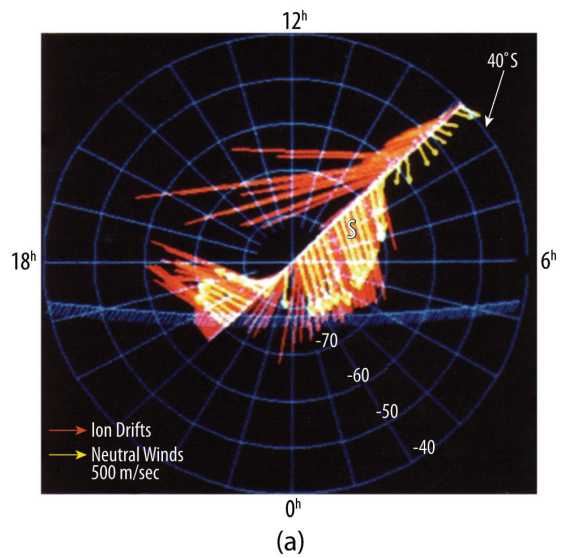


**Fig. 35** (a) The neutral wind, and ion drift vectors measured by DE-2 on a perigee pass over the southern polar region, plotted in geographic polar coordinates. The neutral winds are coded by the yellow arrows, and the ion drifts are coded by the red bars. The curved line represents the location of the solar terminator (90 solar zenith angle) (Killeen et al. 1984). (b) Geophysical quantities measured along the track of DE 2 during the orbit shown in (a). The ion drifts and the neutral winds are shown in the top two traces plotted against time, altitude, and latitude of the spacecraft. The second panel shows the electron, ion, and neutral temperatures measured along the track, and the third panel shows the atomic oxygen and molecular nitrogen number densities (left-hand scale) and the electron density (right-hand scale). The bottom trace shows the ion-neutral coupling time constant measured along the track, as discussed in Killeen et al. (1984).



**Fig. 36** View of the aurora photographed from the International Space Station on March 4, 2012, 17:20:33 UT on a pass over the South Indian Ocean. Figure courtesy NASA.

currents are associated with incoming electromagnetic energy flux into the region manifested in the form of Poynting flux and Alfvén waves (Kelley 2009). The coupling between the solar wind and the magnetosphere-ionosphere (M-I) system is important in determining the global energy budget in the high latitude ionosphere/thermosphere system in which energy is input from the magnetosphere in the form of both electromagnetic fields and particle kinetic energy flux.

Figure 36 shows a photograph of the aurora from the International Space Station in which the auroral optical emissions vary as a function of altitude as the incoming energetic electrons interact with the neutral atmosphere at different altitudes, depending on their energy. Note that at the higher altitudes ( $\sim 130\text{-}250$  km) the aurora is red/pink as the incoming electrons with lower energy interact with atomic oxygen yet is green below these altitudes corresponding to the incoming electrons with higher energy (typically keV) interacting, again, with oxygen.

The influx of precipitating energetic particles into the high latitude upper atmosphere/ionosphere system represents a source of thermal plasma density (i.e., increased conductivity) that results when the energetic electrons are “braked” by the neutral atmosphere. In such cases, incoming beams of energetic particles (mostly electrons) interact with the upper atmosphere which undergo impact ionization to create thermal plasma and heat the ambient gases. The precipitating electrons are a source of field-aligned currents whose circuit is ultimately completed through the lower ionosphere where the Hall and Pedersen mobilities enable the currents to close.

To illustrate how the incoming energetic electrons create thermal plasma, Figure 37 (Pfaff 2012) shows a pass of incoming keV electrons from a perigee pass of the FAST satellite in the upper panel. Each of these groups of energetic electrons corresponds to a spatial extension of energetic electrons through which the satellite has traversed and which would constitute an auroral arc formation where they interact with the ambient neutral gases at lower altitudes. The lower panel shows the thermal panel produced by these electrons, using the model of Strickland et al. (1993). Notice the “clumps” of enhanced thermal plasma (i.e., enhanced conductivity patches) whose altitude depends on the energy of the incoming electrons in the upper panel. This illustrates how “patchy” partially ionized plasmas are formed in the high latitude regions of the earth’s upper atmosphere and may be

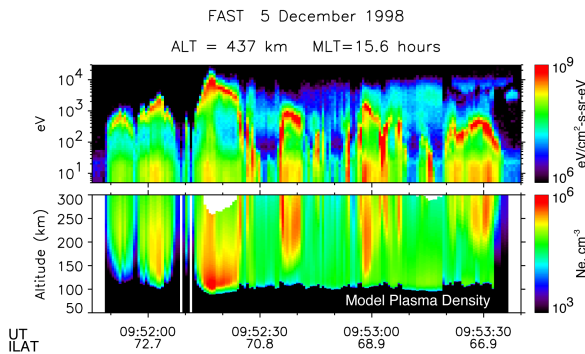


**Fig. 37** Observations gathered on the FAST satellite near 437 km are shown in the top panel and reveal narrow beams of downgoing, energetic electron spectra. The bottom panel shows the corresponding model thermal plasma created by these electrons [Pfaff, 2012].

common in astrophysical plasmas where electron beams with sufficient energy to ionize the neutral gas are present.

### 6.1.6 Response of the Ionosphere to Disturbances/Magnetic storms

Geomagnetic storms can occur in response to enhanced solar activity that interacts with the Earth i.e., sudden changes in the solar wind dynamic pressure at the magnetopause caused by the passage of a coronal mass ejection. The interaction causes a temporary disturbance in the magnetosphere which leads to an expansion of plasma convection and particle precipitation patterns, stronger electric fields, and intensified precipitation (Dremukhina et al. 1999). These changes are accompanied by substantial increases in the Joule and particle heating rates and the electrojet currents. The ionosphere receives a large amount of energy during storms and substorms, and large storms can significantly modify the density, composition, and circulation of the ionosphere on a global scale. Accordingly, neutral flows in the lower ionosphere increase at higher latitudes during storms as well. Substorms correspond to the explosive release of energy in the auroral region near magnetic midnight in which energy is released from the magnetotail and injected into the high latitude ionosphere, often causing discrete auroral arcs. Eventually, the disturbances associated with substorms typically encompass the entire high-latitude region.

The low and mid-latitude ionosphere is also highly subject to magnetic disturbances and storms and reveals a complex response based on penetration electric fields that are applied from the magnetosphere response to the increased solar wind pressure and electric fields associated with the storm. These processes include the abrupt transport of ionospheric plasma to very high altitudes at mid- and low-latitudes. An example of a storm-enhanced plasma density feature is shown in Figure 38 (see also Foster et al. (2005)) and demonstrates how the ionospheric plasma enhancements may be confined within narrow longitude regions based on the magnetic storm input. The neutral gases also respond to this sudden increases of energy. Indeed, the entire upper atmosphere – both neutral and ionized components – respond in dramatic fashion to externally imposed disturbances associated with magnetic storms.



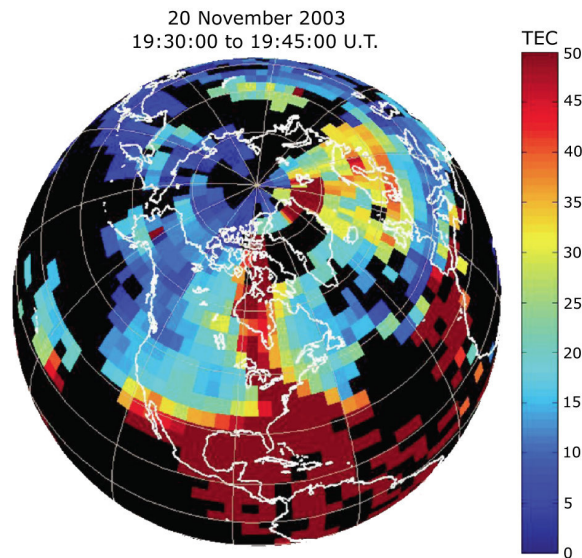


**Fig. 38** Storm-enhanced plasma density (SED) signatures in total electron content (TEC) observed on November 20, 2003. These are believed to be connected to plasmasphere erosion and driven by sub-auroral electric fields from the inner magnetosphere. Strong plasma density gradients are observed by a network of ground-based GPS observatories (Figure courtesy of A. Coster).

In summary, the most accessible partially ionized plasma available for detailed study, the earth's ionosphere/thermosphere system is particularly rich in processes due to the many sources of energy, momentum, and ionization that drive and maintain the coupled system as well as due to the presence of the dipole magnetic field that permeates and helps organize the system. Global patterns of electric fields, currents, plasma density, neutral winds and other parameters are set up which display variations as a function of altitude, latitude, local time, and solar activity. Detailed measurements with satellite, sounding rocket, and remote sensing instruments, as well as advanced modeling techniques, reveal fundamental processes important not only for understanding important physics of planetary ionospheres but also for comparisons with partially ionized plasmas associated with solar and astrophysical gases. Indeed, the coupled neutral and ionized gases that exist within the Earth's upper atmosphere yield a highly complex system with a wide variety of physical processes that are among the most captivating and important topics in space research.

## 6.2 Jupiter's and Saturn's thermosphere and ionospheres

*Thermosphere Parameters* The thermosphere is the uppermost region of a planet's neutral atmosphere. It is characterised as a region in which the temperature steadily increases with altitude until a maximum (exospheric) limit is reached. Mean free path lengths for thermospheric species are long - sometimes up to hundreds of kilometres - and the mixing of the atmosphere by convection is almost non-existent. The level at which convective mixing is no longer important is known as

**Table 2** Key Thermosphere Parameters for Earth, Jupiter and Saturn

Parameters (units)	Earth	Jupiter	Saturn
Homopause temperature (K)	200	200	140
Homopause pressure ( $10^{-6}$ bar)	1.0	2	0.1
Homopause density ( $10^{19} m^{-3}$ )	3.7	7.3	0.52
Homopause scale height <sup>a</sup> (km)	6.0	35.7	64.6
Exospheric temperature (K)	1000	940	420
Exospheric scale height <sup>b</sup> (km)	52.6	335.6	387.0
Critical density ( $10^{13} m^{-3}$ )	10	2.5	2.5
Critical pressure ( $10^{-12}$ bar)	4	1	1

<sup>a</sup> Scale height for  $N_2$  for Earth and  $H_2$  for Jupiter and Saturn.

<sup>b</sup> Scale height for  $O$  for Earth and  $H$  for Jupiter and Saturn.

the homopause. Above the homopause, atmospheric atomic and molecular species settle out diffusively; each species has its own scale height,  $H_S$ , given by:

$$H_S = kT/gm_S \quad (185)$$

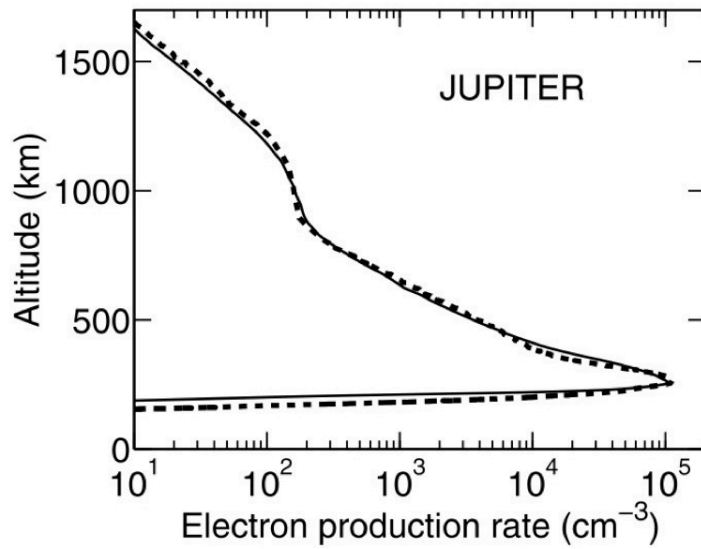
where  $k$  is Boltzman's constant,  $T$  is the thermospheric temperature,  $g$  the acceleration due to gravity and  $m_S$  is the atomic or molecular weight of species  $S$ . At higher altitudes, the thermosphere merges into the exosphere. The base of the exosphere, the exobase, is characterised by a critical density,  $N_C(S)$ , at which the horizontal mean free path of the main thermospheric species,  $S$ , is equal to the scale height.  $N_C(S)$ , is given by:

$$N_C(S) = \frac{1}{\pi d_S^2 H_S} \quad (186)$$

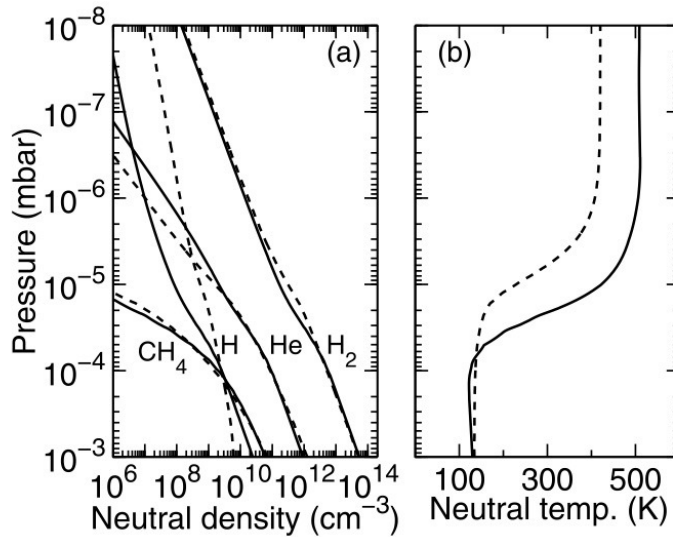
where  $d_S$  is the diameter of species  $S$ . Some approximate values for key parameters for the Earth, Jupiter and Saturn are compared in Table 2 (Miller et al. 2005).

Figure 39 shows a comparison between the electron production rate, which has been calculated by Galand et al. (2011) (solid line) and that derived by Grodent et al. (2001) (dashed line). Both profiles in altitude of the electron production rate assuming the same triple Maxwellian distribution for the incident auroral electrons as Grodent et al. (2001) and similar thermospheric conditions at Jupiter. The Jupiter's ionospheric profile can be compared with number densities of the Earth's ionosphere (see Figure 28)

The Saturn thermospheric densities and temperature extracted at a latitude of  $78^\circ S$  at 12LT at equinox during solar minimum conditions are presented in Figure 40 (Galand et al. 2011). Though the quantities are plotted for noon, no significant local time dependence is found, which is explained by the fast rotation of Saturn. The exospheric temperature,  $T_{exo}$ , is strongly correlated with the amount of Joule heating present in the high-latitude regions. The electron energy flux and convection electric field, which drive the Joule heating, are chosen such that the derived value for  $T_{exo}$  is in agreement with observations from UV occultation.



**Fig. 39** Profile in altitude of the electron production rate (solid line) calculated by Galand et al. (2011) and by Grodent et al. (2001) for similar thermospheric conditions at Jupiter.



**Fig. 40** Saturn neutral atmospheric (a) density and (b) temperature profiles in altitude resulting from the 3D neutral Saturn Thermosphere Ionosphere Magnetosphere (STIM) model at 78°S latitude at equinox ( $T_{exo} = 510\text{ K}$ , solid lines) (Galand et al. 2011). The reference profiles ( $T_{exo} = 420\text{ K}$ ) derived by Moses et al. (2000) are shown as dashed lines.

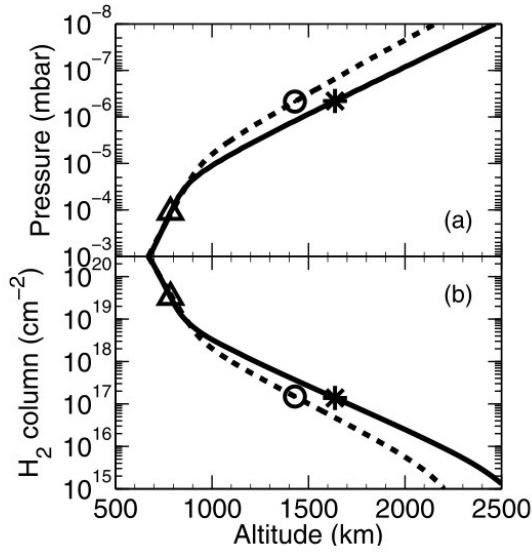


**Fig. 41** (a) Pressure versus altitude derived from the 3D STIM atmospheric profile ( $T_{exo} = 510\text{ K}$  (Galand et al. 2011), solid line) and from the reference profile by (Moses et al. 2000) ( $T_{exo} = 420\text{ K}$ ) (dashed line). (b) Same as Figure (a) but for the  $\text{H}_2$  column density above. The markers correspond to the pressure and  $\text{H}_2$  column density at the altitude of maximum energy deposition for  $E_m = 10\text{ keV}$  (triangle) using the STIM atmosphere and for  $E_m = 500\text{ eV}$  using the  $78^\circ\text{S}$  STIM atmosphere (star) and reference atmosphere (circle). For visibility reasons, the case of  $10\text{ keV}$  using the reference atmosphere has not been plotted as it overlaps with the  $10\text{ keV}$  case using the STIM atmosphere. The transport of auroral electrons and the column density valid along the path were calculated for the dip angle at  $78^\circ\text{S}$ , i.e.,  $82^\circ$ . The reference altitude is taken to be the 1 bar level, and the top of the atmosphere is taken at a pressure of  $4.4 \times 10^{-9}$  mbar.

In Figure 41, the midlatitude atmospheric model of Moses et al. (2000), widely used by the community at high-latitudes (Gérard et al. 2004; Gustin et al. 2009) is shown as dashed lines in Figure 40. The associated exospheric temperature of  $420\text{ K}$  was derived from the analysis of the Voyager 2 UVS solar ingress occultation. Plotted as a function of pressure, the  $\text{H}_2$  density obtained for  $T_{exo} = 510\text{ K}$  is very close to the  $420\text{ K}$  reference model. The same applies to the minor species  $\text{He}$  and  $\text{CH}_4$  at high pressures above  $3 \times 10^{-5}$  mbar, keeping in mind that the mixing ratios assumed for these species at the lower boundary in the STIM model are those from Moses et al. (2000). At lower pressure, large differences in the  $\text{H}$  and  $\text{He}$  densities are clearly apparent between the Saturn Thermosphere-Ionosphere Model (STIM) profiles and the reference profiles. Such differences are primarily due to global dynamics. Because of the difference in temperature profiles between the  $510\text{ K}$  STIM (solid line) and the  $420\text{ K}$  reference (dashed line) atmospheric models, the conversion from pressure to altitude is similar at pressures larger than  $2 \times 10^{-5}$  mbar, but significantly different at pressures smaller than  $2 \times 10^{-5}$  mbar, as illustrated in Figure 41a. For instance, on the one hand,  $10\text{ keV}$  auroral electrons penetrate deeply into the atmosphere to an altitude of  $790\text{ km}$  (triangle in Figure 41a) corresponding to an  $\text{H}_2$  column density of  $3 \times 10^{-19}\text{ cm}^{-2}$  (triangle in Figure 41b) and have a penetration altitude largely insensitive to the

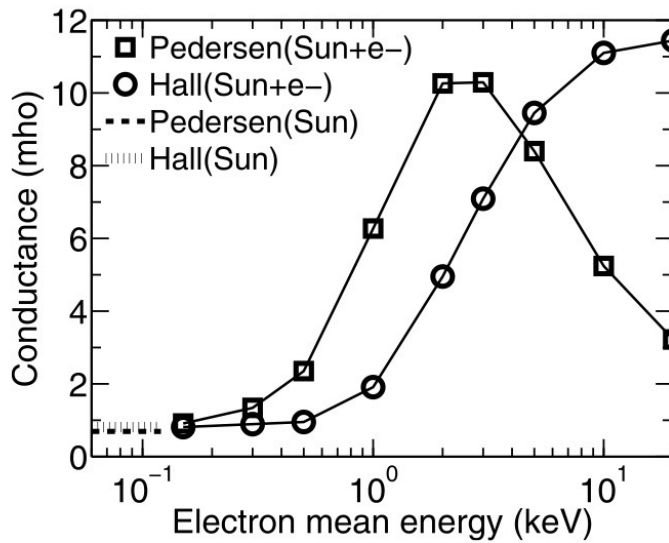


**Fig. 42** Pedersen (squares) and Hall (circles) ionospheric conductances as a function of the mean energy of the incident auroral electrons,  $E_m$ , under solar illumination angle of  $78^\circ$  at noon. The distribution of the incident electrons is assumed to be Maxwellian with an energy flux,  $Q_0$ , of  $0.2 \text{ mW} \cdot \text{m}^{-2}$ . The Pedersen and Hall ionospheric conductances obtained for solar illumination alone (no auroral particle precipitation) are shown with horizontal, dotted and dashed lines, respectively, (Galand et al. 2011).

atmospheric models. On the other hand, for 500 eV electrons there is a difference of 208 km between the high-latitude STIM (stars) and the midlatitude reference (circles) models. Therefore, the conversion between the penetration altitude of auroral electrons and the mean energy of the auroral electrons using alternative atmospheric models needs to be taken with caution when focusing on soft electron precipitation.

In Figure 42, the ionospheric Pedersen conductance SP (squares) and Hall conductance SH (circles) are plotted as a function of the mean energy of the incident electrons. The energy dependence is different between Pedersen and Hall conductances, as their conductivities do not peak in the same altitude region. Auroral electrons with incident mean energy in the 2 - 3 keV range deposit their energy near the homopause, where the Pedersen conductivity peaks. As a result, the Pedersen conductance reaches a maximum in the 2 - 3 keV incident energy range. The Hall conductivity peaks well below the homopause. As a consequence, the Hall conductance is increasing over the whole electron mean energy range considered here spreading from 150 eV to 20 keV. At very low electron mean energy, the auroral deposition peak altitude is located at altitudes higher than the solar deposition peak altitude, in a region less efficient for generating conductivities. As a result, the Pedersen and Hall conductances converge towards the solar values equal to 0.7 mho and 0.8 mho, respectively. At 150 eV, the Pedersen conductance is within 30% of the solar value, while the Hall conductance whose conductivity peaks lower than the Pedersen conductivities, has already reached the solar value.

*Magnetospheric plasma* The plasma features and particles beams are regulated by magnetospheric magnetic field. The general view of the Jupiter and Saturn magnetosphere is given by the magnetospheric models of Belenkaya et al. (2005); Alexeev et al. (2006); Alexeev et al. (2015). Particles, momentum and energy are exchanged between the planetary upper atmosphere and magnetosphere via the ionosphere in the high latitude regions. There is a net momentum transferred from the atmosphere to the magnetosphere, while energy, for instance particle precipitation, is deposited from the magnetosphere to the atmosphere (see e.g., Hill 1979, 2001; Cowley and Bunce 2001). These particles primarily originate from moons (e.g., Io and Europa at Jupiter, and Enceladus at Saturn), and to a lesser extent from the planetary atmosphere and the solar wind (e.g., polar regions at Jupiter). Some of the ions resulting from ionization of the moon's gas torus are neutralized through charge exchange and leave the system; the others are picked up by the planetary magnetic field closely rotating at the planet's rotation rate and flow outward through the planetary magnetosphere (Bagenal and Delamere 2011). The resulting upward currents, flowing from the atmosphere to the magnetosphere, that supply the required angular momentum accelerate the particles, increasing their energy and energy flux (see e.g., Ray et al. 2010; Ray et al. 2012). Particles can also precipitate as a result of wave-particle interactions (e.g. Radioti et al. (2009)).

When the energized particles reach the high latitude upper atmosphere, they collide with the atmospheric species, depositing energy through ionization, excitation and dissociation of the neutral gas. This yields the so-called auroral emissions defined as the photomanifestation of the interaction of energetic, extra-atmospheric particles with an atmosphere (e.g. Bhardwaj and Gladstone (2000); Galand and Chakrabarti (2002); Fox et al. (2008); Slinger et al. (2008)). In the Jupiter system, atmosphere and magnetic field are not just Jupiter, but a light atmosphere and small magnetic field also exist on one of the largest moons, Ganymede. As a result of Jovian magnetospheric plasma flow past Ganymede, we have auroral particle acceleration and Ganymede's auroral emission (see for example Lavrukhin and Alexeev (2015))

Auroral particle degradation results in an increase in ionospheric densities and electrical conductances (e.g. Millward et al. (2002); Hiraki and Tao (2008); Galand et al. (2011)). Ionospheric currents, which allow closure of the magnetospheric current system, are enhanced and induce strong Joule heating of the high-latitude thermosphere (e.g. Miller et al. (2005); I.C.F. Muller-Wodarg (2012)). This high-latitude atmospheric heating is a key player in the energy balance at the giant planets (e.g. Yelle and Miller (2004)). In other words, particle precipitation, which can be traced via auroral emissions, plays a critical role in the thermosphere-ionosphere system and its coupling to the magnetosphere (Alexeev et al. 2014).

The global magnetospheric dimensional sizes are provided in Table 3 (Alexeev et al. 2015). The scaling relations allow one to adapt the magnetopause and the tail current systems developed for the Earth's magnetosphere to the case of Jupiter and Saturn. However, for the currents caused by the rapid planetary rotation (magnetodisk for Jupiter and Saturn) there is no analogy in the terrestrial magnetosphere. The magnetodisk is the main source of Jupiter's magnetospheric magnetic field. Its effective magnetic moment dominates Jupiter's dipole magnetic moment ( $\sim 2.6$  times Alexeev and Belenkaya (2005)).

**Table 3** Solar System Planetary Magnetosphere Parameters

Parameters (units)	Equation	Earth	Jupiter	Saturn
Heliocentric distance (AU)	$r_0$	1	5.2	9.5
Equatorial radius ( $R_E = 6,371$ km)	$r_P$	1	11.2	9.45
Magnetic moment ( $T \cdot km^3$ )	$B_0 \cdot r_P^3$	0.008	150.	4.6
Dipole tilt angle (degrees)	$\psi$	$10.5^\circ$	$10^\circ$	$0^\circ$
Equatorial magnetic field ( $\mu\text{T}$ )	$B_0$	30.	420.	20.
Dipole hemisphere magnetic flux (GWb)	$2\pi B_0 r_P^2$	7.7	13,450	456.
Open field line magnetic flux (GWb)	$\pi B_0 r_P^2 \frac{r_P}{R_{ss}}$	0.42	450	11.4
Polar oval radius (degrees)	$\sin \theta = \sqrt{\frac{r_P}{R_{ss}}}$	$20^\circ$	$15^\circ$	$13^\circ$
Average IMF magnitude (nT)	$\frac{5\sqrt{1+r_0^2}}{\sqrt{2} \cdot r_0^2}$	5	1	0.5
Nominal Parker spiral angle $\phi$	$\tan \phi = \frac{1}{r_0}$	$45^\circ$	$80^\circ$	$85^\circ$
Solar wind ram pressure (nPa)	$\frac{1.7}{r_0^2}$	1.7	0.07	0.015
Subsolar magnetic field magnitude (nT)	$B_{ss} = \frac{74.5}{r_0}$	74.5	14.3	7.8
Subsolar magnetopause distance ( $R_P$ )	$R_{ss}$	$10 R_E$	$70 R_J$	$22 R_S$

The dimensions of planetary magnetospheres may vary by a factor of several hundreds (see Table 3), but different planets have similarly shaped magnetopauses. The front part of the magnetosphere coincides with the paraboloid of revolution, which has a symmetry axis that is a line joining the planet and the Sun. The magnetic field at the subsolar point can be determined from the balance of the solar wind plasma dynamic pressure and the pressure of the magnetic field inside the magnetosphere. This field does not depend on the value of the planetary dipole and is determined unambiguously by the solar wind dynamic pressure. The planetary dipole determines the size of the magnetosphere,  $R_{ss}$ . For Jupiter's and Saturn's magnetospheres the equatorial magnetodisks are formed by the rotational uploading of the satellite's plasma. As a result,  $R_{ss}$  is determined not by the planetary dipole only, but by some "effective" dipole which is bigger than the planetary one.

### 6.2.1 Energy Deposition of Precipitating Auroral Particles

*Energetic Electrons* The incident auroral electron characteristics derived from the spectroscopic analysis of the ultraviolet auroral emissions have been summarized for the main auroral ovals of Jupiter and Saturn in (Gérard et al. 2013). The two sets of values in the corresponding Table of Gérard et al. (2013) correspond to two different atmospheric models used for the analysis. Energetic electrons interact with the atmospheric neutrals through elastic scattering and inelastic

collisions, the latter including ionization, excitation, dissociation or a combination of them. Ionization yields the production of secondary electrons, which can in their turn interact with the atmosphere. Furthermore, suprathermal electrons interact with the thermal, ionospheric electrons through Coulomb collisions. This yields an increase in the ionospheric electron temperature (Grodent et al. 2001; Galand et al. 2011).

A major, additional source of energy originates in the high latitude regions, where magnetospheric currents can deposit globally several tens of TW in Saturn case, more than 50 times the absorbed solar EUV value, as thermal energy, primarily via Joule heating (Cowley et al. 2004). The assessment of Joule heating, plasma flows, and current system at high latitudes, all requires the knowledge of the ionospheric state, and in particular electrical conductances in the auroral regions [e.g., Cowley et al. (2004) and Cowley et al. (2008)].

As a result of the interaction with the atmospheric species, the suprathermal electrons undergo degradation in energy and redistribution in pitch angle (the angle between the electron velocity and the local magnetic field). As the energy loss is a function of the electron energy, and secondary electrons are added towards lower energies, the initial electron energy distribution at the top of the atmosphere changes, as the electrons penetrate deeper in the atmosphere. The calculation of the distribution of electrons in both position and velocity space is required. Three approaches have been applied to auroral electrons at Jupiter and Saturn, all assuming steady-state conditions and the guiding center approximation (Rees and Lummerzheim 1989):

a) The “Continuous Slowing Down Approximation” (CSDA) method assumes that the energy loss is a continuous rather than a discrete process (Gérard and Singh 1982; Singhal et al. 1992; Rego et al. 1994; Prange et al. 1995; Dalgarno et al. 1999). The variation  $dE$  in electron energy per path length  $ds$  in an atmosphere composed of species  $k$  with neutral density  $n_k$  and energy loss  $L_k$  is given by:

$$\frac{dE}{ds} = -\sum_k n_k(s)L_k(E) \quad (187)$$

The method, simple to implement, requires - in order to be able to integrate Eq. (187) - that either the atmospheric composition is independent of altitude (e.g., Dalgarno et al. (1999)) or that atmospheric species have energy losses proportional to each other [e.g., Rego et al. (1994)]. The method is limited to high energies where the assumption of a continuous loss is justified and scattering is neglected. The CSDA method allows the calculation of the profiles in altitude of ionization and excitation rates.

b) An alternative method is to utilize transport models based on the explicit, direct solution of the Boltzmann equation, which can use a two-stream approach (up/down) (Waite et al. 1983; Achilleos et al. 1998; Grodent et al. 2001; Gustin et al. 2009) or multistream approach (more than two pitch angles considered) (Kim et al. 1992; Perry et al. 1999; Menager et al. 2010; Galand et al. 2011). The Boltzmann equation expresses the conservation of the number of particles in the phase space, as given by:

$$\frac{df}{dt} + f\nabla_u \cdot \frac{F}{m} = \left(\frac{\delta f}{\delta t}\right)_{coll} + S_{ext} \quad (188)$$



where  $f(r, u, t)$  is the suprathermal electron distribution at position  $r$ , velocity  $u$  and time  $t$ . The second term on the LHS takes into account the effect of any dissipative forces  $F$ . The first term on the RHS represents variation due to collisions and the second term is associated with external sources (e.g., photoelectrons, secondary electrons from an ion beam).

The Boltzmann equation is solved in terms of the suprathermal electron intensity ( $I_e = \frac{u^2}{m} f$ ), which is a measurable quantity. The phase space is usually reduced to three dimensions, path length  $s$  along the magnetic field line, kinetic energy  $E$ , and cosine  $\mu$  of the pitch angle  $\theta$ . Scattering is included. Beside ionization, excitation, and dissociation rates this method allows the calculation of thermal electron heating rates.

c) Monte Carlo simulations refer to a stochastic method based on the collision-by-collision algorithm (Hiraki and Tao 2008; Gérard et al. 2009; Tao et al. 2011). A large number of particles is considered and followed in the simulated atmosphere. The Monte Carlo approach avoids the use of an energy grid, which can be of great interest for problems with electron energies ranging over five orders of magnitude. Its drawback is that it is computationally expensive, since it requires a large number of particles to reduce the statistical noise. At Jupiter and Saturn, only excitation, ionization and dissociation processes have been included; thermal electron heating, which is efficient at low energies ( $< 1 \text{ eV}$ ), has not been considered.

Suprathermal electron transport models are driven by the electron intensity at the top of the atmosphere, which is a function of energy and pitch angle. For Jupiter and Saturn, it is shown that Joule heating and frictional effects, due to ion-neutral coupling can produce large amounts of energy that may account for their high exospheric temperatures (Miller et al. 2005). One key question for all studies of the upper atmospheres of the giant planets is that measured exospheric temperatures are several hundred degrees higher than can be produced by the effects of solar EUV heating alone (Yelle and Miller 2004).

## 7 Molecular clouds

### 7.1 Introduction

Molecular clouds (MCs) are the densest and coldest structures in the interstellar medium (ISM) of our and other galaxies, and the sites of most, if not all, star formation (SF) in these systems. There, the ionization fraction is  $\sim 10^{-7}$  or lower (e.g., Shu 1992, Ch. 27), and so ambipolar diffusion (AD, often also referred to as ion-neutral drift) has the potential to be important in various aspects of MC dynamics. In particular, AD was central to the so-called “standard model” of magnetically-regulated, AD-mediated star formation (see the reviews of Shu et al. 1987; Mouschovias 1991, and references therein; see also Sec. 7.3.1 below). It has also been considered as a possible mechanism responsible for a number of observed properties in the ISM and the MCs of our galaxy, and in this chapter we will review the most frequently discussed ones among these applications. However, in most cases, other mechanisms have also been proposed as being responsible for those observed properties, and so we will present those alternative processes here as well, hopefully providing a broad and unbiased view. Specifically, we will discuss the formation and collapse of dense cores in MCs (Sec. 7.3), the observed correlation (and lack thereof) between the density and magnetic fields in the ISM, the formation of MC cores, the origin of the nearly constant width of filamentary structures within MCs, and the resolution of the so-called “magnetic braking catastrophe” in protostellar accretion disks. However, because most of these processes are related to the underlying assumptions for the structure and state of MCs, we start with a brief recount of the evolution of our view of MCs. A more detailed account up to the “turbulent support” picture can be found in Mac Low and Klessen (2004).

### 7.2 The Evolving Picture of MCs

#### 7.2.1 *The early scenario of collapse and its demise*

MCs have been known to contain highly supersonic nonthermal motions for over 40 years now, after the discovery that their molecular-line emission exhibits widths corresponding to velocities up to one order of magnitude larger than their thermal speeds (Wilson et al. 1970). Originally, such motions were interpreted as a possible signature of global gravitational contraction (Goldreich and Kwan 1974), but it was soon argued that, if this were the case, then the global SF rate (SFR) of The Galaxy would be much larger than observed (Zuckerman and Palmer 1974). Indeed, assuming that all molecular gas in The Galaxy (with a mass of  $10^9 M_\odot$ , where  $M_\odot \approx 2 \times 10^{30}$  kg is the mass of the Sun), at a mean number density of  $n \sim 10^8 \text{ m}^{-3}$  ( $= 10^2 \text{ cm}^{-3}$ , corresponding to a mass density  $\rho = 3.94 \times 10^{-19} \text{ kg m}^{-3}$ , for a mean particle mass  $\mu = 2.36$ ), is collapsing on its free-fall time ( $\tau_{\text{ff}} = \sqrt{3\pi/32G\rho} \approx 3.35 \text{ Myr} \approx 1.06 \times 10^{14} \text{ s}$ ), then the SFR would be  $\sim 300 M_\odot \text{ yr}^{-1}$ . Instead, the observed SFR is currently estimated to be roughly two orders of magnitude smaller (see, e.g., Chomiuk and Povich 2011, for a current estimate). Moreover, Zuckerman and Evans (1974) suggested that, if MCs were dominated by global collapse (or, in general, any cloud-scale veloc-

ity gradient), such that the envelopes of clouds were infalling onto their centers, then one should observe systematic Doppler shifts between lines produced at the periphery of clouds and the lines produced near the center of the clouds around the newly-formed stars, an effect that is not observed. Therefore, Zuckerman and Evans (1974) concluded that, instead of consisting of global, cloud-scale motions, the observed supersonic linewidths corresponded to small-scale turbulent motions.

### *7.2.2 The magnetic and turbulent support scenarios*

Shortly thereafter, these supersonic motions were reinterpreted as MHD waves (Arons and Max 1975), in particular as Alfvén waves, which were thought to be less dissipative than the shock waves that would be produced by hydrodynamic supersonic turbulence, and thus to allow the motions to persist over the whole lifetimes of the clouds. At the time, these were estimated to be of the order of a few times  $10^7$  yr (recall that  $1 \text{ yr} \approx 3.15 \times 10^7 \text{ s}$ ) (Blitz and Shu 1980). Moreover, the magnetic field was believed to be sufficiently strong to prevent the global collapse of the clouds. This scenario, to which we will refer as the “magnetic support” model of MCs, was reinforced by the observation of significant magnetic fields in MCs (see Myers and Goodman 1988, and references therein), and prevailed until the late 1990s, when numerical simulations of supersonic MHD turbulence became feasible, and showed that MHD turbulence dissipates just as rapidly as pure hydrodynamic turbulence (Mac Low et al. 1998; Stone et al. 1998; Padoan and Nordlund 1999; Avila-Reese and Vázquez-Semadeni 2001), except possibly if the energy flux up and down magnetic field lines is imbalanced (Cho et al. 2002). The supersonic nonthermal motions were then reinterpreted as genuine supersonic MHD turbulence. Moreover, it was also noted that giant molecular clouds (GMCs) exhibit near equipartition between their nonthermal kinetic and gravitational energies (Larson 1981; Heyer et al. 2009). This fact was then interpreted as evidence of near virial equilibrium in the clouds between their self-gravity and turbulence, although the latter required continuous driving in order to be maintained (see, e.g., Vázquez-Semadeni et al. 2000; Mac Low and Klessen 2004; Elmegreen and Scalo 2004; Ballesteros-Paredes et al. 2007; McKee and Ostriker 2007). The prime candidate for injection of kinetic energy into the ISM and MCs in particular was feedback from supernova explosions and HII regions around massive stars, although other mechanisms such as magnetorotational instabilities, protostellar outflows, massive-star winds, the passage of spiral density waves, etc., were also considered (see the review by Mac Low and Klessen 2004, and references therein). We will refer to this view as the “turbulent support” model of MCs.

### *7.2.3 The hierarchical gravitational collapse scenario*

However, in the last decade or so, the turbulent-support paradigm has been questioned by a number of authors, on the following accounts. First, it has been pointed out that the near-equipartition may be a consequence of unimpeded gravitational collapse rather than virial equilibrium (Ballesteros-Paredes et al. 2011b; Dobbs et al. 2014; Palau et al. 2015). Second, in the virial-equilibrium interpretation, stellar-driven turbulence would provide the counteracting agent against the clouds’ self-gravity, through a hypothetical turbulent pressure. However, this interpretation faces some problems: i) The near-equipartition is observed even in clouds

that have little or no ongoing star formation (Maddalena and Thaddeus 1985), so that the source of their kinetic energy cannot be the feedback from stellar sources. ii) There appears to be no *a priori* reason why the energy injection by stellar sources would adjust itself to maintain the clouds in near-equilibrium. Although some idealized models of energy balance have been produced in which the feedback self-regulates to do this (e.g., Krumholz et al. 2006; Goldbaum et al. 2011), full numerical simulations including ionization feedback suggest that, once the star formation activity fully develops in the cloud, the latter is disrupted (partly evaporated, partly torn apart; Vázquez-Semadeni et al. 2010; Dale et al. 2012; Colín et al. 2013), at least for clouds of masses  $< 10^6 M_\odot$ . Moreover, Colín et al. (2013) found that the clouds appear in near equipartition *before* SF has fully developed in the clouds, and attributed the equipartition to the clouds' gravitational contraction instead. Thus, stellar driving of a stabilizing turbulence seems to face significant problems.

Another mechanism that has been advocated as the driver of MC turbulence is a combination of Kelvin-Helmholtz, Rayleigh-Taylor, thermal, and nonlinear thin-shell instabilities in the clouds themselves as they are assembled by the convergence of streams in the warm atomic medium of The Galaxy (Koyama and Inutsuka 2002; Audit and Hennebelle 2005; Heitsch et al. 2005; Vázquez-Semadeni et al. 2006; Heitsch et al. 2006; Klessen and Hennebelle 2010). However, numerical simulations of the process have repeatedly shown that the Mach numbers produced in the clouds by this mechanism fall short of the values observed in MCs (Koyama and Inutsuka 2002; Heitsch et al. 2005; Vázquez-Semadeni et al. 2006). Furthermore, simulations including self-gravity show that the near-equipartition is only established once gravitational contraction has engaged in the clouds, while at earlier times the turbulent kinetic energy dominates over the gravitational energy (Vázquez-Semadeni et al. 2007; Colín et al. 2013).

In consequence, a return to the globally-collapsing scenario has been advocated by some authors, albeit with the novel feature that the collapse should be hierarchical and chaotic rather than monolithic (e.g., Burkert and Hartmann 2004; Vázquez-Semadeni et al. 2007; Peretto et al. 2007; Hartmann and Burkert 2007; Heitsch and Hartmann 2008; Heitsch et al. 2008; Vázquez-Semadeni et al. 2009; Galván-Madrid et al. 2009; Schneider et al. 2010; Ballesteros-Paredes et al. 2011b,a; Peretto et al. 2013). That is, the assembly of the clouds by the collision of streams of diffuse gas produces, via the thermal instability, large masses of cold gas that contain many Jeans masses. Also, the turbulence produced by the collision in turn produces nonlinear density fluctuations, which have shorter free-fall times than the average in the cloud (Heitsch and Hartmann 2008; Vázquez-Semadeni et al. 2009). Thus, the collapse occurs in a multi-scale fashion, with the collapse of the small-scale fluctuations preceding that of the whole cloud, as expected from linear theory.

Molecular clouds in this scenario are then in a hierarchical state of collapse, and their nonthermal motions are dominated by collapses within collapses, rather than by actual random turbulence. The latter rather applies to the large-scale ISM, in which the MCs constitute the sites of collapse. The MCs also contain turbulence, but it is relatively weak, and not coupled to the density or size scales, its only role being to provide the seeds for the hierarchical collapse, but not to provide any support against the collapse. The solution to the SFR conundrum of Zuckerman and Palmer (1974) is accomplished by early destruction of the clouds

by the stellar feedback, before more than  $\sim 10\%$  of their mass has been converted to stars (Vázquez-Semadeni et al. 2010; Dale et al. 2012; Zamora-Avilés et al. 2012; Colín et al. 2013; Zamora-Avilés and Vázquez-Semadeni 2014). We will refer to this as the “hierarchical gravitational collapse” scenario of MCs. At the time of this writing, the turbulent-support scenario is still the most frequently discussed one in the literature, although the hierarchical collapse model is also discussed, in particular for addressing evolutionary features of MCs Zamora-Avilés et al. (2012); Zamora-Avilés and Vázquez-Semadeni (2014).

On the basis of this changing picture of MCs we now describe the role that AD has played as a proposed solution to various features and properties of MCs, together with the alternative mechanisms that have been proposed for accomplishing the same results, thus hoping to provide the reader with a complete and unbiased view of the current status of the field.

### 7.3 The Formation and Collapse of Molecular Cloud Cores

As mentioned in Sec. 7.2, GMCs have typical average mass densities  $\rho \sim 4 \times 10^{19} \text{ kg m}^{-3}$  (molecule number densities  $\sim 100 \text{ cm}^{-3}$ ). Essentially all SF in The Galaxy occurs in the interiors of GMCs, although not throughout their volume, but rather only in their densest regions, called “dense cores”, with typical densities  $\rho \gtrsim 4 \times 10^{21} \text{ kg m}^{-3}$  (number densities  $n \gtrsim 10^4 \text{ cm}^{-3}$ ). The origin and collapse of the dense cores is therefore one of the key issues that needs to be accounted for by the various models for MCs.

#### 7.3.1 The standard model

In the magnetic support model, the fundamental underlying quantity was the ratio between the self-gravitational ( $W$ ) and the magnetic ( $E_m$ ) energies of a certain parcel of the fluid. Assuming, for simplicity, a spherical volume with a uniform density and magnetic fields inside, and neglecting them outside, we can write<sup>1</sup>

$$\frac{|W|}{E_m} = \frac{\eta GM^2 R^{-1}}{\frac{1}{8\pi} \int_V B^2 dV}, \quad (189)$$

where  $\eta = 3/5$  for the spherical, uniform region, but in general it is a factor of order unity accounting for the shape and mass distribution of volume  $V$ . For uniform density and magnetic fields, this then reduces to

$$\frac{|W|}{E_m} = \frac{6\eta GM^2}{R^4 B^2}. \quad (190)$$

Defining the magnetic flux across a cross-sectional area  $A$  across volume  $V$  as

$$\Phi \equiv \int_A \mathbf{B} \cdot \hat{n} dA, \quad (191)$$

---

<sup>1</sup> In this section, for consistency with the most frequent convention in the field, we use cgs units.

where  $\hat{n}$  is the unit vector perpendicular to  $d\mathbf{A}$ , eq. (190) becomes

$$\frac{|W|}{E_m} = \frac{6\pi^2\eta GM^2}{\Phi^2} \quad (192)$$

for our uniform, spherical gas cloud. When this ratio equals unity, the cloud is in balance between its self-gravity and the magnetic pressure gradient (with respect to the exterior), and so we define the “critical” value of the so-called mass-to-magnetic flux ratio as this equilibrium value:

$$\left(\frac{M}{\Phi}\right)_{\text{cr}} \equiv \frac{1}{\sqrt{6\pi^2\eta G}}. \quad (193)$$

In what follows, we denote the mass-to-flux ratio (M2FR), normalized to this critical value, by  $\mu$ .

An important property of the M2FR is that it does not depend on the size of the cloud, but only on its mass and magnetic flux. For Lagrangian fluid parcels (following the mass) and under ideal MHD conditions, this quantity is then invariant, in particular upon compressions, meaning that no amount of external compression may cause the self-gravity of the cloud to dominate over the magnetic support and induce its collapse if the cloud’s M2FR is smaller than the critical value ( $\mu < 1$ ). These clouds are termed *magnetically subcritical*. Conversely, clouds with  $\mu > 1$  cannot be supported against their self-gravity by the magnetic pressure alone. Such clouds are called *magnetically supercritical*. It is important to note that, in general, the energy balance must take into account that the magnetic support is at least partially counteracted by the surface magnetic term arising in the virial theorem (see the discussions in McKee and Zweibel 1992; Shu 1992; Vázquez-Semadeni 1999; Ballesteros-Paredes et al. 1999). In particular, for a uniform magnetic field, the surface term completely cancels the magnetic energy, and so some amount of gravitational contraction that increases the field strength inside the cloud is required before magnetic support can operate on a subcritical cloud, but eventually it will, halting the contraction.

In the magnetic-support model, then, clouds were assumed to be globally magnetically subcritical, and thus absolutely supported against their self-gravity as long as the ideal MHD regime is applicable. In order for *some* fraction of the mass to undergo gravitational collapse, in this model it is necessary for that material to lose magnetic support. This can be accomplished by ambipolar diffusion (AD), a process by which the neutrals, driven by self-gravity, drift away from the ions, effectively losing magnetic flux, which remains anchored on the ions. Eventually, the M2FR of this neutral mass may become larger than unity and proceed to dynamical collapse. We now revisit the standard single-fluid approximation of the process, closely following the discussion by Shu et al. (1987), which has been employed heavily in the description of MCs.

### 7.3.2 The single-fluid approximation for ambipolar diffusion

The main process that needs to be described is the drift between neutrals and ions in a partially ionized plasma. To do this, we consider the drag force between the two types of particles, given by

$$\mathbf{f}_d = \rho_n \rho_i \gamma (\mathbf{u}_i - \mathbf{u}_n), \quad (194)$$

where  $\rho_i$  and  $\rho_n$  are respectively the ion and neutral densities,  $\mathbf{u}_i$  and  $\mathbf{u}_n$  are their velocities, and  $\gamma$  is the drag coefficient (damping rate) associated with momentum exchange in ion-neutral collisions. When the collision process is dominated by the dipole moment induced in the neutral by the passing ion, this coefficient takes the value  $\gamma \approx 3.5 \times 10^{13} \text{ cm}^3 \text{ g}^{-1} \text{ s}^{-1}$  (Draine et al. 1983).

The ion-neutral drift is induced by the Lorentz force, and, at terminal drift velocity, the two forces balance. We thus have, for the drift velocity,

$$\mathbf{v}_d \equiv \mathbf{u}_i - \mathbf{u}_n = \frac{1}{4\pi\rho_n\rho_i\gamma} (\nabla \times \mathbf{B}) \times \mathbf{B}. \quad (195)$$

Now, for MC conditions, the cyclotron frequency  $eB/m_i c$  of the typical ion (an electron) is much greater than the collision frequency, and thus the magnetic field can be considered to be frozen in the ions, because they gyrate many times around the field lines before being knocked off by a collision. In this case, we have the field-freezing condition for the ions:

$$\frac{\partial \mathbf{B}}{\partial t} + \nabla \times (\mathbf{B} \times \mathbf{u}_i) = 0. \quad (196)$$

Substituting eq. (195) into eq. (196) we obtain

$$\frac{\partial \mathbf{B}}{\partial t} + \nabla \times (\mathbf{B} \times \mathbf{u}_n) = \nabla \times \left\{ \frac{\mathbf{B}}{4\pi\rho_n\rho_i\gamma} \times [\mathbf{B} \times (\nabla \times \mathbf{B})] \right\}. \quad (197)$$

Equation (197) has the dimensions of a diffusion equation, of the form

$$\frac{B}{\tau_{AD}} \sim \mathcal{D} \frac{B}{L^2}, \quad (198)$$

where  $\tau_{AD}$  is the characteristic AD timescale,  $L$  is the characteristic length scale of the system, and  $\mathcal{D}$  is the associated ‘‘diffusion coefficient’’. Comparing expression (198) with eq. (197), we see that

$$\mathcal{D} \sim v_A^2 t_{ni}, \quad (199)$$

where  $v_A = B/\sqrt{4\pi\rho_n}$  is the Alfvén speed in the medium (assuming  $\rho_n \gg \rho_i$ ) and

$$t_{ni} \equiv (\gamma\rho_i)^{-1} \quad (200)$$

is the mean collision time with an ion per neutral particle. On the other hand, for the AD timescale, from expression (198) we have

$$\tau_{AD} \sim L^2/\mathcal{D}. \quad (201)$$

It is interesting to compare the AD timescale with the dynamical time,  $\tau_{dyn}$ . For a magnetized medium in which the information-transmission speed is  $\sim v_A$ , we have  $\tau_{dyn} \sim L/v_A$ . In addition, if the medium is in approximate equilibrium between magnetic support and its self-gravity, then the dynamical time should also be of the order of the free-fall time, so that we also have  $\tau_{dyn} \sim (G\rho_n)^{-1/2}$ . Combining these relations, and noting that the ion and neutral densities are related to first order by

$$\rho_i \approx C\rho_n^{1/2}, \quad (202)$$

with  $C \approx 3 \times 10^{-16} \text{ cm}^{-3/2} \text{ g}^{1/2}$  Elmegreen (1979), we find

$$\frac{\tau_{\text{AD}}}{\tau_{\text{dyn}}} \sim \frac{\gamma C}{G^{1/2}} \approx 40. \quad (203)$$

This is only an order-of-magnitude estimate, but more precise calculations (e.g., Shu 1983) still give values  $\sim 10$  for the ratio  $\tau_{\text{AD}}/\tau_{\text{dyn}}$ , implying that AD operates on timescales much longer than the free-fall time. This, together with the fact that only the densest material could proceed to collapse, was the reason, in the magnetic-support model, for the low efficiency of star formation: low-mass star-forming clouds were believed to have subcritical M2FRs in general, and therefore, to be globally supported against collapse. Gravitational contraction would only proceed in the densest regions (cores) as allowed by AD on its characteristic timescale, and thus much more slowly than in free-fall, and involving only a small fraction of the total mass in the MCs. Massive-star-forming clouds, which were then thought to be exceptional, were believed to be the few instances of magnetically supercritical clouds, and undergoing unimpeded collapse.

### 7.3.3 Problems with the magnetic-support model

In recent years, it has come to be realized that there are several problems with the magnetic-support model. We now briefly discuss some of these caveats. A complementary discussion can be found in Mac Low and Klessen (2004).

### 7.3.4 Discrepancy with observed timescales

As discussed in Sec. 7.3.2 (cf. eq. [203]), the AD timescale was originally estimated to be at least one order of magnitude longer than the free-fall time of dense clumps. Since, in the magnetic-support model, this slow-contraction stage corresponded to the prestellar stage of a dense core, this implied that the typical duration of the “starless” stage of a contracting core should be much longer (roughly by one order of magnitude) than the duration of the proto-stellar stage (the stage where a collapsed object — a protostar — has already appeared). However, systematic surveys of dense cores (e.g., Lee and Myers 1999; Jijina et al. 1999) were able to estimate the ratio of the durations of these two stages by measuring the ratio of the number of starless to protostellar cores. The observed ratios turned out to be  $\sim 0.05$ – $0.67$ , indicating that the starless stage was actually *shorter* than the protostellar one, and shorter than the prediction from AD models by factors  $\sim 2$ – $50$  Lee and Myers (1999).

As a solution to this conundrum, Ciolek and Basu (2001) noted that the AD timescale becomes shorter as the initial M2FR of a core is closer to the critical value, so that the measurements of nearly critical values of the M2FR in dense cores would imply contraction times in the prestellar cores shorter by up to an order of magnitude than the “classical” AD timescale, bringing the revised AD timescale into agreement with the observed duration of the prestellar stage of the cores. Similarly, Fatuzzo and Adams (2002) considered the fluctuations in the AD timescale caused by local fluctuations of the magnetic and density fields, concluding that the “effective” AD timescale would be shortened by roughly the same factor.



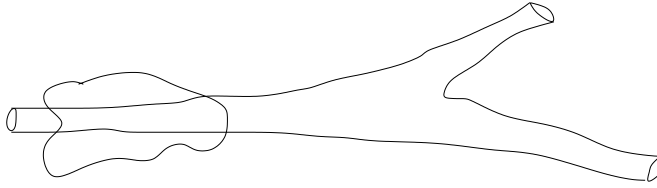


**Fig. 43** Schematic illustration of a flux tube that loses its identity far from a cloud.

However, since the revision to the AD timescale brings it close to the free-fall time, effectively no delay is introduced in the collapse timescale by the AD-mediated contraction, reducing the role of the magnetic field to providing support to the envelopes of the dense cores. But then, as discussed in Sec. 7.3.7, the current state of affairs is that subcritical dense cores are not observed, and in this case the envelopes are not supported by the magnetic field either.

### 7.3.5 The mass-to-flux ratio as a boundary condition

Another important problem is that, due to the condition  $\nabla \cdot \mathbf{B} = 0$ , magnetic field lines do not end, and, as a consequence, flux tubes in general extend indefinitely beyond the boundaries of any cloud that may have been defined by some ad hoc criterion, such as, for example, being detected with a certain tracer, or, in numerical simulations, as a connected region above some density threshold. In fact, the mean magnetic field in the Galactic plane is roughly azimuthal (e.g., Han 2013; Beck 2015), and therefore flux tubes might in principle extend for hundreds or thousands of parsecs. In reality, flux tubes may lose their identities as the field lines that define them drift apart from each other, as schematically illustrated in Fig. 43. Nevertheless, it is in general possible in principle to consider a segment along a flux tube that is long enough to be magnetically supercritical. This critical length is known as the *accumulation length* (see, e.g., Mestel 1985; Hartmann et al. 2001; Vázquez-Semadeni et al. 2011). The mass-to-flux ratio of a system then becomes a boundary condition; that is, it is determined by the size of the system boundaries relative to the accumulation length.

In early studies of AD-mediated core contraction (e.g., Mouschovias 1976), the core was often assumed to be bounded by a warm, tenuous phase that isolated the core and did not contribute to the gravitational potential. Thus, the M2FR was well defined. However, in recent years it has become clear that MCs and their substructures may be accreting in general—the MCs may be accreting from their atomic envelopes (e.g., Hennebelle and Pérault 1999; Ballesteros-Paredes et al. 1999; Audit and Hennebelle 2005, 2010; Heitsch et al. 2005; Heitsch and Hartmann 2008; Vázquez-Semadeni et al. 2006, 2007, 2011; Myers 2009; Molinari et al. 2014; Heiner et al. 2015), while the cores accrete from the filamentary structures in which they are embedded (e.g., Myers 2009; Schneider et al. 2010; Kirk et al. 2013; Peretto et al. 2013; Battersby et al. 2014; Gómez and Vázquez-Semadeni 2014). This makes it impossible to uniquely define “the core”.

In an attempt to resolve this ambiguity, Vázquez-Semadeni et al. (2011) noted that the relevant mass for evaluating a physically meaningful mass-to-flux ratio is the mass that dominates the gravitational potential; that is, the mass in the

densest component, which is increasing due to accretion. For magnetized structures accreting along field lines, the M2FR is increasing with time, not because of AD, but through accumulation along field lines, driven either by large-scale inertial compressions (i.e., larger-scale turbulence) or larger-scale gravitational instabilities in the surroundings of the compact object under consideration.

On the other hand, it should be noted that the notion of accumulation along field lines has been questioned by a number of authors, on the basis that the accumulation lengths necessary for producing magnetically supercritical molecular clouds are too long (on the order of hundreds of parsecs; see, e.g., Hartmann et al. 2001; Vázquez-Semadeni et al. 2011), and so turbulent reconnection diffusion would interfere with the accumulation process (Lazarian 2014), or simply the flows would not have remained coherent over such lengths (e.g., Körtgen and Banerjee 2015). However, these arguments may have overlooked the fact that the flows may orient the magnetic field lines rather than the other way around (e.g., Hennebelle and Pérault 2000; Han 2013) and that converging flows on the scales of kiloparsecs are likely to be set up in spiral arms. In any case, numerical simulations designed to test the feasibility of the accumulation mechanism on the several-kpc scale are necessary.

### 7.3.6 The gradient of mass-to-flux ratio in dense cores

The assembly of dense structures by accumulation of material implies another important difference with the magnetic-support model. In the latter, the redistribution of magnetic flux due to AD implies that the central, densest parts of the cores are those that have already lost part of their magnetic flux to the envelope, and thus are expected to have a *larger* value of  $\mu$  than the average in their parent cloud,  $\mu_0$ . Instead, if the dense structures are assembled by means of partial compression (i.e., accumulation from distant regions along field lines), with no action of AD, the central parts are expected to have a *lower* value of  $\mu$  than the cloud's average. Specifically, the M2FR of a subregion of size  $\ell$  of a cloud of size  $R$  and mean M2FR  $\mu_0$  is expected to lie in the range

$$\mu_0 \frac{\ell}{L} \leq \mu_\ell \leq \mu_0 \quad (204)$$

(Vázquez-Semadeni et al. 2005). This range can be understood as follows: the lower limit applies for the case when the “core” is actually simply a subregion of the whole cloud of size  $L$ , with the same density and magnetic field strength. Since the density and field strength are the same, the mass of the core simply scales as  $(\ell/L)^3$ , while the magnetic flux scales as  $(\ell/L)^2$ . Therefore, the MFR of a subregion of size  $\ell$  scales as  $(\ell/L)$ . Of course, this lower-limit extreme, corresponding to the case of a “core” of the same density and field strength as the whole cloud, is an idealization, since observationally such a structure cannot be distinguished from its parent cloud. Nevertheless, as soon as some compression has taken place, the core will be observationally distinguishable from the cloud (for example, by using a tracer that is only excited at the core's density), and the measurement of the MFR *in the core* will be bounded from below by this limit.

On the other hand, the upper limit corresponds simply to the case where the entire cloud of size  $L$  has been compressed isotropically to a size  $\ell$ , since in this

case both the mass and the magnetic flux are conserved, and so is the MFR. Any intermediate case has an intermediate value of the M2FR given by relation (204).

The ratio of the central-to-envelope M2FR for four cores was measured by (Crutcher et al. 2009), and found to be  $< 1$ , although the uncertainties were large, and the result was challenged by (Mouschovias and Tassis 2010). Nevertheless, a subsequent Bayesian study by (Crutcher et al. 2010) seemed to confirm the result, suggesting that the accumulation scenario for cores may indeed be at work in those cores. These results suggest that the M2FR gradient in dense cores and their envelopes is at least partially due to mass accumulation by turbulent or gravitational compression and fragmentation, and not due to the action of AD (at least in the early stages of the process).

### 7.3.7 The observed lack of magnetically subcritical molecular clouds and cores

Another reason why the magnetic-support model has lost predominance in recent years is that detailed statistical analyses of the magnetic field strengths in clouds and cores, derived from Zeeman observations (Crutcher et al. 2010; Crutcher 2012), have shown that a) for densities  $n \gtrsim 300 \text{ cm}^{-3}$ ,  $B$  scales as  $\sim n^{0.65}$ , in good agreement with models of clouds with magnetic fields too weak to support them, so that they are contracting gravitationally, and dragging the field along with them because of flux freezing. b) There are almost no observations of clouds and/or cores that are clearly magnetically subcritical, suggesting that the clouds start out being already supercritical.

In addition, today we understand that most stars, in particular low-mass stars, form in clusters together with the high-mass stars Lada and Lada (2003). This is in contradiction with the magnetic-support scenario, because there it was postulated that star formation is bimodal, with low-mass stars forming in magnetically subcritical clouds, and massive stars and clusters forming in supercritical clouds. The current evidence suggests instead that most low-mass stars form in the same environment as massive stars and clusters, i.e., in supercritical clouds, negating the bimodal picture of the magnetic-support scenario.

## 7.4 (De)correlation between magnetic and density fields

In a supersonic, turbulent MHD flow, such as that generally assumed to permeate MCs, magnetic fluctuations as well as density and velocity fluctuations are present. Since the field may be capable of providing support against the self-gravity of the density fluctuations, it is important to determine the correlation (if any) between the density and the magnetic fluctuations induced by the turbulence. This problem was first investigated by several numerical studies (Passot et al. 1995; Padoan and Nordlund 1999; Ostriker et al. 1999, 2001). In general, it was found that the magnetic field exhibited a *range* of values at a given density, with indications that, at low densities, the magnetic field tended to approach a constant, minimum value, while at large densities, it tended to increase with increasing density. Moreover, the distribution of points in the  $B$ - $n$  diagram was seen to have a large scatter, so that a full range of values of the field strength was observed at every value of the density (Fig. 44, left panel). This result is consistent with the observed  $B$ - $n$

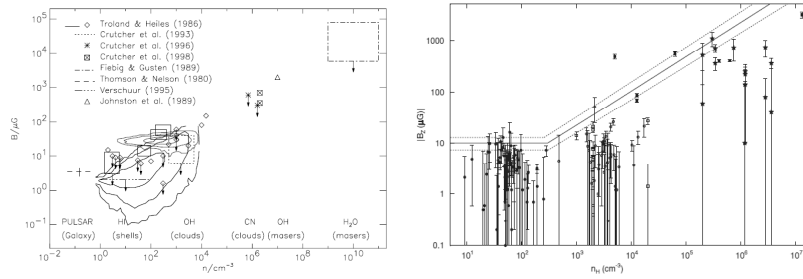


**Fig. 44** *Left Panel:*  $B$ - $n$  correlation in a numerical simulation of super-Alfvénic turbulence and in several observational surveys (from Padoan and Nordlund 1999). *Right panel:* Summary of Zeeman determinations of the magnetic field strength *versus* density  $n$ , as compiled by Crutcher et al. (2010).

correlation from Zeeman splitting in the diffuse atomic medium and molecular gas, as reported, for example, by (Crutcher et al. 2010) (Fig. 44, *right panel*).

Several mechanisms have been proposed to explain this behavior. Heitsch et al. (2004) suggested that turbulence enhances the diffusion of the ratio  $B/\rho$  through an enhancement of ion-neutral drift at small scales, referring to this mechanism as *turbulent ambipolar diffusion*. More recently, (Lazarian et al. 2012, see also the review by Lazarian (2014)) have proposed that the decorrelation between the magnetic and density fields at low densities, as well as the absence of magnetically subcritical dense cores, is due to *turbulent reconnection diffusion*, a process consisting in the enhancement of magnetic dissipation by the enhanced turbulent dissipation (reconnection) induced by turbulence, which brings magnetic field lines in close contact, fostering reconnection and thus dissipating magnetic energy at sites of high densities. It is important to emphasize that turbulent reconnection implies actual dissipation of magnetic energy through Ohmic resistivity, while turbulent ambipolar diffusion implies only a spatial redistribution of the magnetic flux within the core, without actually dissipating magnetic energy. This happens because, as the neutrals percolate through the ions, mass drifts towards the core’s center without dragging the flux with it. Thus, effectively the magnetic flux drifts outward of the core.

Both of the mechanisms proposed above are based on some form of diffusion of the magnetic flux. It is important to remark, however, that it is *not* necessary to have some form of diffusion in order to accomplish a decorrelation of the magnetic and the density fields. In fact, it is common to encounter the erroneous notion that under ideal MHD conditions the magnetic field should be correlated with density. However, this is by no means so, and a lack of correlation is expected in the ideal MHD case as well, because of the possibility of free flow along field lines. This was shown by (Passot and Vázquez-Semadeni 2003, hereafter PV03), who investigated this problem analytically in the isothermal case, by decomposing the flow into nonlinear, so-called “simple” waves (e.g., Landau and Lifshitz 1959; Mann 1995), which are the nonlinear extensions of the well known linear MHD waves, and have the same three well-known modes: fast, slow, and Alfvén.

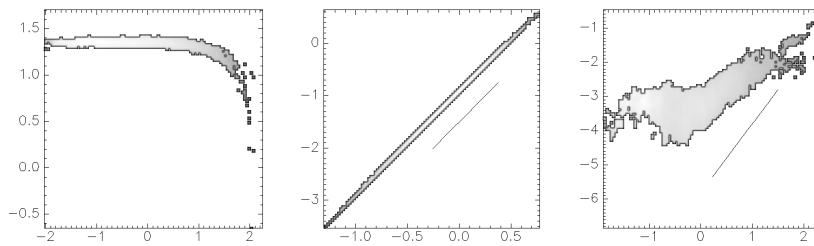


**Fig. 45** Two-dimensional histograms of the grid cells in numerical simulations in the  $\ln B^2$  (vertical axis)- $\ln \rho$  (horizontal axis) space. The gray scale indicates the density of points in this space. *Left panel:* A slab-geometry numerical simulation by PV03 dominated by the slow mode, exhibiting the behavior indicated by eq. (205). *Middle panel:* Same as the *left* panel, but for a numerical simulation dominated by the fast mode, exhibiting the behavior indicated by eq. (206). *Right panel:* Two-dimensional histogram of the grid cells in the  $\ln B^2$ - $\ln n$  space from a numerical simulation by PV03 in which both the slow and the fast modes are active. At low densities, the slow mode causes a density-independent magnetic field strength, while at higher densities, the fast mode produces a positive correlation. The straight-line segment has a slope of 2.

For illustrative purposes, note that compressions along the magnetic field lines are one instance of the *slow* mode, while compressions perpendicular to the field lines (i.e., *magnetosonic* waves) are an instance of the *fast* mode.

PV03 concluded that each of the modes is characterized by a different scaling between the magnetic pressure ( $\propto B^2$ ) and the density, as follows:

$$B^2 \propto c_1 - \beta\rho \quad \text{slow,} \quad (205)$$

$$B^2 \propto \rho^2 \quad \text{fast,} \quad (206)$$

$$B^2 \propto \rho^{\gamma_m} \quad \text{Alfvén,} \quad (207)$$

where  $c_1 > 0$  is a constant, and  $\gamma_m$  is a parameter that can take values in the range (1/2,2) depending on the Alfvénic Mach number (see also McKee and Zweibel 1995). Note that eq. (205) implies that for  $\rho > c_1/\beta$  the slow mode disappears (Mann 1995), so that only the fast and Alfvén modes remain. Conversely, note that, at low density, the magnetic pressure due to the fast and Alfvén modes becomes negligible in comparison with that due to the slow mode, which approaches a constant. This implies that a log-log plot of  $B$  vs.  $\rho$  will exhibit an essentially constant value of  $B$  at very small values of the density. In other words, *at low values of the density, the domination of the slow mode implies that the magnetic field exhibits essentially no correlation with the density.*

PV03 also tested these results numerically, by isolating, or nearly isolating, the three different wave modes. The *left* panel of Fig. 45 shows the distribution of points in the  $\ln B^2$ - $\ln \rho$  space for a simulation dominated by the slow mode, exhibiting the behavior outlined above, corresponding to eq. (205). In contrast, the *middle* panel of Fig. 45 shows the distribution of points in the same space for a simulation dominated by the fast mode, exhibiting the behavior indicated by eq. (206). Finally, the *right* panel of this figure shows a simulation where both modes are active.

The most important conclusion from eqs. (205)–(207) is that, in a turbulent flow in which all modes are active, the net, average scaling of the magnetic field with the density will arise from the combined effect of the various modes. Moreover, since at low densities the values of  $B$  produced by the fast and Alfvén modes are also small, while the field strengths produced by the slow mode remain roughly constant, the field fluctuations will be dominated by the latter mode at low densities, and a roughly density-independent field strength is expected. Conversely, at high densities, the slow mode disappears, while the contribution from the fast and Alfvén modes will dominate, producing a field strength that increases with increasing density. Finally, because each mode produces a different dependence of the magnetic field strength with the density, we expect that the instantaneous value of the density at a certain location in physical space is not enough to determine the value of the magnetic field strength there. Instead, this value depends on the *history of modes* of the nonlinear waves that have passed through that location, naturally implying that, within a large cloud, a large scatter in the measured values of the magnetic field is expected. The expected net scaling of the field strength with the density is illustrated in the *right panel* of Fig. 45. These results are in qualitative agreement with detailed statistical analyses of the magnetic field distribution in the ISM (Crutcher et al. 2010), as illustrated in the *right panel* of Fig. 44.

In conclusion, the observed constancy of the mean magnetic field strength at low densities may be due to either the superposition of the various modes of nonlinear MHD waves in the turbulent ISM, and/or to the diffusion of magnetic flux by AD, and/or to the dissipation of the magnetic energy by turbulent reconnection. Certainly, there is no shortage of available mechanisms for producing it!

## 7.5 Density profiles of filaments in MCs

More recently, AD has been invoked to explain the radial density profiles of filamentary structures in MCs. In recent years, observations with the *Herschel* Space Observatory have revealed that the denser regions of MCs are characterized by having a strongly filamentary structure, and that the filaments host most of the dense cores in MCs (e.g. André et al. 2010; Molinari et al. 2010). Since then, molecular-line observations have additionally provided information on the kinematic structure of the filaments (e.g., Schneider et al. 2010; Kirk et al. 2013; Peretto et al. 2013; Battersby et al. 2014), suggesting that there is flow *onto* the filaments, mainly perpendicular to their axes, from their surroundings, as well as flow *along* the filaments, onto the cores they contain.

One important feature of the filaments is their radial column density structure, which, when averaged along the length of the filaments, exhibits a Plummer-like profile of the form Arzoumanian et al. (2011)

$$\Sigma_P(R) = \frac{A_p \rho_c R_c}{\left[1 + (R/R_c)^2\right]^{\frac{(p-1)}{2}}}, \quad (208)$$

where  $R$  is the distance perpendicular to the filament's long axis,  $p$  is the (negative) logarithmic slope of the volume density profile at large  $R$ , and  $A_p = \int_{-\infty}^{\infty} (1 + u^2)^{-p/2} du$ . Also, Arzoumanian et al. (2011) found that the filaments are well

fitted for values of  $p$  in the range  $1.5 < p < 2.5$ , and a characteristic Gaussian full width at half maximum (FWHM) of 0.1 pc, which corresponds to  $R_c \approx 0.03$  pc, roughly independently of the central column density. Therefore, those authors suggested that this width is probably a universal property of MC filaments.

The value of the slope,  $p \sim 2$ , is significantly different from that expected for a self-gravitating, isothermal, hydrostatic cylinder extending to infinity, but with finite linear density (mass per unit length), for which the theoretically predicted value is  $p = 4$  Ostriker (1964). This value of the slope, and the near-independence of the characteristic width with the central column density of the filaments, have prompted the production of several analytical models. In particular, it has been found by Fischera and Martin (2012) that truncated hydrostatic equilibrium solutions, subjected to a finite, external pressure, change slope as the external pressure is varied. Specifically, they found that the slope is  $\sim 2$  when the ratio of the central to the external pressure is  $\sim 10$ . On the other hand, Heitsch (2013) has taken into account the possibility of accretion onto the filaments and considered magnetized cases (see also Fiege and Pudritz 2000), finding that accreting models produce profile slopes consistent with observations only in the case of low-mass filaments, or when the magnetic field scales weakly with density, for example, as  $B \propto n^{1/2}$ .

More directly related to the subject of this chapter, Hennebelle and André (2013) have proposed that the near column density independence of the central width may be a result of the central region being in virial equilibrium, so that the turbulence in that region (driven by accretion onto the filament) exerts a pressure that balances the ram-pressure exerted by the accretion. Since in this case the rate at which the internal turbulence dissipates is crucial for determining the stationary turbulent Mach number, they tested two different timescales of dissipation: the standard turbulent cascade timescale, given simply by the turbulent crossing time across scale  $\ell$ ,  $\tau_{\text{turb}} = \ell/\sigma_\ell$ , where  $\sigma_\ell$  is the turbulent velocity dispersion at scale  $\ell$ , and the AD dissipation timescale of Alfvén waves, given by Kulsrud and Pearce (1969)

$$\tau_{\text{d,AD}} = \frac{2\gamma\rho_i}{v_A^2(2\pi/\lambda)^2}, \quad (209)$$

where  $\gamma$  is the damping rate introduced in eq. (194),  $\rho_i$  is the ion density, given by eq. (202),  $v_A$  is the Alfvén speed, and  $\lambda$  is the wavelength, assumed to be of the order of the radius of the filament, which is the relevant scale at which energy dissipation is considered. These authors find that the filament's radius  $r_f$  depends on the central density  $\rho_c$  as  $r_f \sim \rho_c^{-1}$  in the case of the standard turbulent dissipation, while, for dissipation dominated by AD, they find  $r_f \sim \rho_c^{-0.2}$ . Thus, they conclude that dissipation due to AD allows a weak enough dependence of the central width on the density as to be in agreement with the observed near constancy of the central width in MC filaments.

However, it should be pointed out that molecular-line studies of filaments often do not recover the same characteristic width as the Herschel observations, showing instead a large scatter of values (e.g., Panopoulou et al. 2014), or much larger widths (e.g., Furuya et al. 2014), suggesting that the 0.1-pc characteristic width of the Herschel data may result from a bias introduced by the analysis procedure Heitsch (2013).

Moreover, numerical simulations not including magnetic fields nor AD (e.g., Gómez and Vázquez-Semadeni 2014; Federrath 2015), as well as simulations including the magnetic field but not AD (e.g., Federrath 2015; Kirk et al. 2015),

also exhibit widths close to the observed values. In particular, Federrath (2015) has interpreted the the width of the filaments as a manifestation of the turbulent “sonic scale”, the scale at which the turbulent velocity dispersion coincides with the sound speed. In addition, he also interpreted the radial density profile as a consequence of the scaling of the post-shock density with the post-shock thickness in the collision of two planar shocks, thus providing an AD-unrelated interpretation of the filament nealy-constant thickness.

One can conclude from the above discussion that there exist several possible explanations for the radial column density structure of MC filaments, with AD being just one of them, but at this point it has not been conclusively determined which mechanism is mainly responsible for it.

## 7.6 Avoiding the magnetic braking catastrophe

During the collapse of a region of a MC, conservation of angular momentum would seem to imply the existence of a strong “angular momentum problem”, which has been known for a long time Hoyle (1945), and according to which, the increase in any initial rotation rate present in the cloud would generate such strong centrifugal forces that the cloud would be disrupted and produce fragments with masses too small compared to actual stellar masses. This is, however, contrary to the observation that the specific angular momentum of cloud substructures seems to decrease with their size (see, e.g., Bodenheimer 1995, and references therein). This implies that, somehow, angular momentum must be transferred outward from the collapsing material during the collapse and fragmentation of a cloud.

One possible mechanism to avoid the angular momentum problem is the so-called “magnetic braking” Mouschovias (1977), by which a rotating protostar permeated by a magnetic field would drag the field lines, causing them to rotate at the same angular velocity, and thus accelerating material outwards, transferring the angular momentum to large radii from the protostar. However, numerical as well as analytical simulations have shown that this effect is too strong under ideal MHD conditions Krasnopolsky and Königl (2002); Allen et al. (2003); Galli et al. (2006), causing a “catastrophic” magnetic braking, which removes too much angular momentum from the protostellar disk. This results in the formation of a “pseudo-disk” which, in spite of having a flattened geometry (because of contraction preferentially along field lines), does not have a Keplerian rotation regime, and so it is not rotationally supported. This is in contradiction with the Keplerian regime often observed in protostellar disks (see, e.g., Mundy et al. 2000, and references therein), although the question of whether this regime is the norm or not is far from settled (see, e.g., the review by Li et al. 2014).

This problem persists even under the presently accepted weaker typical values of the magnetic field strength in MCs and their cores (cf. Sec. 7.3.7), according to which the typical core has a normalized M2FR  $\mu \sim$  a few. This implies that, although the field is not strong enough to prevent collapse of the cores, it is in general still strong enough to cause catastrophic magnetic braking in the ideal MHD regime (e.g., Li et al. 2011).

AD, as well as Ohmic dissipation and the Hall effect, have been proposed as mechanisms capable of preventing catastrophic magnetic braking in the cores, with Ohmic dissipation being the best candidate so far because it really reduces



the magnetic flux, while AD seems to only redistribute it, allowing it to pile up in a small circumstellar region where magnetic braking is still too strong (Dapp and Basu 2010; Li et al. 2011; Dapp et al. 2012, see also the review by Li et al. (2014)).

However, other resolutions have been proposed for the magnetizing braking catastrophe, involving turbulence, either by itself Seifried et al. (2012), or in conjunction with turbulent reconnection Santos-Lima et al. (2012). The former study suggested that the whole magnetic braking catastrophe arises from an unrealistic choice of initial conditions, which neglected the presence of turbulent motions, and presented simulations of gravitational collapse of magnetized cores in which rotationally supported disks readily form. Those authors argued that the formation of Keplerian disks in this case is due to the absence of coherent rotational motions at different scales together with the transport of angular momentum by shearing turbulent motions. This is in qualitative agreement with the result by Jappsen and Klessen (2004) that the specific angular momentum in nonmagnetic turbulence simulations decreases with size, in agreement with observations, in spite of not allowing for magnetic braking. These authors attributed this result to gravitational torques, but it is quite likely that hydrodynamic torques are at play as well. In addition to this, Santos-Lima et al. (2012) also considered turbulent reconnection, pointing out that dissipation of magnetic energy by reconnection is greatly enhanced in the presence of turbulence, allowing magnetic flux to be transported to the outskirts of the disk on timescales comparable to the collapse, and thus the formation of a rotationally supported disk of dimensions up to  $\sim 100$  pc.

## 7.7 Conclusions

In this chapter we have reviewed several applications of AD in the ISM and star formation, from the correlation of the magnetic field with the gas density, through the formation of dense cores and their subsequent gravitational collapse, to the formation of rotationally supported accretion disks around protostars. In each case, we also discussed alternative mechanisms that have been proposed to accomplish the same effects without resorting to AD.

To place the discussion in context, we started with a brief historical recount of how star formation models have evolved in the last 40 years or so, emphasizing the diminishing role played by the magnetic field in the process, as recent observations suggest that MCs and their cores are in general magnetically supercritical. This implies that the field is not strong enough to support the cores against collapse, although the typical values suggest it is still strong enough to cause catastrophic magnetic braking in the ideal MHD regime. In the absence of magnetic support, current theories consider that MCs are either supported by turbulent pressure, or else that they are undergoing global, hierarchical collapse. In the latter case, the role of turbulence is reduced to producing density fluctuations that can collapse earlier than the whole cloud.

We next reviewed the standard single-fluid formulation for AD, introducing its characteristic diffusivity and timescale, and then proceeded to the applications. First was the “standard” model of magnetic support and AD-mediated collapse of dense cores in MCs, presenting the standard results, and then noting the objections to this model. One very important problem is the fact that the M2FR of a cloud

is a rather subjective and ill-defined quantity, depending strongly on the choice of boundary conditions, and becoming a variable of the problem when accretion is considered. Under these considerations, and with the revised values of the M2FR in cores, the effective AD timescale becomes of the order of the free-fall time, and thus the role of AD is significantly weakened.

The second application is the observed lack of correlation of the magnetic field strength with the gas density at low densities ( $n \lesssim 100 \text{ cm}^{-3}$ ). This has been attributed to the diffusion of the magnetic flux caused by turbulent AD and/or reconnection, although it has also been suggested that it may be a consequence of the different scaling of the magnetic field with the density for different modes of MHD waves.

A third application is the possibility that AD may set the observed near-universal width of the filamentary structures in MCs. The specific suggestion is that this width is controlled by a balance between the ram pressure exerted on the filament by material accreting onto it (perpendicularly to its axis) and the pressure from the turbulence driven by the accretion itself in the central parts of the filament. For this balance to produce filament widths consistent with observations, the dissipation of the turbulence should be dominated by AD. However, other mechanisms not involving AD have also been proposed, and nonmagnetic simulations (where dissipation cannot be dominated by AD) exhibit similar widths, so there is no conclusive evidence that AD-dominated turbulence dissipation is the controlling mechanism of the filaments' width.

Finally, we discussed the magnetic braking catastrophe, which consists of excessive removal of angular momentum during core collapse, which prevents the formation of rotationally-supported Keplerian disks in the ideal MHD regime. AD diffusion has been proposed as a possible mechanism to remove magnetic flux from the forming disk, allowing the retention of sufficient angular momentum, but numerical simulations suggest that in general the effect is not sufficient for the task, and it is currently accepted that Ohmic dissipation is a better candidate. However, it has also been proposed that the "catastrophe" rather arises from the choice of unrealistically smooth non-turbulent initial conditions, and numerical simulations with turbulent initial conditions seem to be able to readily form Keplerian disks. This would be due to the nonlinear exchange of angular momentum between fluid parcels in this regime.

It can be concluded that AD has seen a large number of intended applications in various important aspects of the ISM and star formation, but in all cases, there exist alternative possible mechanisms that do not rely on AD to accomplish the same tasks. The remaining challenge lies in being able to discern between the various candidate mechanisms and find the truly dominant mechanism in each case.

## 8 Exoplanets

### 8.1 Introduction

The study of planets beyond the Solar system, exoplanets, is one of the fastest growing fields in present day space science. On one hand, it is driven by the continuously growing number of discovered exoplanets and the goal to find a potentially habitable world similar to our Earth. On the other hand, the specific physical conditions expected on many exoplanets, untypical for the relatively well investigated Solar system planets, inspire researches to investigate them deeply for better understanding their nature. Almost two decades after the discovery of 51 Peg b, the first Jupiter-type gas giant outside our solar system, more than 3000 exoplanets, including about 600 multiple systems, have been detected mainly by space- and ground-based photometric transit surveys ( $\sim 2600$ ) and ground-based radial velocity ( $\sim 600$ ) measurements (<http://exoplanetarchive.ipac.caltech.edu/>; <http://exoplanet.eu/catalog/>). In addition, about  $> 2500$  "planet candidates" have been found by the Kepler mission (Batalha et al. 2013; Vanderburg et al. 2015). The constantly growing number of discovered exoplanets and accumulation of data regarding their physical and orbital characteristics provide an empirical background for more detailed investigation of general principles and major trends in formation and evolution of the planetary systems, including the potential habitability aspect of the terrestrial-type planets.

Although most of the exoplanets discovered so far are thought to be gas or ice giants, like Jupiter or Neptune, some potentially rocky planets have been identified around M stars (Bonfils et al. 2013). The discovery of these planets became possible due to several international ground-based transit search projects, as well as the *COROT* and *Kepler* space observatories. More than a half of known exoplanets have orbits around their host stars shorter than 0.6 AU (Figure 46). By this,

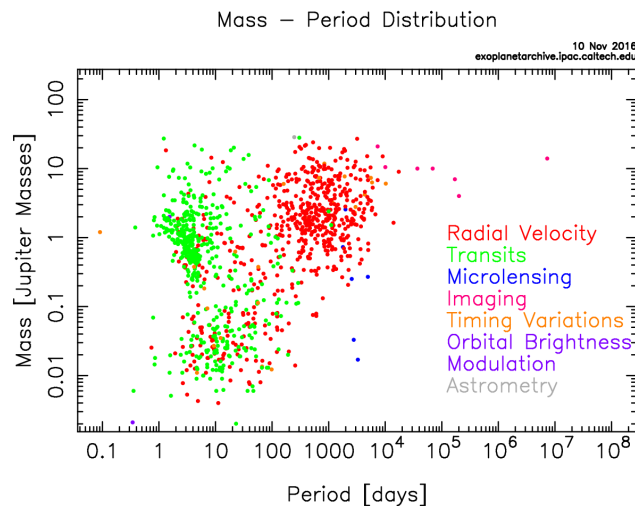


**Fig. 46** Mass-Orbital period distribution of confirmed exoplanets (<http://exoplanetarchive.ipac.caltech.edu/exoplanetplots/>)

an evident maximum in the orbital distribution of exoplanets takes place in the vicinity of 0.05 AU, with two well pronounced major populations there with orbital periods  $P < 30$  days corresponding to the giant type planets ( $0.2M_J < M_p < 8M_J$ ), so called *Hot Jupiters* (HJs), and less massive ( $0.008M_J < M_p < 0.08M_J$ ), *Neptune-* and *super-Earth* type planets. Here  $M_J$  stays for the mass of Jupiter. Altogether the HJs constitute about 16% of the total number of known exoplanets.

The detection of exoplanets at orbital distances  $\leq 0.05$  AU rises questions regarding their upper atmosphere structure, the planet interaction with the extreme stellar radiation and plasma environment (Yelle 2004; Holmström et al. 2008; Ekenbäck et al. 2010; Kislyakova et al. 2013, 2014), the role of possible magnetospheres for atmospheric protection (Khodachenko et al. 2007a,b, 2012), destructive tidal forces between the host star and the planet (Koskinen et al. 2010, 2013; Trammell et al. 2011, 2014), as well as the stability of atmospheres against different erosion and mass loss processes (Guillot et al. 1996). The study of close-orbit exoplanets and their survival in hard stellar radiation and plasma conditions also helps to understand how terrestrial planets and their atmospheres, including early Venus, Earth and Mars evolved during the active early evolution phase of their host stars.

Lammer et al. (2003) were the first to show that a hydrogen-rich thermosphere of a HJ at close orbital distance will be heated to several thousand Kelvin such that hydrostatic conditions will no longer be valid and the thermosphere will dynamically expand (Lammer et al. 2013). The stellar X-ray/EUV (XUV) radiation energy deposition results in heating, ionization, and consequent expansion of atmospheres of the close-orbit exoplanets. These appear the major driving factors for the mass loss of a planet (Lammer et al. 2003; Yelle 2004; Erkaev et al. 2005; Tian et al. 2005; García Muñoz 2007; Penz et al. 2008; Guo 2011, 2013; Koskinen et al. 2010, 2013; Lammer et al. 2013). Applied hydrodynamic (HD) models by Yelle (2004), Tian et al. (2005), García Muñoz (2007), Penz et al. (2008), Guo (2011), Guo (2013), Shaikhislamov et al. (2014), and Khodachenko et al. (2015) as well as the quasi-empirical modeling by Koskinen et al. (2010), also indicate that close-in exoplanets experience extreme heating by stellar XUV radiation, which results in an expanding supersonic planetary wind up to Roche lobe with mass loss rates  $\sim 10^7 - 10^8 \text{ kg}\cdot\text{s}^{-1}$ . Such loss rates are also supported by *Hubble Space Telescope* (*HST*)/Space Telescope Imaging Spectrograph (STIS) observations (Vidal-Madjar et al. 2003, 2004), which detected a  $15\% \pm 4\%$  intensity drop in the high-velocity part of the stellar  $\text{Ly}\alpha$  line during the planet (HD 209458b) transit, which was interpreted as a signature of hot neutral hydrogen atoms in the expanding planetary atmosphere.

The problem of upper atmospheric erosion of close-orbit exoplanets and their mass loss is closely connected with the study of the whole complex of stellar-planetary interactions, including consideration of the influences of intensive stellar radiation and plasma flows (e.g., stellar winds and coronal mass ejections) on the planetary plasma and atmosphere environments. The following processes have to be considered in that respect in their mutual relation and influence.

1. The heating of the planetary upper atmosphere by the stellar XUV radiation results in its expansion, which under certain conditions could be so large that the majority of light atmospheric constituents overcome the gravitational binding and escape from the planet in the form of a HD wind (Yelle 2004;

- Tian et al. 2005; Koskinen et al. 2010, 2013; Erkaev et al. 2013; Shaikhislamov et al. 2014). This contributes to the so-called *thermal* mass loss process of atmospheric material.
2. Simultaneously with the direct radiative heating of the upper atmosphere, the processes of ionization and recombination as well as production of energetic neutral atoms by sputtering and various photochemical and charge exchange reactions take place (Yelle 2004; Lammer et al. 2009, 2013; Shematovich 2012; Guo 2011, 2013). Such processes result in the formation of extended (in some cases) coronas around planets, filled with hot neutral atoms.
  3. The expanding, XUV-heated and photochemically energized, upper planetary atmosphere and the hot neutral corona may appear in a direct contact with the plasma flow of stellar wind and/or coronal mass ejections with the consequent loss due to an ion pickup mechanism. That contributes to the *non-thermal* mass loss process of the atmosphere (Lichtenegger et al. 2009; Khodachenko et al. 2007b; Kislyakova et al. 2013, 2014).

## 8.2 Magnetospheric protection of close-orbit exoplanets

The planetary intrinsic magnetic field appears a crucial factor that influences both, *thermal* and *non-thermal* types of the mass loss of close-orbit exoplanets and protects the planetary upper atmospheric environment. The protective role of planetary magnetic field has two major aspects. First, the large-scale magnetic fields and electric currents, related to the planetary magnetism, form the planetary magnetosphere, which acts as a barrier for the upcoming stellar wind. Magnetosphere protects the ionosphere and upper atmosphere of a planet against direct impact of stellar plasmas and energetic particles, thus reducing the *non-thermal* mass loss (Khodachenko et al. 2007a,b; Lammer et al. 2007). Second, the internal magnetic field of the planetary magnetosphere strongly affects the *thermal* mass loss by influencing the streaming of the expanding planetary wind plasma and its interaction with the stellar wind (Adams 2011; Trammell et al. 2011, 2014; Owen and Adams 2014; Khodachenko et al. 2015). Therefore, the processes of material escape, planetary mass loss, and formation of the planetary magnetosphere have to be considered jointly in a self-consistent way in their mutual interconnection. The expanding partially ionized plasma of the planetary wind interacts with intrinsic magnetic dipole field and appears a strong driver in formation and shaping of exoplanetary magnetosphere, which in its turn influences the overall mass loss of a planet.

### 8.2.1 Planetary magnetism

The intrinsic magnetic field of a planet, which influences the character of the magnetospheric obstacle, as well as the dynamics of the inner magnetospheric plasma, is generated by a magnetic dynamo. The existence and efficiency of the dynamo are closely related to the type of planet and its interior structure. Not all planets have intrinsic magnetic fields, or in other words, – the efficiently operating dynamos. Planetary magnetic dynamo requires the presence of an electrically conducting region (i.e. a liquid outer core for terrestrial planets, or a layer of electrically conducting liquid hydrogen for gas giants) with non-uniform flows organized in

a certain manner, which create a self-sustaining magnetic field. According to dynamo theory, this flow should be convective in nature (Stevenson 1983). Therefore, convection can be regarded as a necessary requirement for a planetary magnetic field (Stevenson 2003).

Limitations of the existing observational techniques make direct measurements of the magnetic fields of exoplanets impossible. At the same time, a rough estimation of an intrinsic planetary magnetic dipole moment  $\mathcal{M}$  can be obtained by simple scaling laws derived by the comparison of different contributions in the governing equations of planetary magnetic dynamo theory (Farrell et al. 1999; Sánchez-Lavega 2004; Grießmeier et al. 2004; Christensen 2010). Most of these scaling laws reveal a connection between the intrinsic magnetic field and the rotation of a planet. Grießmeier et al. (2004) estimated the intrinsic planetary magnetic dipole moments of exoplanets and corresponding sizes of their magnetospheres using the following scaling laws for  $\mathcal{M}$ :

$$\begin{aligned}
 \mathcal{M} &\propto \rho_c^{1/2} \omega_p r_c^4 && \text{Busse 1976,} \\
 \mathcal{M} &\propto \rho_c^{1/2} \omega_p^{1/2} r_c^3 \sigma^{-1/2} && \text{Stevenson 1983,} \\
 \mathcal{M} &\propto \rho_c^{1/2} \omega_p^{3/4} r_c^{7/2} \sigma^{-1/4} && \text{Mizutani et al. 1992,} \\
 \mathcal{M} &\propto \rho_c^{1/2} \omega_p r_c^{7/2} && \text{Sano 1993.}
 \end{aligned} \tag{210}$$

Here  $r_c$  is the radius of the dynamo region (also called the core radius), and  $\omega_p$  is the cyclic frequency of a planet rotation around its axis. The internal properties of a planet, such as the mass density and the conductivity of the dynamo region are denoted by  $\rho_c$  and  $\sigma$ , respectively (for details of the model parameters estimation see Grießmeier et al. (2004)). More recently, Reiners and Christensen (2010), based on scaling properties of convection-driven dynamos (Christensen and Aubert 2006), calculated the evolution of average magnetic fields of HJs and found that (a) extrasolar gas giants may start their evolution with rather high intrinsic magnetic fields, which then decrease during the planet life time, and (b) the planetary magnetic moment may be independent of planetary rotation.

The equations (210) provide a range  $\mathcal{M}_{\min} - \mathcal{M}_{\max}$  of reasonable planetary magnetic moment values. In spite of being different in details, all these models yield an increase of  $\mathcal{M}$  with an increasing planetary angular velocity  $\omega_p$ . In that respect it is necessary to take into account the fact, that close-orbit exoplanets very likely are tidally locked to their host stars. The angular rotation of a tidally locked planet is synchronized with its orbital revolution so, that  $\omega_p$  is equal to the orbital cyclic frequency  $\Omega$  determined by Kepler's law. The time scale for tidal locking  $\tau_{\text{sync}}$  depends on the planetary structure, orbital distance to the host star, and the stellar mass (Showman and Guillot 2002). By this, the planets for which  $\tau_{\text{sync}} \leq 0.1$  Gyr, can be assumed to be tidally locked, since the age of a planet is at least an order of magnitude longer. On the other hand, the planets with  $\tau_{\text{sync}} \geq 10$  Gyr are almost certainly tidally unlocked. The influence of tidal locking on the value of an expected planetary magnetic dipole was studied for different planets (giants and terrestrial-type) in Grießmeier et al. (2004, 2007,?). It was shown, that the magnetic moments of slowly rotating tidally locked exoplanets usually are much smaller than those for similar, but freely rotating tidally unlocked planets. In Table 4 possible ranges of planetary magnetic dipole moments defined by (210) for a Jupiter-type ( $M_p = M_J$ ;  $R_p = R_J$ ) exoplanet orbiting around a solar-analogue

**Table 4** The stellar wind parameters for a solar-analogue G-type star ( $M_* = M_{\text{Sun}}$ ,  $R_* = R_{\text{Sun}}$ , age  $t_* \sim 4$  Gyr) and the ranges of  $\mathcal{M}$  given by (210) as well as corresponding  $R_s = R_s^{(dip)}$  provided by (211) for a Jupiter-type exoplanet at different orbital distances  $d$ . The stellar wind velocity includes also the contribution of the Keplerian planetary orbital velocity  $V_K$  <sup>1</sup>: Tidally locked. <sup>2</sup>: Possible tidally locked. <sup>3</sup>: Not tidally locked.

Orbital distance $d$ [AU]	$n_{\text{sw}}$ [cm <sup>-3</sup> ]	$\tilde{v}_{\text{sw}}$ [km/s]	$\mathcal{M}$ [ $\mathcal{M}_J$ ]	$R_s^{(dip)}(\mathcal{M}_{\text{min}}) / R_s^{(dip)}(\mathcal{M}_{\text{max}})$ [ $R_p$ ]
0.045 <sup>1</sup>	9.1e3	210	0.12...0.3	4.3...6.2
0.1 <sup>2</sup>	1.2e3	260	0.04...1.0	3.8...12
0.3 <sup>3</sup>	92	340	1.0...1.0	15...15

G-type star ( $M_* = M_{\text{Sun}}$ ,  $R_* = R_{\text{Sun}}$ ) are provided. The values of  $\mathcal{M}$  are scaled in units of the present time Jupiter magnetic moment  $\mathcal{M}_J = 1.56 \times 10^{27}$  A m<sup>2</sup>.

### 8.2.2 Magnetic shielding

For the efficient magnetic shielding (i.e. magnetospheric protection) of a planet against the stellar wind, the size of its magnetosphere characterized by the magnetopause stand-off distance  $R_s$  should be much larger than the height of the exobase. By this, the value of  $R_s$  is determined from the balance between the stellar wind ram pressure and the planetary magnetic field pressure at the sub-stellar point (Grießmeier et al. 2004; Khodachenko et al. 2007a). In most studies, the investigation of exoplanetary magnetospheric protection is performed within a highly simplifying assumption of a planetary *dipole-dominated* magnetosphere. This means that only the intrinsic magnetic dipole moment of an exoplanet  $\mathcal{M}$  and the corresponding magnetopause electric currents (i.e., "screened magnetic dipole" case) are considered as the major magnetosphere forming factors. In this case, i.e. assuming  $B(r) \propto \mathcal{M}/r^3$ , the value of  $R_s$  is defined by the following expression:

$$R_s \equiv R_s^{(dip)} = \left[ \frac{\mu_0 f_0^2 \mathcal{M}^2}{8\pi^2 \rho_{\text{sw}} \tilde{v}_{\text{sw}}^2} \right]^{1/6}, \quad (211)$$

where  $\mu_0$  is the diamagnetic permeability of free space,  $f_0 \approx 1.22$  is a form-factor of the magnetosphere caused by the account of the magnetopause electric currents,  $\rho_{\text{sw}} = n_{\text{sw}} m$  is the mass density of the stellar wind, and  $\tilde{v}_{\text{sw}}$  is the relative velocity of the stellar wind plasma which includes also the Keplerian planetary orbital motion velocity  $V_K$ .

The stellar wind parameters appear to be the important factors which influence the planetary magnetosphere size (e.g., see (211)). Recently, there have been important developments towards indirect detections of stellar winds through their interactions with the surrounding interstellar medium. In particular, the stellar mass loss rates and related stellar wind parameters have been estimated by observing astrospheric absorption features of several nearby G- and K- stars. Comparison of the measured absorption to that calculated by hydrodynamic codes made it possible to perform empirical estimation of the evolution of the stellar mass loss rate as a function of stellar age (Wood et al. 2002, 2005) and to conclude about

the dependence of  $n_{\text{sw}}$  and  $v_{\text{sw}}$  on the age of the stellar system. In particular, the younger solar-type G- stars appeared to have much denser and faster stellar winds as compared to the present Sun. Combining the stellar mass loss measurements of Wood et al. (2005) with the results of Newkirk (1980) for the age-dependence of stellar wind velocity, Grießmeier et al. (2007) proposed a method for calculation of stellar wind density  $n_{\text{sw}}$  and velocity  $v_{\text{sw}}$  at a given orbital location of an exoplanet  $d$  for a given mass  $M_*$ , radius  $R_*$  and age  $t_*$  of star. As an example, the values of the stellar wind plasma parameters for a solar-analog G-type star ( $M_* = M_{\text{Sun}}$ , age  $t_* \sim 4$  Gyr) at orbital distances of 0.045 AU, 0.1 AU, and 0.3 AU are given in Table 4. For the tidally locked close-orbit exoplanets with weak magnetic moments exposed to a dense and/or fast stellar wind plasma flows, (211) yields rather small values for sizes of dipole-dominated magnetospheres,  $R_s = R_s^{(dip)}$ , compressed by the stellar wind plasma flow (see Table 4), which in the most extreme cases of collision with CMEs may even shrink down to the planetary surface, i.e.  $R_s \rightarrow R_p$ . Such an approach to estimation of the magnetosphere size, based on (211), resulted in a commonly accepted conclusion, that in order to have an efficient magnetic shield, a planet needs a strong intrinsic magnetic dipole  $\mathcal{M}$ .

Khodachenko et al. (2007b) studied the mass loss of the Hot Jupiter HD 209458b due to the ion pick-up mechanism caused by stellar CMEs, colliding with the planet. In spite of the sporadic character of the CME-planetary collisions, in the case of a moderately active host star of HD 209458b, it has been shown that the integral action of the stellar CME impacts over the exoplanet's lifetime can produce a significant effect on the planetary mass loss. The estimates of the *non-thermal* mass loss of the tidally locked, and therefore, weakly magnetically protected hot giant HD 209458b due to the stellar wind ion pick-up lead to significant and sometimes unrealistic values – up to several tens of planetary masses  $M_p$  lost during the planet life time (Khodachenko et al. 2007b). In view of the fact that multiple close-in giant exoplanets, comparable in mass and size with the Solar System Jupiter exist, and that it is unlikely that all of them began their life as ten times, or even more massive objects, one may conclude that additional factors and processes have to be taken into consideration in order to explain the protection of close-in exoplanets against of destructive *non-thermal* mass loss. Regarding that problem, Khodachenko et al. (2012) proposed a more complete model of the magnetosphere of a giant-type exoplanet, which due to consequent account of the specifics of the close-orbit exoplanets (addressed in the following subsections) provides under similar conditions larger sizes for the planetary magnetospheric obstacles, than those given by the simple screened magnetic dipole model, traditionally considered in such cases.

### 8.3 Magnetodisk-dominated magnetosphere of a Hot Jupiter

The investigation of exoplanetary magnetospheres and their role in evolution of planetary systems forms a new and fast developing branch. Magnetosphere of a close-orbit exoplanet is a complex object, whose formation depends on different external and internal factors. These factors may be subdivided on two basic groups: (a) *stellar factors*, e.g., stellar radiation, stellar wind plasma flow, stellar magnetic field and (b) *planetary factors*, e.g., type of planet, orbital characteristics, escaping material flow, and planetary magnetic field. The structure of an exoplanetary



magnetosphere depends also on the speed regime of the stellar wind and planet interaction (Erkaev et al. 2005; Ip et al. 2004; Matsakos et al. 2015; Strugarek et al. 2015). In particular, for an exoplanet at sufficiently large orbital distance when the stellar wind is super-sonic and super-Alfvénic, i.e. when the ram pressure of the stellar wind dominates the magnetic pressure, an Earth/Jupiter-type magnetosphere with a bow shock, magnetopause, and magnetotail, is formed. At the same time, in the case of an extremely close-orbit location of an exoplanet (e.g.,  $d < 0.03$  AU for the Sun analogue star), where the stellar wind is still under acceleration and remains sub-magnetosonic and sub-Alfvénic (Ip et al. 2004; Preusse et al. 2005; Strugarek et al. 2015), an Alfvénic wing-type magnetosphere without a shock in the upstream region is formed (Woodward and McKenzie 1999; Strugarek et al. 2015). The character of the stellar wind impact on the planetary nearby plasma environment and inner atmosphere is different for the super- and sub-Alfvénic types of the magnetosphere and in each particular planet case it has to be properly taken into account. In the present paper, further on, we do not consider the Alfvénic wing-type magnetospheres, aiming at moderately short orbit giant planets near solar-type stars, under the conditions of a super-Alfvénic stellar wind flow, i.e., with the magnetospheres having in a general case a bow shock, a magnetopause, a magnetotail, similar to the case of the solar system Jupiter.

To explain an obvious survival and, therefore, sufficient magnetospheric protection of close-orbit giant exoplanets under the extreme conditions of their host stars Khodachenko et al. (2012) proposed a generic model of an exoplanetary magnetosphere. A key element in the proposed approach consists of the account of the expanding and escaping dynamical gas layer of the upper atmosphere of planet heated and ionized by the stellar XUV radiation (Johansson et al. 2009; Koskinen et al. 2010, 2013; García Muñoz 2007; Guo 2011, 2013; Shaikhislamov et al. 2014). The interaction of the outflowing atmospheric partially ionized plasma with the rotating planetary magnetic dipole field leads to the development of a current-carrying magnetodisk surrounding the exoplanet. In spite of the generality of the proposed modelling approach, so far it has been applied mainly to HJs – the close-orbit giant exoplanets, as the material escape processes and related magnetic topology effects are expected to be the most pronounced there. According to Khodachenko et al. (2012), the magnetodisk of a HJ can be formed by two different mechanisms, acting simultaneously (see Figure 47): 1) the outflow of the thermally escaping planetary plasma wind, heated and ionized by the stellar radiation, – the so-called *thermally-driven* magnetodisk formation mechanism and 2) the centrifugal acceleration of plasma by the rotating planetary magnetic field in the co-rotation region, with subsequent release of material beyond the centrifugal Alfvénic cylinder, – the so-called *rotation-driven* or "sling" (Alexeev et al. 2003; Alexeev and Belenkaya 2005) mechanism. The inner edge of the magnetodisk is located at the surface where the energy density of plasma (including its kinetic and thermal energies) becomes equal to the energy density of the planetary magnetic field. In the case of a well established and dominating motion of the plasma, like that realized in the co-rotation regime under the conditions of a *rotation-driven* magnetodisk formation (Khodachenko et al. 2012), this boundary surface, from which the magnetodisk builds up, is the Alfvénic surface ( $r = R_A$ ) where the plasma ram pressure gets equal to the magnetic pressure, or the Alfvén Mach number becomes  $M_A^2 = 1$ . In the case of a *thermally-driven* magnetodisk formation, realized during the partially ionized planetary atmospheric material outflow

accelerated by the thermal pressure gradient forces under the conditions of a slowly rotating tidally locked planet, the ruts of magnetodisk are located at the surface where the plasma thermal pressure is equal to the magnetic field energy density, i.e. in the region of plasma  $\beta = 1$ . Beyond the above mentioned boundary surfaces (depending on particular mechanism of the magnetodisk formation) the expanding plasma is not guided any more by the dipole magnetic field. It deforms the field lines leading to creation of a current-carrying magnetodisk (see Figure 47), which in turn crucially changes the topology of the HJ's middle and outer magnetosphere. Two major regions with different topology of the magnetic field (Mestel 1968) can be distinguished in the magnetosphere of a HJ, driven by the escaping plasma flow. The first region corresponds to the inner magnetosphere, or so-called *dead zone*, filled with closed dipole-type magnetic field lines. The magnetic force in the *dead zone* is strong enough to lock plasma with the planet. In the second region, so-called *wind zone*, the expanding plasma drags and opens the magnetic field lines, leading to the formation of a thin current-carrying magnetodisk (see Figure 47). The field of the magnetodisk can exceed significantly the dipole field. Altogether, this leads to the development of a new type of a escaping-wind-driven, magnetodisk-dominated magnetosphere of an exoplanet, which has no analogs among the solar system planets (Khodachenko et al. 2012).

A simultaneous self-consistent description of both, the *rotation-driven* and *thermally-driven*, of the magnetodisk formation is a complex physical problem. So far, these processes are treated separately. It is especially possible in the case of close-orbit tidally locked exoplanets, which are subject to strong radiative energy deposition, whereas the rotational effects are usually much weaker, as the planetary rotation is synchronized with the orbital revolution (Khodachenko et al. 2012; Trammell et al. 2011, 2014; Owen and Adams 2014; Shaikhislamov et al. 2014; Khodachenko et al. 2015). In this case, the radial expansion of hot planetary plasma dominates the co-rotation in the inner magnetosphere. Nowadays, besides a semi-analytical qualitative treatment of origin and interconnection of the inner (dipole dominated) and outer (magnetodisk-dominated) parts of the HJ's magnetosphere (Khodachenko et al. 2012), also laboratory experiments on simulation of the magnetodisk formation under the conditions of outflowing plasma in the background magnetic dipole field have been performed (Antonov et al. 2013).

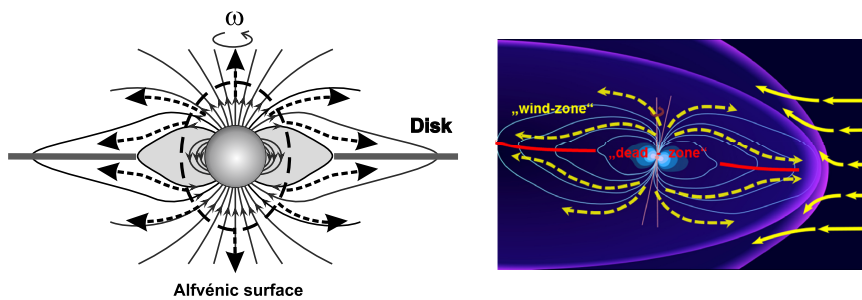


**Fig. 47** Schematic view of the magnetodisk formation mechanisms and structuring of HJ's magnetosphere (adapted from Khodachenko et al. (2012)).

## 8.4 Simulation of Hot Jupiter's *thermally-driven* magnetodisk

Different modeling approaches and approximations for the simulation of expanding exoplanetary atmospheres and related thermal mass losses, proposed so far, have addressed various important factors, such as atmospheric composition and photochemistry, boundary conditions, the spectrum of ionizing radiation and distribution of primary energy input, radiative and adiabatic cooling processes, as well as tidal and centrifugal forces. A number of self-consistent 1D HD models have been developed (Yelle 2004; García Muñoz 2007; Koskinen et al. 2010, 2013; Shaikhislamov et al. 2014) that do not rely anymore on artificial simplifications and idealizations such as isothermal flow, and specific boundary conditions to initiate the wind. However, another crucial factor – the intrinsic planetary magnetic field – was either not considered at all, or included in a non-self-consistent way (e.g., by prescribing specific magnetic configurations). To include the magnetic field, one has to employ instead of the widely used 1D spherically symmetric non-magnetized HD model, at least an axisymmetric 2D magnetohydrodynamics (MHD) approach.

In the first attempts to incorporate planetary magnetic field, a specific topology of the HJ's inner magnetosphere with the predefined *wind* and *dead zones* was assumed, and the material escape of the planetary atmosphere was investigated in a semi-analytic way (Trammell et al. 2011). Adams (2011) considered outflows from close-in gas giants in the regime, where the flow is controlled by a static magnetic field. The isothermal Parker solution was constructed along the open magnetic field lines, which gives a faster supersonic transition (Adams 2011) than in the spherical expansion cases. More self-consistent treatments based on 2D MHD codes has been recently performed by Owen and Adams (2014) and Trammell et al. (2014) in which *dead* and *wind zones* have been shown to form in the expanding planetary wind. However, the thermosphere heating and the MHD flow initiated close to the planetary surface were simulated with rather simplified models, assuming a mono-energetic XUV flux, homogenous (e.g., Trammell et al. (2014)) or empirically estimated gas temperature, and variable boundary conditions at the planet surface. As a result, the obtained estimations for the magnetic field, at which the escaping planetary wind of the particular considered HD 209458b is significantly suppressed, vary in different papers by more than an order of magnitude from less than 0.3 G in Owen and Adams (2014) up to more than 3 G in Trammell et al. (2014). At the same time, the major conclusion of these more advanced simulations stays the same – the exoplanetary *thermal* mass loss can be significantly suppressed by the presence of magnetic field, as compared to the quasi-spherical HD outflows, that often were used in the modeling of the planetary wind and related mass loss. Moreover, despite the recognition of importance of the *dead* and *wind zones* in the context of the planetary magnetosphere topology and related atmospheric mass loss, another important structure - the magnetodisk - which is closely associated with these regions and influences the global size of the magnetosphere (Khodachenko et al. 2012), has not been sufficiently modelled and investigated in these papers.

#### 8.4.1 MHD model of the planetary wind

It should be emphasized that the processes of material escape and planetary magnetosphere formation have to be considered jointly in a self-consistent way in their mutual relation and influence. In that respect, the self-consistent modeling of HJ's planetary wind, driven by the stellar radiative heating in the presence of an intrinsic magnetic field, still remains an actual task. The most recent results on that issue are provided in Khodachenko et al. (2015), where a self-consistent 2D MHD model of an expanding HJ's upper atmosphere in the presence of the planetary intrinsic magnetic dipole field is presented. For the sake of definiteness, typical physical parameters of a modeled HJ were taken as those of HD 209458b (i.e.,  $r_p = 1.38R_J$ ,  $M_p = 0.71M_J$ ) orbiting a Sun-like G-star ( $M_* = 1.148M_{\text{Sun}}$ , age  $\sim 4$  Gyr) at a distance of 0.047 AU. A purely hydrogen atmosphere of a HJ composed in the general case of molecular and atomic hydrogen as well as corresponding ions and electrons was considered. The 2D MHD model by Khodachenko et al. (2015) generalizes the 1D HD model developed in Shaikhislamov et al. (2014) to the case of a magnetized planet. It includes in a self-consistent way (a) a realistic solar-type spectrum of the XUV radiation (to calculate correctly the intensity and column density distribution of radiative energy input); (b) basic hydrogen (photo)chemistry for the appropriate account of atmosphere composition and  $H_3^+$  cooling; (c) stellar-planetary gravitational and rotational forces. The model operates also with such boundary conditions, that does not influence the numerical solution (Shaikhislamov et al. 2014). The basic equations of the model are those of the standard HD (continuity, momentum, and energy balance equations), supplemented by the equations for the magnetic field, hydrogen ionization, by XUV and electron collision, and recombination, as well as the equations for most important chemistry (altogether 16 reactions) and radiation diffusion in a partially ionized plasma (Shaikhislamov et al. 2014; Khodachenko et al. 2015). The model includes the energy- and temperature- dependent reactions between  $H$ ,  $H^+$ ,  $H_2$ ,  $H_2^+$ ,  $H_3^+$ , and  $e$  components. The photo ionization rate is split between  $H$  and  $H_2$  species, correspondingly to their cross sections.

To simulate the expanding upper atmosphere of a HJ, the multi-fluid MHD model by Khodachenko et al. (2015) includes the following species:  $H$ ,  $H^+$ ,  $H_2$ ,  $H_2^+$ ,  $H_3^+$ . A pure molecular hydrogen atmosphere of an HD209458b analogue in a barometric equilibrium with the base (inner boundary) temperature of 1000 K was taken as the initial state for the simulation of the expanding planetary wind driven by the stellar XUV radiative heating. The planetary wind plasma was treated as a quasi-neutral fluid in thermal equilibrium with  $T_e = T_i$ . As it was shown in Shaikhislamov et al. (2014), Khodachenko et al. (2015), as well as in (Yelle 2004) and Koskinen et al. (2010, 2013), the components  $H_2$ ,  $H_2^+$ ,  $H_3^+$  can exist around an HD 209458b analogue planet only at very low heights  $< 0.1r_p$  in a relatively dense thermosphere. The reason for the inclusion of the hydrogen chemistry, besides the need to account for the IR cooling produced by  $H_3^+$  molecule, is that a significant part of stellar XUV energy is absorbed at heights where molecular hydrogen dominates, as compared to the atomic one. In the upper layers of the expanding planetary wind the main processes, responsible for the transformation between neutral and ionized hydrogen particles of the planetary origin are photo-ionization, electron impact ionization and dielectronic recombination (Shaikhislamov et al. 2014; Khodachenko et al. 2015). The radiative heating

term in the energy equation of the model (Shaikhislamov et al. 2014; Khodachenko et al. 2015) is derived by integration of the stellar XUV spectrum. For the solar type host star of HD209458b, the spectrum of the Sun is used as a proxy.

Another kind of important interaction between the considered particle populations is resonant charge-exchange collisions. Indeed, charge-exchange has the cross-section of about  $\sigma_{exc} = 6 \times 10^{-15} \text{cm}^2$  at low energies, which is an order of magnitude larger than the elastic collision cross-section. When planetary atoms and protons slip relative each other, because they have different thermal pressure profiles and protons feel electron pressure while atoms do not, the charge-exchange between them leads to velocity and temperature interchange. (Shaikhislamov et al. 2014; Khodachenko et al. 2015) describe this process in the momentum equation for planetary protons with a collision rate  $n_H \sigma_{exc} V$ , where the interaction velocity  $V$  depends in general on thermal and relative velocities of the interacting fluids (i.e., protons and neutral atoms). For the densities above  $10^5 \text{cm}^{-3}$  and other parameters typical for HD209458b, the charge-exchange between planetary atoms and protons ensures that they move practically together with a relatively small slippage and equal temperatures, constituting a hydrodynamic planetary wind in thermal equilibrium. The model also includes atomic-atomic and proton-atomic elastic collisions with the cross-sections of  $\sim 10^{-16} \text{cm}^2$  which, however, are relatively unimportant. For the typical temperatures  $\leq 10^4 \text{K}$  realized in the upper atmosphere of a HJ (Koskinen et al. 2010, 2013; Shaikhislamov et al. 2014), the proton-proton Coulomb collision cross section is well above  $10^{-13} \text{cm}^2$ . Therefore, as has been also shown in García Muñoz (2007); Trammell et al. (2011); Koskinen et al. (2010, 2013), and Guo (2011), the atomic, charge-exchange, and Coulomb collisions in the most of the modeled regions of a HJ's upper atmosphere are efficient enough to ensure the "nonslippage" approximation for neutral hydrogen, ions, and electrons such that the assumptions of  $\mathbf{V}_n = \mathbf{V}_i = \mathbf{V}_e = \mathbf{V}$  as well as temperature equilibrium  $T_n = T_i = T_e = T$  hold true. Here the indexes  $n$ ,  $i$ , and  $e$  denote the neutral, ionized and electron components of the partially ionized atmospheric gas, respectively. The "nonslippage" assumption may, however, be wrong in the relatively narrow inner (close to the planet) regions of the expanding partially ionized planetary wind filled with a sufficiently strong magnetic field. In these regions the effects of relative motion of species and related energy dissipation processes become important. This constitutes an as yet unstudied so far aspect of the HJ's magnetospheric physics which requires special detailed investigation. The momentum transfer between similar particles due to thermal motion in the fluid approach is described by viscosity. Its dimensionless value can be estimated as relation of mean-free path to the system size. For the planetary protons experiencing the Coulomb collisions at a temperature of  $10^4 \text{K}$  and density of  $\sim (10^6 - 10^5) \text{cm}^{-3}$  the dimensionless viscosity is about  $\sim 10^{-5}$ .

Because of the extremely large system size, the magnetic Reynolds number,  $Re_m$ , of the problem is everywhere exceedingly large, except for a region very close to the planet where the particle density sharply increases. Thus, the dynamics of the magnetic field in the most of the modelled HJ's magnetosphere should be dissipation-less. This is achieved in the numerical code by taking sufficiently high, though finite, conductivity, which corresponds to  $Re_m \geq 10^5$ . Close to the planet surface where electron-atom collisions dominate as compared to the electron-ion collisions, the corresponding expressions from Braginskii (1965) are used to calculate the electric conductivity.

The application of HD/MHD approaches in the planetary (HJ's) aeronomy can be justified only below the exobase, which corresponds to the region where the Knudsen number  $Kn = \bar{l}/\Delta = 1$ , where  $\bar{l}$  is the mean free path of particles and  $\Delta$ , a typical scale of flow. However, in the regions far from the planet,  $\Delta$  may be taken to be of the order of the planetary radius  $R_p$ , and the condition  $Kn \sim 1$  is realized approximately in the layers with density  $\sim 10^4 \text{ cm}^{-3}$ . That remains well above the height range ( $\sim 10R_p$ ) considered in the modeling simulations. Close to the planet surface, the barometric height  $H$ , which is smaller than  $R_p$ , has to be taken as the typical scale  $\Delta$ . Because of much larger densities there, the mean free path  $\bar{l}$  also becomes smaller, and the condition  $Kn < 1$  holds true, making the fluid approach fairly valid.

#### 8.4.2 Planetary wind propulsion force

In the first studies of the planetary atmosphere expansion aimed at estimating the material *thermal* escape rate and related mass loss, an isothermal Parker-type solution was imposed with an a priori prescribed boundary condition at the planetary inner atmosphere (or surface) related to the XUV heating of a fixed, predefined thin layer (Watson et al. 1981). However, it was shown in Tian et al. (2005) that in a thin-layer-heating approximation the expanding atmosphere mass loss rate strongly depends on the altitude of the layer where the radiation energy is deposited. Moreover, as it was suggested already by Parker, the realistic solution that corresponds to an outflowing (expanding) planetary wind regime requires an additional volume heating in order to compensate for the adiabatic cooling of the expanding plasma envelope. This was also confirmed in the follow-up numerical modeling studies. For example, in the case of the solar wind, an additional acceleration factor is called for at a few solar radii. This additional driver is attributed to the dissipation of Alfvén waves (Usmanov et al. 2011). For an outflowing atmosphere of a HJ, one of the possible candidates for the role of such a distributed accelerator is the absorption of XUV, which takes place everywhere atomic or molecular hydrogen is present. However, it turns out that at distances of about several planetary radii, where the additional forcing of the expanding planetary atmospheric material is needed to keep it in the outflowing regime (i.e., to escape the gravity tension), the gas becomes highly ionized, and the absorption of XUV decreases. Nevertheless, the same fact of the increasing ionization degree, which reduces the efficiency of XUV heating, contributes to the additional acceleration of the wind and appears as an additional booster for the planetary plasma wind. That is because the thermal pressure  $p = (n_a + n_i + n_e)kT$  increases (up to two times) at certain intervals of heights (in the ionization region) because of the contribution of the electron and ion pressure, whereas the density of material  $\approx (n_a + n_i)m_i$  remains practically unchanged. The created pressure gradient provides an additional driving force for the expansion of ionized atmospheric material. In the ionization region, the expanding planetary wind experiences an additional acceleration and reaches velocities that sustain the continuous outflow regime.

#### 8.4.3 Magnetic field and plasma flow structure in HJ's inner magnetosphere

The self-consistent MHD model of the expanding magnetized HJ's wind developed in Khodachenko et al. (2015) for the first time enabled the detailed and realistic

simulation of the whole complex of the physical parameters of the planetary inner magnetosphere, including also the formation of a *thermally-driven* magnetodisk and the quantifying of the related magnetically controlled planetary thermal mass loss. To characterize the intrinsic planetary magnetic dipole field, its surface value at equatorial plane  $B_s$  is used. The major physical parameters and results of the simulations are scaled in units of the characteristic values of the problem, defined as follows: for temperature,  $\tilde{T}_c = 10^4$  K; for speed,  $V_{Ti}(T_c) = \tilde{V}_c = 9.1 \text{ km} \cdot \text{s}^{-1}$ ; for distance, the planet radius  $R_p$ ; for time, the typical flow time  $\tilde{t}_c = R_p/\tilde{V}_c \approx 3$  hr.

In line with qualitative expectations, the intrinsic planetary magnetic dipole field influences the dynamics of the escaping plasma and structures the planetary wind. In particular, in the case of a sufficiently small magnetic field, no *dead zone* is formed. This happens if the gas thermal and ram pressures exceed everywhere the magnetic pressure, so that the latter cannot stop the developing flow. For the conditions of an HD 209458b analog planet such a situation takes place at  $B_s < 0.1$  G. The resulting spatial structure of the magnetic field and planetary wind is close to that in the case of radially stretched field lines following the streamlines realized with a broadly distributed azimuthal current  $J_\varphi \sim (\sin \theta)/R^2$  centered on the equatorial plane.

Figure 48 demonstrates the solution obtained with  $B_s = 0.3\text{G}$  and  $B_s = 1\text{G}$ . In these cases the planetary wind is influenced by the magnetic field, and a *dead zone* is formed. The effect of magnetic field is visible close to polar regions, where the flow is unable to fully stretch the dipole field lines near the planet and it follows along them. Due to the larger divergence of the material flow controlled by the magnetic dipole field and the corresponding faster adiabatic cooling, as well

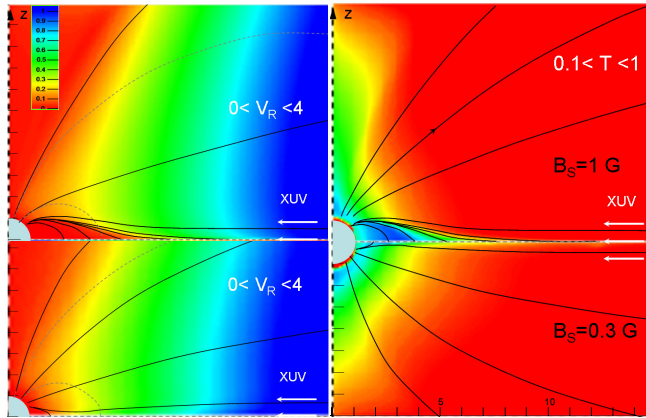


**Fig. 48** HJ's wind radial velocity, temperature and magnetic field structure simulated for a magnetized analog of HD209458b with equatorial surface field  $B_s = 1\text{G}$  (top panels) and  $B_s = 0.3\text{G}$  (bottom panels). Variation ranges of the simulated physical quantities are indicated in the top of the corresponding panels. The color scale between the normalized minimal and maximal values of a simulated physical quantity is presented in the upper left panel. All values below or above the corresponding minimal and maximal values, are plotted as uniformly red or blue, respectively. Magnetic field is shown with black solid lines (adapted from Khodachenko et al. (2015)).

as the suppression of the zonal flow by the magnetic and tidal forces, the bulk velocity in polar regions is significantly diminished and does not reach supersonic values. This effect was predicted in Shaikhislamov et al. (2014). The magnetic field lines passing near the *dead zone* are stretched strongly in the vicinity of the equatorial plane and have the shape typical for the current disk. The regions of increased temperature above the poles and in the *dead zone* where magnetic field and tidal force suppress the plasma outflow are clearly visible in the right panels of Figure 48.

Formation of an extended and thin current sheet in the equatorial plane admits that the reconnection of reversed magnetic field lines might be triggered. According to Khodachenko et al. (2015), the *thermally-driven* magnetodisk shows a cyclic behavior, composed of consequent phases of the disk formation and magnetic flux accumulation followed by its short explosive relaxation during the magnetic reconnection with the ejection of a ring-type plasmoid.

#### 8.4.4 Magnetic control of HJ's mass loss

The reconnection events in the magnetodisk strongly modulate in time the simulated instant mass-loss rate of a HJ measured through the outer boundary of the modelling box. With the increase of the surface magnetic field, the quasi-periodic mass-loss pulses become more pronounced in amplitude and more frequent in time (Khodachenko et al. 2015). The time-averaged dependence of the mass-loss rate on planetary surface magnetic field is presented in Figure 49.

As can be seen in Figure 49, a sharp decrease of the mass-loss rate takes place for the magnetic field values beyond  $B_s \sim 0.3\text{G}$ , and at  $B_s = 1\text{G}$  the averaged mass-loss rate becomes about an order of magnitude smaller than that without

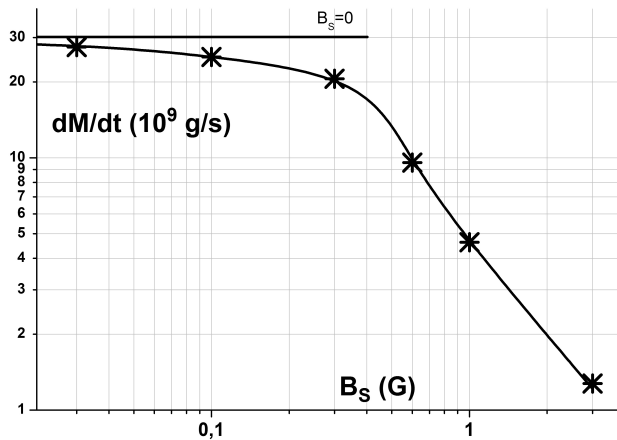


**Fig. 49** Time-averaged mass-loss rate of an HD 209458b analog planet as a function of the planetary equatorial surface magnetic field value  $B_s$ . The horizontal line indicates the mass-loss rate without magnetic field (adapted from Khodachenko et al. (2015)).



the magnetic field. This effect may be explained by the increase of polar- and *dead zone* areas of the suppressed material outflow with the increasing planetary magnetic field at the expense of the size of the wind region.

### 8.5 Scaling of a magnetosphere with magnetodisk

The global large-scale structure of a HJ's magnetosphere formed during the planet interaction with the stellar wind, may be investigated with the Paraboloid Magnetospheric Model (PMM), which enables judging on the shape and size of the planetary magnetosphere and its protective role (Khodachenko et al. 2012). PMM is a semi-analytical approach to the modeling of planetary magnetosphere structure (Alexeev et al. 2003; Alexeev and Belenkaya 2005; Alexeev et al. 2006; Khodachenko et al. 2012). The name of the model is derived from its key simplifying assumption that the magnetopause of a planet may be represented by a paraboloid surface co-axial with the direction of the ambient stellar wind plasma. The PMM calculates the magnetic field generated by a variety of current systems located on the boundaries and within the boundaries of a planetary magnetosphere. Besides the intrinsic planetary magnetic dipole and magnetopause currents, the PMM has, among the main sources of magnetic field, also the electric current system of the magnetotail, and the induced ring currents of the magnetodisk. The model works without any restrictions imposed on the values of interplanetary medium parameters, enabling therefore the description of the whole variety of possible magnetosphere configurations caused by different intrinsic magnetic fields of exoplanets and various stellar wind conditions. The specifics of PMM consist of the substitution of the planetary magnetospheric plasma by the system of electric currents which reproduce the integral electrodynamic effects of plasma. As applied to HJs, PMM reveals that the electric currents induced in the plasma disk produce an essential effect on the overall magnetic field structure around the planet, resulting in the formation of a *magnetodisk-dominated* magnetosphere of a Hot Jupiter. Due to the extension of the plasma disks around close-in exoplanets, the sizes of their magnetodisk-dominated magnetospheres are usually larger than those, followed from the traditional estimates with the equation (211), based on taking into

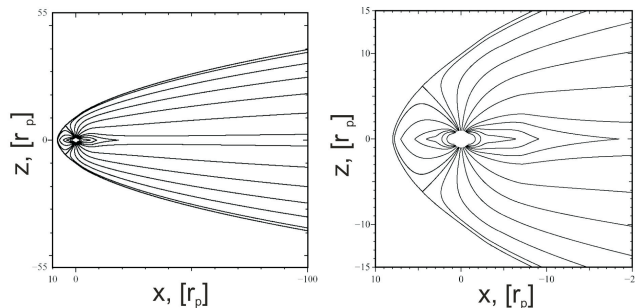


**Fig. 50** Typical view of a magnetodisk-dominated magnetosphere (adapted from Khodachenko et al. (2014).)

account only the screened planetary magnetic dipoles (Gri bmeier et al. 2004; Khodachenko et al. 2007a). In general, the role of the magnetodisk may be attributed to an expansion of a part of the dipole magnetic flux from the inner magnetosphere regions outwards and a resulting increase of the magnetosphere size. The magnetic field produced by the magnetodisk ring currents, dominates above the contribution of the intrinsic magnetic dipole of a HJ and finally determines the size and shape of the whole magnetosphere.

Khodachenko et al. (2012) provided an approximate formula for the estimation of the magnetopause stand-off distance taking into account the contribution of the *rotation-driven* magnetodisk:

$$\frac{R_s^{(dip+MD)}}{R_p} \sim \frac{B_{d0J}^{1/2}(1 + \kappa^2)^{1/4}}{(2\mu_0 p_{sw})^{1/4}} \left(\frac{R_{AJ}}{R_p}\right)^{-1/2} \times \left(\frac{\omega_p}{\omega_J}\right)^{\frac{3\alpha+1}{10}} \left(\frac{dM_p^{(th)}/dt}{dM_J/dt}\right)^{\frac{1}{10}}. \quad (212)$$

where  $R_{AJ}$ ,  $\frac{dM_J}{dt}$ , and  $B_{d0J}$  are the known values corresponding to the Alfv nic radius, mass load to the disk, and surface magnetic field for the solar system Jupiter. The parameter  $\alpha$  appeared in the power index of the ratio of the planetary and Jovian rotation cyclic frequencies in (212) reflects the fact of proportionality of the planetary magnetic dipole moment  $\mathcal{M}$  to certain power  $\alpha$  of  $\omega_p$  (see equation (210)).

The coefficient  $\kappa \approx 2.44$  is an amplifying factor of the inner magnetospheric field at the magnetopause (Alexeev et al. 2003), which is required to take into account the contribution of the magnetopause electric currents (i.e. Chapman-Ferraro field) at the substellar point. It is connected with the form-factor  $f_0$  from (211) as  $\kappa = 2f_0$ . Therefore, according to (212), for a given ram pressure of stellar wind,  $p_{sw}$ , the size of magnetosphere increases with the increasing planetary angular velocity  $\omega_p$  and/or thermal mass loss rate  $dM_p^{(th)}/dt$ . In the case of a *thermally-driven* magnetodisk a similar relatively simple analytic expression cannot be derived, because of the more complicated, as compared to "sling" mechanism (Alexeev et al. 2003; Alexeev and Belenkaya 2005), nature of the thermal planetary wind, which is described only by means of numerical simulations presented above. At the same time, the global effect, in the sense of the HJ's magnetosphere shaping, of the large-scale current system of the magnetodisk is basically the same for both, the *thermally-* and *rotation-driven* magnetodisks.

A slower, than the dipole-type decrease of magnetic field with distance comprises the essential specifics of the HJs' magnetodisk-dominated magnetospheres. According Khodachenko et al. (2012), this results in their 40–70% larger scales, as compared to those traditionally estimated by taking into account only the planetary dipole. Such larger magnetospheres, extending well beyond the planetary exosphere height, provide better protection of close-in planets against the eroding action of extreme stellar winds (Khodachenko et al. 2007a).

Table 5 summarizes the values for the HJ's magnetopause stand-off distance  $R_s^{(dip+MD)}$  at different orbits around a full solar analogue star and gives for comparison the stand-off distance values  $R_s^{(dip)}$ , obtained with equation (211), i.e. in the case when the contribution of magnetodisk is ignored (e.g., a pure dipole case). For the definiteness' sake, the planetary magnetic dynamo model by Stevenson (1983) with  $\mathcal{M} \propto \omega_p^{1/2}$  (i.e.  $\alpha = 1/2$  by) has been taken for these calculations from the set (210).

**Table 5** Hot Jupiter Alfvénic radius,  $R_A$ , and magnetopause stand-off distance for only a dipole controlled magnetosphere,  $R_s^{(dip)}$ , and a magnetosphere with magnetodisk,  $R_s^{(dip+MD)}$ , given by PMM. Full analog of the solar system Jupiter orbiting the Sun analog star at different orbits is considered. <sup>1</sup>: Tidally locked. <sup>2</sup>: Not tidally locked. <sup>3</sup>: Jupiter

$d$ [AU]	$R_s^{(dip+MD)}$ [ $R_p$ ]	$R_s^{(dip)}$ [ $R_p$ ]	$R_A$ [ $R_p$ ]
0.045 <sup>1</sup>	8.0	5.76	3.30
0.1 <sup>1</sup>	8.27	6.16	4.66
0.3 <sup>2</sup>	24.2	15.0	7.30
5.2 <sup>3</sup>	71.9	41.8	19.8

A typical example of the magnetic field structure in the HJ’s magnetosphere, obtained with PMM, is shown in Figure 50.

## 8.6 Conclusions

To summarize this section we would like to repeat its major points and to outline the open-question areas which still require further investigation.

(1) Stellar XUV radiation and stellar wind plasma flow strongly impact the environments of close-orbit exoplanets, such as terrestrial-type exoplanets in the HZs of low mass stars and HJs. In particular, the close location of a planet to its host star results in intense heating and ionization of the planetary upper atmosphere by the stellar X-ray and EUV radiation, which in their turn lead to the expansion of the ionized atmospheric material, contributing to the so-called planetary thermal mass loss. At higher altitudes, i.e. in the region of direct interaction of the expanding atmosphere with the stellar wind, the escaping planetary plasma is picked up by the stellar wind, resulting in a non-thermal mass loss. Both the thermal and non-thermal mass loss processes operating simultaneously contribute the total planetary mass loss and require their detailed description and quantifying. The planetary intrinsic magnetic field is known to be a crucial factor that influences the planetary mass loss and provides a protective effect for the upper atmospheric environment. It has two major aspects. First, the large-scale magnetic fields and electric currents, related to the planetary magnetism, form the planetary magnetosphere, which acts as a barrier for the upcoming stellar wind shielding the upper atmosphere against direct impact of the stellar plasmas. Second, the internal magnetic field of the magnetosphere also influences the streaming of the expanding planetary atmospheric plasma and therefore affects its escape.

(2) The interaction of the outflowing partially ionized planetary plasma wind with the rotating planetary magnetic dipole field leads to the development of a current-carrying magnetodisk. By this, two major regions with different topology of the magnetic field, so-called *dead-* and *wind-zones* are formed in the magnetosphere driven by the escaping plasma flow (Mestel 1968; Adams 2011; Trammell et al. 2011, 2014; Owen and Adams 2014; Khodachenko et al. 2015). The field of the mag-

netodisk under typical conditions of a close-orbit HJ's, by far exceeds the dipole field. Altogether, this leads to the development of a new type of magnetodisk-dominated magnetosphere (Khodachenko et al. 2012). Such expanded magnetospheres of HJs have been shown to be up to 40 – 70% larger, as compared to the traditionally estimated dipole-type ones. That enabled the resolution of a problem of better magnetospheric protection of close-orbit HJs against the non-thermal erosive action of the stellar winds (Khodachenko et al. 2012). At the same time, the thermal mass loss due to the magnetically controlled escaping planetary wind has been shown to depend strongly on the size of the self-consistently formed *dead-zone*, in which the significant portion of the planetary plasma stays locked and appears therefore excluded from the escaping material flow. Note, that the specifics and even existence of magnetodisks as well as the details of the structuring of the inner magnetospheres by lower mass exoplanets (e.g., Neptune- or Terrestrial type), under different stellar wind and radiation conditions, is still a subject for further study.

(3) Investigation of key factors and physical mechanisms which determine the structure, topology and dynamics of exoplanetary magnetospheres at close orbits, form an important branch in the present day space physics. This topic is connected with the study of the whole complex of stellar-planetary interactions, as well as internal processes, including consideration of stellar radiation, plasma flows (e.g., stellar wind and coronal mass ejections), radiative energy deposition at the upper atmospheric layers, as well as planetary and stellar winds interaction. Special attention is paid to the development of a set of modelling tools and approaches for the description and simulation of exoplanetary magnetospheres and their basic elements, taking into account the specifics of exoplanetary conditions at close to host star orbits, such as the expanding upper atmospheric material (escaping planetary wind) heated and ionized by the stellar XUV, and formation in some cases under the conditions of planetary intrinsic magnetic dipole field, of an equatorial current-carrying plasma disk (Khodachenko et al. 2012, 2015). While HD and MHD codes are fairly well developed and available, their use for simulation of expanding planetary plasma winds on exoplanets is a relatively novel area. A special challenge in that respect consists of the necessity to evaluate and then to include in the modeling the major underlying physics and most important factors that have been explored in recent years (Yelle 2004; Erkaev et al. 2005, 2013; Tian et al. 2005; García Muñoz 2007; Penz et al. 2008; Koskinen et al. 2010, 2013; Adams 2011; Guo 2011, 2013; Trammell et al. 2011, 2014; Owen and Adams 2014; Shaikhislamov et al. 2014; Khodachenko et al. 2015). The development of a self-consistent model of an exoplanetary magnetosphere which properly includes all the basic physical effects and conditions still remains a challenging task.

(4) An important aspect consists of the necessity to correctly take into account the effects of plasma partial ionization in the presence of a background magnetic field. So far, the dynamics of the expanding magnetized and partially ionized plasmosphere of an exoplanet has been considered in a simplified way, within an assumption of strong coupling, which ignores the relative motion of species in a restricted area of the inner planetary magnetosphere (Trammell et al. 2011, 2014; Owen and Adams 2014; Shaikhislamov et al. 2014; Khodachenko et al. 2015). At the same time, it is well known that the different interactions of the moving elec-

trons, ions and neutrals with the magnetic field and each other play a crucial role in the processes of electric current generation and energy dissipation. Because of the slippage between the ionized and neutral components, the magnetic field cannot be considered as being frozen into the material flow. The magnetic field causes essential anisotropy of the electric conductivity in the partially ionized plasmas. The increased Joule energy dissipation rate in the partially ionized magnetized plasmas is quantitatively described in terms of Cowling conductivity (*Cowling* 1957). At the bottom of the radiatively heated upper atmosphere the material is weakly ionized. Then the ratio of neutral fraction to the ionized one decreases upwards, and at the heights of several  $R_p$  the planetary wind plasma becomes practically fully ionized (Shaikhislamov et al. 2014; Khodachenko et al. 2015). Braginskii (1965) gave the basic principles of transport processes in plasma including the effects of partial ionization. Neutral atoms change the plasma dynamics through collisions with charged particles, which may lead to different new phenomena in the plasma, for example increased Joule heating rates (Zaitsev and Khodachenko 1992; Khodachenko and Zaitsev 2002; Khodachenko 1996; Khodachenko et al. 2004; Forteza et al. 2007) and the Farley-Buneman instability (Zaitsev and Khodachenko 1992; Fontenla et al. 2008). The influence of a neutral flow on the electric current is significant when two conditions (so-called dynamo conditions) are satisfied. The first condition is that the electron cyclotron frequency,  $\omega_e$ , should be much larger than electron collision frequency,  $\nu_e$ . The second condition implies that  $1 \ll (\omega_e \omega_i) / (\nu_e \nu_i)$ , where  $\omega_i$  is the ion cyclotron frequency and  $\nu_i$  is the ion collision frequency (Sen and White 1972; Khodachenko and Zaitsev 2002). If these two conditions are satisfied then the flow of neutral particles across the ambient magnetic field may create electric currents, due to mechanisms similar to those of the Farley-Buneman instability, which will dissipate due to the ion-neutral collisions and convert part of the kinetic energy of the expanding material into the heat. That would finally influence the dynamics of the planetary wind.

(5) The performed study also confirmed the importance of an appropriate account of the hydrogen chemistry at the upper atmospheric layer adjacent to the inner boundary of the simulation domain, where the most energetic photons are absorbed, as that affects the mass-loss rate (reduction by approximately a factor of two) and the whole numerical solution. That may be even more crucial for exoplanets at larger orbital distances than those typical for HJs, as the  $H3^+$  cooling area tends to increase at lower atmospheric temperatures (Chadney et al. 2015). At the same time, the rates of the most important reactions included in our model were often extrapolated from the temperature range of 300 K at which they were measured to the higher-temperature conditions realized at HJs. Therefore, these, as well as the IR emission function of the  $H3^+$  ion, are a subject for further investigation and reevaluation with the development of more complex chemical models.

**Acknowledgements** JLB and RS want to acknowledge financial support from MINECO AYA2014-54485-P and FEDER Funds, and from The Leverhulme Trust under grant IN-2014-016. RS acknowledges the “Ministerio de Economía, Industria y Competitividad” and the “Conselleria d’Innovació, Recerca i Turisme del Govern Balear (Pla de ciència, tecnologia, innovació i emprenedoria 2013-2017)” for the “Ramón y Cajal” grant RYC-2014-14970. The results presented in this review by MK were obtained within the NFN project S116 “Pathways to Habitability” of the Austrian Science Foundation (FWF) and its related subprojects S11606-N16, S11607-N16. IA, IFS, and MK also acknowledge the support of the FWF projects

I2939-N27, P25587-N27 and P25640-N27, Leverhulme Trust grant IN-2014-016, and the grants No.16-52-14006, No.14-29-06036 of the Russian Fund for Basic Research, as well as RAS presidium program N9 and SB RAS research program (project II.10.1.4, 01201374303). IIA was partially supported by Ministry of Education and Science of the Russian Federation grant 14.616.21.0084. TZ acknowledges support from FWF project P26181-N27 and from the Georgian Shota Rustaveli National Science Foundation projects DI-2016-17 and 217146. Parallel computations crucial for the present study have been performed at the Supercomputing Center of the Lomonosov Moscow State University and at the SB RAS Siberian Super-Computing Center (SSCC) and Computation Center of Novosibirsk State University. EK and MCV are grateful for support by the Spanish Ministry of Science through the project AYA2014-55078-P and by the European Research Council in the frame of the FP7 Specific Program IDEAS through the Starting Grant ERC-2011-StG 277829-SPIA. All the authors want to thank ISSI for the support to the ISSI team on "Partially Ionized Plasmas in Astrophysics (PIPA)" and providing a collaborative environment for research and communication.

## References

- N. Achilleos, S. Miller, J. Tennyson, A.D. Aylward, I. Mueller-Wodarg, D. Rees, Jim: A time-dependent, three-dimensional model of jupiter's thermosphere and ionosphere. *Journal of Geophysical Research: Planets* **103**(E9), 20089–20112 (1998). doi:10.1029/98JE00947. <http://dx.doi.org/10.1029/98JE00947>
- F.C. Adams, Magnetically Controlled Outflows from Hot Jupiters. *Astrophys. J.* **730**, 27 (2011). doi:10.1088/0004-637X/730/1/27
- S.-I. Akasofu, S. Chapman, *Solar-terrestrial physics. an account of the wave and particle radiations from the quiet and the active sun, and of the consequent terrestrial phenomena* 1972
- I.I. Alexeev, E.S. Belenkaya, Modeling of the Jovian Magnetosphere. *Annales Geophysicae* **23**, 809–826 (2005). doi:10.5194/angeo-23-809-2005
- I.I. Alexeev, E.S. Belenkaya, S.Y. Bobrovnikov, V.V. Kalegaev, Modelling of the electromagnetic field in the interplanetary space and in the Earth's magnetosphere. *Space Sci. Rev.* **107**, 7–26 (2003). doi:10.1023/A:1025542915800
- I.I. Alexeev, V.V. Kalegaev, E.S. Belenkaya, S.Y. Bobrovnikov, E.J. Bunce, S.W.H. Cowley, J.D. Nichols, A global magnetic model of saturn's magnetosphere and a comparison with cassini soi data. *Geophysical Research Letters* **33**(8), (2006). L08101. doi:10.1029/2006GL025896. <http://dx.doi.org/10.1029/2006GL025896>
- I.I. Alexeev, M.S. Grygoryan, E.S. Belenkaya, V.V. Kalegaev, M. Khodachenko, Magnetosphere Environment from Solar System Planets/Moons to Exoplanets, in *Characterizing Stellar and Exoplanetary Environments*, ed. by H. Lammer, M. Khodachenko Astrophysics and Space Science Library, vol. 411, 2015, pp. 189–212. doi:10.1007/978-3-319-09749-7-10
- I. Alexeev, E. Belenkaya, M. Khodachenko, M. Grigoryan, Auroral ionosphere Joule heating as a reason of the upper thermosphere overheating in the Jupiter and Saturn systems, in *40th COSPAR Scientific Assembly*. COSPAR Meeting, vol. 40, 2014
- V. Alexiades, G. Amiez, P.-A. Gremaud, Super-time-stepping acceleration of explicit schemes for parabolic problems. *Commun. Numer. Meth. Engng.* **12**, 31–42 (1996). doi:10.1002/(SICI)1099-0887(199601)12:1;31::AID-CNM950;3.0.CO;2-5
- H. Alfven, The plasma universe. *Physics Today* **39**, 22–27 (1986). doi:10.1063/1.881039
- A. Allen, Z.-Y. Li, F.H. Shu, Collapse of Magnetized Singular Isothermal Toroids. II. Rotation and Magnetic Braking. *Astrophys. J.* **599**, 363–379 (2003). doi:10.1086/379243
- P. André, A. Men'shchikov, S. Bontemps, V. Könyves, F. Motte, N. Schneider, P. Didelon, V. Minier, P. Saraceno, D. Ward-Thompson, J. di Francesco, G. White, S. Molinari, L. Testi, A. Abergel, M. Griffin, T. Henning, P. Royer, B. Merín, R. Vavrek, M. Attard, D. Arzoumanian, C.D. Wilson, P. Ade, H. Aussel, J.-P. Baluteau, M. Benedettini, J.-P. Bernard, J.A.D.L. Blommaert, L. Cambrésy, P. Cox, A. di Giorgio, P. Hargrave, M. Hennemann, M. Huang, J. Kirk, O. Krause, R. Launhardt, S. Leeks, J. Le Penec, J.Z. Li, P.G. Martin, A. Maury, G. Olofsson, A. Omont, N. Peretto, S. Pezzuto, T. Prusti, H. Roussel, D. Russeil, M. Sauvage, B. Sibthorpe, A. Sicilia-Aguilar, L. Spinoglio, C. Waelkens, A. Woodcraft, A. Zavagno, From filamentary clouds to prestellar cores to the stellar IMF: Initial highlights from the Herschel Gould Belt Survey. *Astron. Astrophys.* **518**, 102 (2010). doi:10.1051/0004-6361/201014666

- P. Antolin, T.J. Okamoto, B. De Pontieu, H. Uitenbroek, T. Van Doorselaere, T. Yokoyama, Resonant Absorption of Transverse Oscillations and Associated Heating in a Solar Prominence. II. Numerical Aspects. *Astrophys. J.* **809**, 72 (2015). doi:10.1088/0004-637X/809/1/72
- V.M. Antonov, E.L. Boyarinsev, A.A. Boyko, Y.P. Zakharov, A.V. Melekhov, A.G. Ponomarenko, V.G. Posukh, I.F. Shaikhislamov, M.L. Khodachenko, H. Lammer, Inflation of a Dipole Field in Laboratory Experiments: Toward an Understanding of Magnetodisk Formation in the Magnetosphere of a Hot Jupiter. *Astrophys. J.* **769**, 28 (2013). doi:10.1088/0004-637X/769/1/28
- T.D. Arber, C.S. Brady, S. Shelyag, Alfvén Wave Heating of the Solar Chromosphere: 1.5D Models. *Astrophys. J.* **817**, 94 (2016). doi:10.3847/0004-637X/817/2/94
- J. Arons, C.E. Max, Hydromagnetic Waves in Molecular Clouds. *Astrophys. J. Lett.* **196**, 77 (1975). doi:10.1086/181748
- I. Arregui, Wave heating of the solar atmosphere. *Royal Society of London Philosophical Transactions Series A* **373**, 40261 (2015). doi:10.1098/rsta.2014.0261
- I. Arregui, R. Oliver, J.L. Ballester, Prominence Oscillations. *Living Reviews in Solar Physics* **9**, 2 (2012). doi:10.12942/lrsp-2012-2
- D. Arzoumanian, P. André, P. Didelon, V. Könyves, N. Schneider, A. Men'shchikov, T. Soubie, A. Zavagno, S. Bontemps, J. di Francesco, M. Griffin, M. Hennemann, T. Hill, J. Kirk, P. Martin, V. Minier, S. Molinari, F. Motte, N. Peretto, S. Pezzuto, L. Spinoglio, D. Ward-Thompson, G. White, C.D. Wilson, Characterizing interstellar filaments with Herschel in IC 5146. *Astron. Astrophys.* **529**, 6 (2011). doi:10.1051/0004-6361/201116596
- E. Audit, P. Hennebelle, Thermal condensation in a turbulent atomic hydrogen flow. *Astron. Astrophys.* **433**, 1–13 (2005). doi:10.1051/0004-6361:20041474
- E. Audit, P. Hennebelle, On the structure of the turbulent interstellar clouds. Influence of the equation of state on the dynamics of 3D compressible flows. *Astron. Astrophys.* **511**, 76 (2010). doi:10.1051/0004-6361/200912695
- V. Avila-Reese, E. Vázquez-Semadeni, Turbulent Dissipation in the Interstellar Medium: The Coexistence of Forced and Decaying Regimes and Implications for Galaxy Formation and Evolution. *Astrophys. J.* **553**, 645–660 (2001). doi:10.1086/320944
- F. Bagenal, P.A. Delamere, Flow of mass and energy in the magnetospheres of jupiter and saturn. *Journal of Geophysical Research: Space Physics* **116**(A5), (2011). A05209. doi:10.1029/2010JA016294. <http://dx.doi.org/10.1029/2010JA016294>
- N.M. Bakhareva, V.V. Zaitsev, M.L. Khodachenko, Dynamic regimes of prominence evolution. *Solar Phys.* **139**, 299–314 (1992). doi:10.1007/BF00159156
- I. Ballai, R. Oliver, M. Alexandrou, Dissipative instability in partially ionised prominence plasmas. *Astron. Astrophys.* **577**, 82 (2015). doi:10.1051/0004-6361/201423973
- J. Ballesteros-Paredes, E. Vázquez-Semadeni, J. Scalo, Clouds as Turbulent Density Fluctuations: Implications for Pressure Confinement and Spectral Line Data Interpretation. *Astrophys. J.* **515**, 286–303 (1999). doi:10.1086/307007
- J. Ballesteros-Paredes, R.S. Klessen, M.-M. Mac Low, E. Vázquez-Semadeni, Molecular Cloud Turbulence and Star Formation. *Protostars and Planets V*, 63–80 (2007)
- J. Ballesteros-Paredes, E. Vázquez-Semadeni, A. Gazol, L.W. Hartmann, F. Heitsch, P. Colín, Gravity or turbulence? - II. Evolving column density probability distribution functions in molecular clouds. *Month. Not. R. Astron. Soc.* **416**, 1436–1442 (2011a). doi:10.1111/j.1365-2966.2011.19141.x
- J. Ballesteros-Paredes, L.W. Hartmann, E. Vázquez-Semadeni, F. Heitsch, M.A. Zamora-Avilés, Gravity or turbulence? Velocity dispersion-size relation. *Month. Not. R. Astron. Soc.* **411**, 65–70 (2011b). doi:10.1111/j.1365-2966.2010.17657.x
- D.S. Balsara, Wave Propagation in Molecular Clouds. *Astrophys. J.* **465**, 775 (1996). doi:10.1086/177462
- P.M. Banks, G. Kockarts, *Aeronomy*. 1973
- S. Barceló, M. Carbonell, J.L. Ballester, Time damping of non-adiabatic magnetohydrodynamic waves in a partially ionised prominence medium: Effect of a background flow. *Astron. Astrophys.* **525**, 60 (2011). doi:10.1051/0004-6361/201015499
- N.M. Batalha, J.F. Rowe, S.T. Bryson, T. Barclay, C.J. Burke, D.A. Caldwell, J.L. Christiansen, F. Mullally, S.E. Thompson, T.M. Brown, A.K. Dupree, D.C. Fabrycky, E.B. Ford, J.J. Fortney, R.L. Gilliland, H. Isaacson, D.W. Latham, G.W. Marcy, S.N. Quinn, D. Ragozzine, A. Shporer, W.J. Borucki, D.R. Ciardi, T.N. Gautier III, M.R. Haas, J.M. Jenkins, D.G. Koch, J.J. Lissauer, W. Rapin, G.S. Basri, A.P. Boss, L.A. Buchhave, J.A.

- Carter, D. Charbonneau, J. Christensen-Dalsgaard, B.D. Clarke, W.D. Cochran, B.-O. Demory, J.-M. Desert, E. Devore, L.R. Doyle, G.A. Esquerdo, M. Everett, F. Fressin, J.C. Geary, F.R. Girouard, A. Gould, J.R. Hall, M.J. Holman, A.W. Howard, S.B. Howell, K.A. Ibrahim, K. Kinemuchi, H. Kjeldsen, T.C. Klaus, J. Li, P.W. Lucas, S. Meibom, R.L. Morris, A. Prša, E. Quintana, D.T. Sanderfer, D. Sasselov, S.E. Seader, J.C. Smith, J.H. Steffen, M. Still, M.C. Stumpe, J.C. Tarter, P. Tenenbaum, G. Torres, J.D. Twicken, K. Uddin, J. Van Cleve, L. Walkowicz, W.F. Welsh, Planetary Candidates Observed by Kepler. III. Analysis of the First 16 Months of Data. *ApJS* **204**, 24 (2013). doi:10.1088/0067-0049/204/2/24
- C. Battersby, A. Ginsburg, J. Bally, S. Longmore, M. Dunham, J. Darling, The Onset of Massive Star Formation: The Evolution of Temperature and Density Structure in an Infrared Dark Cloud. *Astrophys. J.* **787**, 113 (2014). doi:10.1088/0004-637X/787/2/113
- S.J. Bauer, *Physics of planetary ionospheres* 1973
- R. Beck, Magnetic Fields in Galaxies, in *Magnetic Fields in Diffuse Media*, ed. by A. Lazarian, E.M. de Gouveia Dal Pino, C. Melioli Astrophysics and Space Science Library, vol. 407, 2015, p. 507. doi:10.1007/978-3-662-44625-6-18
- E.S. Belenkaya, S.Y. Bobrovnikov, I.I. Alexeev, V.V. Kalegaev, S.W.H. Cowley, A model of Jupiter's magnetospheric magnetic field with variable magnetopause flaring. *PLSS* **53**, 863–872 (2005). doi:10.1016/j.pss.2005.03.004
- T.E. Berger, R.A. Shine, G.L. Slater, T.D. Tarbell, A.M. Title, T.J. Okamoto, K. Ichimoto, Y. Katsukawa, Y. Suematsu, S. Tsuneta, B.W. Lites, T. Shimizu, Hinode SOT Observations of Solar Quiescent Prominence Dynamics. *Astrophys. J. Lett.* **676**, 89–92 (2008). doi:10.1086/587171
- T.E. Berger, G. Slater, N. Hurlburt, R. Shine, T. Tarbell, A. Title, B.W. Lites, T.J. Okamoto, K. Ichimoto, Y. Katsukawa, T. Magara, Y. Suematsu, T. Shimizu, Quiescent Prominence Dynamics Observed with the Hinode Solar Optical Telescope. I. Turbulent Upflow Plumes. *Astrophys. J.* **716**, 1288–1307 (2010). doi:10.1088/0004-637X/716/2/1288
- A. Bhardwaj, G.R. Gladstone, Auroras on Saturn, Uranus, and Neptune. *Advances in Space Research* **26**(10), 1551–1558 (2000)
- J.A. Bittencourt, *Fundamentals of plasma physics* (Pergamon Press, Oxford, 1986)
- L. Blitz, F.H. Shu, The origin and lifetime of giant molecular cloud complexes. *Astrophys. J.* **238**, 148–157 (1980). doi:10.1086/157968
- P. Bodenheimer, Angular Momentum Evolution of Young Stars and Disks. *Ann. Rev. Astron. Astrophys.* **33**, 199–238 (1995). doi:10.1146/annurev.aa.33.090195.001215
- X. Bonfils, X. Delfosse, S. Udry, T. Forveille, M. Mayor, C. Perrier, F. Bouchy, M. Gillon, C. Lovis, F. Pepe, D. Queloz, N.C. Santos, D. Ségransan, J.-L. Bertaux, The HARPS search for southern extra-solar planets. XXXI. The M-dwarf sample. *Astron. Astrophys.* **549**, 109 (2013). doi:10.1051/0004-6361/201014704
- S.I. Braginskii, Transport Processes in a Plasma. *Reviews of Plasma Physics* **1**, 205 (1965)
- O. Buneman, Excitation of Field Aligned Sound Waves by Electron Streams. *Physical Review Letters* **10**, 285–287 (1963). doi:10.1103/PhysRevLett.10.285
- A. Burkert, L. Hartmann, Collapse and Fragmentation in Finite Sheets. *Astrophys. J.* **616**, 288–300 (2004). doi:10.1086/424895
- P.S. Cally, Phase-mixing and surface waves: a new interpretation. *Journal of Plasma Physics* **45**, 453–479 (1991). doi:10.1017/S002237780001583X
- R.H. Cameron, D. Schmitt, J. Jiang, E. Işık, Surface flux evolution constraints for flux transport dynamos. *Astron. Astrophys.* **542**, 127 (2012). doi:10.1051/0004-6361/201218906
- M. Carbonell, R. Oliver, J.L. Ballester, Time damping of linear non-adiabatic magnetohydrodynamic waves in an unbounded plasma with solar coronal properties. *Astron. Astrophys.* **415**, 739–750 (2004). doi:10.1051/0004-6361:20034630
- M. Carbonell, J. Terradas, R. Oliver, J.L. Ballester, Spatial damping of linear non-adiabatic magnetoacoustic waves in a prominence medium. *Astron. Astrophys.* **460**, 573–581 (2006). doi:10.1051/0004-6361:20065528
- M. Carbonell, P. Forteza, R. Oliver, J.L. Ballester, The spatial damping of magnetohydrodynamic waves in a flowing partially ionised prominence plasma. *Astron. Astrophys.* **515**, 80 (2010). doi:10.1051/0004-6361/200913024
- P. Cargill, I. de Moortel, Solar physics: Waves galore. *Nature* **475**, 463–464 (2011). doi:10.1038/475463a
- M. Carlsson, A computer program for solving multi-level non-LTE radiative transfer problems in moving or static atmospheres. *Uppsala Astronomical Observatory Reports* **33** (1986)



- M. Carlsson, R.F. Stein, Dynamic Hydrogen Ionization. *Astrophys. J.* **572**, 626–635 (2002). doi:10.1086/340293
- S.E. Caunt, M.J. Korpi, A 3D MHD model of astrophysical flows: Algorithms, tests and parallelisation. *Astron. Astrophys.* **369**, 706–728 (2001). doi:10.1051/0004-6361:20010157
- Z. Ceplecha, Influx of interplanetary bodies onto earth. *Astron. Astrophys.* **263**, 361–366 (1992)
- J.M. Chadney, M. Galand, Y.C. Unruh, T.T. Koskinen, J. Sanz-Forcada, XUV-driven mass loss from extrasolar giant planets orbiting active stars. *Icarus* **250**, 357–367 (2015). doi:10.1016/j.icarus.2014.12.012
- S. Chandrasekhar, *Hydrodynamic and hydromagnetic stability* 1961
- S. Chapman, T.G. Cowling, *The mathematical theory of non-uniform gases. an account of the kinetic theory of viscosity, thermal conduction and diffusion in gases* 1970
- J. Cho, A. Lazarian, E.T. Vishniac, Simulations of Magnetohydrodynamic Turbulence in a Strongly Magnetized Medium. *Astrophys. J.* **564**, 291–301 (2002). doi:10.1086/324186
- L. Chomiuk, M.S. Povich, Toward a Unification of Star Formation Rate Determinations in the Milky Way and Other Galaxies. *AJ* **142**, 197 (2011). doi:10.1088/0004-6256/142/6/197
- U.R. Christensen, Dynamo Scaling Laws and Applications to the Planets. *Space Sci. Rev.* **152**, 565–590 (2010). doi:10.1007/s11214-009-9553-2
- U.R. Christensen, J. Aubert, Scaling properties of convection-driven dynamos in rotating spherical shells and application to planetary magnetic fields. *Geophysical Journal International* **166**, 97–114 (2006). doi:10.1111/j.1365-246X.2006.03009.x
- G.E. Ciolek, S. Basu, On the Timescale for the Formation of Protostellar Cores in Magnetic Interstellar Clouds. *Astrophys. J.* **547**, 272–279 (2001). doi:10.1086/318348
- G.E. Ciolek, W.G. Roberge, Time-dependent, Multifluid, Magnetohydrodynamic Shock Waves with Grain Dynamics. I. Formulation and Numerical Tests. *Astrophys. J.* **567**, 947–961 (2002). doi:10.1086/338591
- P. Colín, E. Vázquez-Semadeni, G.C. Gómez, Molecular cloud evolution - V. Cloud destruction by stellar feedback. *Month. Not. R. Astron. Soc.* **435**, 1701–1714 (2013). doi:10.1093/mnras/stt1409
- S. Cowley, E. Bunce, R. Prangé, Saturn's polar ionospheric flows and their relation to the main auroral oval. *Annales Geophysicae* **22**, 1379–1394 (2004). doi:10.5194/angeo-22-1379-2004
- S.W.H. Cowley, E.J. Bunce, J.M. O'Rourke, A simple quantitative model of plasma flows and currents in saturn's polar ionosphere. *Journal of Geophysical Research: Space Physics* **109**(A5), (2004). A05212. doi:10.1029/2003JA010375. <http://dx.doi.org/10.1029/2003JA010375>
- S.W.H. Cowley, C.S. Arridge, E.J. Bunce, J.T. Clarke, A.J. Coates, M.K. Dougherty, J.-C. Gérard, D. Grodent, J.D. Nichols, D.L. Talboys, Auroral current systems in Saturn's magnetosphere: comparison of theoretical models with Cassini and HST observations. *Annales Geophysicae* **26**, 2613–2630 (2008). doi:10.5194/angeo-26-2613-2008
- S.W.H. Cowley, E.J. Bunce, Origin of the main auroral oval in jupiter's coupled magnetosphere-ionosphere system. *Planetary and Space Science* **49**(10A11), 1067–1088 (2001). Magnetosphere of the Outer Planets Part {II}. doi:[http://dx.doi.org/10.1016/S0032-0633\(00\)00167-7](http://dx.doi.org/10.1016/S0032-0633(00)00167-7). <http://www.sciencedirect.com/science/article/pii/S0032063300001677>
- T.E. Cravens (ed.), *Physics of solar system plasmas /Thomas E. Cravens. Cambridge : Cambridge University Press, 1997. QB 529 C72 1997. DA 1997*
- R.M. Crutcher, Magnetic Fields in Molecular Clouds. *Ann. Rev. Astron. Astrophys.* **50**, 29–63 (2012). doi:10.1146/annurev-astro-081811-125514
- R.M. Crutcher, N. Hakobian, T.H. Troland, Testing Magnetic Star Formation Theory. *Astrophys. J.* **692**, 844–855 (2009). doi:10.1088/0004-637X/692/1/844
- R.M. Crutcher, N. Hakobian, T.H. Troland, Self-consistent analysis of OH Zeeman observations. *Month. Not. R. Astron. Soc.* **402**, 64–66 (2010). doi:10.1111/j.1745-3933.2009.00802.x
- J.E. Dale, B. Ercolano, I.A. Bonnell, Ionizing feedback from massive stars in massive clusters - II. Disruption of bound clusters by photoionization. *Month. Not. R. Astron. Soc.* **424**, 377–392 (2012). doi:10.1111/j.1365-2966.2012.21205.x
- A. Dalgarno, M. Yan, W. Liu, Electron energy deposition in a gas mixture of atomic and molecular hydrogen and helium. *The Astrophysical Journal Supplement Series* **125**(1), 237 (1999). <http://stacks.iop.org/0067-0049/125/i=1/a=237>

- W.B. Dapp, S. Basu, Averting the magnetic braking catastrophe on small scales: disk formation due to Ohmic dissipation. *Astron. Astrophys.* **521**, 56 (2010). doi:10.1051/0004-6361/201015700
- W.B. Dapp, S. Basu, M.W. Kunz, Bridging the gap: disk formation in the Class 0 phase with ambipolar diffusion and Ohmic dissipation. *Astron. Astrophys.* **541**, 35 (2012). doi:10.1051/0004-6361/201117876
- B. De Pontieu, G. Haerendel, Weakly damped Alfvén waves as drivers for spicules. *Astron. Astrophys.* **338**, 729–736 (1998)
- B. De Pontieu, R. Erdélyi, S.P. James, Solar chromospheric spicules from the leakage of photospheric oscillations and flows. *Nature* **430**, 536–539 (2004). doi:10.1038/nature02749
- B. De Pontieu, P.C.H. Martens, H.S. Hudson, Chromospheric Damping of Alfvén Waves. *Astrophys. J.* **558**, 859–871 (2001). doi:10.1086/322408
- B. De Pontieu, S.W. McIntosh, M. Carlsson, V.H. Hansteen, T.D. Tarbell, C.J. Schrijver, A.M. Title, R.A. Shine, S. Tsuneta, Y. Katsukawa, K. Ichimoto, Y. Suematsu, T. Shimizu, S. Nagata, Chromospheric Alfvénic Waves Strong Enough to Power the Solar Wind. *Science* **318**, 1574 (2007). doi:10.1126/science.1151747
- B. De Pontieu, S.W. McIntosh, M. Carlsson, V.H. Hansteen, T.D. Tarbell, P. Boerner, J. Martinez-Sykora, C.J. Schrijver, A.M. Title, The Origins of Hot Plasma in the Solar Corona. *Science* **331**, 55 (2011). doi:10.1126/science.1197738
- B. De Pontieu, M. Carlsson, L.H.M. Rouppe van der Voort, R.J. Rutten, V.H. Hansteen, H. Watanabe, Ubiquitous Torsional Motions in Type II Spicules. *Astrophys. J. Lett.* **752**, 12 (2012). doi:10.1088/2041-8205/752/1/L12
- A.J. Díaz, R. Soler, J.L. Ballester, Rayleigh-Taylor Instability in Partially Ionized Compressible Plasmas. *Astrophys. J.* **754**, 41 (2012). doi:10.1088/0004-637X/754/1/41
- C.L. Dobbs, M.R. Krumholz, J. Ballesteros-Paredes, A.D. Bolatto, Y. Fukui, M. Heyer, M.-M.M. Low, E.C. Ostriker, E. Vázquez-Semadeni, Formation of Molecular Clouds and Global Conditions for Star Formation. *Protostars and Planets VI*, 3–26 (2014). doi:10.2458/azu-uapress-9780816531240-ch001
- T.P. Downes, Driven multifluid magnetohydrodynamic molecular cloud turbulence. *Month. Not. R. Astron. Soc.* **425**, 2277–2286 (2012). doi:10.1111/j.1365-2966.2012.21577.x
- T.P. Downes, S. O’Sullivan, Multifluid Magnetohydrodynamic Turbulent Decay. *Astrophys. J.* **730**, 12 (2011). doi:10.1088/0004-637X/730/1/12
- B.T. Draine, Multicomponent, reacting MHD flows. *Month. Not. R. Astron. Soc.* **220**, 133–148 (1986)
- B.T. Draine, W.G. Roberge, A. Dalgarno, Magnetohydrodynamic shock waves in molecular clouds. *Astrophys. J.* **264**, 485–507 (1983). doi:10.1086/160617
- L.A. Dremukhina, Y.I. Feldstein, I.I. Alexeev, V.V. Kalegaev, M.E. Greenspan, Structure of the magnetospheric magnetic field during magnetic storms. *Journal of Geophys. Res.* **104**, 28351–28360 (1999). doi:10.1029/1999JA900261
- R. Dunn, Photometry of the solar chromosphere, PhD thesis, Harvard University, 1960
- A. Ekenbäck, M. Holmström, P. Wurz, J.-M. Grießmeier, H. Lammer, F. Selsis, T. Penz, Energetic Neutral Atoms Around HD 209458b: Estimations of Magnetospheric Properties. *Astrophys. J.* **709**, 670–679 (2010). doi:10.1088/0004-637X/709/2/670
- B.G. Elmegreen, Magnetic diffusion and ionization fractions in dense molecular clouds - The role of charged grains. *Astrophys. J.* **232**, 729–739 (1979). doi:10.1086/157333
- B.G. Elmegreen, J. Scalo, Interstellar Turbulence I: Observations and Processes. *Ann. Rev. Astron. Astrophys.* **42**, 211–273 (2004). doi:10.1146/annurev.astro.41.011802.094859
- O. Engvold, Description and Classification of Prominences, in *Astrophysics and Space Science Library*, ed. by J.-C. Vial, O. Engvold *Astrophysics and Space Science Library*, vol. 415, 2015, p. 31. doi:10.1007/978-3-319-10416-4-2
- R. Erdélyi, V. Fedun, Are There Alfvén Waves in the Solar Atmosphere? *Science* **318**, 1572 (2007). doi:10.1126/science.1153006
- R. Erdélyi, S.P. James, Can ion-neutral damping help to form spicules?. II. Random driver. *Astron. Astrophys.* **427**, 1055–1064 (2004). doi:10.1051/0004-6361:20040345
- N.V. Erkaev, T. Penz, H. Lammer, H.I.M. Lichtenegger, H.K. Biernat, P. Wurz, J.-M. Grießmeier, W.W. Weiss, Plasma and Magnetic Field Parameters in the Vicinity of Short-periodic Giant Exoplanets. *ApJS* **157**, 396–401 (2005). doi:10.1086/427904
- N.V. Erkaev, H. Lammer, P. Odert, Y.N. Kulikov, K.G. Kislyakova, M.L. Khodachenko, M. Güdel, A. Hanslmeier, H. Biernat, XUV-Exposed, Non-Hydrostatic Hydrogen-Rich Upper Atmospheres of Terrestrial Planets. Part I: Atmospheric Expansion and Thermal Escape.

- Astrobiology **13**, 1011–1029 (2013). doi:10.1089/ast.2012.0957
- S.A.E.G. Falle, A numerical scheme for multifluid magnetohydrodynamics. *Month. Not. R. Astron. Soc.* **344**, 1210–1218 (2003). doi:10.1046/j.1365-8711.2003.06908.x
- D.T. Farley Jr., A Plasma Instability Resulting in Field-Aligned Irregularities in the Ionosphere. *Journal of Geophys. Res.* **68**, 6083 (1963)
- W.M. Farrell, M.D. Desch, P. Zarka, On the possibility of coherent cyclotron emission from extrasolar planets. *Journal of Geophys. Res.* **104**, 14025–14032 (1999). doi:10.1029/1998JE900050
- M. Fatuzzo, F.C. Adams, Enhancement of Ambipolar Diffusion Rates through Field Fluctuations. *Astrophys. J.* **570**, 210–221 (2002). doi:10.1086/339502
- C. Federrath, On the universality of interstellar filaments: theory meets simulations and observations. *ArXiv e-prints* (2015)
- T. Felipe, E. Khomenko, Dependence of sunspot photospheric waves on the depth of the source of solar p-modes. *Astron. Astrophys.* **599**, 2 (2017). doi:10.1051/0004-6361/201630123
- L. Feng, B. Inhester, W.Q. Gan, Kelvin-Helmholtz Instability of a Coronal Streamer. *Astrophys. J.* **774**, 141 (2013). doi:10.1088/0004-637X/774/2/141
- J.D. Fiege, R.E. Pudritz, Helical fields and filamentary molecular clouds - I. *Month. Not. R. Astron. Soc.* **311**, 85–104 (2000). doi:10.1046/j.1365-8711.2000.03066.x
- J. Fischera, P.G. Martin, Physical properties of interstellar filaments. *Astron. Astrophys.* **542**, 77 (2012). doi:10.1051/0004-6361/201218961
- J.M. Fontenla, Chromospheric plasma and the Farley-Buneman instability in solar magnetic regions. *Astron. Astrophys.* **442**, 1099–1103 (2005). doi:10.1051/0004-6361:20053669
- J.M. Fontenla, E.H. Avrett, R. Loeser, Energy balance in the solar transition region. III - Helium emission in hydrostatic, constant-abundance models with diffusion. *Astrophys. J.* **406**, 319–345 (1993). doi:10.1086/172443
- J.M. Fontenla, W.K. Peterson, J. Harder, Chromospheric heating by the Farley-Buneman instability. *Astron. Astrophys.* **480**, 839–846 (2008). doi:10.1051/0004-6361:20078517
- P. Forteza, R. Oliver, J.L. Ballester, Time damping of non-adiabatic MHD waves in an unbounded partially ionised prominence plasma. *Astron. Astrophys.* **492**, 223–231 (2008). doi:10.1051/0004-6361:200810370
- P. Forteza, R. Oliver, J.L. Ballester, M.L. Khodachenko, Damping of oscillations by ion-neutral collisions in a prominence plasma. *Astron. Astrophys.* **461**, 731–739 (2007). doi:10.1051/0004-6361:20065900
- J.C. Foster, A.J. Coster, P.J. Erickson, J.M. Holt, F.D. Lind, W. Rideout, M. McCready, A. van Eyken, R.J. Barnes, R.A. Greenwald, F.J. Rich, Multiradar observations of the polar tongue of ionization. *Journal of Geophysical Research (Space Physics)* **110**, 09–31 (2005). doi:10.1029/2004JA010928
- C. Foullon, E. Verwichte, V.M. Nakariakov, K. Nykyri, C.J. Farrugia, Magnetic Kelvin-Helmholtz Instability at the Sun. *Astrophys. J. Lett.* **729**, 8 (2011). doi:10.1088/2041-8205/729/1/L8
- J.L. Fox, M.I. Galand, R.E. Johnson, Energy Deposition in Planetary Atmospheres by Charged Particles and Solar Photons. *Space Sci. Rev.* **139**, 3–62 (2008). doi:10.1007/s11214-008-9403-7
- R.S. Furuya, Y. Kitamura, H. Shinnaga, A Dynamically Collapsing Core and a Precursor of a Core in a Filament Supported by Turbulent and Magnetic Pressures. *Astrophys. J.* **793**, 94 (2014). doi:10.1088/0004-637X/793/2/94
- M. Galand, S. Chakrabarti, Auroral Processes in the Solar System. *Washington DC American Geophysical Union Geophysical Monograph Series* **130**, 55 (2002)
- M. Galand, L. Moore, I. Mueller-Wodarg, M. Mendillo, S. Miller, Response of Saturn's auroral ionosphere to electron precipitation: Electron density, electron temperature, and electrical conductivity. *Journal of Geophysical Research: Space Physics* **116**(A9), (2011). A09306. doi:10.1029/2010JA016412. <http://dx.doi.org/10.1029/2010JA016412>
- D. Galli, S. Lizano, F.H. Shu, A. Allen, Gravitational Collapse of Magnetized Clouds. I. Ideal Magnetohydrodynamic Accretion Flow. *Astrophys. J.* **647**, 374–381 (2006). doi:10.1086/505257
- R. Galván-Madrid, E. Keto, Q. Zhang, S. Kurtz, L.F. Rodríguez, P.T.P. Ho, Formation of an O-Star Cluster by Hierarchical Accretion in G20.08-0.14 N. *Astrophys. J.* **706**, 1036–1053 (2009). doi:10.1088/0004-637X/706/2/1036
- A. García Muñoz, Physical and chemical aeronomy of HD 209458b. *PLSS* **55**, 1426–1455 (2007). doi:10.1016/j.pss.2007.03.007

- J.-C. Gérard, D. Grodent, J. Gustin, A. Saglam, J.T. Clarke, J.T. Trauger, Characteristics of Saturn's FUV aurora observed with the Space Telescope Imaging Spectrograph. *Journal of Geophysical Research (Space Physics)* **109**, 09207 (2004). doi:10.1029/2004JA010513
- J.-C. Gérard, B. Bonfond, J. Gustin, D. Grodent, J.T. Clarke, D. Bisikalo, V. Shematovich, Altitude of Saturn's aurora and its implications for the characteristic energy of precipitated electrons. *Geophysical Research Letters* **36**(2), (2009). L02202. doi:10.1029/2008GL036554. <http://dx.doi.org/10.1029/2008GL036554>
- J.-C. Gérard, J. Gustin, W.R. Pryor, D. Grodent, B. Bonfond, A. Radioti, G.R. Gladstone, J.T. Clarke, J.D. Nichols, Remote sensing of the energy of auroral electrons in Saturn's atmosphere: Hubble and Cassini spectral observations. *Icarus* **223**, 211–221 (2013). doi:10.1016/j.icarus.2012.11.033
- J.-C. Gérard, V. Singh, A model of energy deposition of energetic electrons and euv emission in the jovian and saturnian atmospheres and implications. *Journal of Geophysical Research: Space Physics* **87**(A6), 4525–4532 (1982). doi:10.1029/JA087iA06p04525. <http://dx.doi.org/10.1029/JA087iA06p04525>
- H. Gilbert, Energy Balance, in *Solar Prominences*, ed. by J.-C. Vial, O. Engvold Astrophysics and Space Science Library, vol. 415, 2015, p. 157. doi:10.1007/978-3-319-10416-4-7
- H.R. Gilbert, V.H. Hansteen, T.E. Holzer, Neutral Atom Diffusion in a Partially Ionized Prominence Plasma. *Astrophys. J. Lett.* **706**, 464–474 (2002). doi:10.1086/342165
- H. Gilbert, G. Kilper, D. Alexander, T. Kucera, Comparing Spatial Distributions of Solar Prominence Mass Derived from Coronal Absorption. *Astrophys. J.* **727**, 25 (2011). doi:10.1088/0004-637X/727/1/25
- G. Gogoberidze, Y. Voitenko, S. Poedts, M. Goossens, Farley-Buneman Instability in the Solar Chromosphere. *Astrophys. J. Lett.* **706**, 12–16 (2009). doi:10.1088/0004-637X/706/1/L12
- G. Gogoberidze, Y. Voitenko, S. Poedts, J. De Keyser, Electrostatic plasma instabilities driven by neutral gas flows in the solar chromosphere. *Month. Not. R. Astron. Soc.* **438**, 3568–3576 (2014). doi:10.1093/mnras/stt2469
- N.J. Goldbaum, M.R. Krumholz, C.D. Matzner, C.F. McKee, The Global Evolution of Giant Molecular Clouds. II. The Role of Accretion. *Astrophys. J.* **738**, 101 (2011). doi:10.1088/0004-637X/738/1/101
- P. Goldreich, J. Kwan, Molecular Clouds. *Astrophys. J.* **189**, 441–454 (1974). doi:10.1086/152821
- G.C. Gómez, E. Vázquez-Semadeni, Filaments in Simulations of Molecular Cloud Formation. *Astrophys. J.* **791**, 124 (2014). doi:10.1088/0004-637X/791/2/124
- M.L. Goodman, Conditions for Photospherically Driven Alfvénic Oscillations to Heat the Solar Chromosphere by Pedersen Current Dissipation. *Astrophys. J.* **735**, 45 (2011). doi:10.1088/0004-637X/735/1/45
- M. Goossens, M.S. Ruderman, Conservation laws and connection formulae for resonant MHD waves. *Physica Scripta Volume T* **60**, 171–184 (1995). doi:10.1088/0031-8949/1995/T60/021
- M. Goossens, R. Erdélyi, M.S. Ruderman, Resonant MHD Waves in the Solar Atmosphere. *Space Sci. Rev.* **158**, 289–338 (2011). doi:10.1007/s11214-010-9702-7
- M. Goossens, T. Van Doorsselaere, R. Soler, G. Verth, Energy Content and Propagation in Transverse Solar Atmospheric Waves. *Astrophys. J.* **768**, 191 (2013). doi:10.1088/0004-637X/768/2/191
- P. Gouttebroze, N. Labrosse, Radiative transfer in cylindrical threads with incident radiation. VI. A hydrogen plus helium system. *Astron. Astrophys.* **503**, 663–671 (2009). doi:10.1051/0004-6361/200811483
- O. Gressel, R.P. Nelson, N.J. Turner, U. Ziegler, Global Hydromagnetic Simulations of a Planet Embedded in a Dead Zone: Gap Opening, Gas Accretion, and Formation of a Protoplanetary Jet. *Astrophys. J.* **779**, 59 (2013). doi:10.1088/0004-637X/779/1/59
- O. Gressel, N.J. Turner, R.P. Nelson, C.P. McNally, Global Simulations of Protoplanetary Disks With Ohmic Resistivity and Ambipolar Diffusion. *Astrophys. J.* **801**, 84 (2015). doi:10.1088/0004-637X/801/2/84
- J.-M. Grießmeier, P. Zarka, H. Spreeuw, Predicting low-frequency radio fluxes of known extrasolar planets. *Astron. Astrophys.* **475**, 359–368 (2007). doi:10.1051/0004-6361:20077397
- J.-M. Grießmeier, A. Stadelmann, T. Penz, H. Lammer, F. Selsis, I. Ribas, E.F. Guinan, U. Motschmann, H.K. Biernat, W.W. Weiss, The effect of tidal locking on the magnetospheric and atmospheric evolution of “Hot Jupiters”. *Astron. Astrophys.* **425**, 753–762 (2004). doi:10.1051/0004-6361:20035684

- J.-M. Grießmeier, S. Preusse, M. Khodachenko, U. Motschmann, G. Mann, H.O. Rucker, Exoplanetary radio emission under different stellar wind conditions. *PLSS* **55**, 618–630 (2007). doi:10.1016/j.pss.2006.01.008
- D. Grodent, J.H. Waite, J.-C. Gérard, A self-consistent model of the jovian auroral thermal structure. *Journal of Geophysical Research: Space Physics* **106**(A7), 12933–12952 (2001). doi:10.1029/2000JA900129. <http://dx.doi.org/10.1029/2000JA900129>
- T. Guillot, A. Burrows, W.B. Hubbard, J.I. Lunine, D. Saumon, Giant Planets at Small Orbital Distances. *Astrophys. J. Lett.* **459**, 35 (1996). doi:10.1086/309935
- J.H. Guo, Escaping Particle Fluxes in the Atmospheres of Close-in Exoplanets. I. Model of Hydrogen. *Astrophys. J.* **733**, 98 (2011). doi:10.1088/0004-637X/733/2/98
- J.H. Guo, Escaping Particle Fluxes in the Atmospheres of Close-in Exoplanets. II. Reduced Mass-loss Rates and Anisotropic Winds. *Astrophys. J.* **766**, 102 (2013). doi:10.1088/0004-637X/766/2/102
- J. Gustin, J.-C. Gérard, W. Pryor, P.D. Feldman, D. Grodent, G. Holsclaw, Characteristics of Saturn's polar atmosphere and auroral electrons derived from HST/STIS, FUSE and Cassini/UVIS spectra. *Icarus* **200**, 176–187 (2009). doi:10.1016/j.icarus.2008.11.013
- G. Haerendel, Weakly damped Alfvén waves as drivers of solar chromospheric spicules. *Nature* **360**, 241–243 (1992). doi:10.1038/360241a0
- M. Hahn, D.W. Savin, Evidence for Wave Heating of the Quiet-Sun Corona. *Astrophys. J.* **795**, 111 (2014). doi:10.1088/0004-637X/795/2/111
- J. Han, Magnetic fields in our Milky Way Galaxy and nearby galaxies, in *IAU Symposium*, ed. by A.G. Kosovichev, E. de Gouveia Dal Pino, Y. Yan IAU Symposium, vol. 294, 2013, pp. 213–224. doi:10.1017/S1743921313002561
- J.K. Hargreaves, *The solar-terrestrial environment. an introduction to geospace - the science of the terrestrial upper atmosphere, ionosphere and magnetosphere* 1992
- L. Hartmann, A. Burkert, On the Structure of the Orion A Cloud and the Formation of the Orion Nebula Cluster. *Astrophys. J.* **654**, 988–997 (2007). doi:10.1086/509321
- L. Hartmann, J. Ballesteros-Paredes, E.A. Bergin, Rapid Formation of Molecular Clouds and Stars in the Solar Neighborhood. *Astrophys. J.* **562**, 852–868 (2001). doi:10.1086/323863
- J.S. Heiner, E. Vázquez-Semadeni, J. Ballesteros-Paredes, Molecular cloud formation as seen in synthetic H I and molecular gas observations. *Month. Not. R. Astron. Soc.* **452**, 1353–1374 (2015). doi:10.1093/mnras/stv1153
- P. Heinzel, U. Anzer, Radiative equilibrium in solar prominences reconsidered. *Astron. Astrophys.* **539**, 49 (2012). doi:10.1051/0004-6361/200913537
- P. Heinzel, U. Anzer, S. Gunár, Solar quiescent prominences. Filamentary structure and energetics. *Mem. Soc. As. It.* **81**, 654 (2010)
- P. Heinzel, S. Gunár, U. Anzer, Fast approximate radiative transfer method for visualizing the fine structure of prominences in the hydrogen H $\alpha$  line. *Astron. Astrophys.* **579**, 16 (2015). doi:10.1051/0004-6361/201525716
- F. Heitsch, Gravitational Infall onto Molecular Filaments. II. Externally Pressurized Cylinders. *Astrophys. J.* **776**, 62 (2013). doi:10.1088/0004-637X/776/1/62
- F. Heitsch, L. Hartmann, Rapid Molecular Cloud and Star Formation: Mechanisms and Movies. *Astrophys. J.* **689**, 290–301 (2008). doi:10.1086/592491
- F. Heitsch, E.G. Zweibel, A.D. Slyz, J.E.G. Devriendt, Turbulent Ambipolar Diffusion: Numerical Studies in Two Dimensions. *Astrophys. J.* **603**, 165–179 (2004). doi:10.1086/381428
- F. Heitsch, A. Burkert, L.W. Hartmann, A.D. Slyz, J.E.G. Devriendt, Formation of Structure in Molecular Clouds: A Case Study. *Astrophys. J. Lett.* **633**, 113–116 (2005). doi:10.1086/498413
- F. Heitsch, A.D. Slyz, J.E.G. Devriendt, L.W. Hartmann, A. Burkert, The Birth of Molecular Clouds: Formation of Atomic Precursors in Colliding Flows. *Astrophys. J.* **648**, 1052–1065 (2006). doi:10.1086/505931
- F. Heitsch, L.W. Hartmann, A.D. Slyz, J.E.G. Devriendt, A. Burkert, Cooling, Gravity, and Geometry: Flow-driven Massive Core Formation. *Astrophys. J.* **674**, 316–328 (2008). doi:10.1086/523697
- P. Hennebelle, P. André, Ion-neutral friction and accretion-driven turbulence in self-gravitating filaments. *Astron. Astrophys.* **560**, 68 (2013). doi:10.1051/0004-6361/201321761
- P. Hennebelle, M. Pérault, Dynamical condensation in a thermally bistable flow. Application to interstellar cirrus. *Astron. Astrophys.* **351**, 309–322 (1999)
- P. Hennebelle, M. Pérault, Dynamical condensation in a magnetized and thermally bistable flow. Application to interstellar cirrus. *Astron. Astrophys.* **359**, 1124–1138 (2000)

- V.M.J. Henriques, D. Kuridze, M. Mathioudakis, F.P. Keenan, Quiet-Sun H $\alpha$  Transients and Corresponding Small-scale Transition Region and Coronal Heating. *Astrophys. J.* **820**, 124 (2016). doi:10.3847/0004-637X/820/2/124
- M. Heyer, C. Krawczyk, J. Duval, J.M. Jackson, Re-Examining Larson's Scaling Relationships in Galactic Molecular Clouds. *Astrophys. J.* **699**, 1092–1103 (2009). doi:10.1088/0004-637X/699/2/1092
- J. Heyvaerts, E.R. Priest, Coronal heating by phase-mixed shear Alfvén waves. *Astron. Astrophys.* **117**, 220–234 (1983)
- T.W. Hill, Inertial limit on corotation. *Journal of Geophys. Res.* **84**, 6554–6558 (1979). doi:10.1029/JA084iA11p06554
- T.W. Hill, The Jovian auroral oval. *Journal of Geophys. Res.* **106**, 8101–8108 (2001). doi:10.1029/2000JA000302
- A. Hillier, T. Berger, H. Isobe, K. Shibata, Numerical Simulations of the Magnetic Rayleigh-Taylor Instability in the Kippenhahn-Schlüter Prominence Model. I. Formation of Upflows. *Astrophys. J.* **746**, 120 (2012). doi:10.1088/0004-637X/746/2/120
- Y. Hiraki, C. Tao, Parameterization of ionization rate by auroral electron precipitation in Jupiter. *Annales Geophysicae* **26**(1), 77–86 (2008). doi:10.5194/angeo-26-77-2008. <http://www.ann-geophys.net/26/77/2008/>
- R. Hollerbach, G. Rüdiger, The influence of Hall drift on the magnetic fields of neutron stars. *Month. Not. R. Astron. Soc.* **337**, 216–224 (2002). doi:10.1046/j.1365-8711.2002.05905.x
- R. Hollerbach, G. Rüdiger, Hall drift in the stratified crusts of neutron stars. *Month. Not. R. Astron. Soc.* **347**, 1273–1278 (2004). doi:10.1111/j.1365-2966.2004.07307.x
- J.V. Hollweg, G. Yang, Resonance absorption of compressible magnetohydrodynamic waves at thin 'surfaces'. *Journal of Geophys. Res.* **93**, 5423–5436 (1988). doi:10.1029/JA093iA06p05423
- J.V. Hollweg, S. Jackson, D. Galloway, Alfvén waves in the solar atmosphere. III - Nonlinear waves on open flux tubes. *Solar Phys.* **75**, 35–61 (1982). doi:10.1007/BF00153458
- M. Holmström, A. Ekenbäck, F. Selsis, T. Penz, H. Lammer, P. Wurz, Energetic neutral atoms as the explanation for the high-velocity hydrogen around HD 209458b. *Nature* **451**, 970–972 (2008). doi:10.1038/nature06600
- F. Hoyle, On the structure of disk-shaped extragalactic nebulae. II. On the condensation of stars the luminosity function, and the distribution of bright stars. *Month. Not. R. Astron. Soc.* **105**, 302 (1945). doi:10.1093/MNRAS/105.5.302
- J.D. Huba, *NRL Plasma Formulary* (Naval Research Laboratory, United States, 1998)
- M.M. I.C.F. Müller-Wodarg, L. Moore, G. M., Magnetosphere-atmosphere coupling at Saturn: Response of thermosphere and ionosphere to steady state polar forcing. *Icarus* **221**, 481–494 (2012). doi:10.1016/j.icarus.2012.08.034
- J.A. Ionson, Resonant absorption of Alfvénic surface waves and the heating of solar coronal loops. *Astrophys. J.* **226**, 650–673 (1978). doi:10.1086/156648
- W.-H. Ip, A. Kopp, J.-H. Hu, On the Star-Magnetosphere Interaction of Close-in Exoplanets. *Astrophys. J. Lett.* **602**, 53–56 (2004). doi:10.1086/382274
- S.P. James, R. Erdélyi, Spicule formation by ion-neutral damping. *Astron. Astrophys.* **393**, 11–14 (2002). doi:10.1051/0004-6361:20021126
- S.P. James, R. Erdélyi, B. De Pontieu, Can ion-neutral damping help to form spicules? *Astron. Astrophys.* **406**, 715–724 (2003). doi:10.1051/0004-6361:20030685
- A.-K. Jappsen, R.S. Klessen, Protostellar angular momentum evolution during gravoturbulent fragmentation. *Astron. Astrophys.* **423**, 1–12 (2004). doi:10.1051/0004-6361:20040220
- D.B. Jess, R.J. Morton, G. Verth, V. Fedun, S.D.T. Grant, I. Giagkiozis, Multiwavelength Studies of MHD Waves in the Solar Chromosphere. An Overview of Recent Results. *Space Sci. Rev.* **190**, 103–161 (2015). doi:10.1007/s11214-015-0141-3
- J. Jijina, P.C. Myers, F.C. Adams, Dense Cores Mapped in Ammonia: A Database. *ApJS* **125**, 161–236 (1999). doi:10.1086/313268
- E.P.G. Johansson, T. Bagdonat, U. Motschmann, Consequences of expanding exoplanetary atmospheres for magnetospheres. *Astron. Astrophys.* **496**, 869–877 (2009). doi:10.1051/0004-6361/200810509
- A.C. Jones, T.P. Downes, The Kelvin-Helmholtz instability in weakly ionized plasmas: ambipolar-dominated and Hall-dominated flows. *Month. Not. R. Astron. Soc.* **418**, 390–400 (2011). doi:10.1111/j.1365-2966.2011.19491.x
- A.C. Jones, T.P. Downes, The Kelvin-Helmholtz instability in weakly ionized plasmas - II. Multifluid effects in molecular clouds. *Month. Not. R. Astron. Soc.* **420**, 817–828 (2012).

- doi:10.1111/j.1365-2966.2011.20095.x
- B.-I. Jun, M.L. Norman, J.M. Stone, A Numerical Study of Rayleigh-Taylor Instability in Magnetic Fluids. *Astrophys. J.* **453**, 332 (1995). doi:10.1086/176393
- M.C. Kelley, *The Earth's Ionosphere: Plasma Physics and Electrodynamics*. International Geophysics (Elsevier Science, ???, 2009). ISBN 9780080916576
- M.L. Khodachenko, Modeling the dynamics of partially ionized plasma in solar magnetic tubes. *Astronomy Reports* **40**, 273–285 (1996)
- M.L. Khodachenko, V.V. Zaitsev, Formation of Intensive Magnetic Flux Tubes in a Converging Flow of Partially Ionized Solar Photospheric Plasma. *Astrophys. Space Sci.* **279**, 389–410 (2002). doi:10.1023/A:1015162131331
- M.L. Khodachenko, T.D. Arber, H.O. Rucker, A. Hanslmeier, Collisional and viscous damping of MHD waves in partially ionized plasmas of the solar atmosphere. *Astron. Astrophys.* **422**, 1073–1084 (2004). doi:10.1051/0004-6361:20034207
- M.L. Khodachenko, H.O. Rucker, R. Oliver, T.D. Arber, A. Hanslmeier, On the mechanisms of MHD wave damping in the partially ionized solar plasmas. *Advances in Space Research* **37**, 447–455 (2006). doi:10.1016/j.asr.2005.02.025
- M.L. Khodachenko, I. Ribas, H. Lammer, J.-M. Grießmeier, M. Leitner, F. Selsis, C. Eiroa, A. Hanslmeier, H.K. Biernat, C.J. Farrugia, H.O. Rucker, Coronal Mass Ejection (CME) Activity of Low Mass M Stars as An Important Factor for The Habitability of Terrestrial Exoplanets. I. CME Impact on Expected Magnetospheres of Earth-Like Exoplanets in Close-In Habitable Zones. *Astrobiology* **7**, 167–184 (2007a). doi:10.1089/ast.2006.0127
- M.L. Khodachenko, H. Lammer, H.I.M. Lichtenegger, D. Langmayr, N.V. Erkaev, J.-M. Grießmeier, M. Leitner, T. Penz, H.K. Biernat, U. Motschmann, H.O. Rucker, Mass loss of Hot Jupiters and Implications for CoRoT discoveries. Part I: The importance of magnetospheric protection of a planet against ion loss caused by coronal mass ejections. *PLSS* **55**, 631–642 (2007b). doi:10.1016/j.pss.2006.07.010
- M.L. Khodachenko, I. Alexeev, E. Belenkaya, H. Lammer, J.-M. Grießmeier, M. Leitzinger, P. Odert, T. Zaqarashvili, H.O. Rucker, Magnetospheres of "Hot Jupiters": The Importance of Magnetodisks in Shaping a Magnetospheric Obstacle. *Astrophys. J.* **744**, 70 (2012). doi:10.1088/0004-637X/744/1/70
- M.L. Khodachenko, Y. Sasunov, O.V. Arkhypov, I.I. Alexeev, E.S. Belenkaya, H. Lammer, K.G. Kislyakova, P. Odert, M. Leitzinger, M. Güdel, Stellar CME activity and its possible influence on exoplanets' environments: Importance of magnetospheric protection, in *IAU Symposium*, ed. by B. Schmieder, J.-M. Malherbe, S.T. Wu IAU Symposium, vol. 300, 2014, pp. 335–346. doi:10.1017/S1743921313011174
- M.L. Khodachenko, I.F. Shaikhislamov, H. Lammer, P.A. Prokopov, Atmosphere Expansion and Mass Loss of Close-orbit Giant Exoplanets Heated by Stellar XUV. II. Effects of Planetary Magnetic Field; Structuring of Inner Magnetosphere. *Astrophys. J.* **813**, 50 (2015). doi:10.1088/0004-637X/813/1/50
- E. Khomenko, M. Collados, Heating of the Magnetized Solar Chromosphere by Partial Ionization Effects. *Astrophys. J.* **747**, 87 (2012). doi:10.1088/0004-637X/747/2/87
- E. Khomenko, M. Collados, A. Díaz, N. Vitas, Fluid description of multi-component solar partially ionized plasma. *Physics of Plasmas* **21**(9), 092901 (2014a). doi:10.1063/1.4894106
- E. Khomenko, A. Díaz, A. de Vicente, M. Collados, M. Luna, Rayleigh-Taylor instability in prominences from numerical simulations including partial ionization effects. *Astron. Astrophys.* **565**, 45 (2014b). doi:10.1051/0004-6361/201322918
- T.L. Killeen, P.B. Hays, G.R. Carignan, R.A. Heelis, W.B. Hanson, N.W. Spencer, L.H. Brace, Ion-neutral coupling in the high-latitude F region Evaluation of ion heating terms from Dynamics Explorer 2. *Journal of Geophys. Res.* **89**, 7495–7508 (1984). doi:10.1029/JA089iA09p07495
- Y.H. Kim, J.L. Fox, H.S. Porter, Densities and vibrational distribution of H(3+) in the Jovian auroral ionosphere. *Journal of Geophys. Res.* **97**, 6093–6101 (1992). doi:10.1029/92JE00454
- R. Kippenhahn, A. Schlüter, Eine Theorie der solaren Filamente. Mit 7 Textabbildungen. *Z. f. Astrophysik* **43**, 36 (1957)
- H. Kirk, P.C. Myers, T.L. Bourke, R.A. Gutermuth, A. Hedden, G.W. Wilson, Filamentary Accretion Flows in the Embedded Serpens South Protocluster. *Astrophys. J.* **766**, 115 (2013). doi:10.1088/0004-637X/766/2/115
- H. Kirk, M. Klassen, R. Pudritz, S. Pillsworth, The Role of Turbulence and Magnetic Fields in Simulated Filamentary Structure. *Astrophys. J.* **802**, 75 (2015). doi:10.1088/0004-

- 637X/802/2/75
- K.G. Kislyakova, H. Lammer, M. Holmström, M. Panchenko, P. Odert, N.V. Erkaev, M. Leitzinger, M.L. Khodachenko, Y.N. Kulikov, M. Güdel, A. Hanslmeier, XUV-Exposed, Non-Hydrostatic Hydrogen-Rich Upper Atmospheres of Terrestrial Planets. Part II: Hydrogen Coronae and Ion Escape. *Astrobiology* **13**, 1030–1048 (2013). doi:10.1089/ast.2012.0958
- K.G. Kislyakova, C.P. Johnstone, P. Odert, N.V. Erkaev, H. Lammer, T. Lüftinger, M. Holmström, M.L. Khodachenko, M. Güdel, Stellar wind interaction and pick-up ion escape of the Kepler-11 "super-Earths". *Astron. Astrophys.* **562**, 116 (2014). doi:10.1051/0004-6361/201322933
- R.S. Klessen, P. Hennebelle, Accretion-driven turbulence as universal process: galaxies, molecular clouds, and protostellar disks. *Astron. Astrophys.* **520**, 17 (2010). doi:10.1051/0004-6361/200913780
- B. Körtgen, R. Banerjee, Impact of magnetic fields on molecular cloud formation and evolution. *Month. Not. R. Astron. Soc.* **451**, 3340–3353 (2015). doi:10.1093/mnras/stv1200
- T.T. Koskinen, R.V. Yelle, P. Lavvas, N.K. Lewis, Characterizing the Thermosphere of HD209458b with UV Transit Observations. *Astrophys. J.* **723**, 116–128 (2010). doi:10.1088/0004-637X/723/1/116
- T.T. Koskinen, M.J. Harris, R.V. Yelle, P. Lavvas, The escape of heavy atoms from the ionosphere of HD209458b. I. A photochemical-dynamical model of the thermosphere. *Icarus* **226**, 1678–1694 (2013). doi:10.1016/j.icarus.2012.09.027
- H. Koyama, S.-i. Inutsuka, An Origin of Supersonic Motions in Interstellar Clouds. *Astrophys. J. Lett.* **564**, 97–100 (2002). doi:10.1086/338978
- N.A. Krall, A.W. Trivelpiece, *Principles of plasma physics* 1973
- R. Krasnopolsky, A. Königl, Self-similar Collapse of Rotating Magnetic Molecular Cloud Cores. *Astrophys. J.* **580**, 987–1012 (2002). doi:10.1086/343890
- M.R. Krumholz, C.D. Matzner, C.F. McKee, The Global Evolution of Giant Molecular Clouds. I. Model Formulation and Quasi-Equilibrium Behavior. *Astrophys. J.* **653**, 361–382 (2006). doi:10.1086/508679
- T. Kudoh, K. Shibata, Alfvén Wave Model of Spicules and Coronal Heating. *Astrophys. J.* **514**, 493–505 (1999). doi:10.1086/306930
- V. Kukhianidze, T.V. Zaqarashvili, E. Khutsishvili, Observation of kink waves in solar spicules. *Astron. Astrophys.* **449**, 35–38 (2006). doi:10.1051/0004-6361:200600018
- R. Kulsrud, W.P. Pearce, The Effect of Wave-Particle Interactions on the Propagation of Cosmic Rays. *Astrophys. J.* **156**, 445 (1969). doi:10.1086/149981
- D. Kuridze, R.J. Morton, R. Erdélyi, G.D. Dorrian, M. Mathioudakis, D.B. Jess, F.P. Keenan, Transverse Oscillations in Chromospheric Mottles. *Astrophys. J.* **750**, 51 (2012). doi:10.1088/0004-637X/750/1/51
- D. Kuridze, V. Henriques, M. Mathioudakis, R. Erdélyi, T.V. Zaqarashvili, S. Shelyag, P.H. Keys, F.P. Keenan, The Dynamics of Rapid Redshifted and Blueshifted Excursions in the Solar H $\alpha$  Line. *Astrophys. J.* **802**, 26 (2015). doi:10.1088/0004-637X/802/1/26
- D. Kuridze, T.V. Zaqarashvili, V. Henriques, M. Mathioudakis, F.P. Keenan, A. Hanslmeier, Kelvin-Helmholtz Instability in Solar Chromospheric Jets: Theory and Observation. *Astrophys. J.* **830**, 133 (2016). doi:10.3847/0004-637X/830/2/133
- N. Labrosse, P. Heinzel, J. Vial, T. Kucera, S. Parenti, S. Gunár, B. Schmieder, G. Kilper, Physics of Solar Prominences: I Spectral Diagnostics and Non-LTE Modelling. *Space Sci. Rev.* **151**, 243–332 (2010). doi:10.1007/s11214-010-9630-6
- C.J. Lada, E.A. Lada, Embedded Clusters in Molecular Clouds. *Ann. Rev. Astron. Astrophys.* **41**, 57–115 (2003). doi:10.1146/annurev.astro.41.011802.094844
- H. Lammer, F. Selsis, I. Ribas, E.F. Guinan, S.J. Bauer, W.W. Weiss, Atmospheric Loss of Exoplanets Resulting from Stellar X-Ray and Extreme-Ultraviolet Heating. *Astrophys. J. Lett.* **598**, 121–124 (2003). doi:10.1086/380815
- H. Lammer, H.I.M. Lichtenegger, Y.N. Kulikov, J.-M. Grießmeier, N. Terada, N.V. Erkaev, H.K. Biernat, M.L. Khodachenko, I. Ribas, T. Penz, F. Selsis, Coronal Mass Ejection (CME) Activity of Low Mass M Stars as An Important Factor for The Habitability of Terrestrial Exoplanets. II. CME-Induced Ion Pick Up of Earth-like Exoplanets in Close-In Habitable Zones. *Astrobiology* **7**, 185–207 (2007). doi:10.1089/ast.2006.0128
- H. Lammer, P. Odert, M. Leitzinger, M.L. Khodachenko, M. Panchenko, Y.N. Kulikov, T.L. Zhang, H.I.M. Lichtenegger, N.V. Erkaev, G. Wuchterl, G. Micela, T. Penz, H.K. Biernat, J. Weingrill, M. Steller, H. Ottacher, J. Hasiba, A. Hanslmeier, Determining the mass



- loss limit for close-in exoplanets: what can we learn from transit observations? *Astron. Astrophys.* **506**, 399–410 (2009). doi:10.1051/0004-6361/200911922
- H. Lammer, N.V. Erkaev, P. Odert, K.G. Kislyakova, M. Leitzinger, M.L. Khodachenko, Probing the blow-off criteria of hydrogen-rich ‘super-Earths’. *Month. Not. R. Astron. Soc.* **430**, 1247–1256 (2013). doi:10.1093/mnras/sts705
- L.D. Landau, E.M. Lifshitz, *Fluid mechanics* 1959
- Ø. Langangen, B. De Pontieu, M. Carlsson, V.H. Hansteen, G. Cauzzi, K. Reardon, Search for High Velocities in the Disk Counterpart of Type II Spicules. *Astrophys. J. Lett.* **679**, 167–170 (2008). doi:10.1086/589442
- R.B. Larson, Turbulence and star formation in molecular clouds. *Month. Not. R. Astron. Soc.* **194**, 809–826 (1981)
- A.S. Lavrukhin, I.I. Alexeev, Aurora at high latitudes of ganymede. *Astronomy Letters* **41**(11), 687–692 (2015). doi:10.1134/S1063773715110043. <http://dx.doi.org/10.1134/S1063773715110043>
- A. Lazarian, Reconnection Diffusion in Turbulent Fluids and Its Implications for Star Formation. *Space Science Reviews* **181**, 1–59 (2014). doi:10.1007/s11214-013-0031-5
- A. Lazarian, A. Esquivel, R. Crutcher, Magnetization of Cloud Cores and Envelopes and Other Observational Consequences of Reconnection Diffusion. *Astrophys. J.* **757**, 154 (2012). doi:10.1088/0004-637X/757/2/154
- J.E. Leake, T.D. Arber, The emergence of magnetic flux through a partially ionised solar atmosphere. *Å* **450**, 805–818 (2006). doi:10.1051/0004-6361:20054099
- J.E. Leake, T.D. Arber, M.L. Khodachenko, Collisional dissipation of Alfvén waves in a partially ionised solar chromosphere. *Astron. Astrophys.* **442**, 1091–1098 (2005). doi:10.1051/0004-6361:20053427
- J.E. Leake, V.S. Lukin, M.G. Linton, E.T. Meier, Multi-fluid Simulations of Chromospheric Magnetic Reconnection in a Weakly Ionized Reacting Plasma. *Astrophys. J.* **760**, 109 (2012). doi:10.1088/0004-637X/760/2/109
- J.E. Leake, C.R. DeVore, J.P. Thayer, A.G. Burns, G. Crowley, H.R. Gilbert, J.D. Huba, J. Krall, M.G. Linton, V.S. Lukin, W. Wang, Ionized Plasma and Neutral Gas Coupling in the Sun’s Chromosphere and Earth’s Ionosphere/Thermosphere. *Space Sci. Rev.* **184**, 107–172 (2014a). doi:10.1007/s11214-014-0103-1
- J.E. Leake, C.R. DeVore, J.P. Thayer, A.G. Burns, G. Crowley, H.R. Gilbert, J.D. Huba, J. Krall, M.G. Linton, V.S. Lukin, W. Wang, Ionized Plasma and Neutral Gas Coupling in the Sun’s Chromosphere and Earth’s Ionosphere/Thermosphere. *Space Sci. Rev.* **184**, 107–172 (2014b). doi:10.1007/s11214-014-0103-1
- C.W. Lee, P.C. Myers, A Catalog of Optically Selected Cores. *ApJS* **123**, 233–250 (1999). doi:10.1086/313234
- D. Lee, G. Xia, C. Daley, A. Dubey, S. Gopal, C. Graziani, D. Lamb, K. Weide, Progress in development of HEDP capabilities in FLASH’s Unsplit Staggered Mesh MHD solver. *apss* **336**, 157–162 (2011). doi:10.1007/s10509-011-0654-5
- J. Leenaarts, M. Carlsson, V. Hansteen, R.J. Rutten, Non-equilibrium hydrogen ionization in 2D simulations of the solar atmosphere. *Å* **473**, 625–632 (2007). doi:10.1051/0004-6361:20078161
- P.S. Li, C.F. McKee, R.I. Klein, The Heavy-Ion Approximation for Ambipolar Diffusion Calculations for Weakly Ionized Plasmas. *Astrophys. J.* **653**, 1280–1291 (2006). doi:10.1086/508977
- P.S. Li, A. Myers, C.F. McKee, Ambipolar Diffusion Heating in Turbulent Systems. *Astrophys. J.* **760**, 33 (2012). doi:10.1088/0004-637X/760/1/33
- P.S. Li, C.F. McKee, R.I. Klein, R.T. Fisher, Sub-Alfvénic Nonideal MHD Turbulence Simulations with Ambipolar Diffusion. I. Turbulence Statistics. *Astrophys. J.* **684**, 380–394 (2008). doi:10.1086/589874
- Z.-Y. Li, R. Krasnopolsky, H. Shang, Non-ideal MHD Effects and Magnetic Braking Catastrophe in Protostellar Disk Formation. *Astrophys. J.* **738**, 180 (2011). doi:10.1088/0004-637X/738/2/180
- Z.-Y. Li, R. Banerjee, R.E. Pudritz, J.K. Jørgensen, H. Shang, R. Krasnopolsky, A. Maury, The Earliest Stages of Star and Planet Formation: Core Collapse, and the Formation of Disks and Outflows. *Protostars and Planets VI*, 173–194 (2014). doi:10.2458/azu-uapress-9780816531240-ch008
- H.I.M. Lichtenegger, H. Gröller, H. Lammer, Y.N. Kulikov, V.I. Shematovich, On the elusive hot oxygen corona of Venus. *Geophys. Res. Lett.* **36**, 10204 (2009).

- doi:10.1029/2009GL037575
- A.E. Lifschitz, *Magnetohydrodynamics and Spectral Theory* (Kluwer Academic Publisher, Dordrecht, 1989)
- Y. Lin, Magnetic Field Topology Inferred from Studies of Fine Threads in Solar Filaments, PhD thesis, University of Oslo, Norway, 2004
- Y. Lin, O.R. Engvold, J.E. Wiik, Counterstreaming in a Large Polar Crown Filament. *Solar Phys.* **216**, 109–120 (2003). doi:10.1023/A:1026150809598
- Z.W. Ma, A. Bhattacharjee, Hall magnetohydrodynamic reconnection: The geospace environment modeling challenge. *Journal of Geophysical Research: Space Physics* **106**(A3), 3773–3782 (2001). doi:10.1029/1999JA001004. <http://dx.doi.org/10.1029/1999JA001004>
- M.-M. Mac Low, R.S. Klessen, Control of star formation by supersonic turbulence. *Reviews of Modern Physics* **76**, 125–194 (2004). doi:10.1103/RevModPhys.76.125
- M.-M. Mac Low, R.S. Klessen, A. Burkert, M.D. Smith, Kinetic Energy Decay Rates of Supersonic and Super-Alfvénic Turbulence in Star-Forming Clouds. *Physical Review Letters* **80**, 2754–2757 (1998). doi:10.1103/PhysRevLett.80.2754
- D.H. Mackay, Formation and Large-Scale Patterns of Filament Channels and Filaments, in *Solar Prominences*, ed. by J.-C. Vial, O. Engvold *Astrophysics and Space Science Library*, vol. 415 (Springer, ???, 2015), p. 355
- D.H. Mackay, J.T. Karpen, J.L. Ballester, B. Schmieder, G. Aulanier, Physics of Solar Prominences: II Magnetic Structure and Dynamics. *Space Sci. Rev.* **151**, 333–399 (2010). doi:10.1007/s11214-010-9628-0
- R.J. Maddalena, P. Thaddeus, A large, cold, and unusual molecular cloud in Monoceros. *Astrophys. J.* **294**, 231–237 (1985). doi:10.1086/163291
- C.A. Madsen, Y.S. Dimant, M.M. Oppenheim, J.M. Fontenla, The Multi-species Farley-Buneman Instability in the Solar Chromosphere. *Astrophys. J.* **783**, 128 (2014). doi:10.1088/0004-637X/783/2/128
- G. Mann, Simple magnetohydrodynamic waves. *Journal of Plasma Physics* **53**, 109–125 (1995). doi:10.1017/S0022377800018043
- D. Martínez-Gómez, R. Soler, J. Terradas, Onset of the Kelvin-Helmholtz instability in partially ionized magnetic flux tubes. *Astron. Astrophys.* **578**, 104 (2015). doi:10.1051/0004-6361/201525785
- D. Martínez-Gómez, R. Soler, J. Terradas, Multi-fluid Approach to High-frequency Waves in Plasmas: I. Small-amplitude Regime in Fully Ionized Medium. *Astrophys. J.* **832**, 101 (2016). doi:10.3847/0004-637X/832/2/101
- D. Martínez-Gómez, R. Soler, J. Terradas, Multi-fluid approach to high-frequency waves in plasmas. ii. small-amplitude regime in partially ionized media. *The Astrophysical Journal* **837**(1), 80 (2017). <http://stacks.iop.org/0004-637X/837/i=1/a=80>
- J. Martínez-Sykora, B. De Pontieu, V. Hansteen, Two-dimensional Radiative Magnetohydrodynamic Simulations of the Importance of Partial Ionization in the Chromosphere. *Astrophys. J.* **753**, 161 (2012). doi:10.1088/0004-637X/753/2/161
- T. Matsakos, A. Uribe, A. Königl, Classification of magnetized star-planet interactions: bow shocks, tails, and inspiraling flows. *Astron. Astrophys.* **578**, 6 (2015). doi:10.1051/0004-6361/201425593
- S. Matsushita, Global Presentation of the External  $S_q$  and L Current Systems. *Journal of Geophys. Res.* **70**, 4395–4398 (1965). doi:10.1029/JZ070i017p04395
- S.W. McIntosh, B. de Pontieu, M. Carlsson, V. Hansteen, P. Boerner, M. Goossens, Alfvénic waves with sufficient energy to power the quiet solar corona and fast solar wind. *Nature* **475**, 477–480 (2011). doi:10.1038/nature10235
- C.F. McKee, E.C. Ostriker, Theory of Star Formation. *Ann. Rev. Astron. Astrophys.* **45**, 565–687 (2007). doi:10.1146/annurev.astro.45.051806.110602
- C.F. McKee, E.G. Zweibel, On the virial theorem for turbulent molecular clouds. *Astrophys. J.* **399**, 551–562 (1992). doi:10.1086/171946
- C.F. McKee, E.G. Zweibel, Alfvén Waves in Interstellar Gasdynamics. *Astrophys. J.* **440**, 686 (1995). doi:10.1086/175306
- C.F. McKee, P.S. Li, R.I. Klein, Sub-Alfvénic Non-ideal MHD Turbulence Simulations with Ambipolar Diffusion. II. Comparison with Observation, Clump Properties, and Scaling to Physical Units. *Astrophys. J.* **720**, 1612–1634 (2010). doi:10.1088/0004-637X/720/2/1612
- H. Menager, M. Barthélemy, J. Lilensten, H Lyman  $\alpha$  line in Jovian aurorae: electron transport and radiative transfer coupled modelling. *Astron. Astrophys.* **509**, 56 (2010). doi:10.1051/0004-6361/200912952

- M. Mendillo, A. Nagy, J.H. Waite, Atmospheres in the solar system: comparative aeronomy. Washington DC American Geophysical Union Geophysical Monograph Series **130** (2002)
- C. Mercier, J. Heyvaerts, The downward motions in quiescent prominences. *Astron. Astrophys.* **61**, 685–693 (1977)
- L. Mestel, Magnetic braking by a stellar wind-I. *Month. Not. R. Astron. Soc.* **138**, 359 (1968). doi:10.1093/mnras/138.3.359
- L. Mestel, Magnetic fields, in *Protostars and Planets II*, ed. by D.C. Black, M.S. Matthews, 1985, pp. 320–339
- C.D. Meyer, D.S. Balsara, T.D. Aslam, A second-order accurate Super TimeStepping formulation for anisotropic thermal conduction. *Month. Not. R. Astron. Soc.* **422**, 2102–2115 (2012). doi:10.1111/j.1365-2966.2012.20744.x
- A. Mignone, G. Bodo, S. Massaglia, T. Matsakos, O. Tesileanu, C. Zanni, A. Ferrari, PLUTO: A Numerical Code for Computational Astrophysics. *ApJS* **170**, 228–242 (2007). doi:10.1086/513316
- D. Mihalas, *Stellar atmospheres* (Pergamon Press, Oxford, 1986)
- S. Miller, A. Aylward, G. Millward, Giant Planet Ionospheres and Thermospheres: The Importance of Ion-Neutral Coupling. *Space Sci. Rev.* **116**, 319–343 (2005). doi:10.1007/s11214-005-1960-4
- G. Millward, S. Miller, T. Stallard, A.D. Aylward, N. Achilleos, On the Dynamics of the Jovian Ionosphere and Thermosphere. III. The Modelling of Auroral Conductivity. *Icarus* **160**, 95–107 (2002). doi:10.1006/icar.2002.6951
- S. Molinari, B. Swinyard, J. Bally, M. Barlow, J.-P. Bernard, P. Martin, T. Moore, A. Noriega-Crespo, R. Plume, L. Testi, A. Zavagno, A. Abergel, B. Ali, L. Anderson, P. André, J.-P. Baluteau, C. Battersby, M.T. Beltrán, M. Benedettini, N. Billot, J. Blommaert, S. Bontemps, F. Boulanger, J. Brand, C. Brunt, M. Burton, L. Calzoletti, S. Carey, P. Caselli, R. Cesaroni, J. Cernicharo, S. Chakrabarti, A. Chrysostomou, M. Cohen, M. Compiègne, P. de Bernardis, G. de Gasperis, A.M. di Giorgio, D. Elia, F. Faustini, N. Flagey, Y. Fukui, G.A. Fuller, K. Ganga, P. Garcia-Lario, J. Glenn, P.F. Goldsmith, M. Griffin, M. Hoare, M. Huang, D. Ikhenade, C. Joblin, G. Joncas, M. Juvela, J.M. Kirk, G. Lagache, J.Z. Li, T.L. Lim, S.D. Lord, M. Marengo, D.J. Marshall, S. Masi, F. Massi, M. Matsuura, V. Minier, M.-A. Miville-Deschênes, L.A. Montier, L. Morgan, F. Motte, J.C. Mottram, T.G. Müller, P. Natoli, J. Neves, L. Olmi, R. Paladini, D. Paradis, H. Parsons, N. Peretto, M. Pestalozzi, S. Pezzuto, F. Piacentini, L. Piazzo, D. Polychroni, M. Pomarès, C.C. Popescu, W.T. Reach, I. Ristorcelli, J.-F. Robitaille, T. Robitaille, J.A. Rodón, A. Roy, P. Royer, D. Russeil, P. Saraceno, M. Sauvage, P. Schilke, E. Schisano, N. Schneider, F. Schuller, B. Schulz, B. Sibthorpe, H.A. Smith, M.D. Smith, L. Spinoglio, D. Stamatellos, F. Strafella, G.S. Stringfellow, E. Sturm, R. Taylor, M.A. Thompson, A. Traficante, R.J. Tuffs, G. Umana, L. Valenziano, R. Vavrek, M. Veneziani, S. Viti, C. Waelkens, D. Ward-Thompson, G. White, L.A. Wilcock, F. Wyrowski, H.W. Yorke, Q. Zhang, Clouds, filaments, and protostars: The Herschel Hi-GAL Milky Way. *Astron. Astrophys.* **518**, 100 (2010). doi:10.1051/0004-6361/201014659
- S. Molinari, J. Bally, S. Glover, T. Moore, A. Noreiga-Crespo, R. Plume, L. Testi, E. Vázquez-Semadeni, A. Zavagno, J.-P. Bernard, P. Martin, The Milky Way as a Star Formation Engine. *Protostars and Planets VI*, 125–148 (2014). doi:10.2458/azu-uapress-9780816531240-ch006
- R. Molowny-Horas, E. Wiehr, H. Balthasar, R. Oliver, J.L. Ballester, Prominence Doppler oscillations., in *JOSO Annu. Rep., 1998, p. 126 - 127*, 1999, pp. 126–127
- R.J. Morton, G. Verth, V. Fedun, S. Shelyag, R. Erdélyi, Evidence for the Photospheric Excitation of Incompressible Chromospheric Waves. *Astrophys. J.* **768**, 17 (2013). doi:10.1088/0004-637X/768/1/17
- J.I. Moses, B. Bézard, E. Lellouch, G.R. Gladstone, H. Feuchtgruber, M. Allen, Photochemistry of Saturn's Atmosphere. I. Hydrocarbon Chemistry and Comparisons with ISO Observations. *Icarus* **143**, 244–298 (2000). doi:10.1006/icar.1999.6270
- U.V. Möstl, M. Temmer, A.M. Veronig, The Kelvin-Helmholtz Instability at Coronal Mass Ejection Boundaries in the Solar Corona: Observations and 2.5D MHD Simulations. *Astrophys. J. Lett.* **766**, 12 (2013). doi:10.1088/2041-8205/766/1/L12
- T.C. Mouschovias, Nonhomologous contraction and equilibria of self-gravitating, magnetic interstellar clouds embedded in an intercloud medium: Star formation. II - Results. *Astrophys. J.* **207**, 141–158 (1976). doi:10.1086/154478
- T.C. Mouschovias, A connection between the rate of rotation of interstellar clouds, magnetic

- fields, ambipolar diffusion, and the periods of binary stars. *Astrophys. J.* **211**, 147–151 (1977). doi:10.1086/154912
- T.C. Mouschovias, Single-Stage Fragmentation and a Modern Theory of Star Formation, in *NATO Advanced Science Institutes (ASI) Series C*, ed. by C.J. Lada, N.D. Kylafis NATO Advanced Science Institutes (ASI) Series C, vol. 342, 1991, p. 449
- T.C. Mouschovias, K. Tassis, Self-consistent analysis of OH-Zeeman observations: too much noise about noise. *Month. Not. R. Astron. Soc.* **409**, 801–807 (2010). doi:10.1111/j.1365-2966.2010.17345.x
- L.G. Mundy, L.W. Looney, W.J. Welch, The Structure and Evolution of Envelopes and Disks in Young Stellar Systems. *Protostars and Planets IV*, 355 (2000)
- K. Murawski, T.V. Zaqarashvili, Numerical simulations of spicule formation in the solar atmosphere. *Astron. Astrophys.* **519**, 8 (2010). doi:10.1051/0004-6361/201014128
- N.A. Murphy, V.S. Lukin, Asymmetric Magnetic Reconnection in Weakly Ionized Chromospheric Plasmas. *Astrophys. J.* **805**, 134 (2015). doi:10.1088/0004-637X/805/2/134
- P.C. Myers, Filamentary Structure of Star-forming Complexes. *Astrophys. J.* **700**, 1609–1625 (2009). doi:10.1088/0004-637X/700/2/1609
- P.C. Myers, A.A. Goodman, Evidence for magnetic and virial equilibrium in molecular clouds. *Astrophys. J. Lett.* **326**, 27–30 (1988). doi:10.1086/185116
- A.F. Nagy, A. Balogh, T.E. Cravens, M. Mendillo, I. Müller-Wodarg, *Comparative Aeronomy*. Space Sciences Series of ISSI (Springer New York, ???, 2008). ISBN 9780387878256
- G. Newkirk Jr., Solar variability on time scales of 10 to the 5th years to 10 to the 9.6th years, in *The Ancient Sun: Fossil Record in the Earth, Moon and Meteorites*, ed. by R.O. Pepin, J.A. Eddy, R.B. Merrill, 1980, pp. 293–320
- L. Ofman, B.J. Thompson, SDO/AIA Observation of Kelvin-Helmholtz Instability in the Solar Corona. *Astrophys. J. Lett.* **734**, 11 (2011). doi:10.1088/2041-8205/734/1/L11
- T.J. Okamoto, B. De Pontieu, Propagating Waves Along Spicules. *Astrophys. J. Lett.* **736**, 24 (2011). doi:10.1088/2041-8205/736/2/L24
- T.J. Okamoto, S. Tsuneta, T.E. Berger, K. Ichimoto, Y. Katsukawa, B.W. Lites, S. Nagata, K. Shibata, T. Shimizu, R.A. Shine, Y. Suematsu, T.D. Tarbell, A.M. Title, Coronal Transverse Magnetohydrodynamic Waves in a Solar Prominence. *Science* **318**, 1577 (2007). doi:10.1126/science.1145447
- T.J. Okamoto, P. Antolin, B. De Pontieu, H. Uitenbroek, T. Van Doorselaere, T. Yokoyama, Resonant Absorption of Transverse Oscillations and Associated Heating in a Solar Prominence. I. Observational Aspects. *Astrophys. J.* **809**, 71 (2015). doi:10.1088/0004-637X/809/1/71
- R. Oliver, J.L. Ballester, Oscillations in Quiescent Solar Prominences Observations and Theory (Invited Review). *Solar Phys.* **206**, 45–67 (2002). doi:10.1023/A:1014915428440
- R. Oliver, R. Soler, J. Terradas, T.V. Zaqarashvili, M.L. Khodachenko, Dynamics of Coronal Rain and Descending Plasma Blobs in Solar Prominences. I. Fully Ionized Case. *Astrophys. J.* **784**, 21 (2014). doi:10.1088/0004-637X/784/1/21
- R. Oliver, R. Soler, J. Terradas, T.V. Zaqarashvili, Dynamics of Coronal Rain and Descending Plasma Blobs in Solar Prominences. II. Partially Ionized Case. *Astrophys. J.* **818**, 128 (2016). doi:10.3847/0004-637X/818/2/128
- D.E. Osterbrock, On Ambipolar Diffusion in H I Regions. *Astrophys. J.* **134**, 270–272 (1961). doi:10.1086/147155
- E.C. Ostriker, C.F. Gammie, J.M. Stone, Kinetic and Structural Evolution of Self-gravitating, Magnetized Clouds: 2.5-dimensional Simulations of Decaying Turbulence. *Astrophys. J.* **513**, 259–274 (1999). doi:10.1086/306842
- E.C. Ostriker, J.M. Stone, C.F. Gammie, Density, Velocity, and Magnetic Field Structure in Turbulent Molecular Cloud Models. *Astrophys. J.* **546**, 980–1005 (2001). doi:10.1086/318290
- J. Ostriker, The Equilibrium of Polytropic and Isothermal Cylinders. *Astrophys. J.* **140**, 1056 (1964). doi:10.1086/148005
- S. O’Sullivan, T.P. Downes, An explicit scheme for multfluid magnetohydrodynamics. *Month. Not. R. Astron. Soc.* **366**, 1329–1336 (2006). doi:10.1111/j.1365-2966.2005.09898.x
- S. O’Sullivan, T.P. Downes, A three-dimensional numerical method for modelling weakly ionized plasmas. *Month. Not. R. Astron. Soc.* **376**, 1648–1658 (2007). doi:10.1111/j.1365-2966.2007.11429.x
- J.E. Owen, F.C. Adams, Magnetically controlled mass-loss from extrasolar planets in close orbits. *Month. Not. R. Astron. Soc.* **444**, 3761–3779 (2014). doi:10.1093/mnras/stu1684

- P. Padoan, Å. Nordlund, A Super-Alfvénic Model of Dark Clouds. *Astrophys. J.* **526**, 279–294 (1999). doi:10.1086/307956
- A. Palau, J. Ballesteros-Paredes, E. Vazquez-Semadeni, A. Sanchez-Monge, R. Estalella, S.M. Fall, L.A. Zapata, V. Camacho, L. Gomez, R. Naranjo-Romero, G. Busquet, F. Fontani, Gravity or turbulence? -III. Evidence of pure thermal Jeans fragmentation at  $\sim 0.1$  pc scales. ArXiv e-prints (2015)
- B.P. Pandey, M. Wardle, Hall magnetohydrodynamics of partially ionized plasmas. *Month. Not. R. Astron. Soc.* **385**, 2269–2278 (2008)
- G.V. Panopoulou, K. Tassis, P.F. Goldsmith, M.H. Heyer,  $^{13}\text{CO}$  filaments in the Taurus molecular cloud. *Month. Not. R. Astron. Soc.* **444**, 2507–2524 (2014). doi:10.1093/mnras/stu1601
- T. Passot, E. Vázquez-Semadeni, The correlation between magnetic pressure and density in compressible MHD turbulence. *Astron. Astrophys.* **398**, 845–855 (2003). doi:10.1051/0004-6361:20021665
- T. Passot, E. Vazquez-Semadeni, A. Pouquet, A Turbulent Model for the Interstellar Medium. II. Magnetic Fields and Rotation. *Astrophys. J.* **455**, 536 (1995). doi:10.1086/176603
- S. Patsourakos, J.-C. Vial, Soho Contribution to Prominence Science. *Solar Phys.* **208**, 253–281 (2002). doi:10.1023/A:1020510120772
- H. Pécseli, O. Engvold, Modeling of prominence threads in magnetic fields: Levitation by incompressible MHD waves. *Solar Phys.* **194**, 73–86 (2000). doi:10.1023/A:1005242609261
- T. Penz, N.V. Erkaev, Y.N. Kulikov, D. Langmayr, H. Lammer, G. Micela, C. Cecchi-Pestellini, H.K. Biernat, F. Selsis, P. Barge, M. Deleuil, A. Léger, Mass loss from Hot Jupiters: Implications for CoRoT discoveries, Part II: Long time thermal atmospheric evaporation modeling. *PLSS* **56**, 1260–1272 (2008). doi:10.1016/j.pss.2008.04.005
- T.M.D. Pereira, B. De Pontieu, M. Carlsson, V. Hansteen, T.D. Tarbell, J. Lemen, A. Title, P. Boerner, N. Hurlburt, J.P. Wülser, J. Martínez-Sykora, L. Kleint, L. Golub, S. McKillop, K.K. Reeves, S. Saar, P. Testa, H. Tian, S. Jaeggli, C. Kankelborg, An Interface Region Imaging Spectrograph First View on Solar Spicules. *Astrophys. J. Lett.* **792**, 15 (2014). doi:10.1088/2041-8205/792/1/L15
- N. Peretto, P. Hennebelle, P. André, Probing the formation of intermediate- to high-mass stars in protoclusters. II. Comparison between millimeter interferometric observations of NGC 2264-C and SPH simulations of a collapsing clump. *Astron. Astrophys.* **464**, 983–994 (2007). doi:10.1051/0004-6361:20065653
- N. Peretto, G.A. Fuller, A. Duarte-Cabral, A. Avison, P. Hennebelle, J.E. Pineda, P. André, S. Bontemps, F. Motte, N. Schneider, S. Molinari, Global collapse of molecular clouds as a formation mechanism for the most massive stars. *Astron. Astrophys.* **555**, 112 (2013). doi:10.1051/0004-6361/201321318
- J.J. Perry, Y.H. Kim, J.L. Fox, H.S. Porter, Chemistry of the Jovian auroral ionosphere. *Journal of Geophys. Res.* **104**, 16541–16566 (1999). doi:10.1029/1999JE900022
- R.F. Pfaff, The Near-Earth Plasma Environment. *Space Sci. Rev.* **168**, 23–112 (2012). doi:10.1007/s11214-012-9872-6
- J.M. Picone, A.E. Hedin, D.P. Drob, A.C. Aikin, NRLMSISE-00 empirical model of the atmosphere: Statistical comparisons and scientific issues. *Journal of Geophysical Research (Space Physics)* **107**, 1468 (2002). doi:10.1029/2002JA009430
- J.H. Piddington, Solar atmospheric heating by hydromagnetic waves. *Month. Not. R. Astron. Soc.* **116**, 314 (1956)
- S. Poedts, M. Goossens, W. Kerner, Numerical simulation of coronal heating by resonant absorption of Alfvén waves. *Solar Phys.* **123**, 83–115 (1989). doi:10.1007/BF00150014
- S. Poedts, M. Goossens, W. Kerner, On the efficiency of coronal loop heating by resonant absorption. *Astrophys. J.* **360**, 279–287 (1990). doi:10.1086/169118
- R. Prange, D. Rego, J.-C. Gérard, Auroral Lyman  $\text{H}\alpha$  and  $\text{H}\beta$  bands from the giant planets: 2. effect of the anisotropy of the precipitating particles on the interpretation of the color ratio. *Journal of Geophysical Research: Planets* **100**(E4), 7513–7521 (1995). doi:10.1029/94JE03176. <http://dx.doi.org/10.1029/94JE03176>
- W.H. Press, S.A. Teukolsky, W.T. Vetterling, B.P. Flannery, *Numerical recipes in C. The art of scientific computing* 1992
- S. Preusse, A. Kopp, J. Büchner, U. Motschmann, Stellar wind regimes of close-in extrasolar planets. *Astron. Astrophys.* **434**, 1191–1200 (2005). doi:10.1051/0004-6361:20041680
- G.W. Prölss, *Physics of the Earth's Space Environment: an introduction* (Springer-Verlag Berlin Heidelberg, 2004)

- A. Radioti, D. Grodent, J.-C. GÃ©rard, E. Roussos, C. Paranicas, B. Bonfond, D.G. Mitchell, N. Krupp, S. Krimigis, J.T. Clarke, Transient auroral features at Saturn: Signatures of energetic particle injections in the magnetosphere. *Journal of Geophysical Research: Space Physics* **114**(A3), (2009). A03210. doi:10.1029/2008JA013632. <http://dx.doi.org/10.1029/2008JA013632>
- L.C. Ray, R.E. Ergun, P.A. Delamere, F. Bagenal, Magnetosphere-ionosphere coupling at Jupiter: Effect of field-aligned potentials on angular momentum transport. *Journal of Geophysical Research: Space Physics* **115**(A9), (2010). A09211. doi:10.1029/2010JA015423. <http://dx.doi.org/10.1029/2010JA015423>
- L.C. Ray, R.E. Ergun, P.A. Delamere, F. Bagenal, Magnetosphere-ionosphere coupling at Jupiter: A parameter space study. *Journal of Geophysical Research: Space Physics* **117**(A1), (2012). A01205. doi:10.1029/2011JA016899. <http://dx.doi.org/10.1029/2011JA016899>
- M.H. Rees, D. Lummerzheim, Characteristics of auroral electron precipitation derived from optical spectroscopy. *Journal of Geophysical Research: Space Physics* **94**(A6), 6799–6815 (1989). doi:10.1029/JA094iA06p06799. <http://dx.doi.org/10.1029/JA094iA06p06799>
- D. Rego, R. Prange, J.C. Gerard, Auroral Lyman  $\alpha$  and H $\beta$  bands from the giant planets: 1. excitation by proton precipitation in the jovian atmosphere. *Journal of Geophysical Research: Planets* **99**(E8), 17075–17094 (1994). doi:10.1029/93JE03432. <http://dx.doi.org/10.1029/93JE03432>
- A. Reiners, U.R. Christensen, A magnetic field evolution scenario for brown dwarfs and giant planets. *Astron. Astrophys.* **522**, 13 (2010). doi:10.1051/0004-6361/201014251
- H. Rishbeth, O.K. Garriott, *Introduction to ionospheric physics* 1969
- L. Rouppe van der Voort, J. Leenaarts, B. de Pontieu, M. Carlsson, G. Vissers, On-disk Counterparts of Type II Spicules in the Ca II 854.2 nm and H $\alpha$  Lines. *Astrophys. J.* **705**, 272–284 (2009). doi:10.1088/0004-637X/705/1/272
- V.A. Rozhansky, L.D. Tsedin, *Transport phenomena in partially ionized plasma* (Taylor & Francis, London and New York, 2001)
- M.S. Ruderman, A.N. Wright, Structure of driven Alfvén waves with oblique magnetic field and dissipation. *Physics of Plasmas* **6**, 649–659 (1999). doi:10.1063/1.873300
- A.J.B. Russell, L. Fletcher, Propagation of Alfvénic Waves from Corona to Chromosphere and Consequences for Solar Flares. *Astrophys. J.* **765**, 81 (2013). doi:10.1088/0004-637X/765/2/81
- R.J. Rutten, *Radiative Transfer in Stellar Atmospheres* (Lecture Notes Utrecht University, ???, 2003)
- D. Ryu, T.W. Jones, A. Frank, Numerical Magnetohydrodynamics in Astrophysics: Algorithm and Tests for Multidimensional Flow. *Astrophys. J.* **452**, 785 (1995). doi:10.1086/176347
- M. Ryutova, T. Berger, Z. Frank, T. Tarbell, A. Title, Observation of Plasma Instabilities in Quiescent Prominences. *Solar Phys.* **267**, 75–94 (2010). doi:10.1007/s11207-010-9638-9
- H. Sakai J.; Washimi, 1984, A dynamical model of solar prominences with current sheet. Joint U.S.-Japan Seminar. Kyoto. Japan
- T. Sakurai, M. Goossens, J.V. Hollweg, Resonant behaviour of MHD waves on magnetic flux tubes. I - Connection formulae at the resonant surfaces. *Solar Phys.* **133**, 227–245 (1991). doi:10.1007/BF00149888
- A. Sánchez-Lavega, The Magnetic Field in Giant Extrasolar Planets. *Astrophys. J. Lett.* **609**, 87–90 (2004). doi:10.1086/422840
- T. Sano, J. Stone, The Effect of the Hall Term on the Nonlinear Evolution of the Magnetorotational Instability. II. Saturation Level and Critical Magnetic Reynolds Number. *Astrophys. J.* **577**, 534–553 (2002a). doi:10.1086/342172
- T. Sano, J.M. Stone, The Effect of the Hall Term on the Nonlinear Evolution of the Magnetorotational Instability. I. Local Axisymmetric Simulations. *Astrophys. J.* **570**, 314–328 (2002b). doi:10.1086/339504
- R. Santos-Lima, E.M. de Gouveia Dal Pino, A. Lazarian, The Role of Turbulent Magnetic Reconnection in the Formation of Rotationally Supported Protostellar Disks. *Astrophys. J.* **747**, 21 (2012). doi:10.1088/0004-637X/747/1/21
- G.B. Scharmer, K. Bjelksjo, T.K. Korhonen, B. Lindberg, B. Petterson, The 1-meter Swedish solar telescope, in *Innovative Telescopes and Instrumentation for Solar Astrophysics*, vol. 4853, ed. by S.L. Keil, S.V. Avakyan, 2003, pp. 341–350
- N. Schneider, T. Csengeri, S. Bontemps, F. Motte, R. Simon, P. Hennebelle, C. Federrath, R. Klessen, Dynamic star formation in the massive DR21 filament. *Astron. Astrophys.* **520**,

- 49 (2010). doi:10.1051/0004-6361/201014481
- R.W. Schunk, A.F. Nagy, *Ionospheres: Physics, Plasma Physics, and Chemistry*. Cambridge Atmospheric and Space Science Series (Cambridge University Press, ???, 2004). ISBN 9780521607704
- D. Seifried, R. Banerjee, R.E. Pudritz, R.S. Klessen, Disc formation in turbulent massive cores: circumventing the magnetic braking catastrophe. *Month. Not. R. Astron. Soc.* **423**, 40–44 (2012). doi:10.1111/j.1745-3933.2012.01253.x
- H.K. Sen, M.L. White, A Physical Mechanism for the Production of Solar Flares. *Solar Phys.* **23**, 146–154 (1972). doi:10.1007/BF00153898
- I.F. Shaikhislamov, M.L. Khodachenko, Y.L. Sasunov, H. Lammer, K.G. Kislyakova, N.V. Erkaev, Atmosphere Expansion and Mass Loss of Close-orbit Giant Exoplanets Heated by Stellar XUV. I. Modeling of Hydrodynamic Escape of Upper Atmospheric Material. *Astrophys. J.* **795**, 132 (2014). doi:10.1088/0004-637X/795/2/132
- S. Shelyag, E. Khomenko, A. de Vicente, D. Przybylski, Heating of the Partially Ionized Solar Chromosphere by Waves in Magnetic Structures. *Astrophys. J. Lett.* **819**, 11 (2016). doi:10.3847/2041-8205/819/1/L11
- V.I. Shematovich, Formation of complex chemical species in astrochemistry (a review). *Solar System Research* **46**, 391–407 (2012). doi:10.1134/S0038094612060068
- K. Shibata, T. Nakamura, T. Matsumoto, K. Otsuji, T.J. Okamoto, N. Nishizuka, T. Kawate, H. Watanabe, S. Nagata, S. UeNo, R. Kitai, S. Nozawa, S. Tsuneta, Y. Suematsu, K. Ichimoto, T. Shimizu, Y. Katsukawa, T.D. Tarbell, T.E. Berger, B.W. Lites, R.A. Shine, A.M. Title, Chromospheric Anemone Jets as Evidence of Ubiquitous Reconnection. *Science* **318**, 1591 (2007). doi:10.1126/science.1146708
- A.P. Showman, T. Guillot, Atmospheric circulation and tides of “51 Pegasus b-like” planets. *Astron. Astrophys.* **385**, 166–180 (2002). doi:10.1051/0004-6361:20020101
- F.H. Shu, Ambipolar diffusion in self-gravitating isothermal layers. *Astrophys. J.* **273**, 202–213 (1983). doi:10.1086/161359
- F.H. Shu, *The physics of astrophysics. Volume II: Gas dynamics*. 1992
- F.H. Shu, F.C. Adams, S. Lizano, Star formation in molecular clouds - Observation and theory. *Ann. Rev. Astron. Astrophys.* **25**, 23–81 (1987). doi:10.1146/annurev.aa.25.090187.000323
- R.P. Singhal, S.C. Chakravarty, A. Bhardwaj, B. Prasad, Energetic electron precipitation in jupiter’s upper atmosphere. *Journal of Geophysical Research: Planets* **97**(E11), 18245–18256 (1992). doi:10.1029/92JE01894. <http://dx.doi.org/10.1029/92JE01894>
- T.G. Slanger, T.E. Cravens, J. Crovisier, S. Miller, D.F. Strobel, Photoemission Phenomena in the Solar System. *Space Sci. Rev.* **139**, 267–310 (2008). doi:10.1007/s11214-008-9387-3
- P.D. Smith, J.I. Sakai, Chromospheric magnetic reconnection: two-fluid simulations of coalescing current loops. *Astron. Astrophys.* **486**, 569–575 (2008). doi:10.1051/0004-6361:200809624
- R. Soler, J. Terradas, Magnetohydrodynamic Kink Waves in Nonuniform Solar Flux Tubes: Phase Mixing and Energy Cascade to Small Scales. *Astrophys. J.* **803**, 43 (2015). doi:10.1088/0004-637X/803/1/43
- R. Soler, J. Andries, M. Goossens, Resonant Alfvén waves in partially ionized plasmas of the solar atmosphere. *Astron. Astrophys.* **537**, 84 (2012). doi:10.1051/0004-6361/201118235
- R. Soler, J.L. Ballester, T.V. Zaqarashvili, Overdamped Alfvén waves due to ion-neutral collisions in the solar chromosphere. *Astron. Astrophys.* **573**, 79 (2015a). doi:10.1051/0004-6361/201423930
- R. Soler, M. Carbonell, J.L. Ballester, On the Spatial Scales of Wave Heating in the Solar Chromosphere. *Astrophys. J.* **810**, 146 (2015b). doi:10.1088/0004-637X/810/2/146
- R. Soler, R. Oliver, J.L. Ballester, Nonadiabatic Magnetohydrodynamic Waves in a Cylindrical Prominence Thread with Mass Flow. *Astrophys. J.* **684**, 725–735 (2008). doi:10.1086/590244
- R. Soler, R. Oliver, J.L. Ballester, Magnetohydrodynamic Waves in a Partially Ionized Filament Thread. *Astrophys. J.* **699**, 1553–1562 (2009a). doi:10.1088/0004-637X/699/2/1553
- R. Soler, R. Oliver, J.L. Ballester, Resonantly Damped Kink Magnetohydrodynamic Waves in a Partially Ionized Filament Thread. *Astrophys. J.* **707**, 662–670 (2009b). doi:10.1088/0004-637X/707/1/662
- R. Soler, R. Oliver, J.L. Ballester, Time damping of non-adiabatic magnetohydrodynamic waves in a partially ionized prominence plasma: effect of helium. *Astron. Astrophys.* **512**, 28 (2010). doi:10.1051/0004-6361/200913478
- R. Soler, R. Oliver, J.L. Ballester, Spatial Damping of Propagating Kink Waves in Prominence

- Threads. *Astrophys. J.* **726**, 102 (2011). doi:10.1088/0004-637X/726/2/102
- R. Soler, A.J. Díaz, J.L. Ballester, M. Goossens, Kelvin-Helmholtz Instability in Partially Ionized Compressible Plasmas. *Astrophys. J.* **749**, 163 (2012). doi:10.1088/0004-637X/749/2/163
- R. Soler, M. Carbonell, J.L. Ballester, J. Terradas, Alfvén Waves in a Partially Ionized Two-fluid Plasma. *Astrophys. J.* **767**, 171 (2013). doi:10.1088/0004-637X/767/2/171
- R. Soler, J. Terradas, R. Oliver, J.L. Ballester, The role of Alfvén wave heating in solar prominences. ArXiv e-prints (2016)
- P. Song, V.M. Vasyliūnas, Heating of the solar atmosphere by strong damping of Alfvén waves. *Journal of Geophysical Research (Space Physics)* **116**, 9104 (2011). doi:10.1029/2011JA016679
- P. Song, T.I. Gombosi, A.J. Ridley, Three-fluid Ohm's law. *Journal of Geophys. Res.* **106**, 8149–8156 (2001). doi:10.1029/2000JA000423
- R.F. Stein, Å. Nordlund, Simulations of Solar Granulation. I. General Properties. *Astrophys. J.* **499**, 914–933 (1998). doi:10.1086/305678
- A.C. Sterling, Solar Spicules: A Review of Recent Models and Targets for Future Observations - (Invited Review). *Solar Phys.* **196**, 79–111 (2000). doi:10.1023/A:1005213923962
- D.J. Stevenson, Planetary magnetic fields. *Reports on Progress in Physics* **46**, 555–557 (1983). doi:10.1088/0034-4885/46/5/001
- D.J. Stevenson, Planetary magnetic fields. *Earth and Planetary Science Letters* **208**, 1–11 (2003). doi:10.1016/S0012-821X(02)01126-3
- J.M. Stone, T. Gardiner, Nonlinear evolution of the magnetohydrodynamic Rayleigh-Taylor instability. *Physics of Fluids* **19**(9), 094104–094104 (2007). doi:10.1063/1.2767666
- J.M. Stone, E.C. Ostriker, C.F. Gammie, Dissipation in Compressible Magnetohydrodynamic Turbulence. *Astrophys. J. Lett.* **508**, 99–102 (1998). doi:10.1086/311718
- G. Strang, On the Construction and Comparison of Difference Schemes. *SIAM Journal on Numerical Analysis* **5**, 506–517 (1968). doi:10.1137/0705041
- D.J. Strickland, R.E. Daniell Jr., J.R. Jasperse, B. Basu, Transport-theoretic model for the electron-proton-hydrogen atom aurora. 2: Model results. *Journal of Geophys. Res.* **98**, 21 (1993). doi:10.1029/93JA01645
- A. Strugarek, A.S. Brun, S.P. Matt, V. Réville, Magnetic Games between a Planet and Its Host Star: The Key Role of Topology. *Astrophys. J.* **815**, 111 (2015). doi:10.1088/0004-637X/815/2/111
- Y. Suematsu, K. Shibata, T. Neshikawa, R. Kitai, Numerical hydrodynamics of the jet phenomena in the solar atmosphere. I - Spicules. *Solar Phys.* **75**, 99–118 (1982). doi:10.1007/BF00153464
- C. Tao, S.V. Badman, M. Fujimoto, UV and IR auroral emission model for the outer planets: Jupiter and Saturn comparison. *Icarus* **213**, 581–592 (2011). doi:10.1016/j.icarus.2011.04.001
- J.A. Tataronis, Energy absorption in the continuous spectrum of ideal MHD. *Journal of Plasma Physics* **13**, 87–105 (1975). doi:10.1017/S0022377800025897
- J. Terradas, R. Oliver, J.L. Ballester, Damped Coronal Loop Oscillations: Time-dependent Results. *Astrophys. J.* **642**, 533–540 (2006). doi:10.1086/500730
- J. Terradas, R. Molowny-Horas, E. Wiehr, H. Balthasar, R. Oliver, J.L. Ballester, Two-dimensional distribution of oscillations in a quiescent solar prominence. *Astron. Astrophys.* **393**, 637–647 (2002). doi:10.1051/0004-6361:20020967
- J. Terradas, R. Soler, A.J. Díaz, R. Oliver, J.L. Ballester, Magnetohydrodynamic Waves in Two-dimensional Prominences Embedded in Coronal Arcades. *Astrophys. J.* **778**, 49 (2013). doi:10.1088/0004-637X/778/1/49
- J. Terradas, R. Soler, R. Oliver, J.L. Ballester, On the Support of Neutrals Against Gravity in Solar Prominences. *Astrophys. J. Lett.* **802**, 28 (2015). doi:10.1088/2041-8205/802/2/L28
- J.P. Thayer, High-latitude currents and their energy exchange with the ionosphere-thermosphere system. *Journal of Geophys. Res.* **105**, 23015–23024 (2000). doi:10.1029/1999JA000409
- F. Tian, O.B. Toon, A.A. Pavlov, H. De Sterck, Transonic Hydrodynamic Escape of Hydrogen from Extrasolar Planetary Atmospheres. *Astrophys. J.* **621**, 1049–1060 (2005). doi:10.1086/427204
- W.J. Tirry, M. Goossens, Quasi-Modes as Dissipative Magnetohydrodynamic Eigenmodes: Results for One-dimensional Equilibrium States. *Astrophys. J.* **471**, 501 (1996). doi:10.1086/177986



- G.Z. Tóth, Test of the weak cosmic censorship conjecture with a charged scalar field and dyonic Kerr-Newman black holes. *General Relativity and Gravitation* **44**, 2019–2035 (2012). doi:10.1007/s10714-012-1374-z
- G. Tóth, Y. Ma, T.I. Gombosi, Hall magnetohydrodynamics on block-adaptive grids. *Journal of Computational Physics* **P227**(14), 6967–6984 (2008). doi:http://dx.doi.org/10.1016/j.jcp.2008.04.010. http://www.sciencedirect.com/science/article/pii/S0021999108002076
- G.B. Trammell, P. Arras, Z.-Y. Li, Hot Jupiter Magnetospheres. *Astrophys. J.* **728**, 152 (2011). doi:10.1088/0004-637X/728/2/152
- G.B. Trammell, Z.-Y. Li, P. Arras, Magnetohydrodynamic Simulations of Hot Jupiter Upper Atmospheres. *Astrophys. J.* **788**, 161 (2014). doi:10.1088/0004-637X/788/2/161
- Y.T. Tsap, A.V. Stepanov, Y.G. Kopylova, Energy Flux of Alfvén Waves in Weakly Ionized Plasma and Coronal Heating of the Sun. *Solar Phys.* **270**, 205–211 (2011). doi:10.1007/s11207-011-9727-4
- G. Tsiroula, K. Tziotziou, I. Kontogiannis, M.S. Madjarska, J.G. Doyle, Y. Suematsu, Solar Fine-Scale Structures. I. Spicules and Other Small-Scale, Jet-Like Events at the Chromospheric Level: Observations and Physical Parameters. *Space Sci. Rev.* **169**, 181–244 (2012). doi:10.1007/s11214-012-9920-2
- Y. Tsukamoto, K. Iwasaki, S.-i. Inutsuka, An explicit scheme for ohmic dissipation with smoothed particle magnetohydrodynamics. *Month. Not. R. Astron. Soc.* **434**, 2593–2599 (2013). doi:10.1093/mnras/stt1205
- A.V. Usmanov, W.H. Matthaeus, B.A. Breech, M.L. Goldstein, Solar Wind Modeling with Turbulence Transport and Heating. *Astrophys. J.* **727**, 84 (2011). doi:10.1088/0004-637X/727/2/84
- A. Vanderburg, D.W. Latham, L.A. Buchhave, A. Bieryla, P. Berlind, M.L. Calkins, G.A. Esquerdo, S. Welsh, J.A. Johnson, Planetary Candidates from the First Year of the K2 Mission. *ArXiv e-prints* (2015)
- K. Vanninathan, M.S. Madjarska, E. Scullion, J.G. Doyle, Off-limb (Spicule) DEM Distribution from SoHO/SUMER Observations. *Solar Phys.* **280**, 425–434 (2012). doi:10.1007/s11207-012-9986-8
- B.J. Vasquez, Resonant absorption of an Alfvén wave: Hybrid simulations. *Journal of Geophysical Research (Space Physics)* **110**, 10–02 (2005). doi:10.1029/2004JA010872
- V.M. Vasyliūnas, The physical basis of ionospheric electrodynamics. *Annales Geophysicae* **30**, 357–369 (2012). doi:10.5194/angeo-30-357-2012
- V.M. Vasyliūnas, P. Song, Meaning of ionospheric Joule heating. *Journal of Geophys. Res.* **110**, 20302 (2005). doi:10.1029/2004JA010615
- E. Vázquez-Semadeni, Energy Budget and the Virial Theorem in Interstellar Clouds, in *Millimeter-Wave Astronomy: Molecular Chemistry & Physics in Space.*, ed. by W.F. Wall, A. Carramiñana, L. Carrasco *Astrophysics and Space Science Library*, vol. 241, 1999, p. 143. doi:10.1007/978-94-011-4714-9-8
- E. Vázquez-Semadeni, E.C. Ostriker, T. Passot, C.F. Gammie, J.M. Stone, Compressible MHD Turbulence: Implications for Molecular Cloud and Star Formation. *Protostars and Planets IV*, 3 (2000)
- E. Vázquez-Semadeni, J. Kim, M. Shadmehri, J. Ballesteros-Paredes, The Lifetimes and Evolution of Molecular Cloud Cores. *Astrophys. J.* **618**, 344–359 (2005). doi:10.1086/425951
- E. Vázquez-Semadeni, D. Ryu, T. Passot, R.F. González, A. Gazol, Molecular Cloud Evolution. I. Molecular Cloud and Thin Cold Neutral Medium Sheet Formation. *Astrophys. J.* **643**, 245–259 (2006). doi:10.1086/502710
- E. Vázquez-Semadeni, G.C. Gómez, A.K. Jappsen, J. Ballesteros-Paredes, R.F. González, R.S. Klessen, Molecular Cloud Evolution. II. From Cloud Formation to the Early Stages of Star Formation in Decaying Conditions. *Astrophys. J.* **657**, 870–883 (2007). doi:10.1086/510771
- E. Vázquez-Semadeni, G.C. Gómez, A.-K. Jappsen, J. Ballesteros-Paredes, R.S. Klessen, High and Low-Mass Star-Forming Regions from Hierarchical Gravitational Fragmentation. High Local Star Formation Rates with Low Global Efficiencies. *Astrophys. J.* **707**, 1023–1033 (2009). doi:10.1088/0004-637X/707/2/1023
- E. Vázquez-Semadeni, P. Colín, G.C. Gómez, J. Ballesteros-Paredes, A.W. Watson, Molecular Cloud Evolution. III. Accretion Versus Stellar Feedback. *Astrophys. J.* **715**, 1302–1317 (2010). doi:10.1088/0004-637X/715/2/1302
- E. Vázquez-Semadeni, R. Banerjee, G.C. Gómez, P. Hennebelle, D. Duffin, R.S. Klessen, Molecular cloud evolution - IV. Magnetic fields, ambipolar diffusion and the star for-

- mation efficiency. *Month. Not. R. Astron. Soc.* **414**, 2511–2527 (2011). doi:10.1111/j.1365-2966.2011.18569.x
- J.-C. Vial, O. Engvold (eds.), *Solar Prominences*, in *Astrophysics and Space Science Library*, Astrophysics and Space Science Library, vol. 415 2015. doi:10.1007/978-3-319-10416-4
- A. Vidal-Madjar, A. Lecavelier des Etangs, J.-M. Désert, G.E. Ballester, R. Ferlet, G. Hébrard, M. Mayor, An extended upper atmosphere around the extrasolar planet HD209458b. *Nature* **422**, 143–146 (2003). doi:10.1038/nature01448
- A. Vidal-Madjar, J.-M. Désert, A. Lecavelier des Etangs, G. Hébrard, G.E. Ballester, D. Ehrenreich, R. Ferlet, J.C. McConnell, M. Mayor, C.D. Parkinson, Detection of Oxygen and Carbon in the Hydrodynamically Escaping Atmosphere of the Extrasolar Planet HD 209458b. *Astrophys. J. Lett.* **604**, 69–72 (2004). doi:10.1086/383347
- A. Vögler, S. Shelyag, M. Schüssler, F. Cattaneo, T. Emonet, T. Linde, Simulations of magnetoconvection in the solar photosphere. Equations, methods, and results of the MURaM code. *Astron. Astrophys.* **429**, 335–351 (2005). doi:10.1051/0004-6361:20041507
- J. Vranjes, P.S. Krstic, Collisions, magnetization, and transport coefficients in the lower solar atmosphere. *Å* **554**, 22 (2013)
- J. Vranjes, S. Poedts, B.P. Pandey, B. de Pontieu, Energy flux of Alfvén waves in weakly ionized plasma. *Astron. Astrophys.* **478**, 553–558 (2008). doi:10.1051/0004-6361:20078274
- J.H. Waite, T.E. Cravens, J. Kozyra, A.F. Nagy, S.K. Atreya, R.H. Chen, Electron precipitation and related aeronomy of the jovian thermosphere and ionosphere. *Journal of Geophysical Research: Space Physics* **88**(A8), 6143–6163 (1983). doi:10.1029/JA088iA08p06143. <http://dx.doi.org/10.1029/JA088iA08p06143>
- M. Wardle, C. Ng, The conductivity of dense molecular gas. *Month. Not. R. Astron. Soc.* **303**, 239–246 (1999). doi:10.1046/j.1365-8711.1999.02211.x
- A.J. Watson, T.M. Donahue, J.C.G. Walker, The dynamics of a rapidly escaping atmosphere - Applications to the evolution of earth and Venus. *Icarus* **48**, 150–166 (1981). doi:10.1016/0019-1035(81)90101-9
- C. Watson, E.G. Zweibel, F. Heitsch, E. Churchwell, Kelvin-Helmholtz Instability in a Weakly Ionized Medium. *Astrophys. J.* **608**, 274–281 (2004). doi:10.1086/392500
- R.W. Wilson, K.B. Jefferts, A.A. Penzias, Carbon Monoxide in the Orion Nebula. *Astrophys. J. Lett.* **161**, 43 (1970). doi:10.1086/180567
- B.E. Wood, H.-R. Müller, G.P. Zank, J.L. Linsky, Measured Mass-Loss Rates of Solar-like Stars as a Function of Age and Activity. *Astrophys. J.* **574**, 412–425 (2002). doi:10.1086/340797
- B.E. Wood, H.-R. Müller, G.P. Zank, J.L. Linsky, S. Redfield, New Mass-Loss Measurements from Astrophysical Ly $\alpha$  Absorption. *Astrophys. J. Lett.* **628**, 143–146 (2005). doi:10.1086/432716
- T.I. Woodward, J.F. McKenzie, Stationary incompressible MHD perturbations generated by a current source in a moving plasma. *PLSS* **47**, 545–555 (1999). doi:10.1016/S0032-0633(98)00134-2
- R.V. Yelle, Aeronomy of extra-solar giant planets at small orbital distances. *Icarus* **170**, 167–179 (2004). doi:10.1016/j.icarus.2004.02.008
- R.V. Yelle, S. Miller, Jupiter’s thermosphere and ionosphere, ed. by F. Bagenal, T.E. Dowling, W.B. McKinnon 2004, pp. 185–218
- L. Yin, D. Winske, S.P. Gary, J. Birn, Hybrid and hall-mhd simulations of collisionless reconnection: Dynamics of the electron pressure tensor. *Journal of Geophysical Research: Space Physics* **106**(A6), 10761–10775 (2001). doi:10.1029/2000JA000398. <http://dx.doi.org/10.1029/2000JA000398>
- V.V. Zaitsev, M.L. Khodachenko, Dynamical Regimes and the Possibility of Microflares in a Prominence. *Sov. Astron.* **36**, 81 (1992)
- M. Zamora-Avilés, E. Vázquez-Semadeni, An Evolutionary Model for Collapsing Molecular Clouds and their Star Formation Activity. II. Mass Dependence of the Star Formation Rate. *Astrophys. J.* **793**, 84 (2014). doi:10.1088/0004-637X/793/2/84
- M. Zamora-Avilés, E. Vázquez-Semadeni, P. Colín, An Evolutionary Model for Collapsing Molecular Clouds and Their Star Formation Activity. *Astrophys. J.* **751**, 77 (2012). doi:10.1088/0004-637X/751/1/77
- T.V. Zaqarashvili, Solar Spicules: Recent Challenges in Observations and Theory, in *American Institute of Physics Conference Series*, ed. by I. Zhelyazkov, T. Mishonov American Institute of Physics Conference Series, vol. 1356, 2011, pp. 106–116. doi:10.1063/1.3598099
- T.V. Zaqarashvili, R. Erdélyi, Oscillations and Waves in Solar Spicules. *Space Sci. Rev.* **149**, 355–388 (2009). doi:10.1007/s11214-009-9549-y

- 
- T.V. Zaqarashvili, M.L. Khodachenko, H.O. Rucker, Damping of Alfvén waves in solar partially ionized plasmas: effect of neutral helium in multi-fluid approach. *Astron. Astrophys.* **534**, 93 (2011a). doi:10.1051/0004-6361/201117380
- T.V. Zaqarashvili, M.L. Khodachenko, H.O. Rucker, Magnetohydrodynamic waves in solar partially ionized plasmas: two-fluid approach. *Astron. Astrophys.* **529**, 82 (2011b). doi:10.1051/0004-6361/201016326
- T.V. Zaqarashvili, M.L. Khodachenko, R. Soler, Torsional Alfvén waves in partially ionized solar plasma: effects of neutral helium and stratification. *Astron. Astrophys.* **549**, 113 (2013). doi:10.1051/0004-6361/201220272
- T.V. Zaqarashvili, Z. Vörös, I. Zhelyazkov, Kelvin-Helmholtz instability of twisted magnetic flux tubes in the solar wind. *Astron. Astrophys.* **561**, 62 (2014). doi:10.1051/0004-6361/201322808
- T.V. Zaqarashvili, I. Zhelyazkov, L. Ofman, Stability of Rotating Magnetized Jets in the Solar Atmosphere. I. Kelvin-Helmholtz Instability. *Astrophys. J.* **813**, 123 (2015). doi:10.1088/0004-637X/813/2/123
- T.V. Zaqarashvili, E. Khutsishvili, V. Kukhianidze, G. Ramishvili, Doppler-shift oscillations in solar spicules. *Astron. Astrophys.* **474**, 627–632 (2007). doi:10.1051/0004-6361:20077661
- T.V. Zaqarashvili, A.J. Díaz, R. Oliver, J.L. Ballester, Instability of twisted magnetic tubes with axial mass flows. *Astron. Astrophys.* **516**, 84 (2010). doi:10.1051/0004-6361/200913874
- T.V. Zaqarashvili, M. Carbonell, J.L. Ballester, M.L. Khodachenko, Cut-off wavenumber of Alfvén waves in partially ionized plasmas of the solar atmosphere. *Astron. Astrophys.* **544**, 143 (2012). doi:10.1051/0004-6361/201219763
- J.B. Zirker, O. Engvold, S.F. Martin, Counter-streaming gas flows in solar prominences as evidence for vertical magnetic fields. *Nature* **396**, 440–441 (1998). doi:10.1038/24798
- B. Zuckerman, N.J. Evans II, Models of massive molecular clouds. *Astrophys. J. Lett.* **192**, 149–152 (1974). doi:10.1086/181613
- B. Zuckerman, P. Palmer, Radio radiation from interstellar molecules. *Ann. Rev. Astron. Astrophys.* **12**, 279–313 (1974). doi:10.1146/annurev.aa.12.090174.001431